



HAL
open science

Synthesis of Metal-semiconductor Heterostructures by Laser Photodeposition

Fenghuan Zhao

► **To cite this version:**

Fenghuan Zhao. Synthesis of Metal-semiconductor Heterostructures by Laser Photodeposition. Material chemistry. Université de Bordeaux, 2022. English. NNT : 2022BORD0229 . tel-04678914

HAL Id: tel-04678914

<https://theses.hal.science/tel-04678914v1>

Submitted on 27 Aug 2024

HAL is a multi-disciplinary open access archive for the deposit and dissemination of scientific research documents, whether they are published or not. The documents may come from teaching and research institutions in France or abroad, or from public or private research centers.

L'archive ouverte pluridisciplinaire **HAL**, est destinée au dépôt et à la diffusion de documents scientifiques de niveau recherche, publiés ou non, émanant des établissements d'enseignement et de recherche français ou étrangers, des laboratoires publics ou privés.

THÈSE PRÉSENTÉE
POUR OBTENIR LE GRADE DE
DOCTEUR DE
L'UNIVERSITÉ DE BORDEAUX

ÉCOLE DOCTORALE DES SCIENCES CHIMIQUES
SPÉCIALITÉ : PHYSICO-CHIMIE DE LA MATIÈRE CONDENSÉE

Par Mme Fenghuan ZHAO

**Synthesis of Metal-semiconductor Heterostructures by
Laser Photodeposition**

Sous la direction de : Dr. Marie-Hélène DELVILLE,
Co-directeur : Dr. Jean-Pierre DELVILLE

Soutenue le : 18 Juillet 2022

Membres du jury :

Mme BEGIN Sylvie	Professeur	Université de Strasbourg	Rapporteur
M. COTTINEAU Thomas	Chargé de recherche	CNRS-Strasbourg	Rapporteur
M. HESEMANN Peter	Directeur de recherche	CNRS-Montpellier	Examineur
M. AYMONIER Cyril	Directeur de recherche	CNRS-Bordeaux	Examineur
Mme DELVILLE Marie-Hélène	Directeur de recherche	CNRS-Bordeaux	Directeur de thèse
M. DELVILLE Jean-Pierre	Directeur de recherche	CNRS-Bordeaux	Co-Directeur de thèse

Acknowledgments

This thesis would not have been accomplished without the continuous support from all the people who accompanied me during my four-year Ph.D. study at the University of Bordeaux. It is to them that I owe my deepest gratitude and every line I wrote permeates memories of the great times we spent together.

First of all, I would like to acknowledge my two supervisors, Dr. Marie-Hélène Delville and Dr. Jean-Pierre Delville, for their great support and patient guidance along the way and for what I have learned from their prudent scientific attitude and high sense of responsibility. They are a perfect match of a scientific couple that guided me to understand the principles of reactions from both chemical and physical perspectives. What I learned from them will be a treasure of my life. These unforgettable experiences will be definitely beneficial to my future career. I would also like to thank all jury members, Prof. Sylvie Begin, Dr. Thomas Cottineau, Dr. Peter Hesemann, and Dr. Cyril Aymonier, for devoting their precious time to evaluating my thesis.

During my Ph.D. I have also received much support and help from my colleagues in both ICMCB and LOMA. I want to thank my officemates Dr. Qingguo Bai and Dr. Junjie Hao for helping me solve problems I met in the lab as well as in daily life. Big thanks go to Mme Lydia Roudier for her support on TEM characterizations, and Mme Marion Gayot on EDX characterization. I would also like to thank everyone in ICMCB and LOMA, in particular, the entire group V and group Optofluidique for a great time we had together.

Life is not always about scientific research. I also enjoy the time, the friends, and the stories in Bordeaux. Here, I met many good friends, Naixin Kang, Junjing Che, Lei Hou, Chenhao Yao, Peizhao Liu, and Fujin Ma. Mengzhe Xiao and Fan Jiang, I also would like to thank you separately for being your neighbor and for helping me solve lots of administrative-related problems.

Lastly, I would like to thank my family, my husband, and my parents, especially my lovely daughter Junnuo. You are with me since I started my Ph.D. in 2018. Taking care of you while pursuing a Ph.D. is challenging. Whenever I'm about to give up, thinking

of you always made me energetic and recovered immediately.

Finally, I would like to acknowledge the China Scholarship Council for its financial support.

RESUME EN FRANCAIS

Au cours des derniers siècles, l'amélioration du niveau de vie a considérablement favorisé l'explosion démographique et la poursuite de la révolution industrielle, ce qui a entraîné une forte demande d'énergie provenant principalement de combustibles fossiles. L'utilisation de ces combustibles conventionnels entraîne une augmentation spectaculaire des émissions mondiales de CO₂ et une grave pollution de l'environnement. Au cours du dernier demi-siècle, les températures mondiales moyennes ont déjà augmenté d'environ 1,5 °C par rapport à l'époque préindustrielle,¹⁻² ce qui entraîne une fonte accélérée des glaciers et une augmentation du niveau des mers. Face à ces problèmes, il est urgent de développer une nouvelle énergie durable et respectueuse de l'environnement. Parmi les nombreuses énergies, l'énergie solaire a été considérée comme l'énergie propre la plus prometteuse en raison de sa grande accessibilité et de son approvisionnement inépuisable. La photocatalyse à base de semi-conducteurs est une technologie prometteuse pour convertir l'énergie solaire abondante en hydrogène ou en hydrocarbures utilisables et pour éliminer le dioxyde de carbone et dégrader les polluants.

La photocatalyse est l'utilisation de porteurs de charge photoexcités générés dans des semi-conducteurs pour augmenter la vitesse des réactions chimiques ou modifier leur sélectivité. Plus précisément, lorsque le photocatalyseur est irradié par une lumière incidente de fréquence appropriée, l'énergie photonique fait passer les électrons dans la bande de conduction, laissant ainsi les trous dans la bande de valence. Ces électrons ou trous générés sont ensuite utilisés efficacement pour un grand nombre d'applications, par exemple le traitement des eaux usées,³⁻⁴ la purification de l'air,⁵⁻⁸ la dégradation des colorants organiques,⁹⁻¹⁰ et la synthèse des combustibles solaires.¹¹⁻¹³ Bien que les photocatalyseurs semi-conducteurs soient

d'une grande importance dans ces domaines, la majorité d'entre eux (par ex, TiO_2 et ZnO) ont des bandes interdites extrêmement larges qui ne sont responsables que de la lumière UV qui ne représente que 4% du flux solaire.¹⁴ De plus, ils présentent des longueurs de diffusion courtes pour transmettre des porteurs de charge faibles, ce qui entrave considérablement la pleine utilisation de ces matériaux.¹⁴⁻¹⁵

Pour résoudre ces problèmes, les photocatalyseurs hybrides métal-semiconducteur ont attiré une attention croissante. La présence de nanoparticules métalliques (NPs) à la surface d'un semi-conducteur a deux grands impacts sur leurs propriétés photocatalytiques. Premièrement, elle peut supprimer de manière significative la recombinaison des excitons photogénérés.^{14, 16-18} Deuxièmement, en couplant les semi-conducteurs et les métaux avec une forte résonance plasmonique de surface localisée (LSPR), les efficacités de capture et d'absorption de la lumière des semi-conducteurs peuvent être considérablement améliorées,^{14, 16-18} À ce jour, diverses méthodes sont utilisées pour la fabrication de nanocristaux de métal-semiconducteur, par exemple la synthèse hydrothermale/solvothermale,¹⁹⁻²¹ l'échange d'ions,²²⁻²³ la photodéposition,^{4, 24-26} le dépôt-précipitation.²⁷⁻²⁸ Parmi ces stratégies, la photodéposition a attiré de plus en plus d'attention car cette méthode ne nécessite pas d'augmenter la température ou d'appliquer une tension.¹⁶ De plus, les principaux avantages de la photodéposition comprennent (i) un contrôle délicat de la distribution géométrique des nanoparticules métalliques (ND) à la surface des semi-conducteurs à facettes et (ii) une grande flexibilité dans le contrôle de la taille et de l'état d'oxydation des NP déposées en manipulant les précurseurs de réaction ainsi que la longueur d'onde et l'intensité de l'éclairage.¹⁶

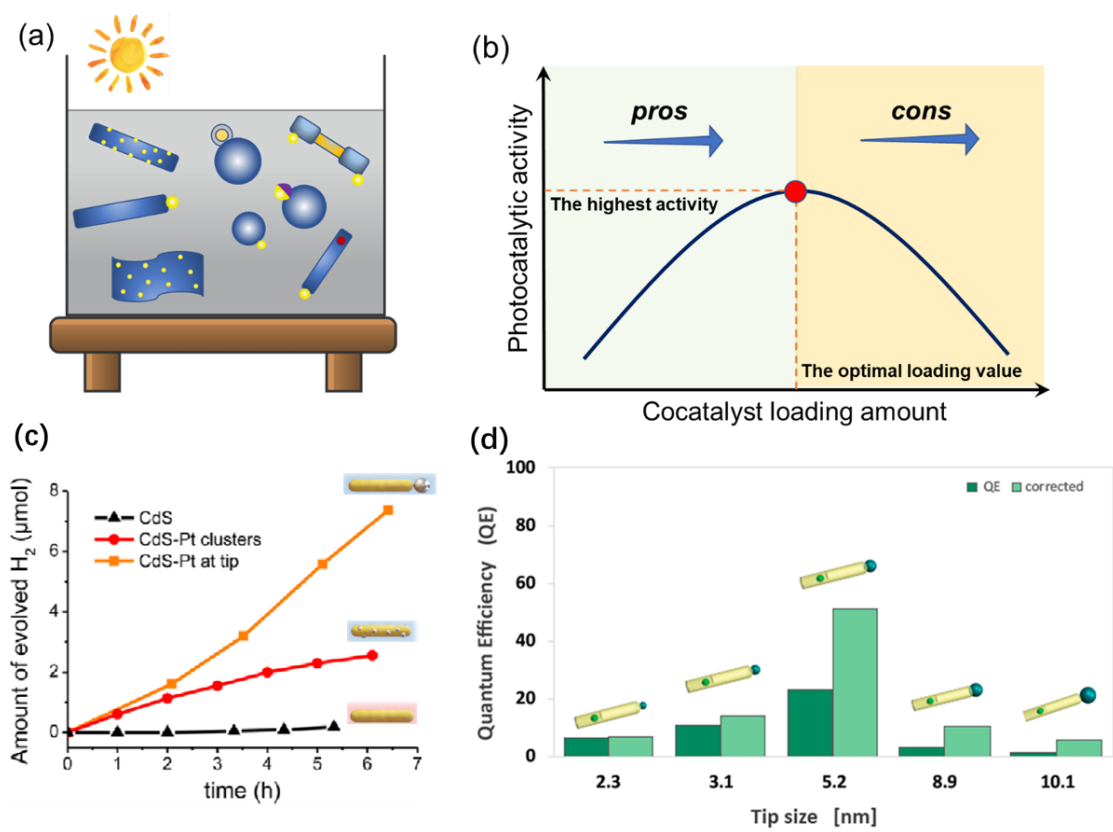


Figure 1. (a) Représentation schématique de différentes nanostructures contenant des NPs plasmoniques et des semi-conducteurs. (b) Variation de l'activité photocatalytique avec la quantité de cocatalyseur à la surface d'un photocatalyseur. Adapté de la réf.²⁹ (c) Génération photocatalytique de H₂ sur trois photocatalyseurs différents à base de nanorods de CdS : nanorods de CdS purs, nanorods de CdS décorés de plusieurs sites de Pt et nanorods de CdS décorés de pointes de Pt. Adapté de la réf.³⁰ (d) Efficacité quantique photocatalytique pour la demi-réaction de réduction de l'eau obtenue avec les photocatalyseurs nanorod CdSe@CdS décorés avec des pointes de Ni de différentes tailles. Efficacité quantique expérimentale dans les barres vert foncé, et efficacité quantique corrigée pour l'absorption du métal dans les barres vert clair. Adapté de la réf.³¹

Les techniques de photodéposition ont été largement adoptées pour charger divers métaux (par exemple, Ag, Au, Pt, etc.) sur des semi-conducteurs, notamment des oxydes métalliques (par exemple, TiO₂, ZnO, WO₃, etc.) et des chalcogénures métalliques (par exemple, CdS, Bi₂S₃, Cu_{2-x}S, etc.).^{14, 16, 18, 32-37} Cette technique a également été utilisée avec succès pour obtenir des particules cœur/coquille,³⁸⁻⁴⁰ des cocatalyseurs bimétalliques,^{7, 38} ou même des systèmes plus complexes, comme le montre la **figure 1a**.^{4, 41} En outre, les métaux peuvent également être chargés sur différents substrats avec diverses morphologies. (**Figure 1a**).

De nombreux chercheurs ont tenté d'optimiser la charge métallique pour générer des matériaux photocatalytiques efficaces.⁴²⁻⁴³ Comme le montre la figure 1b, l'activité photocatalytique augmente généralement avec la charge de métal déposée sur la surface du semi-conducteur. Cependant, l'activité diminue progressivement en raison d'une surcouverture de la surface du semi-conducteur par les métaux, ce qui bloque les sites actifs pour la réaction photoredox ainsi que la lumière d'atteindre les photocatalyseurs.^{16, 29} De plus, si les charges métalliques sont trop élevées, les ND métalliques peuvent également agir comme des centres de recombinaison des charges, empêchant ainsi les électrons libres ou les trous d'atteindre les réactions photocatalytiques.^{16, 29} Stolarczyk *et al.*,³⁰ ont fait varier la décoration des nanoparticules de Pt sur les nanorods de CdS et ont découvert que les nanorods de CdS décorés de pointes de Pt sont les plus actifs pour la production d'hydrogène (**Figure 1c**). Nakibli et ses collègues³¹ ont étudié des nanorods CdSe@CdS décorés de Ni avec différentes tailles de pointe, et une taille optimale de domaine métallique de 5,2 nm a été obtenue (**Figure 1d**). Ils ont révélé que la nature d'une nanojonction formée entre un nanorod semi-conducteur et un cocatalyseur de nanoparticules métalliques est sensible à la taille de la particule métallique, comme le reflète l'activité de production d'hydrogène, le rendement quantique de l'émission et la quantité de séparation de charge. Par conséquent, il est très important de contrôler précisément le nombre de sites métalliques et la taille du métal sur la surface du semi-conducteur.^{26, 44} En raison de leur faible intensité de puissance, les réactions ont ensuite pris plusieurs heures pour achever le dépôt de nanodots métalliques, et les métaux chargés avaient généralement une taille assez petite (moins de 3 nm).⁴⁴⁻⁴⁵ Cela rend extrêmement difficile l'étude de l'influence de la taille et de la forme du métal sur les propriétés photocatalytiques des produits obtenus. Ce problème peut être résolu en utilisant des lasers à haute énergie qui peuvent générer une intensité de flux de photons de plusieurs ordres de grandeur supérieure à celle des lampes prototypes.^{24, 46} Par conséquent, un grand nombre d'électrons photogénérés peuvent être produits en peu de temps et être ensuite utilisés pour réduire les ions métalliques sur les surfaces semi-conductrices à un taux élevé. Par exemple, Bai *et al.*,²⁵ ont rapporté que

des nanohétérodimères (NHD) de métal (Ag et Au)-TiO₂ pouvaient être obtenus par photodéposition pilotée par laser dans un réacteur microfluidique continu. L'utilisation d'un faisceau laser focalisé d'une intensité aussi élevée que 430 W/cm² permet la formation de NDs métalliques d'une taille aussi grande que 14 nm en quelques secondes. Ils ont également montré que (i) la taille moyenne des NDs métalliques augmentait proportionnellement (avec une polydispersité stable autour de 20%) avec l'augmentation de la puissance d'excitation, et (ii) que la croissance des nano-points d'Ag sur TiO₂ pouvait être modélisée précisément. Cependant, le système de réaction est compliqué et la photodéposition se produit à une vitesse si élevée que l'étude de la nucléation et de la croissance précoce des nanoparticules métalliques est très difficile. Cet inconvénient peut être combattu en utilisant une cuvette au lieu d'un microcanal comme récipient de réaction. L'utilisation d'une cuvette réduit raisonnablement le flux de photons et ralentit donc la vitesse de réaction. En combinaison avec le système de réaction stable, la nucléation et la croissance des nano-points métalliques peuvent être facilement surveillées. Par exemple, Hao et al.²⁴ ont très récemment rapporté la photodéposition pilotée par laser de nano-points d'Ag sur des nanorods de CdSe/CdS. Ils ont montré que le nombre et la position spatiale des NDs d'Ag sur les nanorods pouvaient être finement ajustés. Ils peuvent faire des croissances en sites multiples, sur les deux pointes doubles et sur une seule pointe en manipulant le flux de photons traversant les cuvettes de réaction. De plus, la taille des nanoparticules d'Ag a été bien contrôlée, passant de moins de 3 nm à 9 nm en moins de 20 minutes. Ce système de réaction fournit une configuration idéale pour étudier efficacement la nucléation et la croissance de NDs métalliques sur des surfaces semi-conductrices.

Dans cette thèse, nous nous concentrons sur les réactions de photodéposition pilotée par laser de métaux sur des surfaces semi-conductrices dans une cellule de réaction à cuvette stable, en mettant l'accent sur la synthèse contrôlée et les mécanismes de réaction. Nous avons systématiquement étudié la photodéposition de divers métaux (par exemple Au, Ag et Pd) sur deux types de substrats semi-

conducteurs, à savoir les oxydes métalliques (TiO_2) en phase aqueuse et les chalcogénures métalliques ($\text{Cu}_{2-x}\text{S}/\text{CuInS}_2$) dans le toluène. Ces deux types de semi-conducteurs nous permettent (i) d'avoir une compréhension plus approfondie des mécanismes de formation de nanodots métalliques similaires sur différents substrats ainsi que (ii) d'étudier les influences du milieu réactionnel sur les réactions de photodéposition. Dans ce qui suit, nous présentons aux lecteurs une brève description de chaque chapitre et de ses interconnexions.

Dans le chapitre 1, nous décrivons les principes de base et passons en revue les avancées récentes dans la photodéposition de métaux sur deux types de substrats semi-conducteurs, à savoir les oxydes métalliques et les chalcogénures métalliques. Les facteurs clés fondamentaux pour la synthèse contrôlée ainsi que leur grand impact sur les activités photocatalytiques dans ces deux systèmes sont intensivement discutés. Nous mettons également en évidence plusieurs problèmes difficiles à résoudre et proposons quelques directions de recherche prospectives qui sont bénéfiques pour une meilleure compréhension du processus de photodéposition et une meilleure performance des activités photocatalytiques dans la récolte d'énergie, la catalyse et les applications environnementales. Dans le chapitre 2, nous présentons les deux montages différents construits et utilisés pour réaliser la photodéposition des nano-points métalliques sur des nanocristaux de TiO_2 et de $\text{Cu}_{2-x}\text{S}/\text{CuInS}_2$. L'utilisation de différents types de lumières pour les réactions de photodéposition, les paramètres détaillés et la configuration des montages construits seront décrits en détail. Dans les trois chapitres suivants, nous présenterons les résultats de la photodéposition de divers métaux à la surface des nanocristaux de TiO_2 . Dans le chapitre 3, nous présentons la photodéposition de particules d'au sur le TiO_2 . Les effets de nombreux paramètres sur la photodéposition sont étudiés pour tenter d'améliorer le rendement global de Janus des nanohétérodimères Au-TiO_2 et atteindre des valeurs proches de 100%. De plus, nous étudions le mécanisme d'adsorption des réactifs sur la surface du TiO_2 pendant le processus de photodéposition en modélisant les données expérimentales ; nous essayons également de faire la distinction entre la

physisportion et la chimisportion. Nous décrivons l'ensemble de la croissance de l'or jusqu'à son achèvement. Outre le dépôt d'or, nous avons également essayé la même procédure pour déposer des particules d'Ag, Pd sur TiO₂ dans le chapitre 4. Les effets de nombreux paramètres, par exemple le piègeur de trous (HS), le temps d'exposition, la puissance du laser et le précurseur sur le processus de photodéposition seront étudiés en détail. Dans le chapitre 5, nous présenterons une photodéposition en deux étapes de nanoparticules bimétalliques structurées en cœur-coquille Au@Au, Au@Ag et Au@Pd sur TiO₂. Pour le système Au@Au core@shell, la coquille Au peut être contrôlée avec précision et la taille et l'épaisseur du noyau et de la coquille Au répondent parfaitement à nos attentes. Pour le système Au@Ag, la coquille d'Ag obtenue était limitée à environ 1 nm d'épaisseur, ce qui était moins que prévu et résulte de la faible électronégativité de l'Ag (1,9) par rapport aux autres Au (2,4). Pour le système Au@Pd, le Pd a montré une croissance non isotrope sur le noyau d'Au, ce qui a donné lieu à une coquille de Pd non uniforme, ce qui est dû à la grande disparité de réseau entre Au et Pd. Dans le chapitre 6, nous nous intéresserons à la photodéposition de nano-points d'Au sur des hétéro-nanocristaux de Cu_{2-x}S/CuInS₂ dans le toluène. La distribution géométrique (par exemple, le nombre et l'emplacement) des NDs d'Au, ainsi que leurs tailles, peuvent être bien contrôlées en ajustant la concentration des piègeurs de trous et des précurseurs d'Au, la puissance d'illumination et le temps d'exposition. De plus, nous avons constaté que les NDs d'Au individuelles préfèrent se déposer d'abord sur les pointes des pièces de Cu_{2-x}S. Sous irradiation continue, ces Au NDs se comportent différemment de ceux déposés sur TiO₂ et semblent fusionner avec le substrat Cu_{2-x}S, ce qui entraîne une augmentation de la bande interdite et un réalignement des bandes avec CuInS₂. Cet alignement décalé des bandes favorise le flux d'électrons photogénérés de Cu_{2-x}S vers CuInS₂, ce qui entraîne le dépôt ultérieur des Au NDs sur le côté des parties allongées de CuInS₂.

La thèse se termine par les conclusions et les perspectives en résumant brièvement les résultats les plus essentiels que nous avons obtenus, et en proposant quelques

sujets de recherche prometteurs pour des études futures.

On peut se référer à l'annexe pour mieux comprendre le calcul théorique de la taille du métal (annexe 1) et les techniques de caractérisation (annexe 2).

References

1. GISS Surface Temperature Analysis (GISTEMP), version 4. <https://data.giss.nasa.gov/gistemp/> (accessed Oct 28).
2. Lenssen, N. J. L.; Schmidt, G. A.; Hansen, J. E.; Menne, M. J.; Persin, A.; Ruedy, R.; Zyss, D., Improvements in the GISTEMP Uncertainty Model. *J. Geophys. Res. Atmos.* **2019**, *124* (12), 6307-6326.
3. Park, J.; Deshmukh, P. R.; Sohn, Y.; Shin, W. G., ZnO-TiO₂ Core-Shell Nanowires Decorated with Au Nanoparticles for Plasmon-Enhanced Photoelectrochemical Water Splitting. *J. Alloys Compd.* **2019**, *787*, 1310-1319.
4. Ha, H. D.; Yan, C.; Katsoukis, G.; Kamat, G. A.; Moreno-Hernandez, I. A.; Frei, H.; Alivisatos, A. P., Precise Colloidal Plasmonic Photocatalysts Constructed by Multistep Photodepositions. *Nano Lett.* **2020**, *20* (12), 8661-8667.
5. Li, X.; Yu, J.; Jaroniec, M.; Chen, X., Cocatalysts for Selective Photoreduction of CO₂ Into Solar Fuels. *Chem. Rev.* **2019**, *119* (6), 3962-4179.
6. Chen, X.; Li, N.; Kong, Z.; Ong, W. J.; Zhao, X., Photocatalytic Fixation of Nitrogen to Ammonia: State-of-the-Art Advancements and Future Prospects. *Mater. Horiz.* **2018**, *5* (1), 9-27.
7. Yu, Y.; Dong, X. a.; Chen, P.; Geng, Q.; Wang, H.; Li, J.; Zhou, Y.; Dong, F., Synergistic Effect of Cu Single Atoms and Au-Cu Alloy Nanoparticles on TiO₂ for Efficient CO₂ Photoreduction. *ACS Nano* **2021**, *15* (9), 14453-14464.
8. Li, H.; Zhang, L.; Cao, Y., Synthesis of Palladium-Modified MnS Photocatalysts with Enhanced Photocatalytic Activity in the Photoreduction of CO₂ to CH₄. *Appl. Surf. Sci.* **2021**, *541*, 148519.
9. Ham, S.; Choi, D.; Jang, D.-J., Photodeposition of Gold Nanoparticles on ZnS Nanobelts for Enhanced Dye Decomposition. *Mater. Res. Bull.* **2019**, *116*, 32-39.
10. Kaushik, R.; Singh, P. K.; Halder, A., Modulation Strategies in Titania Photocatalyst for Energy Recovery and Environmental Remediation. *Catalysis Today* **2022**, *384-386*, 45-69.
11. Kosco, J.; Moruzzi, F.; Willner, B.; McCulloch, I., Photocatalysts Based on Organic Semiconductors with Tunable Energy Levels for Solar Fuel Applications. *Adv. Energy Mater.* **2020**, *10* (39), 2001935.
12. Sun, R.; Zhang, Z.; Li, Z.; Jing, L., Review on Photogenerated Hole Modulation Strategies in Photoelectrocatalysis for Solar Fuel Production. *ChemCatChem* **2019**, *11* (24), 5875-5884.
13. Kush, P.; Deka, S., Multifunctional Copper-Based Quaternary Chalcogenide Semiconductors Toward State-of-the-Art Energy Applications. *ChemNanoMat* **2019**, *5* (4), 373-402.
14. Zada, A.; Muhammad, P.; Ahmad, W.; Hussain, Z.; Ali, S.; Khan, M.; Khan, Q.; Maqbool, M., Surface Plasmonic-Assisted Photocatalysis and Optoelectronic Devices with Noble Metal Nanocrystals: Design, Synthesis, and Applications. *Adv. Funct. Mater.* **2020**, *30* (7), 1906744.
15. Tamirat, A. G.; Rick, J.; Dubale, A. A.; Su, W.-N.; Hwang, B.-J., Using Hematite for Photoelectrochemical Water Splitting: a Review of Current Progress and Challenges. *Nanoscale Horizons* **2016**, *1* (4), 243-267.
16. Wenderich, K.; Mul, G., Methods, Mechanism, and Applications of Photodeposition in Photocatalysis: A Review. *Chem. Rev.* **2016**, *116* (23), 14587-14619.
17. Kumar, A.; Choudhary, P.; Kumar, A.; Camargo, P. H. C.; Krishnan, V., Recent Advances in Plasmonic Photocatalysis Based on TiO₂ and Noble Metal Nanoparticles for Energy Conversion, Environmental Remediation, and Organic Synthesis. *Small* **2021**, 2101638.

18. Chakhtouna, H.; Benzeid, H.; Zari, N.; Qaiss, A.; Bouhfid, R., Recent Progress on Ag/TiO₂ Photocatalysts: Photocatalytic and Bactericidal Behaviors. *Environ. Sci. Pollut. Res.* **2021**, *28* (33), 44638-44666.
19. Zhang, Q.; Zhang, Y.; Xiao, K.; Meng, Z.; Tong, W.; Huang, H.; An, Q., Plasmonic Gold Particle Generation in Layer-by-Layer 2D Titania Films as an Effective Immobilization Strategy of Composite Photocatalysts for Hydrogen Generation. *Chem. Eng. J.* **2019**, *358*, 389-397.
20. Zhao, M.; Xu, H.; Ouyang, S.; Tong, H.; Chen, H.; Li, Y.; Song, L.; Ye, J., Fabricating a Au@TiO₂ Plasmonic System To Elucidate Alkali-Induced Enhancement of Photocatalytic H₂ Evolution: Surface Potential Shift or Methanol Oxidation Acceleration? *ACS Catal.* **2018**, *8* (5), 4266-4277.
21. He, Q.; Sun, H.; Shang, Y.; Tang, Y.; She, P.; Zeng, S.; Xu, K.; Lu, G.; Liang, S.; Yin, S.; Liu, Z., Au@TiO₂ Yolk-shell Nanostructures for Enhanced Performance in both Photoelectric and Photocatalytic Solar Conversion. *Appl. Surf. Sci.* **2018**, *441*, 458-465.
22. Gao, W.; Zhang, X.; Su, X.; Wang, F.; Liu, Z.; Liu, B.; Zhan, J.; Liu, H.; Sang, Y., Construction of Bimetallic Pd-Ag Enhanced AgBr/TiO₂ Hierarchical Nanostructured Photocatalytic Hybrid Capillary Tubes and Devices for Continuous Photocatalytic Degradation of VOCs. *Chem. Eng. J.* **2018**, *346*, 77-84.
23. Tian, H.; Zhang, X. L.; Scott, J.; Ng, C.; Amal, R., TiO₂-Supported Copper Nanoparticles Prepared via Ion Exchange for Photocatalytic Hydrogen Production. *J. Mater. Chem. A* **2014**, *2* (18), 6432-6438.
24. Hao, J.; Liu, H.; Wang, K.; Sun, X. W.; Delville, J.-P.; Delville, M.-H., Hole Scavenging and Electron-Hole Pair Photoproduction Rate: Two Mandatory Key Factors to Control Single-Tip Au-CdSe/CdS Nanoheterodimers. *ACS Nano* **2021**, *15* (9), 15328-15341.
25. Bai, Q.; Shupyk, I.; Vauriot, L.; Majimel, J.; Labrugere, C.; Delville, M.-H.; Delville, J.-P., Design of Metal@Titanium Oxide Nano-Heterodimers by Laser-Driven Photodeposition: Growth Mechanism and Modeling. *ACS Nano* **2021**, *15* (2), 2947-2961.
26. Veziroglu, S.; Obermann, A.-L.; Ullrich, M.; Hussain, M.; Kamp, M.; Kienle, L.; Leißner, T.; Rubahn, H.-G.; Polonskyi, O.; Strunskus, T.; Fiutowski, J.; Es-Souni, M.; Adam, J.; Faupel, F.; Aktas, O. C., Photodeposition of Au Nanoclusters for Enhanced Photocatalytic Dye Degradation over TiO₂ Thin Film. *ACS Appl. Mater. Interfaces* **2020**, *12* (13), 14983-14992.
27. Bao, N.; Miao, X.; Hu, X.; Zhang, Q.; Jie, X.; Zheng, X., Novel Synthesis of Plasmonic Ag/AgCl@TiO₂ Continuous Fibers with Enhanced Broadband Photocatalytic Performance. *Catalysts* **2017**, *7* (4), 117.
28. Dilsaver, P. S.; Reichert, M. D.; Hallmark, B. L.; Thompson, M. J.; Vela, J., Cu₂ZnSnS₄-Au Heterostructures: Toward Greener Chalcogenide-Based Photocatalysts. *J. Phys. Chem. C* **2014**, *118* (36), 21226-21234.
29. Ran, J.; Zhang, J.; Yu, J.; Jaroniec, M.; Qiao, S. Z., Earth-Abundant Cocatalysts for Semiconductor-Based Photocatalytic Water Splitting. *Chemical Society reviews* **2014**, *43* (22), 7787-7812.
30. Yuan, Y.-J.; Chen, D.; Yu, Z.-T.; Zou, Z.-G., Cadmium sulfide-based nanomaterials for photocatalytic hydrogen production. *Journal of Materials Chemistry A* **2018**, *6* (25), 11606-11630.
31. Nakibli, Y.; Mazal, Y.; Dubi, Y.; Wachtler, M.; Amirav, L., Size Matters: Cocatalyst Size Effect on Charge Transfer and Photocatalytic Activity. *Nano letters* **2018**, *18* (1), 357-364.
32. Cheng, X.; Liu, J.; Feng, J.; Zhang, E.; Wang, H.; Liu, X.; Liu, J.; Rong, H.; Xu, M.; Zhang, J., Metal@I₂-II-IV-VI₄ Core-shell Nanocrystals: Controlled Synthesis by Aqueous Cation Exchange for Efficient Photoelectrochemical Hydrogen Generation. *J. Mater. Chem. A* **2018**, *6* (25), 11898-11908.

33. Lee, Y.; Kim, E.; Park, Y.; Kim, J.; Ryu, W.; Rho, J.; Kim, K., Photodeposited metal-semiconductor nanocomposites and their applications. *J Materiomics*. **2018**, *4* (2), 83-94.
34. Xing, Z.; Zhang, J.; Cui, J.; Yin, J.; Zhao, T.; Kuang, J.; Xiu, Z.; Wan, N.; Zhou, W., Recent Advances in Floating TiO₂-Based Photocatalysts for Environmental Application. *Appl. Catal. B*. **2018**, *225*, 452-467.
35. Yuan, Y.-J.; Chen, D.; Yu, Z.-T.; Zou, Z.-G., Cadmium Sulfide-Based Nanomaterials for Photocatalytic Hydrogen Production. *J. Mater. Chem. A* **2018**, *6* (25), 11606-11630.
36. Shen, R.; Ren, D.; Ding, Y.; Guan, Y.; Ng, Y. H.; Zhang, P.; Li, X., Nanostructured CdS for Efficient Photocatalytic H₂ Evolution: A Review. *Sci. China Mater.* **2020**, *63* (11), 2153-2188.
37. Volokh, M.; Mokari, T., Metal/Semiconductor Interfaces in Nanoscale Objects: Synthesis, Emerging Properties and Applications of Hybrid Nanostructures. *Nanoscale Adv.* **2020**, *2* (3), 930-961.
38. Aronovitch, E.; Houben, L.; Bar-Sadan, M., Seeded Rods with Ag and Pd Bimetallic Tips-Spontaneous Rearrangements of the Nanoalloys on the Atomic Scale. *Chem. Mater.* **2019**, *31* (18), 7231-7237.
39. Fujishima, M.; Ikeda, T.; Akashi, R.; Tada, H., In Situ Shape Change of Au Nanoparticles on TiO₂ by CdS Photodeposition: Its Near-Field Enhancement Effect on Photoinduced Electron Injection from CdS to TiO₂. *ACS Omega* **2018**, *3* (6), 6104-6112.
40. Fudo, E.; Tanaka, A.; Iguchi, S.; Kominami, H., Modification of Gold Nanoparticles with a Hole-transferring Cocatalyst: a New Strategy for Plasmonic Water Splitting under Irradiation of Visible Light. *Sustain. Energy Fuels*. **2021**, *5* (13), 3303-3311.
41. Kontoleta, E.; Tsoukala, A.; Askes, S. H. C.; Zoethout, E.; Oksenberg, E.; Agrawal, H.; Garnett, E. C., Using Hot Electrons and Hot Holes for Simultaneous Cocatalyst Deposition on Plasmonic Nanostructures. *ACS Appl. Mater. Interfaces* **2020**, *12* (32), 35986-35994.
42. Gärtner, F.; Losse, S.; Boddien, A.; Pohl, M.-M.; Denurra, S.; Junge, H.; Beller, M., Hydrogen Evolution from Water/Alcohol Mixtures: Effective In Situ Generation of an Active Au/TiO₂ catalyst. *ChemSusChem* **2012**, *5* (3), 530-533.
43. Murdoch, M.; Waterhouse, G. I. N.; Nadeem, M. A.; Metson, J. B.; Keane, M. A.; Howe, R. F.; Llorca, J.; Idriss, H., The Effect of Gold Loading and Particle Size on Photocatalytic Hydrogen Production from Ethanol Over Au/TiO₂ Nanoparticles. *Nat. Chem.* **2011**, *3* (6), 489-492.
44. Carbone, L.; Jakab, A.; Khalavka, Y.; Sönnichsen, C., Light-Controlled One-Sided Growth of Large Plasmonic Gold Domains on Quantum Rods Observed on the Single Particle Level. *Nano letters* **2009**, *9* (11), 3710-3714.
45. Berr, M.; Vaneski, A.; Susha, A. S.; Rodríguez-Fernández, J.; Döblinger, M.; Jäckel, F.; Rogach, A. L.; Feldmann, J., Colloidal CdS Nanorods Decorated with Subnanometer Sized Pt Clusters for Photocatalytic Hydrogen Generation. *Appl. Phys. Lett.* **2010**, *97* (9), 093108.
46. Dukovic, G.; Merkle, M. G.; Nelson, J. H.; Hughes, S. M.; Alivisatos, A. P., Photodeposition of Pt on Colloidal CdS and CdSe/CdS Semiconductor Nanostructures. *Adv. Mater.* **2008**, *20* (22), 4306-4311.

Glossary

Au	Gold
1-DDT	1-dodecanethiol
Ag	Silver
AgNO ₃	Silver nitrate
BNPs	Bimetallic Nanoparticles
CB	Conduction Band
DDA	Dodecylamine
Ds	Interface diameter
EG	Ethylene glycol
H ₂ PdCl ₄	Tetrachloropalladic acid
HAADF-	The high-angle annular dark-field scanning transmission
STEM	electron microscopy
HCOONa	Sodium formate
HNCs	Heteronanocrystals
HRTEM	High-resolution TEM
HS	Hole scavenger
KAuCl ₄	Potassium gold (III) chloride
LSPR	Localized surface plasmon resonance
MeOH	Methanol
Na ₂ PdCl ₄	Di Sodium tetrachloropalladate
NCs	Nanocrystals
NDs	Nanodots
NHDs	Nanoheterodimers
NHE	Normal hydrogen electrode
NPs	Nanoparticles
NRs	Nanorods
NWs	Nanowires

OA	Oleic acid
OLAM	Oleylamine
PMMA	Polymethyl methacrylate
PVP	Polyvinylpyrrolidone
SC	Semiconductor
SD	Standard Deviation
SPR	Surface plasmon resonance
TEM	Transmission electron microscopy
TEOA	Triethanolamine
TiO ₂	Titanium Dioxide
VB	Valence band
XPS	X-ray photoelectron spectroscopy
XRD	X-ray diffraction
ZnO	Zinc oxide
ZPC	Zero point charge

Table of contents

General Introduction	1
Chapter 1	15
Principles and Recent Advances in Photodeposition of Metals on Colloidal Semiconductor Nanocrystals	15
Abstract	19
1.1 Principles of photodeposition reactions	19
1.2 Photodeposition of metals on TiO ₂ surface.....	22
1.3 Photodeposition of metals on metal-chalcogenide surfaces.....	30
1.3.1 Photodeposition of metals on Cd-chalcogenides	30
1.3.2 Photodeposition of metals on heavy-metal-free chalcogenides	34
1.4 Conclusion and Perspective	39
1.5 References	41
Chapter 2	49
Setup Configuration and Laser Control	49
Abstract	53
2.1 Choice of light sources	53
2.1.1 Types of light sources	53
2.1.2 Impact of photon flux on the photodeposition reaction.....	54
2.2 Cuvette setup using UV laser illumination	56
2.2.1 Schematic picture of the cuvette setup using UV laser	56
2.2.2 Excitation power in the cuvette	57
2.3 Cuvette setup using blue laser illumination	59
2.3.1 Schematic picture of the cuvette setup using blue laser	59
2.3.2 Excitation power in the cuvette	60
2.4 Conclusion.....	62
2.5 References	64
Chapter 3	65
Photodeposition of Au Nanodots on TiO₂ Nanoparticles	65

3.1 Introduction to photodeposition of Au nanodots (NDs) onto TiO ₂ particle surface.....	69
3.2 Experimental part	72
3.2.1 Synthesis and characterization of TiO ₂ particles	72
3.2.2 Procedure of photodeposition	74
3.3 Results and discussions	75
3.3.1 Variation of exposure time.....	76
3.3.2 Variation of the Au precursor concentration	81
3.3.3 Variation of KAuCl ₄ content at different concentrations of TiO ₂	83
3.3.4 Variation of the exposure time at varying beam intensities	91
3.4 Mechanism of Au NDs growth onto TiO ₂ NPs.....	95
3.4.1 Photochemical reaction scheme	95
3.4.2 Growth law	98
3.4.3 Adsorption at the surface of TiO ₂	99
3.4.3.1 Chemisorption at the surface of TiO ₂	99
3.4.3.1.1 Load q and number of TiO ₂ NPs	100
3.4.3.1.2 Concentration of hole scavengers at the surface of TiO ₂	101
3.4.3.1.3 Concentration of gold ions at the surface of TiO ₂	102
3.4.3.2 Physisorption at the surface of TiO ₂ (The Eley-Rideal mechanism)	
.....	103
3.4.4 Calculation of the Au ⁰ concentration produced by photoreduction for the growth of a gold ND	106
3.4.4.1 Set-up of the equations	106
3.4.4.2 Conclusion.....	109
3.4.5 Growth Analysis-Global.....	110
3.4.5.1 Variation in exposure time at a varying gold concentration.....	110
3.4.5.2 Variation of exposure times for different beam intensities	112
3.4.5.3 Variation in gold ion concentration for varying TiO ₂ NPs concentrations	113
3.4.5.4 Variation in gold ion concentration for multi-addition	115

3.4.5.5 Varying both gold ion concentration and TiO ₂ NPs concentrations	116
3.4.5.6 First scaling analysis	117
3.4.5.7 Chemisorption or physisorption: experiments in beam intensity	119
3.4.5.8 Physisorption mechanism for both cuvette and microchannel experiments	121
3.4.6 Conclusion of modeling	125
3.5 Conclusion	125
3.6 References	127
Chapter 4	131
Photodeposition of Ag, and Pd Nanodots on TiO₂ Nanoparticles	131
4.1 Introduction to the photodeposition of Ag NDs on TiO ₂ NPs	135
4.1.2 Experimental method	138
4.1.3 Results and discussion	138
4.1.3.1 The effects of the hole scavenger on Ag photodeposition	139
4.1.3.2 The effects of the exposure time on Ag photodeposition	140
4.1.3.3 The effects of the laser power on the Ag photodeposition	143
4.1.3.4 The effects of PVP on the Ag photodeposition	146
4.1.3.5 Different silver precursors	147
4.1.4 Conclusion	150
4.2 Introduction to the photodeposition of Pd NDs on TiO ₂ NPs	150
4.2.1 Experiment method	152
4.2.2 Result and discussion	153
4.2.2.1 The effects of the hole scavenger on the Pd photodeposition	153
4.2.2.2 The respective influence of HNO ₃ and HCl on the Pd photodeposition	154
4.2.2.3 The effects of the metal precursor on the Pd photodeposition	156
4.2.2.4 The effects of the exposure time on the Pd photodeposition	158
4.2.2.5 The effects of TiO ₂ and Pd ²⁺ concentrations on the Pd photodeposition	160

4.2.3 Conclusion	163
4.3 Laser deposition of Pd and Ag NDs onto TiO ₂ NPs in the cuvette and microchannel setups from growth to completion	164
4.3.1 Overall analysis of the experiments on Silver photodeposition	168
4.3.2 Overall analysis of the experiments on Palladium photodeposition ..	172
4.4 Conclusion.....	177
4.5 References	179
Chapter 5	183
Photodeposition of Au@Au, Au@Ag, and Au@Pd Core-Shell Structured Bimetallic Nanodots on TiO₂ Nanoparticles.....	183
5.1 Introduction.....	187
5.2 Experimental methods.....	189
5.3 Photodeposition of Au on Au-TiO ₂	190
5.3.1 Size-controlled deposition of Au on TiO ₂ nanoparticles.....	191
5.3.2 Varying the KAuCl ₄ amount added in the second step.....	193
5.3.3 Conclusion	197
5.4 Photodeposition of Ag on Au-TiO ₂	197
5.4.1 Photodeposition of Ag on Au-TiO ₂ without chloride ions.....	199
5.4.1.1 HCOONa as a hole scavenger	199
5.4.1.1.1 Varying amounts of AgNO ₃	199
5.4.1.1.2 Influence of the laser power.....	203
5.4.1.2 Methanol as hole scavenger.....	204
5.4.2 Photodeposition of Ag on Au-TiO ₂ with chloride ions.....	207
5.4.2.1 Varying exposure times and laser powers	207
5.4.2.2 Varying the amounts of AgNO ₃	209
5.4.2.3 Depositing Ag on Au-TiO ₂ which contains big Au particle	211
5.4.3 Conclusion	212
5.5 Photodeposition of Pd on Au-TiO ₂	213
5.5.1 Effect of the hole scavenger.....	213
5.5.2 Different Pd precursors	217

5.5.3 Conclusion	222
5.6 Conclusion.....	222
5.7 References	224
Chapter 6	227
Selective Photodeposition of Au Nanodots on Janus-Type Cu_{2-x}S/CuInS₂	
Heteronanorods.....	227
6.1 Introduction.....	231
6.2 Experimental part	233
6.2.1 Chemicals	233
6.2.2 Synthesis of Cu _{2-x} S/CuInS ₂ HNCs.....	233
6.2.3 Phase Transfer of KAuCl ₄ from Water to Toluene	234
6.2.4 Laser-induced deposition of Au Nanodots onto Cu _{2-x} S/CuInS ₂ HNCs	
.....	234
6.2.5 Characterization.....	235
6.3 Photodeposition of Au NDs on long Cu _{2-x} S/CuInS ₂ HNCs	236
6.3.1 Characterization of Cu _{2-x} S/CuInS ₂ HNCs	236
6.3.2 Laser-induced photodeposition of gold on Cu _{2-x} S/CuInS ₂ HNCs.....	237
6.3.2.1 Effect of the hole scavenger on Au photodeposition.....	238
6.3.2.2 Effect of the laser beam intensity on the Au photodeposition	239
6.3.2.3 Effect of Au precursor on Au photodeposition.....	242
6.3.2.4 Effect of the exposure time on the Au photodeposition	245
6.3.2.5 Structural characterization of Au-Cu _{2-x} S/CuInS ₂ hybrid HNCs ..	248
6.3.2.6 Formation mechanism of Au photodeposition on Cu _{2-x} S/CuInS ₂	
HNCs.....	253
6.3.3 Conclusion	254
6.4 References	256
Conclusions and Perspectives	259
Appendix 1.....	263
Prediction of metal size deposited on TiO₂ nanoparticles	263
A1.1 Concentration of TiO ₂ particles.....	265

A1.2 Estimation of the size of Au NDs deposited on TiO ₂ particles	265
A1.3 General method to estimate the size of the metal (Au, Ag, Pd) NDs on TiO ₂ particles	266
A1.4 Estimation of the metal size of the second-step deposition.....	267
Appendix 2.....	269
Characterization techniques	269
References	272

General Introduction

Over the past few centuries, the rapid development of science and technology has brought mankind a high level of economic prosperity and prolonged lifetimes of human beings. The improvement of living standards significantly fosters population explosion and further industrial revolution, thus leading to sharp demands for energy which mainly comes from burning coal and fossil fuels. The use of these conventional fuels results in a dramatic increase in global CO₂ emissions and severe environmental pollution. For example, over the past half-century the average global temperatures are already about 1.5 °C higher than in pre-industrial times (**Figure 1**),¹⁻² which brings about accelerated melt of glaciers and increases in sea levels. This means that tens of thousands of people are threatened by the associated effects of saltwater intrusion, flooding, infrastructure damage as well as deadly hurricanes and other extreme weather events. To protect our living environment from deterioration, researchers from various fields are working on developing clean and renewable energy, such as biofuels, wind, tidal, solar, and hydraulic energy. Amongst these energies, solar power has been considered the most promising clean energy due to its high accessibility and inexhaustible supply without any pollutant emission. The utilization of solar energy can be mainly divided into two parts. The first one is to convert solar energy into electricity directly or indirectly (stored in batteries or capacitors) for human society, while the other is to convert solar energy into green fuels in the form of H₂ by water splitting³⁻⁴ or hydrocarbons by the reduction of CO₂ through photocatalysis.⁵⁻⁶ Apart from the storage of solar energy, photocatalysis can also be applied to manage environmental issues such as the degradation of harmful compounds in wastewater, e.g. dyes, bacteria, or metal ions.⁷⁻⁸

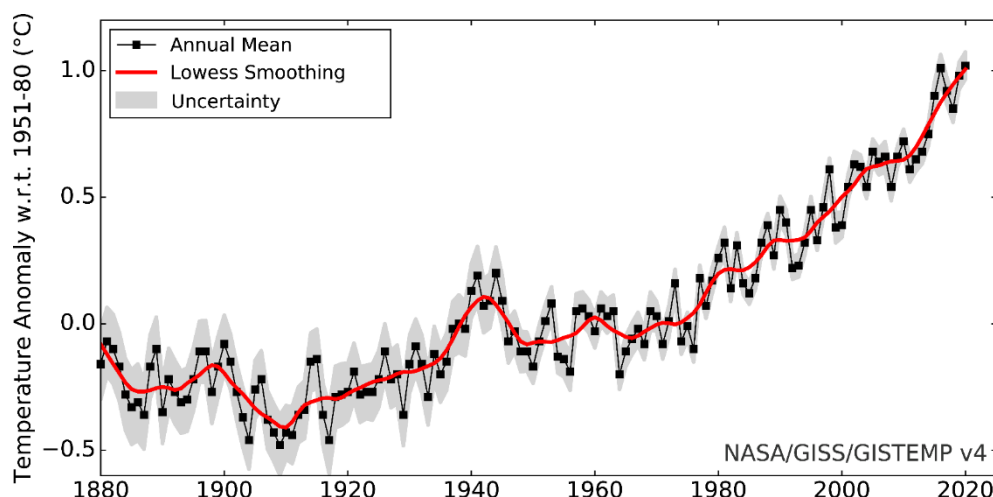


Figure 1. Global warming: monthly temperature anomaly. The combined land-surface air and sea-surface water temperature anomaly are given as the deviation from 1951 to 1980 mean. The data source comes from the National Aeronautics and Space Administration, Godard Institute for Space Studies.¹⁻² The gray shading represents the total annual uncertainty at a 95% confidence interval.

Photocatalysis involves the use of photoexcited charge carriers generated in a semiconductor to enhance the rate of chemical reactions or alter their selectivity. Specifically, when a photocatalyst is illuminated by incident light with an appropriate frequency, the photon energy pumps the electron to the conduction band, thus leaving the hole behind in the valence band. These generated electrons or holes are then efficiently used for a plethora of applications, e.g. wastewater treatment,⁹⁻¹¹ air purification,¹²⁻¹⁵ organic dye degradation,^{10, 16-17} and solar fuel synthesis.¹⁸⁻²¹ Although semiconductor photocatalysts are of great importance in these fields, the majority of them (e.g., TiO_2 and ZnO) have extremely large band gaps that are only responsible for UV light which accounts for only 4% of the solar flux.²² Several other visible-light absorbers, such as $\alpha\text{-Fe}_2\text{O}_3$,²³ WO_3 ,²⁴ and $\text{g-C}_3\text{N}_4$ ²⁵ have also been investigated. However, they exhibit short diffusion lengths to impart weak charge carriers, which dramatically hinders the full use of these materials.²²⁻²³ Therefore, the development of efficient photocatalysts that are active over a broader range of the solar spectrum has been in great demand.

To solve this problem, researchers focused on hybrid metal-semiconductor photocatalysts that have attracted increasing attention. In these systems, the

magnetic, optical, and catalytic properties of the different materials can be synergistically combined and their chemical-physical properties can be tailored by tuning the size, shape, and composition of each part of the heterostructures. The presence of metal nanoparticles (NPs) on the surface of a semiconductor has two great impacts on their photocatalytic properties. First, it can significantly suppress the recombination of photogenerated excitons as well as reduce the activation energies of the photoredox reactions and thus increase the reaction rates.^{22, 24, 26-30} Second, coupling semiconductors and metals with strong localized surface plasmon resonance (LSPR), light-harvesting and absorption efficiencies of the semiconductors can be significantly improved.^{22, 24, 26-27} To date, many researchers have developed various ways to perform the fabrication of metal-semiconductor hybrid nanocrystals, *e.g.* hydrothermal/solvothermal synthesis,³¹⁻³³ ion exchange,³⁴⁻³⁵ sputtering,³⁶⁻³⁷ photodeposition,^{11, 38-40} deposition–precipitation,⁴¹⁻⁴² and the enzyme-mediated biomimetic approach.⁴³⁻⁴⁴ Among these strategies, photodeposition has drawn increasing attention since this method does not require raising the temperature or applying a voltage, and is therefore considered an environmentally-friendly approach.²⁴ Moreover, the major advantages of photodeposition include (i) a delicate control of the geometric distribution of metal nanodots (NDs) on the surface of facet-engineered semiconductors and (ii) great flexibility in controlling the size and the oxidation state of the deposited NPs by manipulating the reaction precursors as well as the illumination wavelength and the intensity.²⁴

Photodeposition techniques have been widely adopted to load various metals (*e.g.*, Ag, Au, Pt, *etc.*) on semiconductors including metal oxides (*e.g.*, TiO₂, ZnO, WO₃, *etc.*) and metal chalcogenides (*e.g.*, CdS, Bi₂S₃, Cu_{2-x}S, *etc.*).^{10, 21-22, 24, 27, 45-51} In some cases, this technique has also been successfully used to obtain core/shell particles,⁵²⁻⁵⁴ bimetallic cocatalysts,^{14, 52, 55-56} or even more complicated systems, as depicted in **Figure 2a**.^{11, 57} Furthermore, the metals can also be loaded on different substrates with various morphologies, such as spheres, rods, sheets, dumbbells and tubes (**Figure 2a**).

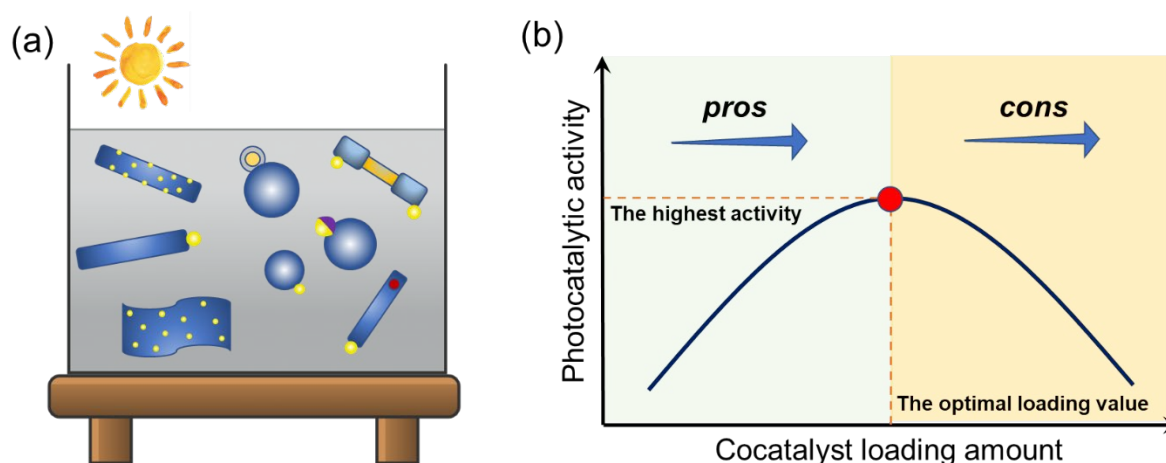


Figure 2. (a) Schematic representation of different nanostructures containing plasmonic NPs and semiconductors. (b) Variation of the photocatalytic activity with the amount of cocatalyst on the surface of a photocatalyst. Adapted from ref.⁵⁸

Despite a large body of research where photodeposition on semiconductors has been employed, the availability of studies on understanding the reaction mechanisms of photodeposition is very much behind. Moreover, the photocatalytic activities of the resulting materials usually experience poor reproducibility and show significant differences depending on the synthesis methods.²⁶ To remove the veil of mystery, precisely tracking the nucleation and growth of the metal NDs on the semiconductor surface is of great importance. This will help achieve full control over the size, morphology, oxidation state, and heterointerface of the metals on the semiconductors and therefore tune the photocatalytic activities. Many researchers have attempted to optimize the metal loading to generate effective photocatalytic materials.⁵⁹⁻⁶⁰ As shown in **Figure 2b**, photocatalytic activity generally increases with a load of metal deposited on the semiconductor surface. However, the activity gradually decreases due to an over-coverage of the semiconductor surface by the metals, which blocks the active sites for the photoredox reaction as well as the light from reaching the photocatalysts.^{24, 58} Moreover, if the metal loadings are too high, the metal NDs may also act as charge recombination centers, thus preventing free electrons or holes from photocatalytic reactions.^{24, 58} Beyond the influence of metal loadings, studies on the influence of other factors such as the influence of precursors,^{59, 61-62} influence of pH,⁶³⁻⁶⁴ the role of a sacrificial reagent,⁶⁵⁻⁶⁶ etc. also have a great impact on the

photocatalytic activities, which however remain underdeveloped.

Aside from the parameters in the reaction medium, the selection of suitable light sources for photodeposition reactions also plays an important role. In most previously reported literature, conventional UV or visible lamps with an excitation power intensity typically less than 5 mW/cm^2 were used for experiments.^{40, 67-70} Due to their low power intensity, reactions then took several hours to complete the deposition of metal nanodots, and the loaded metals usually had a quite small size (less than 3 nm).^{69, 71} This makes it extremely difficult to study the influence of metal size and shape on the photocatalytic properties of the resulting products. This issue can be addressed by using as light sources, high-energy lasers which can generate a photon flux intensity orders of magnitude higher than prototypical lamps.^{38-39, 72} Consequently, a large number of photogenerated electrons can be produced in a short time and then be used to reduce metal ions on the semiconductor surfaces at a high rate. For example, Bai *et al.*,³⁹ reported that metal (Ag and Au)-TiO₂ nanoheterodimers (NHDs) could be obtained with a laser-driven photodeposition in a continuous microfluidic reactor. Using a focused laser beam with an intensity as high as 430 W/cm^2 allows the formation of metal NDs with a size as large as 14 nm in a few seconds. They also showed that (i) the average size of the metallic NDs did increase proportionally (with a stable polydispersity around 20%) with the increase of excitation power, and (ii) the growth of Ag nanodots on TiO₂ could be modeled precisely. However, the reaction system is complicated and the photodeposition occurs at such a high rate that studying nucleation and early-stage growth of metal nanodots is very challenging. This drawback can be combated by using a cuvette instead of a microchannel as a reaction vessel. The use of a cuvette reasonably reduces the photon flux and thus slows down the reaction rate. Combined with the steady reaction system, the nucleation, and growth of metal nanodots can be readily monitored. For instance, Hao *et al.*³⁸ very recently reported the laser-driven photodeposition of Au nanodots on CdSe/CdS nanorods. They showed that the number and spatial position of Au NDs on the nanorods could be finely tuned starting from multiple sites, to double-tips and single-tip by manipulating the photon flux passing through the reaction cuvettes. Moreover,

the size of the Au nanodots was well controlled from less than 3 nm to 9 nm in less than 20 min. This reaction system provides an ideal setup to efficiently investigate the nucleation and growth of metal NDs on semiconductor surfaces.

In this thesis, we focus on laser-driven photodeposition reactions of metals on semiconductor surfaces in a steady cuvette reaction cell, with an emphasis on the controlled synthesis and reaction mechanisms. We have systematically studied the photodeposition of various metals (e.g., Au, Ag, and Pd) on two types of semiconductor substrates, *i.e.*, metal oxides (TiO₂) in the water phase and metal chalcogenides (Cu_{2-x}S/CuInS₂) in toluene. These two types of semiconductors allow us to (i) have a more in-depth understanding of the formation mechanisms of similar metal nanodots on different substrates as well as (ii) study the influences of the reaction medium on the photodeposition reactions. In the following, we will show readers a brief description of each chapter and its interconnections.

In **Chapter 1**, we will describe the basic principles and review recent advances in the photodeposition of metals on two types of semiconductor substrates, *i.e.*, metal oxides and metal chalcogenides. The fundamental key factors for the controlled synthesis as well as their great impact on the photocatalytic activities in these two systems will be intensively discussed. We will also point out several challenging problems that need to be solved and propose some prospective research directions that are beneficial for a better understanding of the photodeposition process and a higher performance of photocatalytic activities in energy harvesting, catalysis, and environmental applications. In **Chapter 2**, we will introduce the two different setups built and used to perform the photodeposition of the metal nanodots onto TiO₂ and Cu_{2-x}S/CuInS₂ nanocrystals. The use of different types of lights for the photodeposition reactions, detailed parameters, and configuration of the built setups will be fully described. In the three next chapters, we will report the results of the photodeposition of various metals on the surface of TiO₂ NPs. In **Chapter 3**, we introduce the photodeposition of Au particles on TiO₂. The effects of numerous parameters on photodeposition are investigated to try to improve the overall Janus yield of Au-TiO₂ nanoheterodimers and reach values close to 100%. Moreover, we study the

adsorption mechanism of the reactants on the TiO₂ surface during the photodeposition process by modeling experimental data; we also try to discriminate between physical and chemical adsorption. We describe the entire gold growth to completion. Besides gold deposition, we also tried the same procedure to deposit Ag, Pd particles on TiO₂ in **Chapter 4**. The effects of numerous parameters, e.g., hole scavenger (HS), exposure time, laser power, and precursor on the photodeposition process will be investigated in detail. In **Chapter 5**, we will report a two-step photodeposition of Au@Au, Au@Ag, and Au@Pd core-shell structured bimetallic nanodots on TiO₂. For the Au@Au core@shell, the Au shell can be precisely controlled and the size and thickness of the Au core and shell perfectly our expectations. For the Au@Ag system, the Ag shell obtained was limited to around 1 nm thickness which was less than expected and results from the low electronegativity of Ag (1.9) compared to other Au (2.4). For the Au@Pd system, Pd showed a non-isotropic growth on the Au core resulting in a nonuniform Pd shell which was due to the big lattice mismatch between Au and Pd. In **Chapter 6**, we will shift our attention to investigating the photodeposition of Au nanodots on Cu_{2-x}S/CuInS₂ heteronanocrystals in toluene. The geometric distribution (e.g., number and location) of Au NDs, as well as their sizes, can be well controlled by tuning the concentration of the hole scavengers and Au precursors, illumination power, and exposure time. Moreover, we found that individual Au NDs prefer to deposit first on the tips of Cu_{2-x}S parts. Under continuous irradiation, these Au NDs behave in a different way as when deposited on TiO₂ and seem to fuse with the Cu_{2-x}S substrate which leads to an increase in bandgap and band re-alignment with CuInS₂. This staggered band alignment promotes the photogenerated electrons flow from Cu_{2-x}S to CuInS₂ resulting in subsequent deposition of the Au NDs on the side of elongated CuInS₂ parts.

The thesis ends up with Conclusions and Perspectives by briefly summarizing the most essential results we obtained, providing an overview contribution to the relevant research society, and proposing some promising research topics for future studies.

One may refer to the **Appendix** for a better understanding of the theoretical calculation of metal size (Appendix 1) and the characterization techniques (Appendix 2).

References

1. GISS Surface Temperature Analysis (GISTEMP), version 4. <https://data.giss.nasa.gov/gistemp/> (accessed Oct 28).
2. Lenssen, N. J. L.; Schmidt, G. A.; Hansen, J. E.; Menne, M. J.; Persin, A.; Ruedy, R.; Zyss, D., Improvements in the GISTEMP Uncertainty Model. *J. Geophys. Res. Atmos.* **2019**, *124* (12), 6307-6326.
3. Navarro Yerga, R. M.; Álvarez Galván, M. C.; del Valle, F.; Villoria de la Mano, J. A.; Fierro, J. L. G., Water Splitting on Semiconductor Catalysts under Visible-Light Irradiation. *ChemSusChem* **2009**, *2* (6), 471-485.
4. Kudo, A.; Miseki, Y., Heterogeneous Photocatalyst Materials for Water Splitting. *Chem. Soc. Rev.* **2009**, *38* (1), 253-278.
5. Ran, J.; Jaroniec, M.; Qiao, S. Z., Cocatalysts in Semiconductor-Based Photocatalytic CO₂ Reduction: Achievements, Challenges, and Opportunities. *Advanced materials* **2018**, *30* (7), 1704649.
6. Roy, S. C.; Varghese, O. K.; Paulose, M.; Grimes, C. A., Toward Solar Fuels: Photocatalytic Conversion of Carbon Dioxide to Hydrocarbons. *ACS Nano* **2010**, *4* (3), 1259-1278.
7. Di Paola, A.; García-López, E.; Marci, G.; Palmisano, L., A Survey of Photocatalytic Materials for Environmental Remediation. *J. Hazard. Mater.* **2012**, *211-212*, 3-29.
8. Kabra, K.; Chaudhary, R.; Sawhney, R. L., Treatment of Hazardous Organic and Inorganic Compounds through Aqueous-Phase Photocatalysis: A Review. *Ind. Eng. Chem. Res* **2004**, *43* (24), 7683-7696.
9. Park, J.; Deshmukh, P. R.; Sohn, Y.; Shin, W. G., ZnO-TiO₂ Core-Shell Nanowires Decorated with Au Nanoparticles for Plasmon-Enhanced Photoelectrochemical Water Splitting. *J. Alloys Compd.* **2019**, *787*, 1310-1319.
10. Xing, Z.; Zhang, J.; Cui, J.; Yin, J.; Zhao, T.; Kuang, J.; Xiu, Z.; Wan, N.; Zhou, W., Recent Advances in Floating TiO₂-Based Photocatalysts for Environmental Application. *Appl. Catal. B.* **2018**, *225*, 452-467.
11. Ha, H. D.; Yan, C.; Katsoukis, G.; Kamat, G. A.; Moreno-Hernandez, I. A.; Frei, H.; Alivisatos, A. P., Precise Colloidal Plasmonic Photocatalysts Constructed by Multistep Photodepositions. *Nano Lett.* **2020**, *20* (12), 8661-8667.
12. Li, X.; Yu, J.; Jaroniec, M.; Chen, X., Cocatalysts for Selective Photoreduction of CO₂ Into Solar Fuels. *Chem. Rev.* **2019**, *119* (6), 3962-4179.
13. Chen, X.; Li, N.; Kong, Z.; Ong, W. J.; Zhao, X., Photocatalytic Fixation of Nitrogen to Ammonia: State-of-the-Art Advancements and Future Prospects. *Mater. Horiz.* **2018**, *5* (1), 9-27.
14. Yu, Y.; Dong, X. a.; Chen, P.; Geng, Q.; Wang, H.; Li, J.; Zhou, Y.; Dong, F., Synergistic Effect of Cu Single Atoms and Au-Cu Alloy Nanoparticles on TiO₂ for Efficient CO₂ Photoreduction. *ACS Nano* **2021**, *15* (9), 14453-14464.
15. Li, H.; Zhang, L.; Cao, Y., Synthesis of Palladium-Modified MnS Photocatalysts with Enhanced Photocatalytic Activity in the Photoreduction of CO₂ to CH₄. *Appl. Surf. Sci.* **2021**, *541*, 148519.
16. Ham, S.; Choi, D.; Jang, D.-J., Photodeposition of Gold Nanoparticles on ZnS Nanobelts for Enhanced Dye Decomposition. *Mater. Res. Bull.* **2019**, *116*, 32-39.
17. Kaushik, R.; Singh, P. K.; Halder, A., Modulation Strategies in Titania Photocatalyst for Energy

Recovery and Environmental Remediation. *Catalysis Today* **2022**, 384-386, 45-69.

18. Kosco, J.; Moruzzi, F.; Willner, B.; McCulloch, I., Photocatalysts Based on Organic Semiconductors with Tunable Energy Levels for Solar Fuel Applications. *Adv. Energy Mater.* **2020**, 10 (39), 2001935.
19. Sun, R.; Zhang, Z.; Li, Z.; Jing, L., Review on Photogenerated Hole Modulation Strategies in Photoelectrocatalysis for Solar Fuel Production. *ChemCatChem* **2019**, 11 (24), 5875-5884.
20. Kush, P.; Deka, S., Multifunctional Copper-Based Quaternary Chalcogenide Semiconductors Toward State-of-the-Art Energy Applications. *ChemNanoMat* **2019**, 5 (4), 373-402.
21. Kumaravel, V.; Mathew, S.; Bartlett, J.; Pillai, S. C., Photocatalytic Hydrogen Production Using Metal Doped TiO₂: A Review Of Recent Advances. *Appl. Catal. B.* **2019**, 244, 1021-1064.
22. Zada, A.; Muhammad, P.; Ahmad, W.; Hussain, Z.; Ali, S.; Khan, M.; Khan, Q.; Maqbool, M., Surface Plasmonic-Assisted Photocatalysis and Optoelectronic Devices with Noble Metal Nanocrystals: Design, Synthesis, and Applications. *Adv. Funct. Mater.* **2020**, 30 (7), 1906744.
23. Tamirat, A. G.; Rick, J.; Dubale, A. A.; Su, W.-N.; Hwang, B.-J., Using Hematite for Photoelectrochemical Water Splitting: a Review of Current Progress and Challenges. *Nanoscale Horizons* **2016**, 1 (4), 243-267.
24. Wenderich, K.; Mul, G., Methods, Mechanism, and Applications of Photodeposition in Photocatalysis: A Review. *Chem. Rev.* **2016**, 116 (23), 14587-14619.
25. Zada, A.; Ali, N.; Subhan, F.; Anwar, N.; Shah, M. I. A.; Ateeq, M.; Hussain, Z.; Zaman, K.; Khan, M., Suitable Energy Platform Significantly Improves Charge Separation of g-C₃N₄ for CO₂ Reduction and Pollutant Oxidation Under Visible-Light. *Progress in Natural Science: Materials International* **2019**, 29 (2), 138-144.
26. Kumar, A.; Choudhary, P.; Kumar, A.; Camargo, P. H. C.; Krishnan, V., Recent Advances in Plasmonic Photocatalysis Based on TiO₂ and Noble Metal Nanoparticles for Energy Conversion, Environmental Remediation, and Organic Synthesis. *Small* **2021**, 2101638.
27. Chakhtouna, H.; Benzeid, H.; Zari, N.; Qaiss, A.; Bouhfid, R., Recent Progress on Ag/TiO₂ Photocatalysts: Photocatalytic and Bactericidal Behaviors. *Environ. Sci. Pollut. Res.* **2021**, 28 (33), 44638-44666.
28. Liu, X.; Zhang, Q.; Ma, D., Advances in 2D/2D Z-scheme heterojunctions for photocatalytic applications. *Solar RRL* **2021**, 5 (2), 2000397.
29. Chai, Z., Light-Driven Alcohol Splitting by Heterogeneous Photocatalysis: Recent Advances, Mechanism and Prospects. *Chem. Asian J.* **2021**, 16 (5), 460-473.
30. Zhang, F.; Wang, X.; Liu, H.; Liu, C.; Wan, Y.; Long, Y.; Cai, Z., Recent Advances and Applications of Semiconductor Photocatalytic Technology. *Appl. Sci.* **2019**, 9 (12).
31. Zhang, Q.; Zhang, Y.; Xiao, K.; Meng, Z.; Tong, W.; Huang, H.; An, Q., Plasmonic Gold Particle Generation in Layer-by-Layer 2D Titania Films as an Effective Immobilization Strategy of Composite Photocatalysts for Hydrogen Generation. *Chem. Eng. J.* **2019**, 358, 389-397.
32. Zhao, M.; Xu, H.; Ouyang, S.; Tong, H.; Chen, H.; Li, Y.; Song, L.; Ye, J., Fabricating a Au@TiO₂ Plasmonic System To Elucidate Alkali-Induced Enhancement of Photocatalytic H₂ Evolution: Surface Potential Shift or Methanol Oxidation Acceleration? *ACS Catal.* **2018**, 8 (5), 4266-4277.
33. He, Q.; Sun, H.; Shang, Y.; Tang, Y.; She, P.; Zeng, S.; Xu, K.; Lu, G.; Liang, S.; Yin, S.; Liu, Z., Au@TiO₂ Yolk-shell Nanostructures for Enhanced Performance in both Photoelectric and Photocatalytic Solar Conversion. *Appl. Surf. Sci.* **2018**, 441, 458-465.
34. Gao, W.; Zhang, X.; Su, X.; Wang, F.; Liu, Z.; Liu, B.; Zhan, J.; Liu, H.; Sang, Y., Construction of

- Bimetallic Pd-Ag Enhanced AgBr/TiO₂ Hierarchical Nanostructured Photocatalytic Hybrid Capillary Tubes and Devices for Continuous Photocatalytic Degradation of VOCs. *Chem. Eng. J.* **2018**, *346*, 77-84.
35. Tian, H.; Zhang, X. L.; Scott, J.; Ng, C.; Amal, R., TiO₂-Supported Copper Nanoparticles Prepared via Ion Exchange for Photocatalytic Hydrogen Production. *J. Mater. Chem. A* **2014**, *2* (18), 6432-6438.
36. Singh, J.; Sahu, K.; Pandey, A.; Kumar, M.; Ghosh, T.; Satpati, B.; Som, T.; Varma, S.; Avasthi, D. K.; Mohapatra, S., Atom Beam Sputtered Ag-TiO₂ Plasmonic Nanocomposite Thin Films for Photocatalytic Applications. *Appl. Surf. Sci.* **2017**, *411*, 347-354.
37. Singh, J.; Sahu, K.; Choudhary, S.; Bisht, A.; Mohapatra, S., Thermal Annealing Induced Cave in and Formation of Nanoscale Pits in Ag-TiO₂ Plasmonic Nanocomposite Thin Film. *Ceram. Int.* **2020**, *46* (3), 3275-3281.
38. Hao, J.; Liu, H.; Wang, K.; Sun, X. W.; Delville, J.-P.; Delville, M.-H., Hole Scavenging and Electron-Hole Pair Photoproduction Rate: Two Mandatory Key Factors to Control Single-Tip Au-CdSe/CdS Nanoheterodimers. *ACS Nano* **2021**, *15* (9), 15328-15341.
39. Bai, Q.; Shupyk, I.; Vauriot, L.; Majimel, J.; Labrugere, C.; Delville, M.-H.; Delville, J.-P., Design of Metal@Titanium Oxide Nano-Heterodimers by Laser-Driven Photodeposition: Growth Mechanism and Modeling. *ACS Nano* **2021**, *15* (2), 2947-2961.
40. Veziroglu, S.; Obermann, A.-L.; Ullrich, M.; Hussain, M.; Kamp, M.; Kienle, L.; Leißner, T.; Rubahn, H.-G.; Polonskyi, O.; Strunskus, T.; Fiutowski, J.; Es-Souni, M.; Adam, J.; Faupel, F.; Aktas, O. C., Photodeposition of Au Nanoclusters for Enhanced Photocatalytic Dye Degradation over TiO₂ Thin Film. *ACS Appl. Mater. Interfaces* **2020**, *12* (13), 14983-14992.
41. Bao, N.; Miao, X.; Hu, X.; Zhang, Q.; Jie, X.; Zheng, X., Novel Synthesis of Plasmonic Ag/AgCl@TiO₂ Continuous Fibers with Enhanced Broadband Photocatalytic Performance. *Catalysts* **2017**, *7* (4), 117.
42. Dilsaver, P. S.; Reichert, M. D.; Hallmark, B. L.; Thompson, M. J.; Vela, J., Cu₂ZnSnS₄-Au Heterostructures: Toward Greener Chalcogenide-Based Photocatalysts. *J. Phys. Chem. C* **2014**, *118* (36), 21226-21234.
43. Liu, C.; Yang, D.; Jiao, Y.; Tian, Y.; Wang, Y.; Jiang, Z., Biomimetic Synthesis of TiO₂-SiO₂-Ag Nanocomposites with Enhanced Visible-Light Photocatalytic Activity. *ACS Appl. Mater. Interfaces* **2013**, *5* (9), 3824-3832.
44. Yang, D.; Sun, Y.; Tong, Z.; Tian, Y.; Li, Y.; Jiang, Z., Synthesis of Ag/TiO₂ Nanotube Heterojunction with Improved Visible-Light Photocatalytic Performance Inspired by Bioadhesion. *J. Phys. Chem. C* **2015**, *119* (11), 5827-5835.
45. Cheng, X.; Liu, J.; Feng, J.; Zhang, E.; Wang, H.; Liu, X.; Liu, J.; Rong, H.; Xu, M.; Zhang, J., Metal@I₂-II-IV-VI₄ Core-shell Nanocrystals: Controlled Synthesis by Aqueous Cation Exchange for Efficient Photoelectrochemical Hydrogen Generation. *J. Mater. Chem. A* **2018**, *6* (25), 11898-11908.
46. Lee, Y.; Kim, E.; Park, Y.; Kim, J.; Ryu, W.; Rho, J.; Kim, K., Photodeposited metal-semiconductor nanocomposites and their applications. *J. Materiomics*. **2018**, *4* (2), 83-94.
47. Yuan, Y.-J.; Chen, D.; Yu, Z.-T.; Zou, Z.-G., Cadmium Sulfide-Based Nanomaterials for Photocatalytic Hydrogen Production. *J. Mater. Chem. A* **2018**, *6* (25), 11606-11630.
48. Shen, R.; Ren, D.; Ding, Y.; Guan, Y.; Ng, Y. H.; Zhang, P.; Li, X., Nanostructured CdS for Efficient Photocatalytic H₂ Evolution: A Review. *Sci. China Mater.* **2020**, *63* (11), 2153-2188.
49. Volokh, M.; Mokari, T., Metal/Semiconductor Interfaces in Nanoscale Objects: Synthesis, Emerging Properties and Applications of Hybrid Nanostructures. *Nanoscale Adv.* **2020**, *2* (3), 930-961.

50. Zhang, G.; Wu, H.; Chen, D.; Li, N.; Xu, Q.; Li, H.; He, J.; Lu, J., A Mini-Review on ZnIn₂S₄-Based Photocatalysts for Energy and Environmental Application. *Green Energy Environ.* **2020**.
51. Jiménez-Calvo, P.; Caps, V.; Keller, V., Plasmonic Au-Based Junctions onto TiO₂, gC₃N₄, and TiO₂-gC₃N₄ Systems for Photocatalytic Hydrogen Production: Fundamentals and Challenges. *Renew. Sust. Energ. Rev.* **2021**, *149*, 111095.
52. Aronovitch, E.; Houben, L.; Bar-Sadan, M., Seeded Rods with Ag and Pd Bimetallic Tips-Spontaneous Rearrangements of the Nanoalloys on the Atomic Scale. *Chem. Mater.* **2019**, *31* (18), 7231-7237.
53. Fujishima, M.; Ikeda, T.; Akashi, R.; Tada, H., In Situ Shape Change of Au Nanoparticles on TiO₂ by CdS Photodeposition: Its Near-Field Enhancement Effect on Photoinduced Electron Injection from CdS to TiO₂. *ACS Omega* **2018**, *3* (6), 6104-6112.
54. Fudo, E.; Tanaka, A.; Iguchi, S.; Kominami, H., Modification of Gold Nanoparticles with a Hole-transferring Cocatalyst: a New Strategy for Plasmonic Water Splitting under Irradiation of Visible Light. *Sustain. Energy Fuels.* **2021**, *5* (13), 3303-3311.
55. Zhang, X.-F.; Wang, Z.; Zhong, Y.; Qiu, J.; Zhang, X.; Gao, Y.; Gu, X.; Yao, J., TiO₂ Nanorods Loaded with AuPt Alloy Nanoparticles for the Photocatalytic Oxidation of Benzyl Alcohol. *J. Phys. Chem. Solids* **2019**, *126*, 27-32.
56. Shahini, P.; Ashkarran, A. A., Immobilization of Plasmonic Ag-Au NPs on the TiO₂ Nanofibers as an Efficient Visible-light Photocatalyst. *Colloids Surf. A Physicochem. Eng. Asp.* **2018**, *537*, 155-162.
57. Kontoleta, E.; Tsoukala, A.; Askes, S. H. C.; Zoethout, E.; Oksenberg, E.; Agrawal, H.; Garnett, E. C., Using Hot Electrons and Hot Holes for Simultaneous Cocatalyst Deposition on Plasmonic Nanostructures. *ACS Appl. Mater. Interfaces* **2020**, *12* (32), 35986-35994.
58. Ran, J.; Zhang, J.; Yu, J.; Jaroniec, M.; Qiao, S. Z., Earth-Abundant Cocatalysts for Semiconductor-Based Photocatalytic Water Splitting. *Chemical Society reviews* **2014**, *43* (22), 7787-7812.
59. Gärtner, F.; Losse, S.; Boddien, A.; Pohl, M.-M.; Denurra, S.; Junge, H.; Beller, M., Hydrogen Evolution from Water/Alcohol Mixtures: Effective In Situ Generation of an Active Au/TiO₂ catalyst. *ChemSusChem* **2012**, *5* (3), 530-533.
60. Murdoch, M.; Waterhouse, G. I. N.; Nadeem, M. A.; Metson, J. B.; Keane, M. A.; Howe, R. F.; Llorca, J.; Idriss, H., The Effect of Gold Loading and Particle Size on Photocatalytic Hydrogen Production from Ethanol Over Au/TiO₂ Nanoparticles. *Nat. Chem.* **2011**, *3* (6), 489-492.
61. Mahlamvana, F.; Kriek, R., Photocatalytic Reduction of Platinum (II and IV) from Their Chloro Complexes In a Titanium Dioxide Suspension in the Absence of an Organic Sacrificial Reducing Agent. *Applied Catalysis B: Environmental* **2014**, *148*, 387-393.
62. Herrmann, J. M.; Disdier, J.; Pichat, P., Photoassisted Platinum Deposition on TiO₂ Powder Using Various Platinum Complexes. *The Journal of Physical Chemistry* **1986**, *90* (22), 6028-6034.
63. Zhang, F.; Chen, J.; Zhang, X.; Gao, W.; Jin, R.; Guan, N.; Li, Y., Synthesis of Titania-Supported Platinum Catalyst: The Effect of pH on Morphology Control and Valence State during Photodeposition. *Langmuir* **2004**, *20* (21), 9329-9334.
64. Iliev, V.; Tomova, D.; Bilyarska, L.; Tyuliev, G., Influence of the Size of Gold Nanoparticles Deposited on TiO₂ Upon the Photocatalytic Destruction of Oxalic Acid. *Journal of Molecular Catalysis A: Chemical* **2007**, *263* (1-2), 32-38.
65. Xin, G.; Yu, B.; Xia, Y.; Hu, T.; Liu, L.; Li, C., Highly Efficient Deposition Method of Platinum over CdS for H₂ Evolution under Visible Light. *J. Phys. Chem. C* **2014**, *118* (38), 21928-21934.

66. Lee, J.; Choi, W., Photocatalytic Reactivity of Surface Platinized TiO₂: Substrate Specificity and the Effect of Pt Oxidation State. *The Journal of Physical Chemistry B* **2005**, *109* (15), 7399-7406.
67. Khalavka, Y.; Harms, S.; Henkel, A.; Strozyk, M.; Ahijado-Guzmán, R.; Sönnichsen, C., Synthesis of Au–CdS@CdSe Hybrid Nanoparticles with a Highly Reactive Gold Domain. *Langmuir* **2018**, *34* (1), 187-190.
68. Demortière, A.; Schaller, R. D.; Li, T.; Chattopadhyay, S.; Krylova, G.; Shibata, T.; dos Santos Claro, P. C.; Rowland, C. E.; Miller, J. T.; Cook, R.; Lee, B.; Shevchenko, E. V., In Situ Optical and Structural Studies on Photoluminescence Quenching in CdSe/CdS/Au Heterostructures. *J. Am. Chem. Soc.* **2014**, *136* (6), 2342-2350.
69. Carbone, L.; Jakab, A.; Khalavka, Y.; Sönnichsen, C., Light-Controlled One-Sided Growth of Large Plasmonic Gold Domains on Quantum Rods Observed on the Single Particle Level. *Nano letters* **2009**, *9* (11), 3710-3714.
70. Zhang, R.; Wang, H.; Li, Y.; Wang, D.; Lin, Y.; Li, Z.; Xie, T., Investigation on the Photocatalytic Hydrogen Evolution Properties of Z-Scheme Au NPs/CuInS₂/NCN-CN_x Composite Photocatalysts. *ACS Sustain. Chem. Eng.* **2021**, *9* (21), 7286-7297.
71. Berr, M.; Vaneski, A.; Susha, A. S.; Rodríguez-Fernández, J.; Döblinger, M.; Jäckel, F.; Rogach, A. L.; Feldmann, J., Colloidal CdS Nanorods Decorated with Subnanometer Sized Pt Clusters for Photocatalytic Hydrogen Generation. *Appl. Phys. Lett.* **2010**, *97* (9), 093108.
72. Dukovic, G.; Merkle, M. G.; Nelson, J. H.; Hughes, S. M.; Alivisatos, A. P., Photodeposition of Pt on Colloidal CdS and CdSe/CdS Semiconductor Nanostructures. *Adv. Mater.* **2008**, *20* (22), 4306-4311.

Chapter 1

Principles and Recent Advances in Photodeposition of Metals on Colloidal Semiconductor Nanocrystals

Table of contents

Chapter 1.....	15
Principles and Recent Advances in Photodeposition of Metals on Colloidal Semiconductor Nanocrystals	15
Abstract.....	19
1.1 Principles of photodeposition reactions	19
1.2 Photodeposition of metals on TiO ₂ surface.....	22
1.3 Photodeposition of metals on metal-chalcogenide surfaces	30
1.3.1 Photodeposition of metals on Cd-chalcogenides	30
1.3.2 Photodeposition of metals on heavy-metal-free chalcogenides	34
1.4 Conclusion and Perspective.....	39
1.5 References	41

Abstract

The presence of metal nanoparticles on the surface of a semiconductor can significantly suppress the recombination of photogenerated excitons as well as reduce the activation energies of the photoredox reactions and thus increases reaction rates.¹⁻⁷ Moreover, by coupling the metals (*e.g.*, Ag, Au, Pt) with strong localized surface plasmon resonance (LSPR), the efficiency of light-harvesting and absorption of semiconductors can be dramatically improved.¹⁻⁴ These unique properties are of great interest in the field of photocatalysis, such as wastewater treatment,⁸⁻¹⁰ air purification,¹¹⁻¹⁴ organic dye degradation^{9, 15-16} and photocatalytic solar fuel synthesis.¹⁷⁻²⁰ To date, many researchers have developed various ways to perform the fabrication of metal-semiconductor hybrid nanocrystals, *e.g.*, hydrothermal/solvothermal synthesis,²¹⁻²³ ion exchange,²⁴⁻²⁵ sputtering,²⁶⁻²⁷ photodeposition,^{5, 10, 28-29} deposition–precipitation,³⁰⁻³¹ and enzyme-mediated biomimetic approach.³²⁻³³ Among these strategies, photodeposition has drawn increasing attention since this method does not require elevated temperature or applied voltage, and can therefore be considered an environmentally-friendly approach.³⁴ Moreover, the major advantages of photodeposition include delicate control of the geometric distribution of metal nanodots on the surface of facet-engineered semiconductors and great flexibility in controlling the size and oxidation state of the deposited NDs by manipulating the reaction precursors as well as the intensity of illumination.³⁴ In this context, we will focus on introducing the working principle and recent advances in the photodeposition technique in designing metal-semiconductor hybrid nanocrystals.

1.1 Principles of photodeposition reactions

The observation of the photodeposition phenomenon was first described by G. Tammann in 1920.³⁵ He found that a finely dispersed suspension of crystalline zinc oxide (ZnO) in water in the presence of a small quantity of silver (Ag) nitrate was rapidly darkened when exposed to white light. After that, several scientists repeated

his experiments under more carefully controlled conditions and they indeed observed that fibrous Ag crystals did grow on the ZnO and titanium dioxide (TiO₂) under illumination.³⁶⁻³⁷ However, the latter discovery vanished for over half a century. In 1978, Kraeutler and Bard reported a synthesis protocol for the deposition of highly dispersed platinum (Pt) nanoparticles on the surface of TiO₂ by light irradiation on a slurry of TiO₂ powder with hexachloroplatinic acid in the presence of hydrochloric acid, sodium carbonate and acetic acid.³⁸ This research result is of paramount significance as it provides a general approach to extend the scope of metal photodeposition on colloidal semiconductors. Since then, interest in photodeposition has blossomed significantly, as shown in **Figure 1.1**.

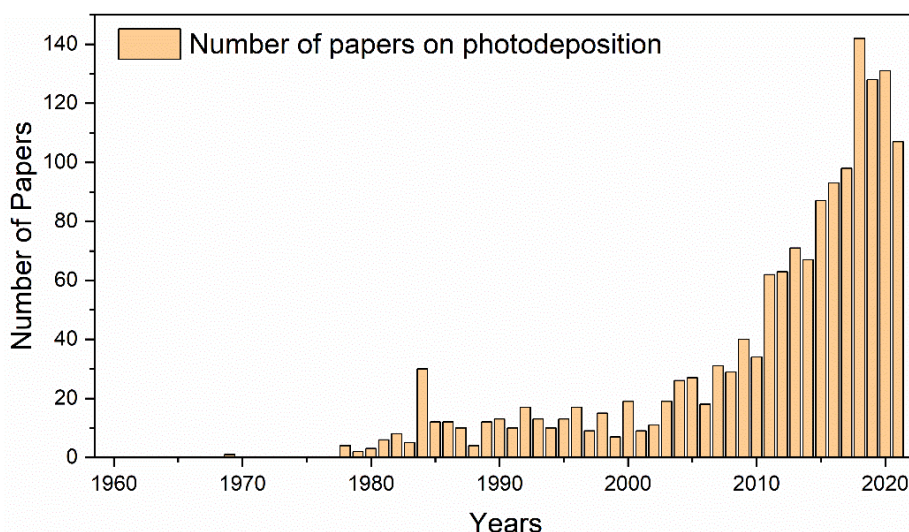


Figure 1.1 Statistical overview of the number of papers related to “photodeposition” as a function of years, as searched in Scopus on Oct 01, 2021. Note: not all publications related to photodeposition are shown in this figure since it can also be named “photochemical deposition” or “photoreduction”.

A photodeposition reaction is based on light-induced electrochemistry occurring in a mixed solution that contains colloidal semiconductor nanocrystals and metal ion precursors. Upon light irradiation with appropriate frequency, the photon energy pumps the electrons in semiconductors to the conduction band (CB), leaving holes behind in the valence band (VB). The electrons are used to reduce the metal precursors, thus leading to the deposition of the metal nanodots on the surface of the semiconductor (**Figure 1.2**).³⁴

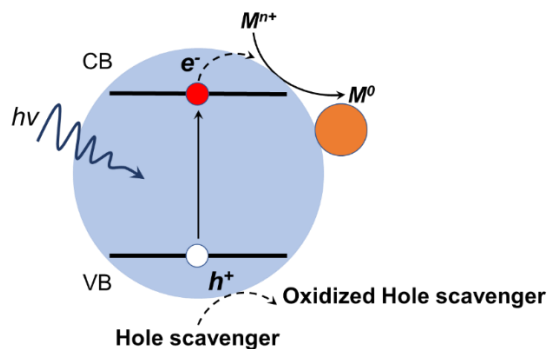


Figure 1.2 Schematic diagram of the photodeposition reaction. When light is absorbed in the bandgap, electrons from the VB are excited to the CB and then migrate to the semiconductor (blue sphere) surface where metal ions are reduced to metal (orange sphere). $h\nu$ represents light energy, e^- is the photoexcited electron, h^+ is the photogenerated hole, M^{n+} and M^0 describe metal ion and metal, respectively. The reduction reaction can be written as, $M^{n+}(\text{liquid}) + ne^- \rightarrow M^0(\text{solid})$.

To allow efficient photodeposition of metals on semiconductors, several key points should be carefully considered. First, the reduction potential of the metal ion should be more positive than the CB energy level of the semiconductor.^{11, 34} **Figure 1.3** shows the band positions of several commonly used semiconductors and redox potentials of several aqueous metal ions in solutions.

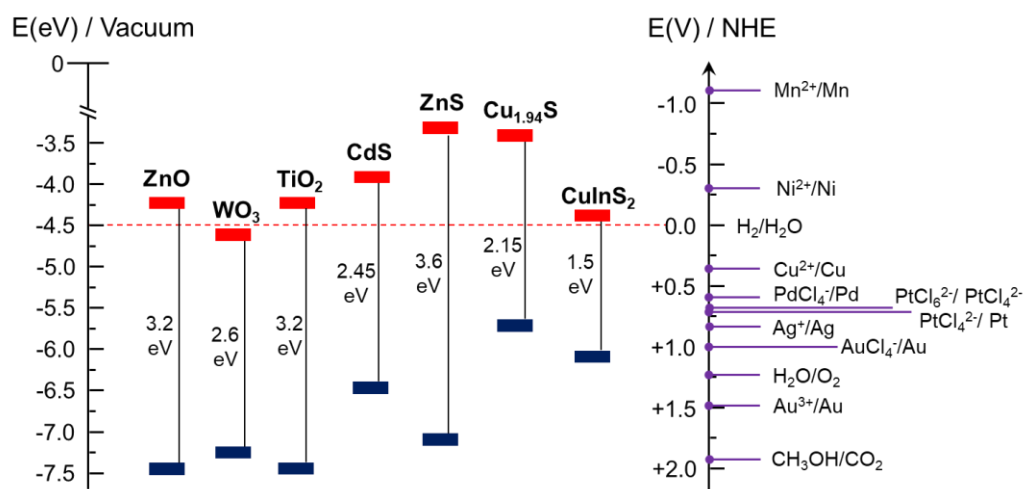


Figure 1.3 Schematic overview of the band positions of several semiconductors on an energy scale in electron volts relative to the vacuum level, or volts relative to the normal hydrogen electrode (NHE). The lowest CB (red) and the highest VB (dark blue) are displayed along with the bandgap in electron volts and figure adapted from previous works.³⁹⁻⁴⁰ Redox potentials of several aqueous metals in solutions relevant for photodeposition are shown using NHE as a reference.³⁴

Obviously, most metal ions can be reduced by the electrons from the excited semiconductors except Mn^{2+} which has a very negative reduction potential of -1.18 V at 298 K .³⁴ Secondly, the photon energy of illumination has to exceed the band-gap energy of the semiconductor to excite the materials and induce the generation of excitons, *viz.*, pairs of electron/hole.^{11, 34} Moreover, the recombination rate of photogenerated carriers should be as slow as possible, preferably a complete charge separation is targeted.^{11, 34, 41} In this case, the electrons can migrate to the semiconductor surfaces and are then efficiently used for reduction of metal ions. To avoid the accumulation of holes, scavengers (*e.g.*, methanol, Na_2S , Na_2SO_3 , *etc.*) are usually used in these reactions. Last but not least, the semiconductor needs to provide sufficient active surface sites for the photodeposition reaction to take place.^{11, 34}

1.2 Photodeposition of metals on TiO_2 surface

TiO_2 is one of the most intensively studied semiconductor materials in the field of photocatalysis due to its great photoactivity, chemical stability, long-term durability, and low cost.^{2, 9, 20, 34} Despite these great prospects, the full use of this material has encountered two main challenges, *i.e.*, the high recombination rate of the photogenerated charge carriers and the limited absorption of photons in the visible and near-infrared range.^{2, 9, 20, 34} To overcome these issues, adding metals with strong LSPR onto the surface of TiO_2 has been widely accepted as an efficient solution.^{2, 4, 34} The most commonly reported plasmonic metals are Ag, Au, and Pt.⁴² For conciseness, in the following subsection we will focus on summarizing the most recent advances in using photodeposition method for constructing plasmonic Au- TiO_2 Schottky junctions in the past few years. For the discussions on the other plasmonic metals on TiO_2 , readers can refer to several recent review articles.^{2-4, 34}

In classical chemical reactions in solutions, the selection of Au precursors has a great impact on the nucleation and growth of Au nanodots.⁴³⁻⁴⁴ To elucidate this

phenomenon in the photodeposition method, Gärtner and coauthors⁴⁵ systematically investigated the influence of different gold precursors such as $\text{NaAuCl}_4 \cdot 2\text{H}_2\text{O}$, AuCl_3 , and $[\text{Au}(\text{PPh}_3)]\text{Cl}$ on the formation of Au NDs on the surface of TiO_2 and the photoactivity of the resulting Au- TiO_2 materials. The use of $\text{NaAuCl}_4 \cdot 2\text{H}_2\text{O}$ and AuCl_3 showed the highest yields of Au loadings ($\geq 0.96\%$), while the $[\text{Au}(\text{PPh}_3)]\text{Cl}$ complex gave an extremely low value of ~ 0.09 wt% (**Table 1.1**). Though all of the Au nanodots are claimed to have a comparable size of 3-15 nm (which in fact is not so comparable), the catalysts are not equivalent and the product with the highest photocatalytic efficiency (H_2 evolution rate of $8.4 \mu\text{mol mg}^{-1} \text{h}^{-1}$) is the system formed using $\text{NaAuCl}_4 \cdot 2\text{H}_2\text{O}$ as precursors. This indicates that AuCl_4^- is a better Au precursor for the photodeposition and it also suggests that tuning the amount of Au loading is a key factor in improving the photocatalytic efficiency.

Table 1.1 Photocatalytic hydrogen production from MeOH/ H_2O mixtures with TiO_2 in the presence of various co-catalysts. TON means turnover number, $n_{\text{H}_2}/n_{\text{Au}}$, calculated based on the amount of Au added. TOF represents turnover frequency, calculated based on the amount of Au added. The Au loading is determined by inductively coupled plasma spectrometry. The data is adapted from ref⁴⁵.

Au precursor	V_{H_2} (mL)	H_2 evolution rate ($\mu\text{mol mg}^{-1} \text{h}^{-1}$)	TON	TOF (h^{-1})	Au loading (wt %)	Au Size (nm)
$\text{NaAuCl}_4 \cdot 2\text{H}_2\text{O}$	31	8.4	1006	168	0.97	3-15
AuCl_3	28	7.6	915	152	0.96	3-15
AuCl	22	6.0	709	118	0.65	3-15
$[\text{Au}(\text{PPh}_3)]\text{Cl}$	<2	<0.5	-	-	0.09	-
None	<0.2	-	-	-	-	-

It is also well-considered that the size of Au and the nature of the TiO_2 substrates can each, in turn, influence the photoreaction rates. Murdoch *et al.*⁴⁶ investigated the effect of Au particle size, Au loading, and TiO_2 phase on H_2 evolution from aqueous ethanol solutions. They found that Au NDs in the size range of 3-30 nm were highly active in photocatalysis and the photoreaction rate was independent of the size of Au particles in the range of 3-12 nm, as reported by Gärtner *et al.*⁴⁵ Moreover, they noticed

that the crystal phase of TiO₂ had a great impact not only on the size of the Au NDs but also on the photocatalytic activities of the hybrid NHDs. **Figure 1.4a** shows that the size of Au particles on TiO₂ anatase is generally smaller than that on TiO₂ rutile due to the stronger electronic interaction between anatase and Au particles, which prohibits Au agglomeration/sintering during thermal activation.⁴⁶⁻⁴⁷ More importantly, Au particles on TiO₂ anatase are about 100 times more active than those of a similar size on TiO₂ rutile, (anatase, ~15 nm; rutile fibre, 20 nm × 50 nm), as a result of different exciton recombination rates for these two species.^{46, 48-49} In the case of anatase, Au/TiO₂ hybrids exhibit an increased rate with increased Au loading (up to 4 wt%) with a corresponding increase in the mean Au particle size from 3 to 12 nm (**Figure 1.4b**). A further increase in Au loading (to 8 wt%) leads to an increased particle size of 16 nm. The H₂ production rate however decreases due to a reduction in the available substrate active sites where both metal and support are needed for the photoredox reaction to occur.

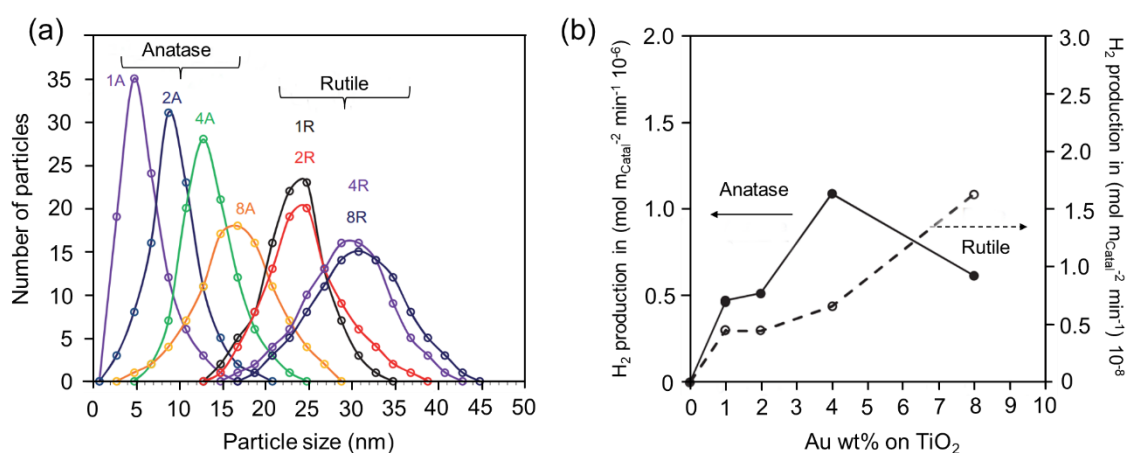


Figure 1.4 (a) Particle size distribution of Au on TiO₂ photocatalysts for hydrogen production. The mean Au nanoparticle size on anatase (A) is smaller than that on rutile (R). 1A, 2A, and so on, refer to 1wt%, 2wt%, and so on, of Au. **(b)** H₂ photoproduction from ethanol over Au/TiO₂ anatase and rutile as a function of Au loading. The left-handed-axis presents the normalized rate per unit area for Au/TiO₂ anatase nanoparticles and the right-handed-axis is that for Au/TiO₂ rutile nanoparticles. The x-axis presents the weight % of Au on the TiO₂ support. Adapted from ref.⁴⁶

Later, Priebe *et al.*⁵⁰ performed more comprehensive studies on the photoactivity of

plasmonic Au–TiO₂ catalysts with various TiO₂ substrate phases (anatase, rutile, brookite, or composites thereof) using a combination of *in situ* spectroscopic techniques (electron paramagnetic resonance spectroscopy, X-ray absorption near-edge structure, and UV-vis spectroscopy). They also found that the H₂ evolution rate of Au-anatase was twice as high as that of Au-rutile under UV-vis illumination. Moreover, anatase/rutile composites (e.g., P25, anatase/rutile = 85:15) provided the highest H₂ evolution rate under both UV-vis and visible lights due to improved charge separation and an electron transfer across the anatase/rutile interface.

Based on these initial studies on the photoactivity of plasmonic Au–TiO₂ catalysts, researchers started to shift their attention to how to fine-tune the photodeposition of Au on highly photoactive TiO₂ anatase or anatase/rutile mixtures, and how to control the size of Au nanodots. Similar to the prototypical synthesis of Au particles in solution,⁴³⁻⁴⁴ the size of Au NDs were readily regulated by adjusting the concentration of Au precursors.⁵¹ In the case of photodeposition, the size control of Au particles was also dictated by irradiation time. Deepagan and coauthors⁵² developed a strategy to control the size and size distribution of the deposited Au NDs on TiO₂ by varying the ultraviolet exposure time. After illumination for less than 3 min, many unimodal small Au nanoparticles (< 2 nm) were obtained. Prolonging the exposure time led to the formation of larger Au NDs (> 5 nm) at the expense of the small ones. Very recently, Bai *et al.*²⁸ reported the synthesis of metal (Ag and Au)-TiO₂ nanoheterodimers by laser-driven photodeposition in a continuous microfluidic reactor (**Figure 1.5a**). Instead of the conventional ultraviolet lamp, the authors used a focused laser beam which creates a tremendous number of electron-hole pairs in a short time scale, thus ensuring a large number of charge carriers for the reduction of metal ions and promoting the growth of a single metallic dot on the TiO₂ surface (**Figure 1.5b,c**), the average size of the metallic nanoparticles proportionally increased with the increase of the excitation power with a stable polydispersity around 20%. The authors also modeled the growth of Ag NDs on TiO₂ and showed that the diameter of Ag was proportional to $t^{1/3}$. This work provides new insight into the controlled synthesis of Au

or Ag-TiO₂ hybrid NHDs and is of great interest to be extended to the construction of other metal-semiconductor systems.

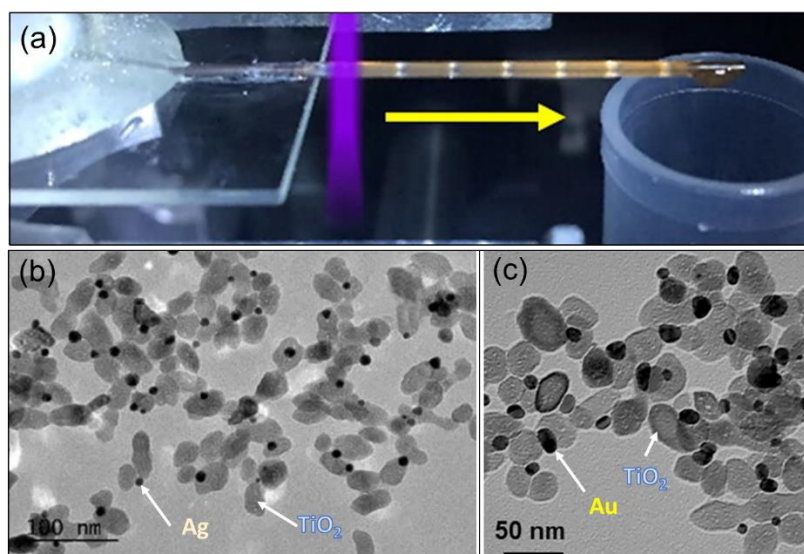


Figure 1.5 (a) Digital image of the experimental setup used for the photoproduction of M/TiO₂ (M = Ag, Au) in a microchannel configuration. The color change of the solution from transparent to orange after crossing the laser beam materialized by the purple color (the solution flows from left to right according to the direction of the yellow arrow) indicates the formation of metal nanoparticles. (b) TEM images of the Ag/TiO₂ NHDs. (c) TEM image of the Au/TiO₂ NHDs. Adapted from ref.²⁸

With the advanced development of the photodeposition method, this technique has also been successfully employed to deposit plasmonic metals on diverse TiO₂ morphologies and the product composites show great prospects in many photocatalytic applications. Shahini *et al.*⁵³ demonstrated the immobilization of plasmonic Ag-Au nanoparticles on TiO₂ nanofibers using such a photodeposition method. The synthesized Ag-Au/TiO₂ nanocomposites exhibit improved absorption ability in the visible-light range due to the contribution of LSPR from Ag-Au. The yielded materials show notable enhancement of photocatalytic efficiency as evidenced by visible-light decomposition of rhodamine B as a model dye. Shoueir *et al.*,⁵⁴ introduced a rational design of photoactive plasmonic fibers by photodepositing Au metals on TiO₂ fibers. These materials exhibit enhanced degradation activity and can be used to clean

harmful water pollutants such as organic dyes as well as toxic chromium and Cr(VI) in the presence of citric acid within 21 min. Park *et al.*⁸ reported the development of photodeposited Au nanodots (~ 5-9 nm) decorated ZnO-TiO₂ core-shell nanowires on the Si-wafer (**Figure 1.6a**). After Au modification, the nanowires exhibit an enhanced photocurrent density upon illumination by visible light and high photoelectrochemical water splitting activity due to the enhanced absorbance in the visible region owing to the surface plasmon resonance (SPR) effect of Au-nanodots as well as the excellent separation of photogenerated charge carriers and hot electron transportation. Veziroglu *et al.*²⁹ proposed an efficient method to prepare a TiO₂ thin film decorated by photodeposition with highly active Au nanoclusters (**Figure 1.6b**). The extent of surface coverage of TiO₂ by the Au nanoclusters governed by the type of solvent and the illumination time has great impacts on both the electron storage capacity and the optical absorption of the Au-TiO₂ system. They found that a low Au surface coverage (19.2-29.5%) could significantly enhance the absorption of TiO₂ under UV wavelength which therefore resulted in a higher photocatalytic performance.

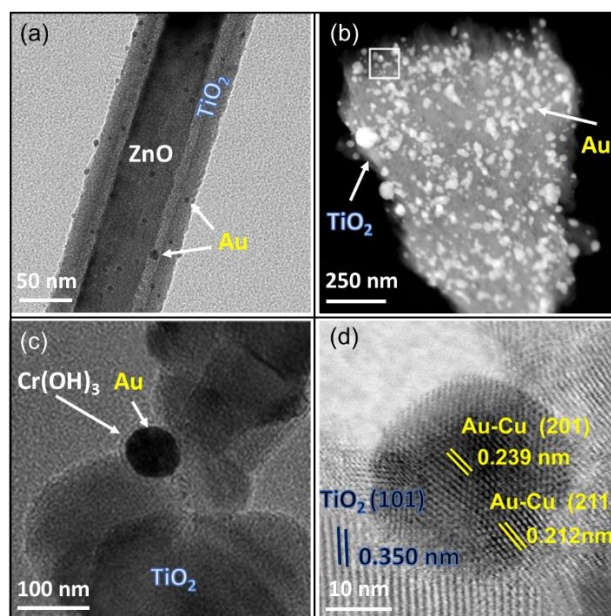


Figure 1.6 (a) Transmission electron microscope (TEM) image of Au NPs decorated ZnO-TiO₂ core-shell nanowires. Adapted from ref.⁸ (b) Scanning TEM (STEM) image under high-angle annular dark-field (HAADF) mode of Au nanocluster decorated TiO₂ thin film at low magnification. Adapted from ref.²⁹ (c) TEM image of Cr(OH)₃(y)/Au/TiO₂ obtained by two-step photodeposition method. Adapted from ref.⁵⁵ (d)

STEM-HAADF image of light-induced co-loading Au–Cu alloy nanoparticles on TiO₂. Adapted from ref.¹³

Aside from the single-step photodeposition of metals on TiO₂, more complicated multi-step photodeposition methods have very recently been adopted to obtain even more complex nanostructures with synergistically combined optoelectronic or catalytic properties. Fudo *et al.*⁵⁵ described a two-step photodeposition method toward a Cr(OH)₃ modified Au/TiO₂ photocatalyst. After depositing Au metal NDs on TiO₂, a chromium species was further introduced and a thin layer of Cr(OH)₃ was successfully formed on the Au nanoparticles (**Figure 1.6c**). The Cr(OH)₃ acted as a hole transferring cocatalyst in the Au/TiO₂ system and significantly enhanced the oxygen production (with a max rate of 0.72 μmol h⁻¹) by water oxidation under visible light irradiation. Yu *et al.*¹³ developed a facile step-by-step photodeposition method to co-load Au–Cu alloy nanodots on TiO₂ for the photocatalytic synthesis of solar fuels with CO₂ and H₂O (**Figure 1.6d**). The ratio of Au-Cu alloys was controlled by tuning the amount of Cu(NO₃)₂·3H₂O to HAuCl₄ in the reaction solution. The Cu_{0.8}Au_{0.2}/TiO₂ can reduce CO₂ and achieve an ultrahigh photocatalytic performance with formation rates of 3578.9 and 369.8 μmol g⁻¹ h⁻¹ for CH₄ and C₂H₄, respectively, which is greatly superior to most works on CO₂ photoreduction. Theoretical calculation predicts that the combination of single Cu atoms and Au-Cu alloys on TiO₂ could reduce the overall activation energy barriers of CH₄ and C₂H₄ formation process, which is the key factor to enhance the CO₂ Photoreduction efficiency.

Another very interesting example of using multi-step photodeposition to design complex nanostructures was reported by Ha *et al.*¹⁰ in 2020. They introduced a plasmonic photocatalyst synthesized by photodepositing multiple inorganic components on Au/TiO₂ nanodumbbell structures (**Figure 1.7**).

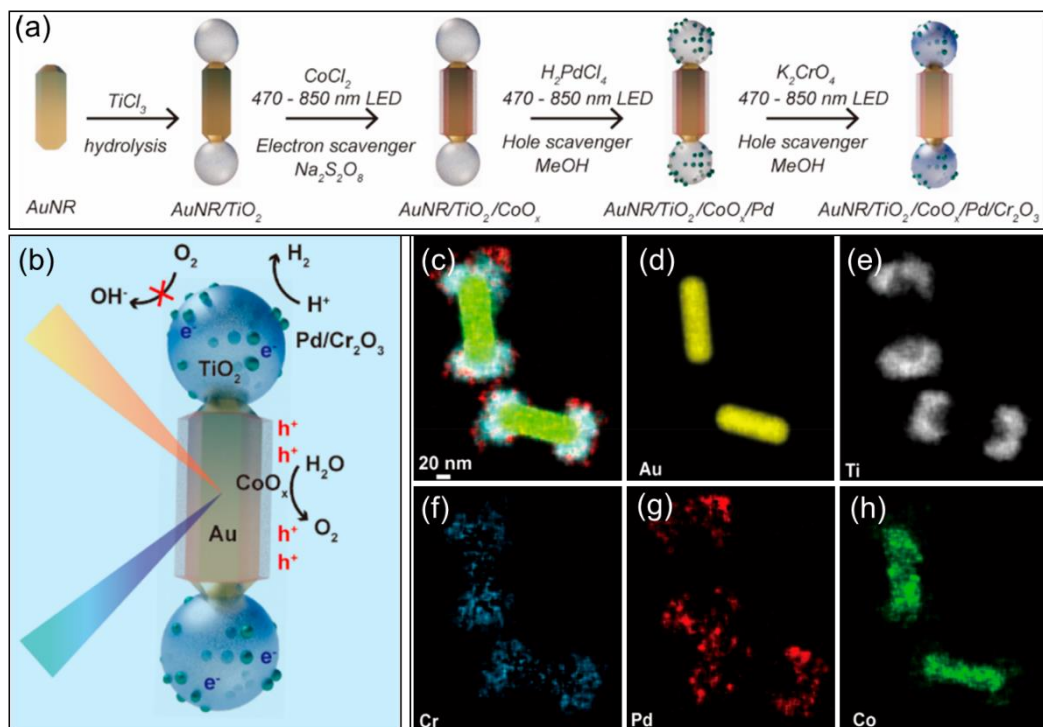


Figure 1.7 (a) Synthetic scheme with multi-step photodepositions that lead to the precisely integrated Au/TiO₂/CoO_x/Pd/Cr₂O₃ photocatalyst. **(b)** Schematic illustration of the functional design of nanoparticles including all the individual components. **(c-h)** Elemental maps of the nanostructures. Adapted from ref.¹⁰

With the coordination of all essential components, including Au, TiO₂, CoO_x, Pd, and Cr₂O₃, the designed nanostructure exhibits impressive photocatalytic activity for oxygen evolution reaction (with a rate of 1.3 mmol g⁻¹ h⁻¹) from water without scavenger under visible light irradiation. Although the deposited metal is not Au, the idea of constructing multifunctional materials into a single system *via* photodeposition is of great significance to broadening the horizon for the design of efficient photocatalysts. Apart from TiO₂, this photodeposition method has also been adopted for metal oxides, such as ZnO, WO₃, Ga₂O₃, and Ta₂O₅. These investigations will not be specifically discussed in this chapter and can be referred to in some review articles.^{34, 56-57}

1.3 Photodeposition of metals on metal-chalcogenide surfaces

Compared with metal oxide semiconductors, metal chalcogenides generally exhibit much higher absorption coefficients over a wide spectral range and narrower bandgap tunable by size and composition, making them promising alternatives as visible-light-driven photocatalysts.^{19, 58-61} However, their photocatalytic performance remains poor due to the fast exciton recombination rates (a few nanoseconds scale⁶²) and their poor photostability (photo-oxidation of metal ions³⁴). To combat these issues, researchers also coupled these metal-chalcogenides with other semiconductors or metals to promote charge separation and transport in heterojunctions. The photo-corrosion of metal ions can be relieved by adding hole scavengers to the photoredox reaction solution. In the following subsection, we will focus on introducing two NHDs obtained by the photodeposition method: 1) metals coupling with Cd-chalcogenides; 2) metals combining with heavy-metal-free chalcogenide semiconductors.

1.3.1 Photodeposition of metals on Cd-chalcogenides

Cadmium sulfide (CdS) is one of the most investigated metal chalcogenides for photocatalysis due to its narrow bandgap and high photocatalytic activity.^{59, 61} The early pioneer work on photodeposition of metals on Cd-chalcogenides was reported by the group of Alivisatos in 2008.⁶³ They performed the photodeposition of Pt nanodots on colloidal CdS and CdSe/CdS nanorods in an organic solvent under visible light irradiation (458 nm) in the presence of (1,5-cyclooctadiene)dimethylplatinum(II) and tertiary amines (e.g., triethylamine and diisopropylethylamine). Interestingly, they observed the deposition of a varying number of small Pt (< 3 nm) nanodots ranging from 0 to 6 on the CdS nanorods (**Figure 1.9a**) with no specific location. In sharp contrast, most of the CdSe/CdS core/shell nanorods had only a single Pt nanodot which was specifically located near the CdSe core (**Figure 1.9b**). The underlying reasons for this difference remain unclear. Wilker *et al.*⁶² suggested that the

photoreduction rate of Pt^{II} to Pt^0 was slow in the presence of tertiary amines. Nucleation of Pt NDs thus prefers to occur at the locations on the CdS surface (**Figure 1.9a**) with relatively long-lived carrier trap states, e.g., un-passivated Cd^{2+} sites which are typically located at the side of the rod due to their large surface areas.⁶² The growth of Pt NDs on the length of the CdS rod is then promoted by the fast electron transfer from CdS to Pt islands, followed by the reduction of Pt precursors. However, the Pt deposited near the CdSe cores (**Figure 1.9b**) is possibly due to the strong localization of electrons or holes at the cores as a result of a band alignment between the CdSe core and the CdS shell.⁶³ Though this topic has been investigated for more than ten years, the fundamental mechanisms responsible for the locations of Pt nanoparticles on CdS and CdSe/CdS nanorods are still under development.

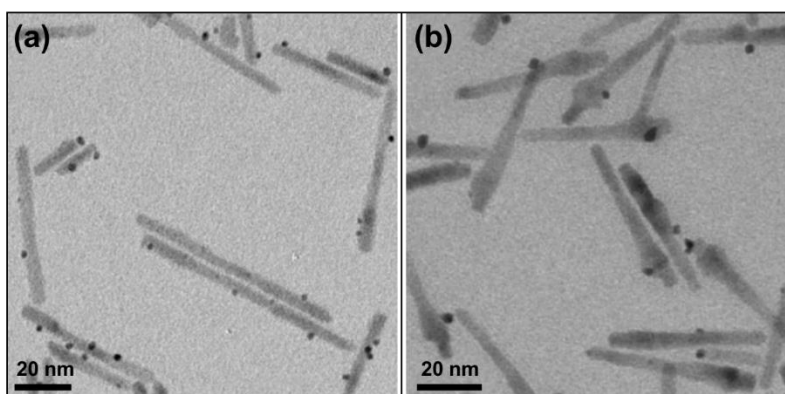


Figure 1.9 (a) TEM image of photodeposited Pt/CdS nanorods. Pt nanodots appear along the side of the nanorods. (b) TEM image of photodeposited Pt/CdSe-CdS core-shell nanorods. Pt nanodots locate near the CdSe cores of the rods. Adapted from ref.⁶³

Notably, the deposition of Pt on CdS nanorods behaves in significantly different ways depending on the synthesis methods. Habas *et al.*⁶⁴ demonstrated the synthesis of three systems: Pt-CdS, PtNi-CdS, and PtCo-CdS hybrid nanostructures with controllable size and composition *via* thermal reactions at 200 °C in the presence of oleylamine and oleic acid. Instead of a heterogeneous distribution on the rod length,⁶³ the authors observed a selective metal dot deposition at the tip of CdS rods. They claimed that such growth was ascribed to the preferential metal nucleation on the end

of facets, which had much higher surface energies due to less ligand passivation.⁶⁴ A more explicit comparison of thermal and photochemical approaches in the deposition of Au on CdS and CdSe/CdS core/shell nanorods was performed by Banin and co-workers.⁶⁵ They found that the thermal route resulted in the growth of Au on the side of nanorods, while the photodeposition method led to the selective deposition of Au on the tips of nanorods. This observation was completely at variance with the deposition of Pt on CdS nanorods mentioned above.⁶⁴ The reason for this difference is unclear and may be related to surface ligand effects associated with the strength of the Au-S bond as well as the existence of sulfur-rich terminal facets of CdS nanorods.⁶²

The recent work by Hao *et al.*⁵ further extended this topic and achieved a fine control of the Au sites on CdSe/CdS using tunable laser excitation in the presence of a controlled amount of hole scavenger, *i.e.*, methanol. With this method, the Au was deposited on the tips of the as-prepared nanorods, and the results were consistent with previous observations.⁶⁵ Moreover, they found that the hole scavengers play an important role in tuning the number of gold NDs per CdSe/CdS nanorods. With the increase of methanol, the percentage of Au on one tip of nanorods can reach a ratio close to 85%, while Au double tips or multi-sites significantly decrease.⁵

The control of hole scavengers also has a great impact on the photostability as well as the photocatalytic activity of Cd chalcogenides. Compared to metal oxides, Cd chalcogenides usually have poor photostability since they can be readily oxidized and then dissolved in solution under light irradiation ($CdS + 2h^+ \rightarrow Cd^{2+} + S$).^{34, 66} To prevent the CdS photocorrosion, hole scavengers are generally added to the reaction mixture. To date, various sacrificial agents including ethanol,⁶⁷ methanol,^{5, 68} 2-propanol,⁶⁹ acetic acid,^{68, 70-72} formaldehyde,⁷³ $(NH_4)_2SO_3$,⁶⁸ a mixture of Na_2S and Na_2SO_3 ,^{70, 74} have been used. Xin *et al.*⁷⁵ systematically investigated the influence of different scavengers (*i.e.*, methanol, lactic acid, and Na_2S/Na_2SO_3) during *in situ*

photodeposition of 0.1 wt% Pt on a mixture of cubic and hexagonal CdS nanocrystals. The authors found that the amount of Pt deposited on the CdS surfaces varied significantly when different sacrificial agents were adopted. The use of methanol gives rise to the highest deposition of Pt (0.0894%), while that of Na₂S/Na₂SO₃ and lactic acid results in the lowest and medium yield of Pt on CdS (0.0124% and 0.0248%, respectively). Interestingly, the use of lactic acid as a hole scavenger gave the highest H₂ evolution rate (**Figure 1.10**). Yao *et al.*⁶⁸ further studied the photodeposition of Pt (0.5 wt %) on CdS by using different hole scavengers, such as methanol, glacial acetic acid, and (NH₄)₂SO₃. They noticed that the use of methanol and (NH₄)₂SO₃ did not show noteworthy activity, while that of glacial acetic acid led to the highest photoactivity, being consistent with the observation reported by Xin *et al.*⁷⁵ They proposed that this was mainly because acetic acid did prevent the formation of CdO, which is detrimental for the photocatalytic activity, on the surface of CdS semiconductors.⁶⁸

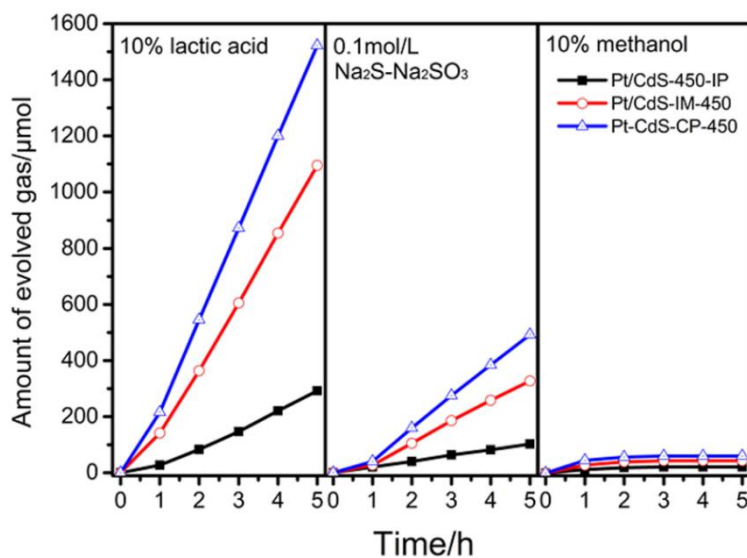


Figure 1.10 Photocatalytic H₂ evolution on 0.1 wt % Pt/CdS-450-IP (prepared by photodeposition), 0.1 wt % Pt/CdS-IM-450 (prepared by impregnation), and 0.1 wt % Pt/CdS-CP-450 (prepared by coprecipitation) in the presence of different hole scavengers. Adapted from ref.⁷⁵

Another note should be taken that the photodeposition of metals on metal chalcogenides is usually performed in an organic solution rather than in an aqueous solution. This is because most metal chalcogenides are synthesized by one-pot heating up or hot injection methods in organic solutions.⁷⁶⁻⁷⁸ Thanks to the development of colloidal science, the reactions in both organic and aqueous solutions can be performed thanks to either phase transfer of water-soluble metal precursors into organic solvents (e.g., toluene) or that of non-polar solvent-soluble Cdchalcogenides into polar solution (e.g., water). The first case has been used by Hao *et al.*⁵ The latter one has also been reported. For example, Berr *et al.*⁷⁹ reported a strategy to obtain water-soluble CdS nanorods by exchanging the original phosphonic acid for D,L-cysteine hydrochloride. Photodeposition of Pt onto CdS nanorods was carried out in an aqueous solution under UV-illumination at 366 nm in the presence of triethanolamine (as a hole scavenger) and ascorbic acid (as a mild reducing agent). They demonstrated a highly selective decoration of the CdS nanorods with uniform Pt nanoparticles (~4.8 nm), randomly distributed along the rod length and very seldom located at the tips, with a remarkably high yield (~90%) of samples decorated with one Pt per rod.⁷⁹ Apart from Pt and Au, many other metals (e.g., Ag, Rh, Ni, Ru, Pd) have also been successfully deposited on Cd chalcogenides. For conciseness, we do not discuss them in this chapter and readers can refer to several recent articles.^{34, 59, 80-85}

1.3.2 Photodeposition of metals on heavy-metal-free chalcogenides

Despite their superior optoelectronic and photocatalytic properties, Cd chalcogenides are still not ideal for practical applications due to their inherent toxic nature. The development of non- or low-toxic alternative metal chalcogenides is therefore of great significance. To date, many heavy-metal-free chalcogenides (e.g., ZnS,^{60, 86-92} Cu_{2-x}S,^{60, 86, 92-93} ZnIn₂S₄,^{60, 94} Cu₂ZnSnS₄,^{31, 95-98} MoS₂,⁶⁰ MnS,¹⁴ SnS₂,⁹⁹ In₂S₃,⁸⁶ CuInS₂,^{95, 100} etc.) have been widely used as photocatalysts. However, the

majority of these environmentally-friendly materials exhibit photocatalytic activity less efficient than that of the above-mentioned TiO₂ and Cd chalcogenides. To improve their activities, various metals have been successfully coupled with these chalcogenides *via* different strategies, such as hydrothermal/ solvothermal synthesis, ion exchange, sputtering, photodeposition,^{87, 99} electrodeposition, atomic-layer deposition, and deposition-precipitation.⁸⁹ Amongst these ways, the development of light-induced deposition of metals on heavy-metal-free chalcogenides has not yet reached the same level as that of TiO₂ and Cd chalcogenides. This may be related to at least two reasons. First, the controlled synthesis and fundamental understanding (*e.g.*, surface chemistry, chemical stability, optoelectronic and photocatalytic properties) of heavy-metal-free chalcogenides are underdeveloped. Second, photodeposition methods involve a complex interplay of multiple aspects (*e.g.*, excitation conditions, absorption of photons, exciton dynamics, surface defects, sacrificial agents, *etc.*) that make the understanding of the photodeposition process very challenging. Most of the previously reported photodepositions are based on empirical data and lack of a theoretical foundation. Due to the limited number of references, we present only a few recent examples of metal photodeposition on these heavy-metal-free chalcogenides.

Photodeposition of metals on ZnS nanocrystals. ZnS semiconductors have extremely large band gaps (~ 3.6 eV),^{15, 87, 101} making them only responsive to UV light irradiation. To improve this absorption ability in the visible region, Sacco *et al.*⁸⁷ reported the fabrication of a highly efficient Ag/ZnS photocatalyst by photodeposition for 1 h using two UV lamps (nominal power of 8 W for each lamp) emitting at 365 nm. The addition of Ag to the ZnS substrate significantly increased its absorbance in the visible region due to the contribution of Ag LSPR. The photocatalytic activity of Ag/ZnS was sharply improved compared to pure ZnS as evaluated by the photodegradation of methylene blue and phenol as model organic dyes. Later, Ham *et al.*¹⁵ introduced a photodeposition process to reduce HAuCl₄ directly on ZnS nanobelts and to form junction structures between Au NDs and ZnS nanobelts (**Figure 1.11a**). The amount

and average size of the Au NDs on the ZnS nanobelts were controlled by adjusting the concentration of the Au precursor (**Figure 1.11b,c**). The existence of Au nanoparticles promoted an efficient charge separation in the ZnS nanobelts evidenced by the photoluminescence spectra and decay kinetic profiles. Compared with pure ZnS nanobelts and commercial ZnS, the product Au(0.2 wt%)-ZnS nanobelts showed a dramatic improvement in the photocatalytic activity (2.1 and 5.2 times, respectively) demonstrated by the photodegradation of 4-nitrophenol.

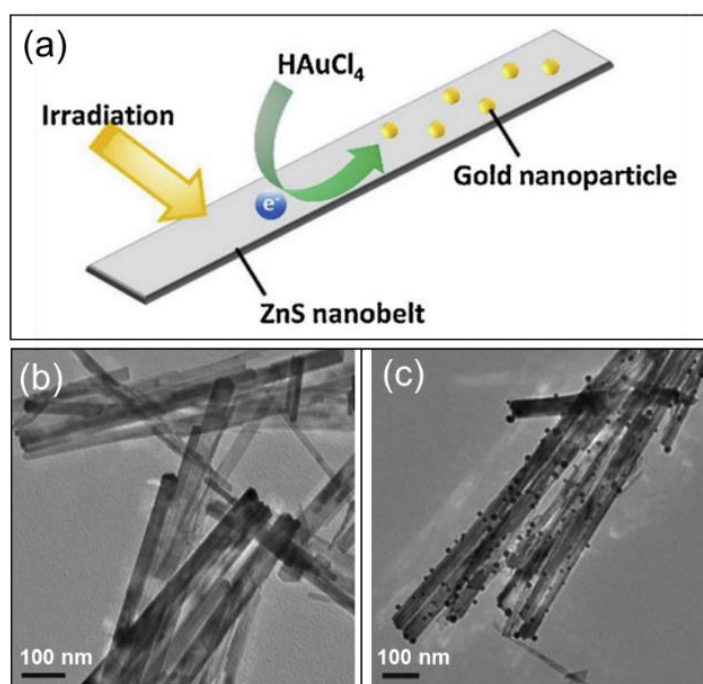


Figure 1.11 (a) Schematics of the photodeposition of Au nanoparticles on a ZnS nanobelt. (b-c) TEM images of Au(x%)-ZnS nanobelts with x values are 0 (b) and 2.0 (c). Adapted from ref.¹⁵

Very recently, Zhu *et al.*⁹⁰ reported a very interesting way to dramatically increase photocatalytic activity by photodepositing low-cost metal phosphides (Ni-P) on defect-rich ZnS nanospheres (**Figure 1.12a**). The optimized Ni-P/ZnS nanostructures exhibit a superior visible-light-driven H₂ evolution rate (69.92 μmol/h), 29 times and 3.6 times higher than that of the bare defect-rich ZnS and Pt/ZnS, respectively (**Figure 1.12b**). The authors suggested that the introduction of Zn vacancy defects was beneficial to the formation of defect energy levels within the bandgap of ZnS, which fosters the

visible-light absorption ability (**Figure 1.12a**). Moreover, the formed Schottky junction between ZnS and Ni-P alloy not only accelerates the photogenerated electron transfer from ZnS to Ni-P but also prohibits the electrons from flowing back.⁹⁰ These combined effects thus significantly improve their photocatalytic performance. This piece of work provides new insights into designing efficient photocatalysts through integrating defect engineering in semiconductors and Schottky junctions with some low-cost metals or alloys.

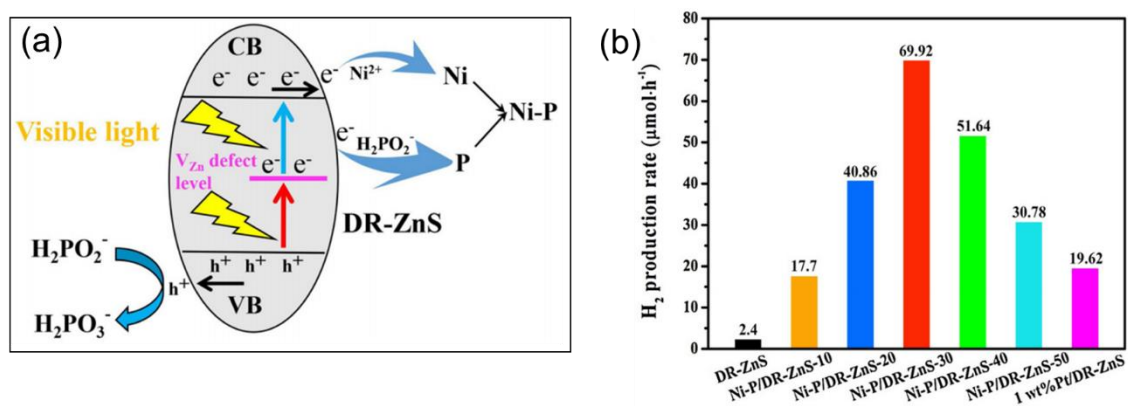


Figure 1.12 (a) Formation process of anchoring Ni-P alloy onto the surface of defect-rich (DR) ZnS via photodeposition. **(b)** Average H₂ production rates of a serial of ZnS samples. Ni-P/DR-ZnS-t represents Ni-P alloy on defect-rich ZnS nanocrystals, (where t = 10, 20, 30, 40, or 50 min) stands for the illumination time. Adapted from ref.⁹⁰

Photodeposition of metals on Cu-chalcogenide nanocrystals. Cu-chalcogenides are other potential semiconductors used as photocatalysts due to their exceptional visible light absorption properties, their nontoxic composition, their environmentally benign character, their unique plasmonic properties, and their suitable band alignment compared to the reduction potential of H₂ (**Figure 1.3**).⁵⁸ They have been successfully used for the production of H₂, reduction of CO₂, water splitting, and degradation of organic pollutants.^{58, 102} However, a fatal weakness of these materials is their photostability. Indeed, the Cu ions of the majority of Cu-chalcogenide semiconductors have an oxidation state of one, these Cu⁺ ions being able to be either oxidized to Cu²⁺ or reduced to Cu⁰, thus making them extremely unstable under ambient conditions or light irradiation. To the best of our knowledge, only an accountable number of articles

have shown the photodeposition of metals on Cu-chalcogenides. Early work, reported by the group of Vela,³¹ systematically compared four methods of preparation of Cu₂ZnSnS₄-Au hetero-nanostructures. Specifically, the reaction of Cu₂ZnSnS₄ nanorods with either a solution of Au precursors (AuCl₃ in toluene) or preformed Au particles (~ 2 nm), each under thermal reaction (60 °C) or photodeposition under 350 nm illumination (room temperature) (**Figure 1.13**). Using a solution of Au precursor led to a much higher affinity of the formed Au nanodots with the Cu₂ZnSnS₄ surface than using preformed Au nanoparticles. Moreover, a thermally induced deposition of Au on Cu₂ZnSnS₄ nanorods showed better control of the homogeneous distribution of Au NDs along the length of Cu₂ZnSnS₄ (**Figure 1.13**). No matter the method, the Cu₂ZnSnS₄-Au hybrid nanoheterostructures exhibited a much higher photocatalytic activity than the bare Cu₂ZnSnS₄ starting materials as evidenced by the subsequent photocatalytic reduction of methylene blue. Impressively, the Cu₂ZnSnS₄-Au nanoheterostructures are rather robust and remain active after two-month storage in the dark. These results open up a new area of greener photocatalysts for solar-to-chemical energy conversion.

Recently, Zhang *et al.*¹⁰³ illustrated a multi-step strategy to prepare a new series of Au/CuInS₂/C₃N₄ composite photocatalysts for H₂ evolution. They performed a photodeposition to load Au nanoparticles on CuInS₂/C₃N₄ nanostructures. The resulting materials show improved light absorption ability thanks to the Au LSPR. The designed Z-scheme transfer system from CuInS₂/C₃N₄ associated with the Au LSPR effect significantly enhances the photocatalytic activity with an H₂ evolution rate of 10.72 mmol h⁻¹ g⁻¹, about 21 times higher than that of pure g-C₃N₄. These studies show that Cu-chalcogenides are promising alternatives as photocatalysts. However, systematic investigations on the loading of metals on Cu-chalcogenides by photodeposition are rare, this motivated us to further explore and contribute to this field. Detailed studies are described in the last chapter.

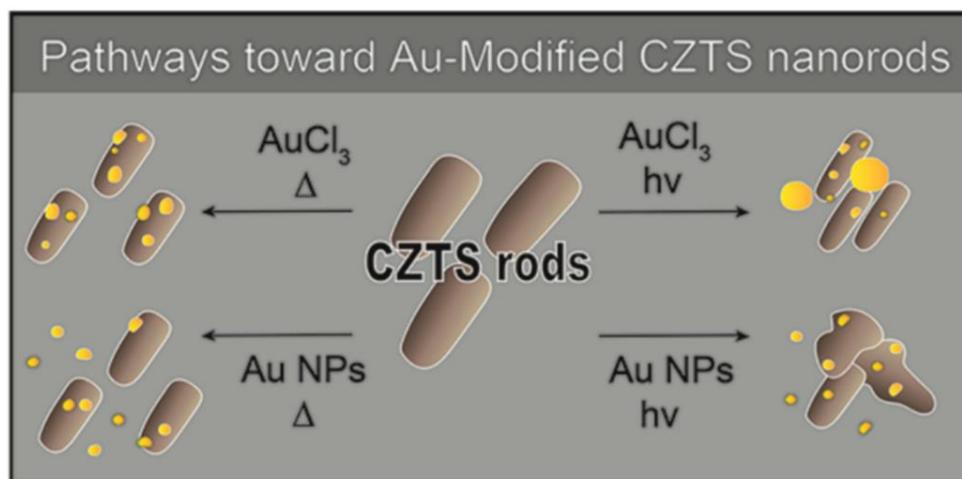


Figure 1.13 Schematic diagram of different pathways and outcomes of the Au NDs deposition on $\text{Cu}_2\text{ZnSnS}_4$ Nanorods. Adapted from ref.³¹

1.4 Conclusion and Perspective

In this chapter, we discussed the working principle of photodeposition and the bright prospects for providing an efficient way of coupling metal nanoparticles to photocatalytic materials. We have intensively discussed relevant research in photodeposition that has been applied to design plasmonic metal/ TiO_2 , especially pointing out several fundamental key factors controlling their synthesis as well as the strong impact on their photocatalytic activities. We have also discussed the recent development of photodeposition methods used for the metal loading on Cd-chalcogenides and heavy-metal-free chalcogenides. Though relevant research on the later photocatalytic materials is far behind, they are extremely promising for expanding current horizons and creating new efficient environmentally-friendly photocatalysts for practical applications. We have briefly provided an overview of the research in this area and have also highlighted several key issues that need to be addressed. In the future, more systematic experimental studies and relevant theoretical investigations should be performed to thoroughly understand the complex interplay of the multiple factors involved in the photodeposition process. With the right set of conditions,

photodeposition methods should provide a precise way of fabricating complex inorganic building blocks and colloidal assemblies with desirable photocatalytic properties for energy harvesting, catalysis, and environmental applications.

1.5 References

1. Wenderich, K.; Mul, G., Methods, mechanism, and applications of photodeposition in photocatalysis: a review. *Chemical reviews* **2016**, *116* (23), 14587-14619.
2. Kumar, A.; Choudhary, P.; Kumar, A.; Camargo, P. H. C.; Krishnan, V., Recent Advances in Plasmonic Photocatalysis Based on TiO₂ and Noble Metal Nanoparticles for Energy Conversion, Environmental Remediation, and Organic Synthesis. *Small* **2021**, 2101638.
3. Chakhtouna, H.; Benzeid, H.; Zari, N.; Qaiss, A.; Bouhfid, R., Recent Progress on Ag/TiO₂ Photocatalysts: Photocatalytic and Bactericidal Behaviors. *Environ. Sci. Pollut. Res.* **2021**, *28* (33), 44638-44666.
4. Zada, A.; Muhammad, P.; Ahmad, W.; Hussain, Z.; Ali, S.; Khan, M.; Khan, Q.; Maqbool, M., Surface Plasmonic-Assisted Photocatalysis and Optoelectronic Devices with Noble Metal Nanocrystals: Design, Synthesis, and Applications. *Adv. Funct. Mater.* **2020**, *30* (7), 1906744.
5. Hao, J.; Liu, H.; Wang, K.; Sun, X. W.; Delville, J.-P.; Delville, M.-H., Hole Scavenging and Electron–Hole Pair Photoproduction Rate: Two Mandatory Key Factors to Control Single-Tip Au–CdSe/CdS Nanoheterodimers. *ACS Nano* **2021**, *15* (9), 15328-15341.
6. Chai, Z., Light-Driven Alcohol Splitting by Heterogeneous Photocatalysis: Recent Advances, Mechanism and Prospects. *Chem. Asian J.* **2021**, *16* (5), 460-473.
7. Zhang, F.; Wang, X.; Liu, H.; Liu, C.; Wan, Y.; Long, Y.; Cai, Z., Recent Advances and Applications of Semiconductor Photocatalytic Technology. *Appl. Sci.* **2019**, *9* (12).
8. Park, J.; Deshmukh, P. R.; Sohn, Y.; Shin, W. G., ZnO–TiO₂ Core-Shell Nanowires Decorated with Au Nanoparticles for Plasmon-Enhanced Photoelectrochemical Water Splitting. *J. Alloys Compd.* **2019**, *787*, 1310-1319.
9. Xing, Z.; Zhang, J.; Cui, J.; Yin, J.; Zhao, T.; Kuang, J.; Xiu, Z.; Wan, N.; Zhou, W., Recent Advances in Floating TiO₂-based Photocatalysts for Environmental Application. *Appl. Catal. B.* **2018**, *225*, 452-467.
10. Ha, H. D.; Yan, C.; Katsoukis, G.; Kamat, G. A.; Moreno-Hernandez, I. A.; Frei, H.; Alivisatos, A. P., Precise Colloidal Plasmonic Photocatalysts Constructed by Multistep Photodepositions. *Nano Lett.* **2020**, *20* (12), 8661-8667.
11. Li, X.; Yu, J.; Jaroniec, M.; Chen, X., Cocatalysts for Selective Photoreduction of CO₂ Into Solar Fuels. *Chem. Rev.* **2019**, *119* (6), 3962-4179.
12. Chen, X.; Li, N.; Kong, Z.; Ong, W. J.; Zhao, X., Photocatalytic Fixation of Nitrogen to Ammonia: State-of-the-art Advancements and Future Prospects. *Mater. Horiz.* **2018**, *5* (1), 9-27.
13. Yu, Y.; Dong, X. a.; Chen, P.; Geng, Q.; Wang, H.; Li, J.; Zhou, Y.; Dong, F., Synergistic Effect of Cu Single Atoms and Au–Cu Alloy Nanoparticles on TiO₂ for Efficient CO₂ Photoreduction. *ACS Nano* **2021**, *15* (9), 14453-14464.
14. Li, H.; Zhang, L.; Cao, Y., Synthesis of Palladium-Modified MnS Photocatalysts with Enhanced Photocatalytic Activity in the Photoreduction of CO₂ to CH₄. *Appl. Surf. Sci.* **2021**, *541*, 148519.

15. Ham, S.; Choi, D.; Jang, D.-J., Photodeposition of Gold Nanoparticles on ZnS Nanobelts for Enhanced Dye Decomposition. *Mater. Res. Bull.* **2019**, *116*, 32-39.
16. Kaushik, R.; Singh, P. K.; Halder, A., Modulation Strategies in Titania Photocatalyst for Energy Recovery and Environmental Remediation. *Catal. Today.* **2021**.
17. Kosco, J.; Moruzzi, F.; Willner, B.; McCulloch, I., Photocatalysts Based on Organic Semiconductors with Tunable Energy Levels for Solar Fuel Applications. *Adv. Energy Mater.* **2020**, *10* (39), 2001935.
18. Sun, R.; Zhang, Z.; Li, Z.; Jing, L., Review on Photogenerated Hole Modulation Strategies in Photoelectrocatalysis for Solar Fuel Production. *ChemCatChem* **2019**, *11* (24), 5875-5884.
19. Kush, P.; Deka, S., Multifunctional Copper-Based Quaternary Chalcogenide Semiconductors Toward State-of-the-Art Energy Applications. *ChemNanoMat* **2019**, *5* (4), 373-402.
20. Kumaravel, V.; Mathew, S.; Bartlett, J.; Pillai, S. C., Photocatalytic Hydrogen Production Using Metal Doped TiO₂: A Review Of Recent Advances. *Appl. Catal. B.* **2019**, *244*, 1021-1064.
21. Zhang, Q.; Zhang, Y.; Xiao, K.; Meng, Z.; Tong, W.; Huang, H.; An, Q., Plasmonic Gold Particle Generation in Layer-by-Layer 2D Titania Films as an Effective Immobilization Strategy of Composite Photocatalysts for Hydrogen Generation. *Chem. Eng. J.* **2019**, *358*, 389-397.
22. Zhao, M.; Xu, H.; Ouyang, S.; Tong, H.; Chen, H.; Li, Y.; Song, L.; Ye, J., Fabricating a Au@TiO₂ Plasmonic System To Elucidate Alkali-Induced Enhancement of Photocatalytic H₂ Evolution: Surface Potential Shift or Methanol Oxidation Acceleration? *ACS Catal.* **2018**, *8* (5), 4266-4277.
23. He, Q.; Sun, H.; Shang, Y.; Tang, Y.; She, P.; Zeng, S.; Xu, K.; Lu, G.; Liang, S.; Yin, S.; Liu, Z., Au@TiO₂ Yolk-shell Nanostructures for Enhanced Performance in both Photoelectric and Photocatalytic Solar Conversion. *Appl. Surf. Sci.* **2018**, *441*, 458-465.
24. Gao, W.; Zhang, X.; Su, X.; Wang, F.; Liu, Z.; Liu, B.; Zhan, J.; Liu, H.; Sang, Y., Construction of Bimetallic Pd-Ag Enhanced AgBr/TiO₂ Hierarchical Nanostructured Photocatalytic Hybrid Capillary Tubes and Devices for Continuous Photocatalytic Degradation of VOCs. *Chem. Eng. J.* **2018**, *346*, 77-84.
25. Tian, H.; Zhang, X. L.; Scott, J.; Ng, C.; Amal, R., TiO₂-Supported Copper Nanoparticles Prepared via Ion Exchange for Photocatalytic Hydrogen Production. *J. Mater. Chem. A* **2014**, *2* (18), 6432-6438.
26. Singh, J.; Sahu, K.; Pandey, A.; Kumar, M.; Ghosh, T.; Satpati, B.; Som, T.; Varma, S.; Avasthi, D. K.; Mohapatra, S., Atom Beam Sputtered Ag-TiO₂ Plasmonic Nanocomposite Thin Films for Photocatalytic Applications. *Appl. Surf. Sci.* **2017**, *411*, 347-354.
27. Singh, J.; Sahu, K.; Choudhary, S.; Bisht, A.; Mohapatra, S., Thermal Annealing Induced Cave in and Formation of Nanoscale Pits in Ag-TiO₂ Plasmonic Nanocomposite Thin Film. *Ceram. Int.* **2020**, *46* (3), 3275-3281.
28. Bai, Q.; Shupyk, I.; Vauriot, L.; Majimel, J.; Labrugere, C.; Delville, M.-H.; Delville, J.-P., Design of Metal@Titanium Oxide Nano-heterodimers by Laser-Driven Photodeposition: Growth Mechanism and Modeling. *ACS Nano* **2021**, *15* (2), 2947-2961.
29. Veziroglu, S.; Obermann, A.-L.; Ullrich, M.; Hussain, M.; Kamp, M.; Kienle, L.; Leißner, T.; Rubahn, H.-G.; Polonskyi, O.; Strunskus, T.; Fiutowski, J.; Es-Souni, M.; Adam, J.; Faupel, F.; Aktas, O. C.,

Photodeposition of Au Nanoclusters for Enhanced Photocatalytic Dye Degradation over TiO₂ Thin Film. *ACS Appl. Mater. Interfaces* **2020**, *12* (13), 14983-14992.

30. Bao, N.; Miao, X.; Hu, X.; Zhang, Q.; Jie, X.; Zheng, X., Novel Synthesis of Plasmonic Ag/AgCl@TiO₂ Continuous Fibers with Enhanced Broadband Photocatalytic Performance. *Catalysts* **2017**, *7* (4), 117.

31. Dilsaver, P. S.; Reichert, M. D.; Hallmark, B. L.; Thompson, M. J.; Vela, J., Cu₂ZnSnS₄-Au Heterostructures: Toward Greener Chalcogenide-Based Photocatalysts. *J. Phys. Chem. C* **2014**, *118* (36), 21226-21234.

32. Liu, C.; Yang, D.; Jiao, Y.; Tian, Y.; Wang, Y.; Jiang, Z., Biomimetic Synthesis of TiO₂-SiO₂-Ag Nanocomposites with Enhanced Visible-Light Photocatalytic Activity. *ACS Appl. Mater. Interfaces* **2013**, *5* (9), 3824-3832.

33. Yang, D.; Sun, Y.; Tong, Z.; Tian, Y.; Li, Y.; Jiang, Z., Synthesis of Ag/TiO₂ Nanotube Heterojunction with Improved Visible-Light Photocatalytic Performance Inspired by Bioadhesion. *J. Phys. Chem. C* **2015**, *119* (11), 5827-5835.

34. Wenderich, K.; Mul, G., Methods, Mechanism, and Applications of Photodeposition in Photocatalysis: A Review. *Chem. Rev.* **2016**, *116* (23), 14587-14619.

35. Tammann, G., Über die Lichtwirkung auf schwer lösliche Oxyde im den Lösungen von Silbersalzen. *Z. Anorg. Allg. Chem.* **1920**, *114* (1), 151-152.

36. Kohlschütter, V.; d'Almendra, A., Über topochemische Reaktionsbeeinflussung und Formentwicklung. *Ber. Dtsch. Chem. Ges.* **1921**, *54* (8), 1961-1974.

37. Goetz, A.; Inn, E. C. Y., Reversible Photolysis of Ag Sorbed on Colloidal Metal Oxides. *Rev. Mod. Phys.* **1948**, *20* (1), 131-142.

38. Kraeutler, B.; Bard, A. J., Heterogeneous Photocatalytic Preparation of Supported Catalysts. Photodeposition of Platinum on Titanium Dioxide Powder and Other Substrates. *Journal of the American Chemical Society* **1978**, *100* (13), 4317-4318.

39. Grätzel, M., Photoelectrochemical Cells. *Nature* **2001**, *414* (6861), 338-344.

40. Zhu, D.; Ye, H.; Liu, Z.; Liu, J.; Fu, H.; Huang, Y.; Teng, F.; Wang, Z.; Tang, A., Seed-Mediated Growth of Heterostructured Cu_{1.94}S-MS (M = Zn, Cd, Mn) and Alloyed CuNS₂ (N = In, Ga) Nanocrystals for Use in Structure- and Composition-Dependent Photocatalytic Hydrogen Evolution. *Nanoscale* **2020**, *12* (10), 6111-6120.

41. Huang, J.; Guo, W.; Hu, Y.; Wei, W. D., Plasmonic Metal-Semiconductor Heterostructures for Hot-Electron-Driven Photochemistry. *MRS Bull.* **2020**, *45* (1), 37-42.

42. Kelly, K. L.; Coronado, E.; Zhao, L. L.; Schatz, G. C., The Optical Properties of Metal Nanoparticles: The Influence of Size, Shape, and Dielectric Environment. *The Journal of Physical Chemistry B* **2003**, *107* (3), 668-677.

43. Ji, X.; Song, X.; Li, J.; Bai, Y.; Yang, W.; Peng, X., Size Control of Gold Nanocrystals in Citrate Reduction: The Third Role of Citrate. *Journal of the American Chemical Society* **2007**, *129* (45), 13939-13948.

44. An, L.; Wang, Y.; Tian, Q.; Yang, S., Small Gold Nanorods: Recent Advances in Synthesis, Biological Imaging, and Cancer Therapy. *Materials* **2017**, *10* (12), 1372.
45. Gärtner, F.; Losse, S.; Boddien, A.; Pohl, M.-M.; Denurra, S.; Junge, H.; Beller, M., Hydrogen Evolution from Water/Alcohol Mixtures: Effective In Situ Generation of an Active Au/TiO₂ Catalyst. *ChemSusChem* **2012**, *5* (3), 530-533.
46. Murdoch, M.; Waterhouse, G. I. N.; Nadeem, M. A.; Metson, J. B.; Keane, M. A.; Howe, R. F.; Llorca, J.; Idriss, H., The Effect of Gold Loading and Particle Size on Photocatalytic Hydrogen Production from Ethanol Over Au/TiO₂ Nanoparticles. *Nat. Chem.* **2011**, *3* (6), 489-492.
47. Cárdenas-Lizana, F.; Gómez-Quero, S.; Idriss, H.; Keane, M. A., Gold Particle Size Effects in the Gas-Phase Hydrogenation of m-dinitrobenzene over Au/TiO₂. *J. Catal.* **2009**, *268* (2), 223-234.
48. Katoh, R.; Murai, M.; Furube, A., Electron–Hole Recombination in the Bulk of a Rutile TiO₂ Single Crystal Studied by Sub-Nanosecond Transient Absorption Spectroscopy. *Chem. Phys. Lett.* **2008**, *461* (4), 238-241.
49. Yamakata, A.; Ishibashi, T.-a.; Onishi, H., Time-Resolved Infrared Absorption Study of Nine TiO₂ Photocatalysts. *Chem. Phys.* **2007**, *339* (1), 133-137.
50. Priebe, J. B.; Radnik, J.; Lennox, A. J. J.; Pohl, M.-M.; Karnahl, M.; Hollmann, D.; Grabow, K.; Bentrup, U.; Junge, H.; Beller, M.; Brückner, A., Solar Hydrogen Production by Plasmonic Au–TiO₂ Catalysts: Impact of Synthesis Protocol and TiO₂ Phase on Charge Transfer Efficiency and H₂ Evolution Rates. *ACS Catal.* **2015**, *5* (4), 2137-2148.
51. Wang, D.; Bi, Q.; Yin, G.; Wang, P.; Huang, F.; Xie, X.; Jiang, M., Photochemical Preparation of Anatase Titania Supported Gold Catalyst for Ethanol Synthesis from CO₂ Hydrogenation. *Catal. Lett.* **2018**, *148* (1), 11-22.
52. Deepagan, V. G.; You, D. G.; Um, W.; Ko, H.; Kwon, S.; Choi, K. Y.; Yi, G.-R.; Lee, J. Y.; Lee, D. S.; Kim, K.; Kwon, I. C.; Park, J. H., Long-Circulating Au-TiO₂ Nanocomposite as a Sonosensitizer for ROS-Mediated Eradication of Cancer. *Nano Lett.* **2016**, *16* (10), 6257-6264.
53. Shahini, P.; Ashkarran, A. A., Immobilization of Plasmonic Ag-Au NPs on the TiO₂ Nanofibers as an Efficient Visible-light Photocatalyst. *Colloids Surf. A Physicochem. Eng. Asp.* **2018**, *537*, 155-162.
54. Shoueir, K.; Kandil, S.; El-hosainy, H.; El-Kemary, M., Tailoring The Surface Reactivity of Plasmonic Au@TiO₂ Photocatalyst Bio-Based Chitosan Fiber Towards Cleaner of Harmful Water Pollutants Under Visible-Light Irradiation. *J. Clean. Prod.* **2019**, *230*, 383-393.
55. Fudo, E.; Tanaka, A.; Iguchi, S.; Kominami, H., Modification of Gold Nanoparticles with a Hole-transferring Cocatalyst: a New Strategy for Plasmonic Water Splitting under Irradiation of Visible Light. *Sustain. Energy Fuels.* **2021**, *5* (13), 3303-3311.
56. Lee, Y.; Kim, E.; Park, Y.; Kim, J.; Ryu, W.; Rho, J.; Kim, K., Photodeposited Metal-Semiconductor Nanocomposites and Their Applications. *Journal of Materiomics* **2018**, *4* (2), 83-94.
57. Kavitha, R.; Kumar, S. G., A Review on Plasmonic Au-ZnO Heterojunction Photocatalysts: Preparation, Modifications and Related Charge Carrier Dynamics. *Mater. Sci. Semicond. Process.* **2019**, *93*, 59-91.

58. Coughlan, C.; Ibáñez, M.; Dobrozhan, O.; Singh, A.; Cabot, A.; Ryan, K. M., Compound Copper Chalcogenide Nanocrystals. *Chem. Rev.* **2017**, *117* (9), 5865–6109.
59. Yuan, Y.-J.; Chen, D.; Yu, Z.-T.; Zou, Z.-G., Cadmium Sulfide-Based Nanomaterials for Photocatalytic Hydrogen Production. *J. Mater. Chem. A* **2018**, *6* (25), 11606-11630.
60. Lee, S. L.; Chang, C.-J., Recent Progress on Metal Sulfide Composite Nanomaterials for Photocatalytic Hydrogen Production. *Catalysts* **2019**, *9* (5), 457.
61. Yang, K.; Yang, Z.; Zhang, C.; Gu, Y.; Wei, J.; Li, Z.; Ma, C.; Yang, X.; Song, K.; Li, Y.; Fang, Q.; Zhou, J., Recent Advances in CdS-based Photocatalysts for CO₂ Photocatalytic Conversion. *Chem. Eng. J.* **2021**, *418*, 129344.
62. Wilker, M. B.; Schnitzenbaumer, K. J.; Dukovic, G., Recent Progress in Photocatalysis Mediated by Colloidal II-VI Nanocrystals. *Isr. J. Chem.* **2012**, *52* (11-12), 1002-1015.
63. Dukovic, G.; Merkle, M. G.; Nelson, J. H.; Hughes, S. M.; Alivisatos, A. P., Photodeposition of Pt on Colloidal CdS and CdSe/CdS Semiconductor Nanostructures. *Adv. Mater.* **2008**, *20* (22), 4306-4311.
64. Habas, S. E.; Yang, P.; Mokari, T., Selective Growth of Metal and Binary Metal Tips on CdS Nanorods. *J. Am. Chem. Soc.* **2008**, *130* (11), 3294-3295.
65. Menagen, G.; Macdonald, J. E.; Shemesh, Y.; Popov, I.; Banin, U., Au Growth on Semiconductor Nanorods: Photoinduced versus Thermal Growth Mechanisms. *J. Am. Chem. Soc.* **2009**, *131* (47), 17406-17411.
66. Borgarello, E.; Serpone, N.; Pelizzetti, E.; Barbeni, M., Efficient Photochemical Conversion of Aqueous Sulphides and Sulphites to Hydrogen Using a Rhodium-Loaded Cds Photocatalyst. *J. Photochem.* **1986**, *33* (1), 35-48.
67. Li, C.; Yuan, J.; Han, B.; Jiang, L.; Shangguan, W., TiO₂ Nanotubes Incorporated with CdS for Photocatalytic Hydrogen Production from Splitting Water Under Visible Light Irradiation. *Int. J. Hydrog. Energy.* **2010**, *35* (13), 7073-7079.
68. Yao, W.; Song, X.; Huang, C.; Xu, Q.; Wu, Q., Enhancing Solar Hydrogen Production Via Modified Photochemical Treatment of Pt/CdS Photocatalyst. *Catal. Today.* **2013**, *199*, 42-47.
69. Muruganandham, M.; Kusumoto, Y.; Okamoto, C.; Muruganandham, A.; Abdulla-Al-Mamun, M.; Ahmmad, B., Mineralizer-Assisted Shape-Controlled Synthesis, Characterization, and Photocatalytic Evaluation of CdS Microcrystals. *J. Phys. Chem. C* **2009**, *113* (45), 19506-19517.
70. Wang, Y.; Wang, Y.; Xu, R., Photochemical Deposition of Pt on CdS for H₂ Evolution from Water: Markedly Enhanced Activity by Controlling Pt Reduction Environment. *J. Phys. Chem. C* **2013**, *117* (2), 783-790.
71. Buehler, N.; Meier, K.; Reber, J. F., Photochemical Hydrogen Production with Cadmium Sulfide Suspensions. *J. Phys. Chem.* **1984**, *88* (15), 3261-3268.
72. Reber, J. F.; Rusek, M., Photochemical Hydrogen Production with Platinized Suspensions of Cadmium Sulfide and Cadmium Zinc Sulfide Modified by Silver Sulfide. *J. Phys. Chem.* **1986**, *90* (5), 824-834.
73. Dung, D.; Ramsden, J.; Graetzel, M., Dynamics of Interfacial Electron-Transfer Processes in

Colloidal Semiconductor Systems. *J. Am. Chem. Soc.* **1982**, *104* (11), 2977-2985.

74. He, K.; Wang, M.; Guo, L., Novel-CdS-Nanorod with Stacking Fault Structures: Preparation and Properties of Visible-Light-Driven Photocatalytic Hydrogen Production From Water. *Chem. Eng. J.* **2015**, *279*, 747-756.
75. Xin, G.; Yu, B.; Xia, Y.; Hu, T.; Liu, L.; Li, C., Highly Efficient Deposition Method of Platinum over CdS for H₂ Evolution under Visible Light. *J. Phys. Chem. C* **2014**, *118* (38), 21928-21934.
76. Owen, J.; Brus, L., Chemical Synthesis and Luminescence Applications of Colloidal Semiconductor Quantum Dots. *J. Am. Chem. Soc.* **2017**.
77. van Embden, J.; Chesman, A. S. R.; Jasieniak, J. J., The Heat-Up Synthesis of Colloidal Nanocrystals. *Chem. Mater.* **2015**, *27* (7), 2246-2285.
78. Hühn, J.; Carrillo-Carrion, C.; Soliman, M. G.; Pfeiffer, C.; Valdeperez, D.; Masood, A.; Chakraborty, I.; Zhu, L.; Gallego, M.; Yue, Z.; Carril, M.; Feliu, N.; Escudero, A.; Alkilany, A. M.; Pelaz, B.; del Pino, P.; Parak, W. J., Selected Standard Protocols for the Synthesis, Phase Transfer, and Characterization of Inorganic Colloidal Nanoparticles. *Chem. Mater.* **2017**, *29* (1), 399-461.
79. Berr, M.; Vaneski, A.; Susha, A. S.; Rodríguez-Fernández, J.; Döblinger, M.; Jäckel, F.; Rogach, A. L.; Feldmann, J., Colloidal CdS Nanorods Decorated with Subnanometer Sized Pt Clusters for Photocatalytic Hydrogen Generation. *Appl. Phys. Lett.* **2010**, *97* (9), 093108.
80. Aronovitch, E.; Houben, L.; Bar-Sadan, M., Seeded Rods with Ag and Pd Bimetallic Tips—Spontaneous Rearrangements of the Nanoalloys on the Atomic Scale. *Chem. Mater.* **2019**, *31* (18), 7231-7237.
81. Gupta, S. S.; van Huis, M. A., Intermetallic Differences at CdS–Metal (Ni, Pd, Pt, and Au) Interfaces: From Single-Atom to Subnanometer Metal Clusters. *J. Phys. Chem. C* **2019**, *123* (14), 9298-9310.
82. Ha, M.; Kim, J.-H.; You, M.; Li, Q.; Fan, C.; Nam, J.-M., Multicomponent Plasmonic Nanoparticles: From Heterostructured Nanoparticles to Colloidal Composite Nanostructures. *Chem. Rev.* **2019**, *119* (24), 12208-12278.
83. Akyüz, D.; Rıza Özkaya, A.; Koca, A., Photocatalytic and Photoelectrochemical Performances of Mo, Ni and Cu Decorated Metal Chalcogenides. *Mater. Sci. Semicond. Process.* **2020**, *116*, 105127.
84. Shen, R.; Ren, D.; Ding, Y.; Guan, Y.; Ng, Y. H.; Zhang, P.; Li, X., Nanostructured CdS for Efficient Photocatalytic H₂ Evolution: A Review. *Sci. China Mater.* **2020**, *63* (11), 2153-2188.
85. Dong, K.; Chen, Q.-C.; Xing, Z.; Chen, Y.; Qi, Y.; Pavlopoulos, N. G.; Amirav, L., Silver Tipping of CdSe@CdS Nanorods: How To Avoid Cation Exchange. *Chem. Mater.* **2021**, *33* (16), 6394-6402.
86. Li, H.; Sun, T.; Zhang, L.; Cao, Y., Matching and Adjusting Energy Band Structures of Pd-modified Sulphides (ZnS, In₂S₃ and CuS) and Improving the Photocatalytic Activity of CO₂ Photoreduction. *Nanoscale* **2020**, *12* (35), 18180-18192.
87. Sacco, O.; Vaiano, V.; Sannino, D.; Picca, R. A.; Cioffi, N., Ag Modified ZnS for Photocatalytic Water Pollutants Degradation: Influence of Metal Loading and Preparation Method. *J. Colloid Interface Sci.* **2019**, *537*, 671-681.
88. Choi, Y. I.; Lee, S.; Kim, S. K.; Kim, Y.-I.; Cho, D. W.; Khan, M. M.; Sohn, Y., Fabrication of ZnO,

ZnS, Ag-ZnS, and Au-ZnS Microspheres for Photocatalytic Activities, CO Oxidation and 2-Hydroxyterephthalic Acid Synthesis. *J. Alloys Compd.* **2016**, 675, 46-56.

89. Zhang, J.; Wang, Y.; Zhang, J.; Lin, Z.; Huang, F.; Yu, J., Enhanced Photocatalytic Hydrogen Production Activities of Au-Loaded ZnS Flowers. *ACS Appl. Mater. Interfaces* **2013**, 5 (3), 1031-1037.

90. Zhu, S.; Qian, X.; Lan, D.; Yu, Z.; Wang, X.; Su, W., Accelerating Charge Transfer for Highly Efficient Visible-Light-Driven Photocatalytic H₂ Production: In-situ Constructing Schottky Junction via Anchoring Ni-P Alloy Onto Defect-Rich ZnS. *Appl. Catal. B.* **2020**, 269, 118806.

91. Kim, Y.; Giribabu, K.; Kim, J. G.; Lee, J. B.; Hong, W. G.; Huh, Y. S.; Kim, H. J., Electrochemical Sensors Based on Au-ZnS Hybrid Nanorods with Au-Mediated Efficient Electron Relay. *ACS Sustain. Chem. Eng.* **2019**, 7 (4), 4094-4102.

92. Chen, D.; Wang, A.; Buntine, M. A.; Jia, G., Recent Advances in Zinc-Containing Colloidal Semiconductor Nanocrystals for Optoelectronic and Energy Conversion Applications. *ChemElectroChem* **2019**, 6 (18), 4709-4724.

93. Sun, C.; Liu, M.; Zou, Y.; Wei, J.; Jiang, J., Synthesis of Plasmonic Au-CuS Hybrid Nanocrystals for Photothermal Transduction and Chemical Transformations. *RSC Adv.* **2016**, 6 (31), 26374-26379.

94. Zhang, G.; Wu, H.; Chen, D.; Li, N.; Xu, Q.; Li, H.; He, J.; Lu, J., A Mini-Review on ZnIn₂S₄-Based Photocatalysts for Energy and Environmental Application. *Green Energy Environ.* **2020**.

95. Regulacio, M. D.; Han, M.-Y., Multinary I-III-VI₂ and I₂-II-IV-VI₄ Semiconductor Nanostructures for Photocatalytic Applications. *Acc. Chem. Res.* **2016**, 49 (3), 511-519.

96. Ganai, A.; Maiti, P. S.; Houben, L.; Bar-Ziv, R.; Bar Sadan, M., Inside-Out: The Role of Buried Interfaces in Hybrid Cu₂ZnSnS₄-Noble Metal Photocatalysts. *J. Phys. Chem. C* **2017**, 121 (12), 7062-7068.

97. Yu, X.; Du, R.; Li, B.; Liu, L.; Zhang, Y., Cu₂ZnSnS₄-AuAg Heterodimers and Their Enhanced Catalysis for Oxygen Reduction Reaction. *J. Phys. Chem. C* **2017**, 121 (12), 6712-6720.

98. Cheng, X.; Liu, J.; Feng, J.; Zhang, E.; Wang, H.; Liu, X.; Liu, J.; Rong, H.; Xu, M.; Zhang, J., Metal@I₂-II-IV-VI₄ Core-shell Nanocrystals: Controlled Synthesis by Aqueous Cation Exchange for Efficient Photoelectrochemical Hydrogen Generation. *J. Mater. Chem. A* **2018**, 6 (25), 11898-11908.

99. Zhang, F.; Shen, L.; Li, J.; Zhang, Y.; Wang, G.; Zhu, A., Room Temperature Photocatalytic Deposition of Au Nanoparticles on SnS₂ Nanoplates for Enhanced Photocatalysis. *Powder Technol.* **2021**, 383, 371-380.

100. Patra, B. K.; Khilari, S.; Pradhan, D.; Pradhan, N., Hybrid Dot-Disk Au-CuInS₂ Nanostructures as Active Photocathode for Efficient Evolution of Hydrogen from Water. *Chem. Mater.* **2016**, 28 (12), 4358-4366.

101. Lange, T.; Reichenberger, S.; Rohe, M.; Bartsch, M.; Kampermann, L.; Klein, J.; Strunk, J.; Bacher, G.; Schlögl, R.; Barcikowski, S., Alumina-Protected, Durable and Photostable Zinc Sulfide Particles from Scalable Atomic Layer Deposition. *Adv. Funct. Mater.* **2021**, 31 (14), 2009323.

102. Volokh, M.; Mokari, T., Metal/Semiconductor Interfaces in Nanoscale Objects: Synthesis, Emerging Properties and Applications of Hybrid Nanostructures. *Nanoscale Adv.* **2020**, 2 (3), 930-961.

103. Zhang, R.; Wang, H.; Li, Y.; Wang, D.; Lin, Y.; Li, Z.; Xie, T., Investigation on the Photocatalytic Hydrogen Evolution Properties of Z-Scheme Au NPs/CuInS₂/NCN-CN_x Composite Photocatalysts. *ACS Sustain. Chem. Eng.* **2021**, *9* (21), 7286-7297.

Chapter 2

Setup Configuration and Laser Control

Table of contents

Chapter 2.....	49
Setup Configuration and Laser Control	49
Abstract.....	53
2.1 Choice of light sources	53
2.1.1 Types of light sources.....	53
2.1.2 Impact of photon flux on the photodeposition reaction	54
2.2 Cuvette setup using UV laser illumination	56
2.2.1 Schematic picture of the cuvette setup using UV laser.....	56
2.2.2 Excitation power in the cuvette.....	57
2.3 Cuvette setup using blue laser illumination.....	59
2.3.1 Schematic picture of the cuvette setup using blue laser.....	59
2.3.2 Excitation power in the cuvette.....	60
2.4 Conclusion.....	62
2.5 References	64

Abstract

In this chapter, we will introduce two setups used to perform photochemical deposition of metals on semiconductor nanocrystals. The first setup uses a linearly polarized continuous UV laser (364 nm) with a controlled beam size (~1 cm) as a light source passing through a 1 cm path length polymethyl methacrylate (PMMA) cuvette. This wavelength is specifically designed for the photodeposition of metals on TiO₂ nanocrystals. The other setup has a similar configuration but with a sample loaded in a sealed quartz cuvette under excitation of a continuous blue laser (473 nm) as a light source and it is typically used for photodeposition experiments on Cu_{2-x}S/CuInS₂ heteronanocrystals. The detailed configuration and excitation power control of these two setups are presented and discussed below. Quartz cells were used because PMMA is toluene sensitive.

2.1 Choice of light sources

The right choice of light sources is essential to control the photodeposition process since it directly affects the generation of charge carriers. Though previous reports described the detailed irradiative parameters, the photon flux shed on the reaction solution is generally ignored. This implicit factor may alter the nucleation and growth of metallic nanodots, thus leading to poor reproducibility in controlling the formation of metals on semiconductor surfaces as well as their photocatalytic activities.

2.1.1 Types of light sources

With the advanced development of science and technology, various commercial light sources have been developed to meet the demands of daily life, industry, and scientific research. **Figure 2.1a** shows an overlay plot of the spectral distribution curves of the most commonly used visible lights.¹ The energy of tungsten light increases as wavelength increases while that of mercury vapor lamp shows distinct

sharp lines at short wavelengths (< 600 nm). In contrast, white LED exhibits a broad spectral distribution highly similar to sunlight at noon. Lasers are another important source of visible light, which have been used in applications ranging from compact disk readers to sculpture, medical devices, and so forth. Lasers are unique since they emit a continuous beam of light made up of a single wavelength that exits in a single-phase or so-called coherent light. The wavelength of the light emitted by a laser depends on the material from which the laser crystal or gas is composed. The light produced in the gaseous mixture is bounced back and forth between the two mirrored surfaces at the ends of the laser tube, steadily increasing in energy. When a critical threshold is reached, light pierces the slightly transparent mirror on one end of the laser tube, as depicted in **Figure 2.1b**.¹ As different light sources show different characteristics, the decision of which type of lighting should be applied for photodeposition depends on the practical applications.

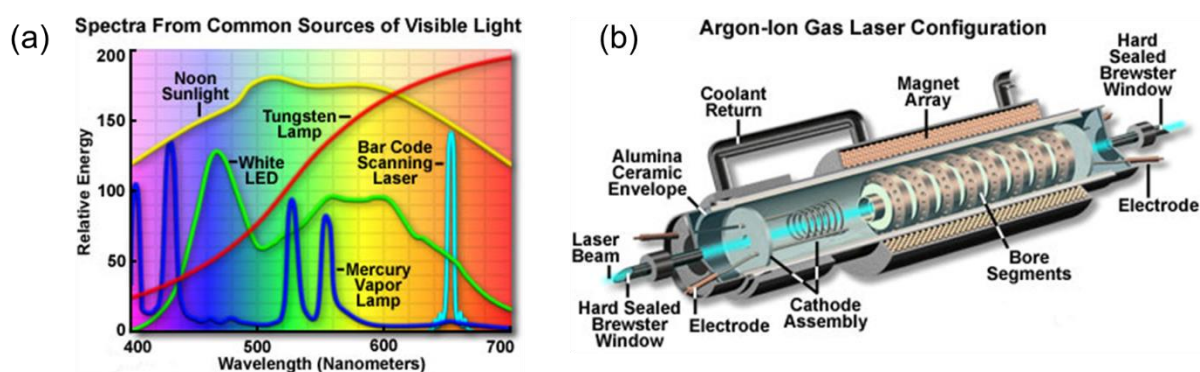


Figure 2.1 (a) Spectral distribution curves demonstrating the relative energy variation with the wavelength in nanometer for different light sources. Adapted from ref.¹ (b) Scheme of argon-ion gas laser configuration. Adapted from ref.¹

2.1.2 Impact of photon flux on the photodeposition reaction

The selection of light sources is of great importance in the photodeposition of metals on semiconductor surfaces. To date, most reported protocols use UV or visible lamps with an excitation power intensity typically less than 5 mW/cm^2 for the experiments.²⁻⁶ Due to their low power intensity, the photodeposition process usually

needs to run for several hours to ensure homogeneous deposition of metallic dots. Moreover, the deposited metal NDs are generally small (< 3 nm) and show low photocatalytic activity.^{4, 7} To increase their sizes, the illumination duration has to be extensively prolonged, which is time-consuming.^{3, 8} The use of lasers can solve these issues since they can generate photon flux intensities orders of magnitude significantly higher than conventional lamps.⁹⁻¹¹ Therefore, a tremendous rate of photogenerated charge carriers can be produced so that the numerous electrons dramatically accelerate the reduction rate of metallic ions in the solution. This leads to two consequences. First, the electron availability for the metal deposition is not any more sensitive to the trapping by the bulk or the surface defects of the semiconductors.¹⁰⁻¹² In this case, tiny dots will not necessarily grow on the defect sites on the semiconductor surfaces and the configuration of deposited metal nanodots can be controlled. For instance, Hao *et al.*¹⁰ very recently reported that tuning the photon flux could effectively control the configuration of Au NDs on CdSe/CdS nanorods. They could obtain selectively on-demand multiple sites, or double-tips or single-tip deposition. Second, the enhanced photoreduction rate of metallic ions is beneficial to the nucleation and growth of metal NDs, thus leading to the formation of bigger metal dots in a much shorter illumination time.¹² For example, Bai *et al.*,¹¹ reported the synthesis of metal (Ag and Au)-TiO₂ nanoheterodimers by laser-driven photodeposition in a continuous microfluidic reactor. The use of a focused laser beam with an intensity as high as 430 W/cm² gave rise to the formation of metals with a size as large as 14 nm in a few seconds. In order to monitor efficiently the nucleation and growth of the metal nanodots on semiconductors, we, therefore, selected focused laser beams, instead of UV lamps, to perform the photodeposition reaction. Moreover, we intend to use conventional cuvettes as reaction cells since this provides a steady reaction system that is convenient for sampling in time.

2.2 Cuvette setup using UV laser illumination

The setup uses a UV laser with a continuous wavelength of 364 nm as excitation source. The beam waist is adjusted to be ~ 1 cm in diameter at the sample to realize a complete illumination of 1 cm path length PMMA cuvette. A stirring bar can be loaded into a cuvette to ensure a homogeneous reaction.

2.2.1 Schematic picture of the cuvette setup using UV laser

The schematic diagram of the cuvette setup using UV laser is displayed in **Figure 2.2**. The laser beam is reflected by one mirror (m1) and then elevated by two other mirrors (m2 and m3) to reach the same height as the reaction cell. The laser beam is then enlarged by passing through an objective (Newport U-13x) and a lens with a focal length of 75 mm. With these settings, the beam size exposed on the reaction cuvette is approximately 1 cm in diameter, thus ensuring a complete illumination of the reaction solution in a 1 cm length quart cuvette with a volume of 1 mL. The cuvette is placed on a magnetic stirring plate and the solution is stirred at 300 rpm to homogenize the reaction solution and prevent sedimentation. All experiments were conducted at room temperature unless otherwise noted.

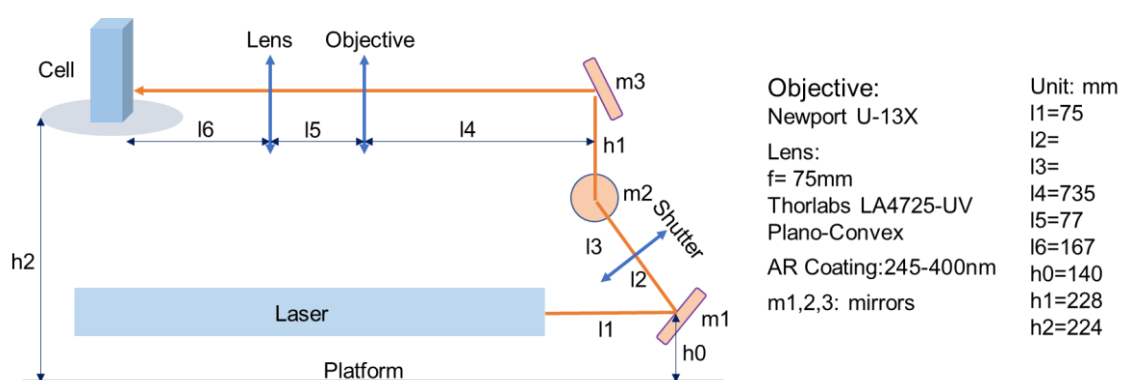


Figure 2.2 Schematic diagram of the cuvette setup using UV laser illumination.

2.2.2 Excitation power in the cuvette

Polymer cuvettes are attractive because of their low cost and the fact that they can be discarded after use, while quartz cuvettes usually have better resistance to organic solvents and higher transmission at short wavelengths, but are much more expensive. As the photodeposition reactions on TiO₂ nanocrystals take place in a mixture of water and alcohol, PMMA cuvette is suggested to be used for their low cost. The transmission quality of the PMMA of dimensions (1×1×4 cm³) was carefully examined.

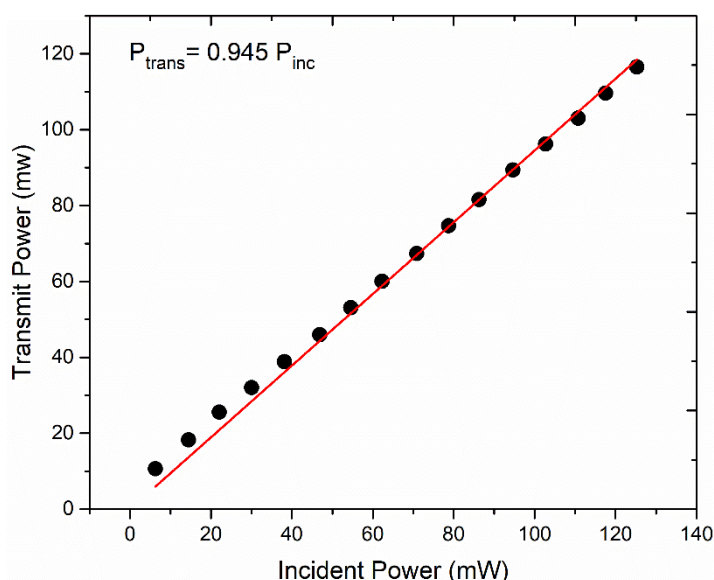


Figure 2.3 Transmission measurements of PMMA containing pure water as a medium at an excitation wavelength of 364 nm.

As shown in **Figure 2.3**, the PMMA cuvette exhibited a good transmission quality above 94%. The power in the middle of a cuvette $P_{1/2}$ can be estimated by,

$$P_{1/2} = P_{inc} \sqrt{\frac{P_{trans}}{P_{inc}}} = \sqrt{0.945} P_{inc} = 0.972 P_{inc} \quad \text{eq 2.1}$$

where the P_{inc} and the P_{trans} are the incident powers before arriving at and after passing through the UV cuvette, respectively.

As the laser beam is reflected by mirrors, lens, and objectives, inevitable energy losses should occur before it reaches the reaction cuvette. To have better control of

the excitation power at samples, we measured and established the relationship between the power before passing through the cuvette and the power on the laser controller (P_{panel}).

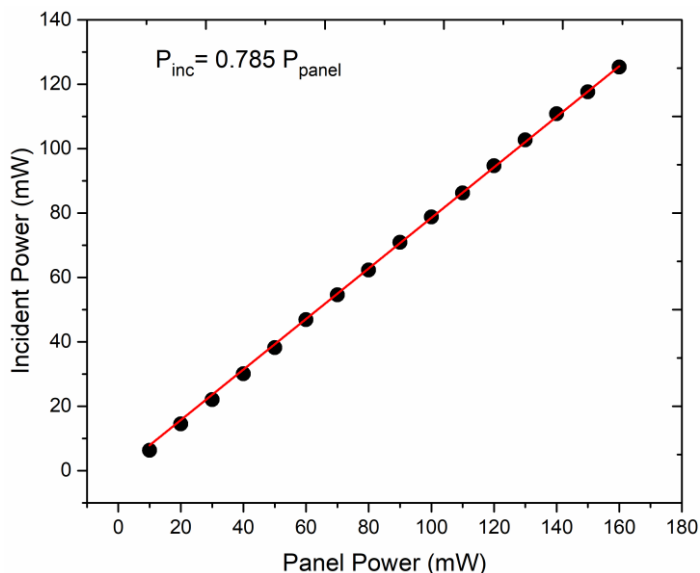


Figure 2.4 Incident power as a function of panel power.

As shown in **Figure 2.4**, the relation is linearly dependent and can be written as,

$$P_{inc} = 0.785P_{panel} \quad \text{eq 2.2}$$

The concentration of TiO_2 is usual 0.44 mg/ml when performing photodeposition. However, with 0.44 mg/mL TiO_2 solution, the transmission of the solution is quite weak due to both absorption and scattering (note that scattering is not a problem because photons are not lost) so it is quite difficult to estimate the power in the middle of the cuvette. Thus, we used the power incident to the solution after crossing one wall (called P_{applied}).

As shown in **Figure 2.3**, the transmission of the PMMA cell containing pure water is 0.945. This transmission equals $\exp(-2x) = 0.945$. Thus, for a single PMMA wall, a transmission is of $\exp(-x) = (0.945)^{1/2} = 0.972$.

Then, the applied power can be deduced and written as,

$$P_{applied} = 0.972P_{inc} = 0.972 \times 0.785P_{panel} = 0.76P_{panel} \quad \text{eq 2.3}$$

Therefore, the estimated power inside the cuvette can be precisely tuned by changing the power on the laser control panel.

2.3 Cuvette setup using blue laser illumination

The cuvette setup using blue laser illumination is designed for the photodeposition of metals on $\text{Cu}_{2-x}\text{S}/\text{CuInS}_2$ heteronanocrystals. Thanks to their broad absorption across a whole visible region, the $\text{Cu}_{2-x}\text{S}/\text{CuInS}_2$ nanocrystals can be efficiently excited using a blue laser and generate charge carriers for the photochemical deposition reaction. Moreover, as the $\text{Cu}_{2-x}\text{S}/\text{CuInS}_2$ nanocrystals are hydrophobic and the photodeposition reactions are performed in toluene, a quartz cuvette should be used.

2.3.1 Schematic picture of the cuvette setup using blue laser

The scheme of the cuvette setup using a blue laser is depicted in **Figure 2.5**. A laser with a continuous wavelength of 473 nm is used as an irradiation source. After coming out from the laser head, the beam is vertically elevated by a mirror (m1) and then reflected to the second mirror (m2). The beam size is amplified to about 1 cm in diameter by passing through a cylindrical lens and another lens with a focal length of 70 mm. The enlarged beam is then reflected to the reaction cell. To ensure all the volume of the reaction solution is fully illuminated, the reaction solution is loaded in a $1 \times 1 \times 4 \text{ cm}^3$ sealed quartz cuvette with a volume of 1 mL.

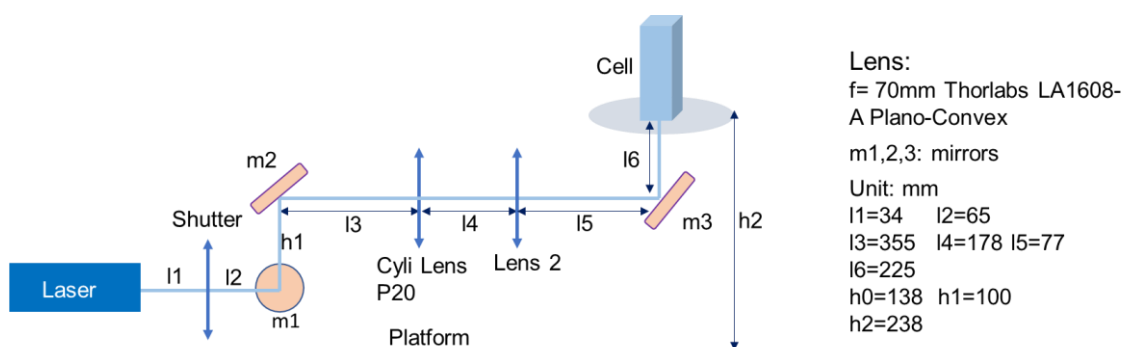


Figure 2.5 Schematic diagram of the cuvette setup using blue laser illumination.

2.3.2 Excitation power in the cuvette

The blue laser excitation power is controlled by the current with a maximum value of 5 Amperes (A). The relationship between exit power P_{Head} and applied current I is shown in **Figure 2.6a**. Clearly, they have a linear dependence and can be described as,

$$P_{Head} = 116.7 \times I - 221.6 \quad \text{eq 2.4}$$

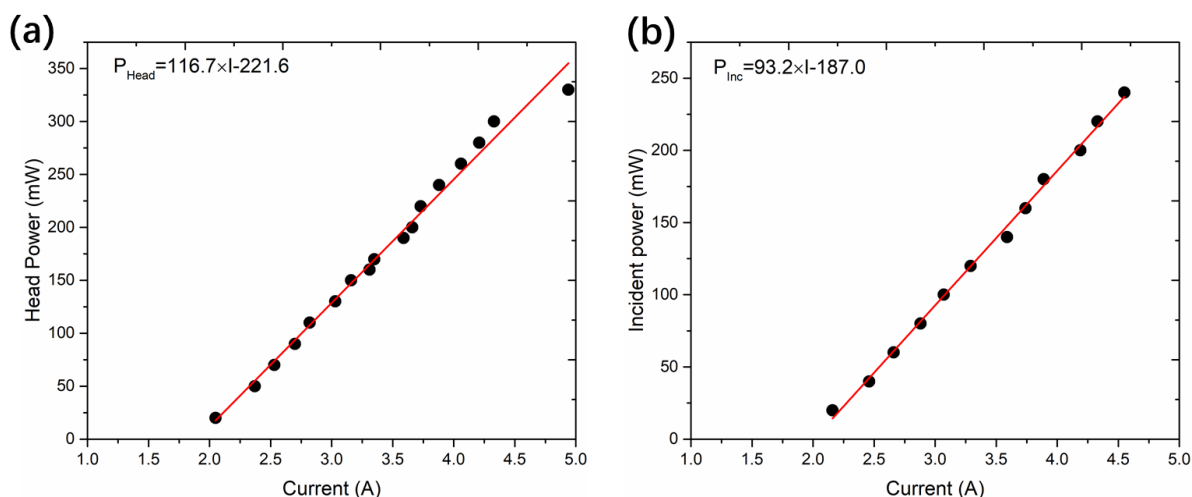


Figure 2.6 (a) The relationship between the power of the laser head and the applied current for the blue laser (MLL-N-473 nm-300 mW-19012905, supplied from CNI Lasers). **(b)** The relationship between the power of laser right before reaction cuvette and applied current for the blue laser.

As the laser beam is reflected by several mirrors and passes through two lenses, an inevitable energy loss should occur before arriving at the reaction cell. The

relationship between excitation power in front of the cuvette and applied current is shown in **Figure 2.6b**. They also have a linear dependence and can be written as,

$$P_{Inc} = 93.2 \times I - 187.0 \quad \text{eq 2.5}$$

Interestingly, when the power of the laser head and incident power right before the cuvette are both 0 mW, the current values are not the same (1.899 A and 2.006 A). To reduce the error, we propose to take the mean value (1.9525 A) as the applied current when the laser power is zero and refit the data as in **Figure 2.7**.

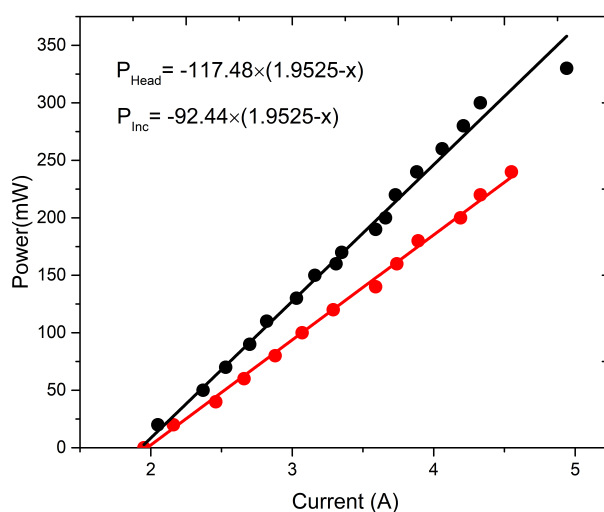


Figure 2.7 Fits of the variations of the power at the laser head (black) and of the incident to the cuvette (red) as a function of the applied current with the same onset of the laser emission.

The two fits can be described as,

$$P_{Head} = -117.48 \times (1.9525 - I) \quad \text{eq 2.6}$$

$$P_{Inc} = -92.44 \times (1.9525 - I) \quad \text{eq 2.7}$$

Combining eq 2.6 and eq 2.7 results in the relationship between P_{Head} and P_{Inc} ,

$$P_{Inc} = 0.7868 P_{Head} \quad \text{eq 2.8}$$

As the photodeposition reaction of $\text{Cu}_{2-x}\text{S}/\text{CuInS}_2$ heteronanocrystals is performed in a mixture of toluene and reaction precursors, the transmission is estimated using the reaction solution in the quartz cuvettes (**Figure 2.8**).

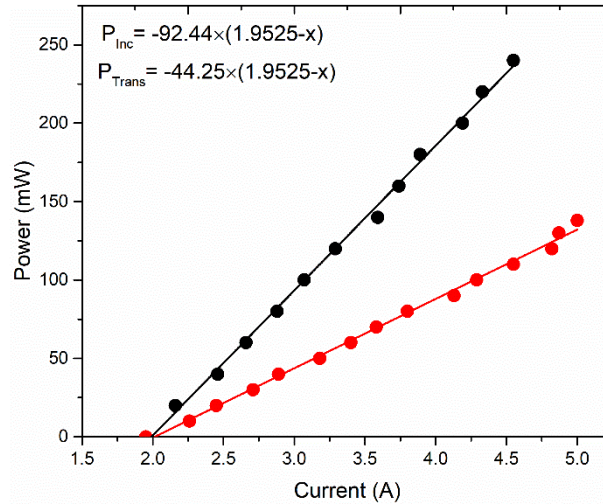


Figure 2.8 Fits of the variations of the power of the Incident (black) and transmission (red) to the cuvette as a function of the applied current with the same onset of the laser emission.

The relationship between the excitation power before arriving at and passing through the cuvette can be described as,

$$P_{Trans} = 0.4787P_{Inc} \quad \text{eq 2.9}$$

The power in the middle of the cuvette can be written as,

$$P_{1/2} = P_{Inc} \sqrt{\frac{P_{Trans}}{P_{Inc}}} = \sqrt{0.4787}P_{Inc} = 0.692P_{Inc} \quad \text{eq 2.10}$$

Substituting eq 2.7 into eq 2.10 leads to,

$$P_{1/2} = 63.97 \times I - 124.9 \quad \text{eq 2.11}$$

In this way, the applied power inside the cuvette $P_{1/2}$ can be manipulated just by tuning the current of the blue laser.

2.4 Conclusion

There is a wide variety of light sources available, but the selection of the appropriate ones has a great impact on the formation of metallic dots on semiconductor surfaces. In this chapter, we have introduced the use of different types of lights for the photodeposition reaction. The utilization of lasers is essential to

provide a large amount of photon flux density and control the growth and configuration of metallic dots on semiconductors. We have also described the detailed setups specifically designed for the photodeposition of metals on the surfaces of either TiO_2 and $\text{Cu}_{2-x}\text{S}/\text{CuInS}_2$ nanocrystals.

2.5 References

1. Olympus Sources of Visible Light. <https://www.olympus-lifescience.com.cn/zh/microscope-resource/primer/lightandcolor/lightsourcesintro/> (accessed 22/10/2021).
2. Khalavka, Y.; Harms, S.; Henkel, A.; Strozyk, M.; Ahijado-Guzmán, R.; Sönnichsen, C., Synthesis of Au–CdS@CdSe Hybrid Nanoparticles with a Highly Reactive Gold Domain. *Langmuir* **2018**, *34* (1), 187-190.
3. Demortière, A.; Schaller, R. D.; Li, T.; Chattopadhyay, S.; Krylova, G.; Shibata, T.; dos Santos Claro, P. C.; Rowland, C. E.; Miller, J. T.; Cook, R.; Lee, B.; Shevchenko, E. V., In Situ Optical and Structural Studies on Photoluminescence Quenching in CdSe/CdS/Au Heterostructures. *J. Am. Chem. Soc.* **2014**, *136* (6), 2342-2350.
4. Carbone, L.; Jakab, A.; Khalavka, Y.; Sönnichsen, C., Light-Controlled One-Sided Growth of Large Plasmonic Gold Domains on Quantum Rods Observed on the Single Particle Level. *Nano letters* **2009**, *9* (11), 3710-3714.
5. Zhang, R.; Wang, H.; Li, Y.; Wang, D.; Lin, Y.; Li, Z.; Xie, T., Investigation on the Photocatalytic Hydrogen Evolution Properties of Z-Scheme Au NPs/CuInS₂/NCN-CN_x Composite Photocatalysts. *ACS Sustain. Chem. Eng.* **2021**, *9* (21), 7286-7297.
6. Veziroglu, S.; Obermann, A.-L.; Ullrich, M.; Hussain, M.; Kamp, M.; Kienle, L.; Leißner, T.; Rubahn, H.-G.; Polonskyi, O.; Strunskus, T.; Fiutowski, J.; Es-Souni, M.; Adam, J.; Faupel, F.; Aktas, O. C., Photodeposition of Au Nanoclusters for Enhanced Photocatalytic Dye Degradation over TiO₂ Thin Film. *ACS Appl. Mater. Interfaces* **2020**, *12* (13), 14983-14992.
7. Berr, M.; Vaneski, A.; Susha, A. S.; Rodríguez-Fernández, J.; Döblinger, M.; Jäckel, F.; Rogach, A. L.; Feldmann, J., Colloidal CdS Nanorods Decorated with Subnanometer Sized Pt Clusters for Photocatalytic Hydrogen Generation. *Appl. Phys. Lett.* **2010**, *97* (9), 093108.
8. Bai, Q. Synthesis of nano-heterodimers by laser photodeposition of metal nanoplots on TiO₂ nanoparticles. Université de Bordeaux, Bordeaux, 2019.
9. Dukovic, G.; Merkle, M. G.; Nelson, J. H.; Hughes, S. M.; Alivisatos, A. P., Photodeposition of Pt on Colloidal CdS and CdSe/CdS Semiconductor Nanostructures. *Adv. Mater.* **2008**, *20* (22), 4306-4311.
10. Hao, J.; Liu, H.; Wang, K.; Sun, X. W.; Delville, J.-P.; Delville, M.-H., Hole Scavenging and Electron–Hole Pair Photoproduction Rate: Two Mandatory Key Factors to Control Single-Tip Au–CdSe/CdS Nanoheterodimers. *ACS Nano* **2021**, *15* (9), 15328-15341.
11. Bai, Q.; Shupyk, I.; Vauriot, L.; Majimel, J.; Labrugere, C.; Delville, M.-H.; Delville, J.-P., Design of Metal@Titanium Oxide Nano-heterodimers by Laser-Driven Photodeposition: Growth Mechanism and Modeling. *ACS Nano* **2021**, *15* (2), 2947-2961.
12. Wilker, M. B.; Schnitzenbaumer, K. J.; Dukovic, G., Recent Progress in Photocatalysis Mediated by Colloidal II-VI Nanocrystals. *Isr. J. Chem.* **2012**, *52* (11-12), 1002-1015.

Chapter 3

Photodeposition of Au Nanodots on TiO₂ Nanoparticles

Table of contents

Chapter 3.....	65
Photodeposition of Au Nanodots on TiO ₂ Nanoparticles	65
3.1 Introduction to photodeposition of Au nanodots (NDs) onto TiO ₂ particle surface	69
3.2 Experimental part.....	72
3.2.1 Synthesis and characterization of TiO ₂ particles	72
3.2.2 Procedure of photodeposition	74
3.3 Results and discussions	75
3.3.1 Variation of exposure time.....	76
3.3.2 Variation of the Au precursor concentration.....	81
3.3.3 Variation of KAuCl ₄ content at different concentrations of TiO ₂	83
3.3.4 Variation of the exposure time at varying beam intensities	91
3.4 Mechanism of Au NDs growth onto TiO ₂ NPs	95
3.4.1 Photochemical reaction scheme	95
3.4.2 Growth law	98
3.4.3 Adsorption at the surface of TiO ₂	99
3.4.3.1 Chemisorption at the surface of TiO ₂	99
3.4.3.1.1 Load q and number of TiO ₂ NPs.....	100
3.4.3.1.2 Concentration of hole scavengers at the surface of TiO ₂	101
3.4.3.1.3 Concentration of gold ions at the surface of TiO ₂	102
3.4.3.2 Physisorption at the surface of TiO ₂ (The Eley-Rideal mechanism).....	103
3.4.4 Calculation of the Au ⁰ concentration produced by photoreduction for the growth of a gold ND.....	106
3.4.4.1 Set-up of the equations.....	106
3.4.4.2 Conclusion	109
3.4.5 Growth Analysis-Global.....	110
3.4.5.1 Variation in exposure time at a varying gold concentration.....	110
3.4.5.2 Variation of exposure times for different beam intensities.....	112
3.4.5.3 Variation in gold ion concentration for varying TiO ₂ NPs concentrations ...	113

3.4.5.4 Variation in gold ion concentration for multi-addition	115
3.4.5.5 Varying both gold ion concentration and TiO ₂ NPs concentrations	116
3.4.5.6 First scaling analysis	117
3.4.5.7 Chemisorption or physisorption: experiments in beam intensity	119
3.4.5.8 Physisorption mechanism for both cuvette and microchannel experiments	121
3.4.6 Conclusion of modeling	125
3.5 Conclusion	125
3.6 References	127

3.1 Introduction to photodeposition of Au nanodots (NDs) onto TiO₂ particle surface

Today, fossil fuels constitute an indispensable energy source because of their abundant reserves and high energy density. Fossil fuel consumption has increased significantly over the past half-century, with around an eight-fold since 1950, and a more or less two-fold since 1980. However, with the growing energy demand, energy depletion is a major problem facing human society. Additionally, its widespread use results in massive greenhouse gas emissions. Given these problems, there is an urgent need to develop a new sustainable and environmentally friendly energy. Semiconductor-based photocatalysis is a promising technology for converting abundant solar energy into usable hydrogen or hydrocarbons, as well as removing carbon dioxide and degrading pollutants. Among various photocatalysts, TiO₂ is considered one of the most promising candidates due to its high photoactivity, chemical stability, low cost, and “green” characteristics.¹⁻³

However, the photocatalytic activity of TiO₂ is restricted to the ultraviolet light region because of its large bandgap (3.2 eV for anatase), and only 4% of the solar spectrum is used. Furthermore, TiO₂ suffers from considerable recombination of the photogenerated electron/hole pairs.^{1, 4} Metal-TiO₂ heteronanocrystals (HNCs) have been widely studied as efficient photocatalysts because noble metal nanoparticles (*i.e.*, Au, and Ag) strongly absorb the light in the visible range thanks to the surface plasmon resonance (SPR) effect. Furthermore, the intimate interface contact between the metal and the TiO₂ induces the formation of a heterojunction facilitating the separation and the transfer of the charge carriers.⁵⁻⁷ Recently, TiO₂-Au HNCs have been widely studied and applied as visible-light responding photocatalysts both physically and chemically stable under light irradiation.⁸⁻⁹

Various methods including chemical reduction,¹⁰⁻¹¹ impregnation,¹²⁻¹⁴ deposition-precipitation,^{13, 15-17} electrodeposition,¹⁸⁻¹⁹ photodeposition (PD)^{4, 20-21} have been

developed to introduce Au nanodots onto the TiO₂ surface. Compared to other processes, PD is easy to operate and control. It is as simple as (i) introducing a photocatalyst and a metal precursor into a reaction solution containing alcohol as a sacrificial agent and (ii) illuminating this suspension with a light source.⁶ The initial report on the photodeposition of gold on TiO₂ was by Bamwenda²² in 1995 and this process was carried out using TiO₂ powders in aqueous suspensions containing HAuCl₄·4H₂O. Moreover, they deposited Au on TiO₂ powders in three different ways deposition-precipitation (DP), impregnation (IMP), photodeposition (PD), and they found that the activity of the Au catalysts for H₂ production strongly depended on the preparation method and decreased in the order Au-TiO₂-PD > Au-TiO₂-DP > Au-TiO₂-IMP. Great efforts have already been made to optimize the PD process and obtain efficient catalytic Au-TiO₂ HNCs materials; impressive accomplishments have been achieved over the past decade.^{20, 23-24}

The Au nanodot deposited on TiO₂ is a result of several different factors, including the pH of the solution, the sacrificial hole scavengers, the stability of the precursor, and the duration and intensity of the exposure. Iliev *et al.*²⁵ depositing Au NPs on commercially available TiO₂ photocatalyst (Degussa P25) by the photoreduction method at different pHs found that the Au NPs size decreased with the increase in the medium pH, which was due to the Au³⁺ complex species' dependence on this same pH. Gartner *et al.*²⁶ studied the influence of different gold precursors on the activity of TiO₂ catalysts using several commercially available gold salts including NaAuCl₄, AuCl₃, AuCl, and [Au(PPh₃)]Cl. They found that NaAuCl₄ and AuCl₃ gave gold nanodots which had the best activity on the photocatalytic hydrogen evolution from alcohol/water mixtures. Hidalgo *et al.*²⁷ studied the influence of photodeposition experimental conditions on the preparation of supported Au on TiO₂ especially light intensity and deposition time. They found that under a low light intensity, the amount of gold effectively deposited and the agglomeration could be controlled by changing the deposition time, a potential method to tailor Au-TiO₂ with high photocatalytic activity. Deepagan *et al.*²⁸ controlled the size distribution of the deposited Au NPs by varying

the UV exposure time; they reported that an exposure time of up to 3 min resulted in the formation of monomodal small Au NPs (< 2 nm) on the surface of the TiO₂ NPs and lengthening the UV exposure time resulted in the appearance of larger Au NPs (> 5 nm) at the expense of the existing small ones. Prolonged exposure over 12 h led to the growth of large Au NPs with the complete disappearance of the small ones. In addition to varying the light density and exposure time to control the size of Au NPs, research about tuning the size of photodeposited Au NPs *via* manipulating the structures of the surface defects on TiO₂ nanocrystals was published recently.²⁹

The size and amount of deposited Au on TiO₂ are both very important factors for photocatalysis. Yoshida *et al.*³⁰ succeeded to prepare Au-TiO₂ photocatalysts with a controlled size of Au NPs of around 8 nm; they also varied the number density using a postdeposition method. They found that the photocatalytic decomposition of formic acid was significantly improved with a rather small density of Au NPs but disappeared with a higher density because the latter enhanced the electron capture by the neighboring Au NPs.

Nonetheless, in most syntheses and research works on photodeposition of Au onto the surface of TiO₂, **multiple** Au nanodots (NDs) are usually obtained whether large or small on TiO₂ particle, no matter the gold content loading or the kind of TiO₂ or its morphology.^{27, 31-32} Recently, Bai *et al.*³³ synthesized well-controlled Au-TiO₂ nanoheterodimers using a laser-focused beam inside microfluidic reactors which was more efficient than the use of UV lamps and allowed the formation of heterodimers. This research indicates that what primarily matters for the synthesis of nanoheterodimers (NHDs) is the rate of production of electron-hole pairs and not the number of pairs which is produced. A good Au-TiO₂ nanoheterodimer structure has been obtained, unfortunately, not all the TiO₂ particles were decorated with Au NPs which would influence the photocatalytic activity in applications. Therefore, in this chapter, our main first goal is to find and control the conditions to synthesize TiO₂ nanoheterodimers with a high Janus yield. Another goal is to clarify the adsorption of the hole scavenger and reaction species on the TiO₂ surface and build a growth model

of Au nanodot (ND) in the photodeposition process. The UV laser was used as a light source and a very simple cuvette setup was used for deposition experiments. The effects of the exposure time, laser power, and reactant concentration on the Au size distribution and Janus yield are investigated.

3.2 Experimental part

3.2.1 Synthesis and characterization of TiO₂ particles

The TiO₂ particles which were used as photodeposition substrates were synthesized by the gel-sol method published by Sugimoto *et al.*³⁴ with some slight modifications because the gel-sol method has not only advantages in producing monodispersed particles in a simple process, but also in controlling their mean size and shape in a facile manner. In this method, TiO₂ NPs are synthesized in two steps, *i.e.*, (1) the formation of a hydroxide gel by heating of Ti(TEOA)₂ (TEOA: triethanolamine) complex previous made by reacting the titanium precursor with two equivalent of triethanolamine and (2) nucleation and growth to anatase particles.

Practically, 14.80 mL titanium tetraisopropoxide (TTIP) and 13.27 mL TEOA were mixed in a molar ratio of 1:2 under an Argon atmosphere and generate a pale-yellow stock solution. After being stirred for 24 h, 18 mL of the stock solution were mixed with 72 mL of deionized H₂O to make an aqueous stock solution of 0.25 M in Ti⁴⁺. Then, this solution is transferred into three Teflon-lined autoclaves, and aged at 100 °C for 24 h for gelation. After the first aging, the color solution changed to orange and no more gel was present. Finally, second aging at 140 °C for 3 days was performed to trigger nucleation and growth of the TiO₂ particles. The precipitate was collected by centrifugation and washed with a pH 12 NaOH solution three times. Then, the sample was purified three times using 2 M HNO₃ solution and deionized H₂O. Finally, the precipitate was redispersed in H₂O for storage.

TEM and X-ray diffraction (XRD) were conducted to characterize the as-synthesized TiO₂ particles. The TEM result (**Figure 1 a, b**) showed that TiO₂ NPs with

polyhedron shapes were successfully obtained. As these polyhedron-like TiO₂ NPs are close to an ellipsoid of revolution, length and width were measured for at least 300 TiO₂ particles to obtain their size distributions as shown in **Figure 3.1c,d**. The mean values for length and width are (35 ± 8) nm and (22 ± 4) nm, respectively.

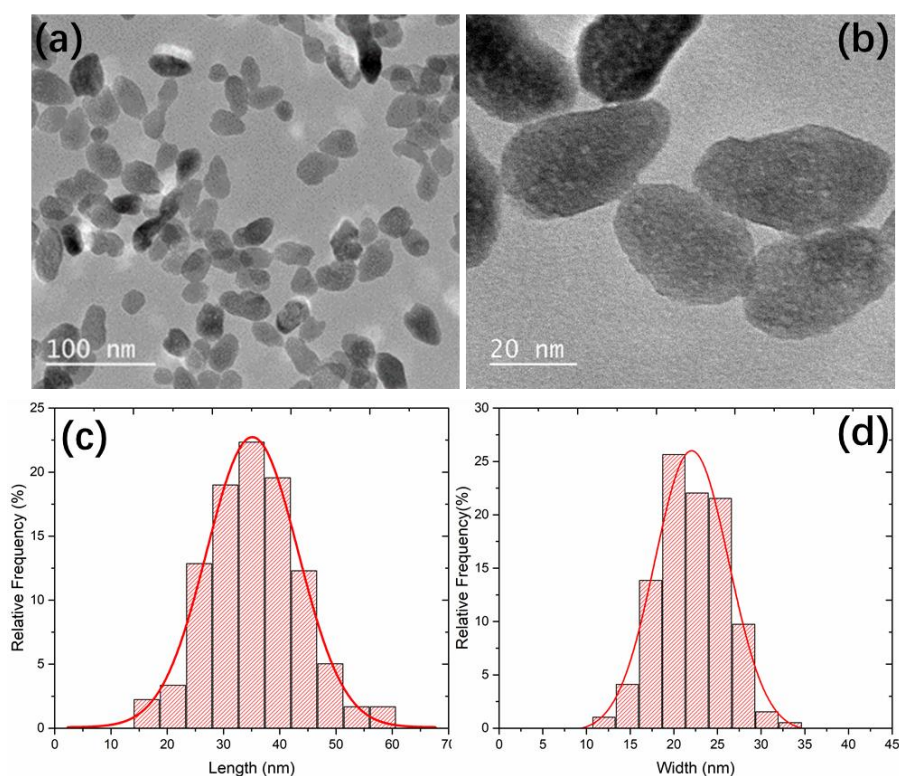


Figure 3.1 TEM images of TiO₂ polyhedrons (a, b) and size distribution (c, d); The mean length and width are (35 ± 8) and (22 ± 4) nm, respectively.

The crystallographic structure of TiO₂ particles is confirmed by XRD as shown in **Figure 2**. The diffraction pattern indicates that this sample belongs to a pure anatase phase with the peaks 25.3° , 37.9° , 48.0° , 53.9° , 55.1° , 62.9° , 68.8° , 70.2° , and 75.1° corresponding to the (101), (004), (200), (105), (211), (204), (116), (220), and (215) diffractions planes, respectively of the anatase phase (JCPDS 21-1272).

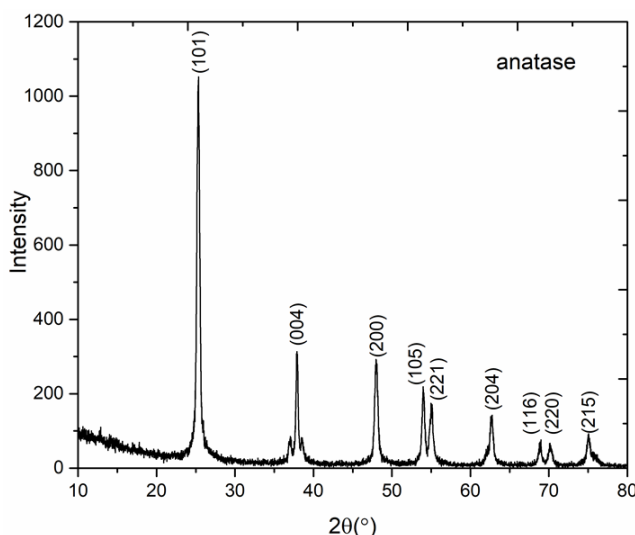


Figure 3.2 XRD pattern of TiO₂ nanoparticles showing that they are constituted of anatase phase.

3.2.2 Procedure of photodeposition

The reaction solution is prepared by mixing an already made TiO₂ aqueous solution (19 mM) at a chosen pH, and a systematically freshly prepared KAuCl₄ aqueous solution (10 mM). The range of experiments typically involves: concentrations [TiO₂] = 0.1-5.5 mM, and [KAuCl₄] = 0.125-1 mM. A 50 vol. % volume of methanol which behaves as an oxygen-free hole scavenger (HS) is added to get the final solution. The pH of the mixture is adjusted at pH 3.3 using nitric acid solution (pH = 1) to preserve a good TiO₂ dispersion below the isoelectric point of TiO₂ (pH 6.5).^{33, 35} All the solutions were purged with a flux of argon for around 10 min and mixed subsequently before exposure to laser light. Then 1 cm³ of the solution is poured into a 1 cm wide square PMMA cuvette exposed to a circular laser beam of a diameter of 1 cm. In such conditions, the whole solution is always exposed to laser light. During the irradiation process, the cuvette is capped with a rubber cap, and the solution is continuously stirred at a speed of 300 rpm with a magnetic stirrer. The beam power and the exposure time of the experiment can be easily adjusted as needed. All experiments are performed at room temperature.

The procedure for the preparation of a TEM grid: The solution exposed to laser light is then treated by ultrasonication for 5 min to disperse the nanoparticles, and finally

one drop (3-4 μL) of this solution is cast on a TEM grid. A paper tissue is used to absorb the liquid from below the grid, pumping the liquid through the grid and leaving the nanoparticles on its top side. Three or more nitric acid drops (at pH 3.3) are also cast to clean the sample particles.

3.3 Results and discussions

Previously, Dr. Bai in our group had performed some preliminary experiments on the photodeposition of Au NDs on TiO₂ using this cuvette setup; he had studied the effect of the beam power and exposure time when varying the amount of HS. He had reached the following conclusions³⁶ based on a reasonable set of experiments:

- (1) A hole scavenger (methanol) volumetric ratio of 50 % seemed to result in the best NHDs yield (49%) with the smallest SD of the grown Au nanodots. NHD yield is the ratio of TiO₂ particles which are decorated with single metal nanodot. SD is the standard deviation of size distribution of metal nanodots.
- (2) For an exposure time of 4 min, an increase of the incident laser beam power from 6.94 to 112 mW slightly increased the NHDs yield for powers larger than 50.8 mW but not the gold size.

Since the highest yield of Au-TiO₂ NHDs he obtained was surprisingly as low as 49%, we decided that the main objective of the present investigation would be to understand this statement and improve this NHDs yield by performing new experiments. The objectives were to significantly vary numerous other parameters, such as exposure time, but mainly laser power and concentrations of TiO₂ and metal precursor, and scrutinize how they impact the size of the gold nanodot and the heterodimer yield. Other objectives were

- (i) to understand the growth of Au ND until the total consumption of the gold ions present in the solution,
- (ii) to build a model of nanodot growth that takes this consumption into account (since most of Bai's work was performed with a solution flowing in a

micochannel , the initial modeling just described the growth at constant oncentration),and

- (iii) to eventually predict the final size of Au nanodots for further photocatalysis applications.

3.3.1 Variation of exposure time

The first parameter we investigate here is the effect of the exposure time from 120 to 960 s while keeping the other parameters constant: [TiO₂] = 5.5 mM, [KAuCl₄] = 0.5 mM, Power = 56.1 mW, 50 vol.% methanol as a hole scavenger, pH 3.3. TEM characterization was performed to, besides confirming the existence of Au NDs, show their morphology and their size distribution as single Au onto the TiO₂ NPs. The TEM images and data are shown in **Figure 3.3** and **Table 3.1**.

Table 3.1 Data about the Au size and yield of Au-TiO₂ NHDs prepared at different exposure times. Experimental conditions are: [TiO₂] = 5.5 mM, [KAuCl₄] = 0.5 mM, Power = 56.1 mW, 50 vol.% methanol as a hole scavenger. The calculation for theoretical Au size in Appendix 1.2.

Exposure time (s)	Au diameter (SD) (nm)	NHDs yield (%)	Predicted Au diameter (nm)
120	10.5(2.6)	48	11.9
240	10.7(2.8)	50	11.8
480	11.0(2.4)	49	11.9
720	11.0(2.2)	53	11.6
960	10.9(2.7)	51	11.7

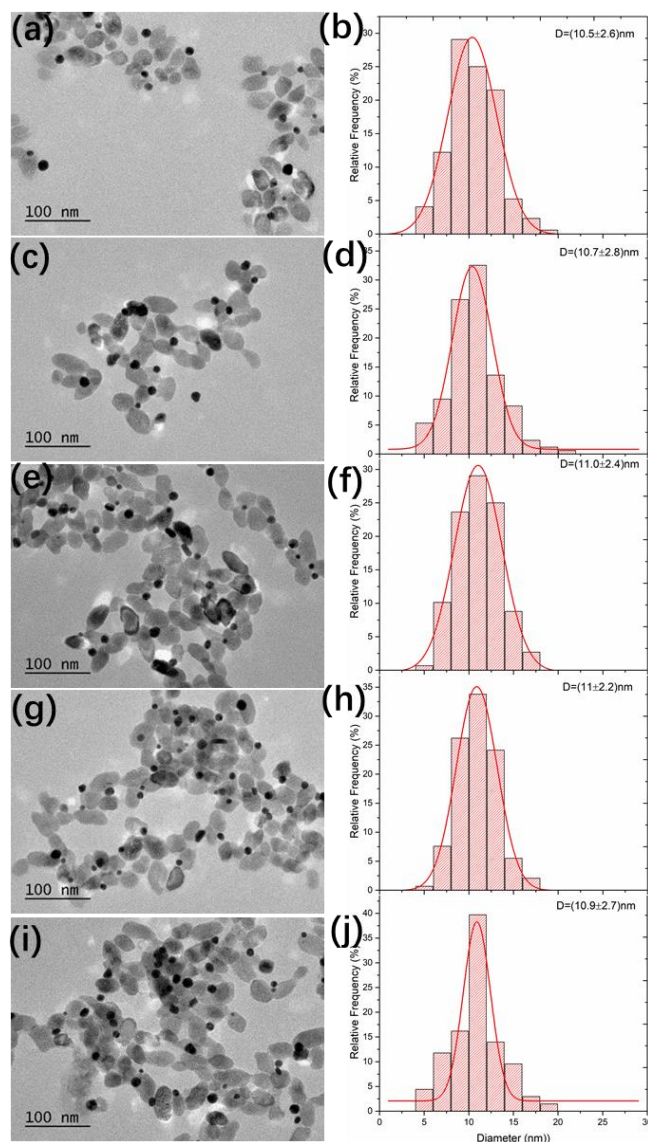


Figure 3.3 TEM images of Au-TiO₂ NHDs synthesized at different exposure times, (a) 120 s, (c) 240 s, (e) 480 s, (g) 720 s, (i) 960 s and their corresponding size distribution in (b), (d), (f), (h) and (j), respectively; statistics are performed on at least 200 TiO₂ NPs. Experimental conditions are: [TiO₂] = 5.5 mM, [KAuCl₄] = 0.5 mM, Power = 56.1 mW, 50 vol.% methanol as a hole scavenger pH3.3.

As shown in **Figure 3.3**, the TEM images confirm the formation of Au-TiO₂ NHDs and the deposition of a single Au ND on the surface of the TiO₂ particle. The diameter of Au did not change when increasing the exposure time. Moreover, the yield of Au-TiO₂ NHDs obtained at the different exposure times was also stable at around 50% (**Table 3.1**), confirming Bai's results.

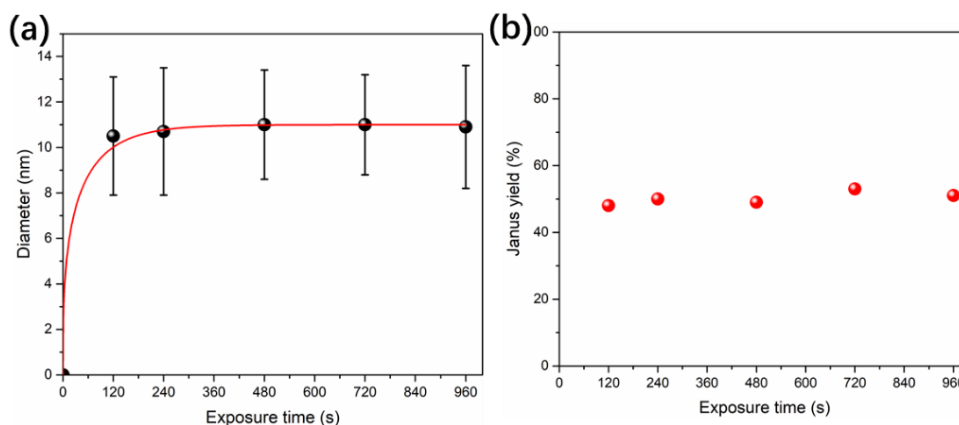


Figure 3. 4 (a) Au NDs size and (b) yields of Au-TiO₂ NHDs synthesized at various exposure times. Experimental conditions are: [TiO₂] = 5.5 mM, [KAuCl₄] = 0.5 mM, Power = 56.1 mW, 50 vol.% methanol as a hole scavenger. The red curve is a fit according to the modeling described below.

The stable size and heterodimer yield (**Figure 3.4**) suggest that in these specific conditions, growth is quite fast and that a complete consumption of the gold ions in the reaction solution is reached after 2 min laser irradiation. We got NHDs with a given gold diameter and a given yield, the purpose then was to know whether not the Au³⁺ content was all consumed during this reaction. Then based on the yield we estimated assuming a 100% conversion of gold ions, the final size of the Au NDs (**Table 3.1, column 4**). A detailed calculation is given in (Appendix 1.2). Comparing columns 2 and 4 of **Table 3.1**, we see that it is effectively the case and that the gold in the solution is consumed in a few minutes of illumination.

In addition to the TEM characterization, the optical characterization of Au-TiO₂ prepared at the different exposure times was conducted by UV-vis spectroscopy shown in **Figure 3.5**.

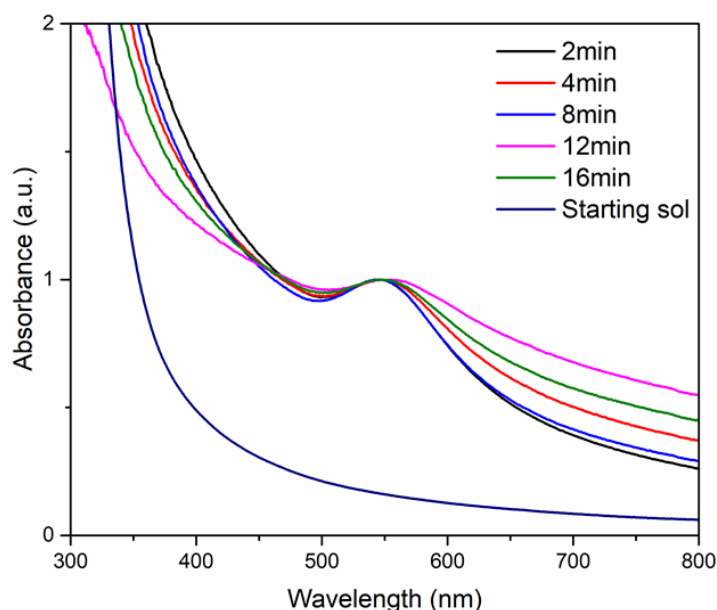


Figure 3.5 UV-vis spectra of Au-TiO₂ NHDs synthesized at different exposure times. Experimental conditions are: [TiO₂] = 5.5 mM, [KAuCl₄] = 0.5 mM, Power = 56.1 mW, 50 vol.% methanol as a hole scavenger. Starting solution is the reaction solution before irradiation.

The spectra exhibit an absorption band with a maximum peak located at around 548 nm, which corresponds to the specific absorption of the surface plasmon resonance (SPR) of Au NDs.³⁷ This confirms the presence of Au NDs after the photodeposition process. Moreover, the SPR of all the spectra is located at the same wavelength 548 nm which indicates that the size of Au nanodots deposited onto TiO₂ is almost the same for different exposure times. This result is coherent with the TEM analysis of the growth of Au NDs, showing that it is almost complete after 2 min laser irradiation. The spectrum of the starting solution indicates (i) the strong absorption in the UV range of TiO₂ (anatase) associated with its bandgap located around 380 nm,^{35, 38} (ii) the absence of Au particles before laser irradiation. The characteristic absorption peaks of AuCl₄⁻ anion located at 229 and 315 nm cannot show up because of the strong absorption of TiO₂ in this UV range.

The effect of the exposure time was also studied for a lower KAuCl₄ concentration (0.25 mM) (**Figures 3.6, 3.7, and Table 3.2**).

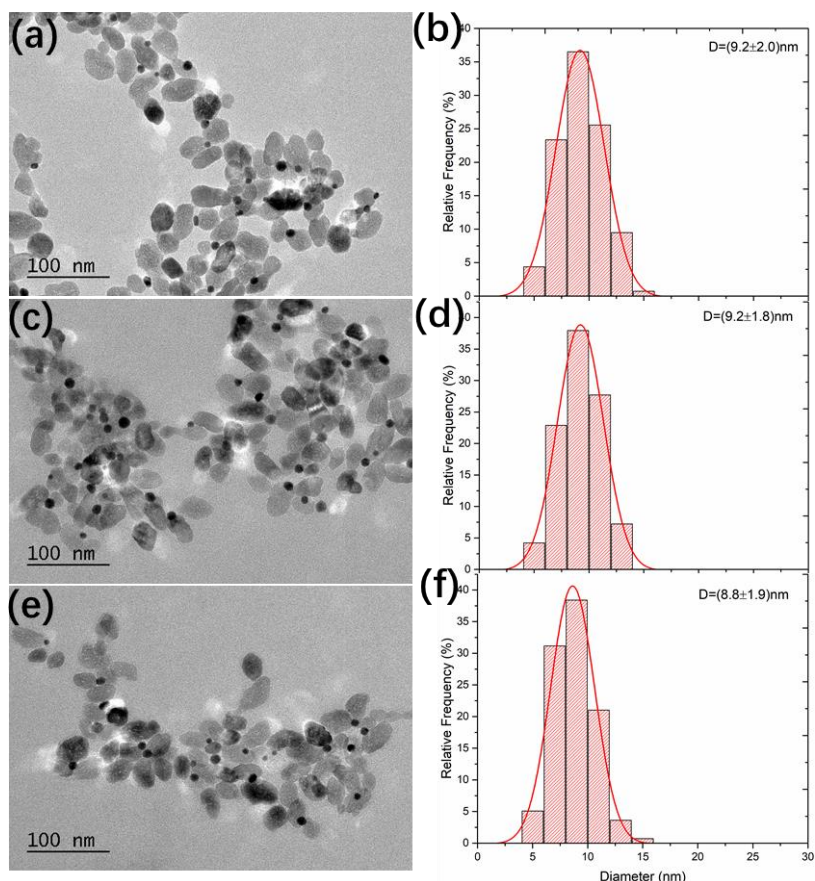


Figure 3.6 TEM images of Au-TiO₂ NHDs synthesized at different exposure times, (a)120 s, (c) 240 s, (e) 960 s and their corresponding size distribution in (b), (d), (f) respectively. Experimental conditions are: [TiO₂] = 5.5 mM, [KAuCl₄] = 0.25 mM, Power = 56.1 mW, 50 vol.% methanol as a hole scavenger.

Table 3.2 Data of Au size and yield of Au-TiO₂ NHDs prepared at different exposure times. Experimental conditions are: [TiO₂] = 5.5 mM, [KAuCl₄] = 0.25 mM, Power=56.1 mW, 50 vol.% methanol as a hole scavenger.

Exposure time (s)	Au diameter (SD) (nm)	NHDs yield (%)	Predicted Au diameter(nm)
120	9.2(2.0)	45	9.7
240	9.2(1.8)	49	9.4
960	8.8(1.9)	40	10

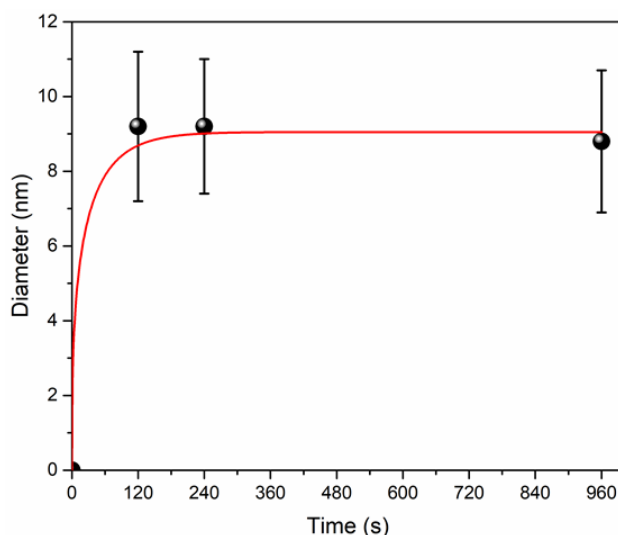


Figure 3.7 Au size of Au-TiO₂ NHDs synthesized at various exposure times. Experimental conditions are: [TiO₂] = 5.5 mM, [KAuCl₄] = 0.25 mM, Power = 56.1 mW, 50 vol.% methanol as a hole scavenger. The red curve is a fit according to the modeling described below (part 3.4).

It appears that the mean size of Au nanodots (about 9 nm) is smaller than that obtained when the concentration of KAuCl₄ is 0.5 mM (around 11 nm). From **Figure 3.6** and **Table 3.3**, we can also see that the Au NDs sizes are not only very close to one another whatever the exposure times (120, 240, and 960 s) but also to the predicted value assuming 100% gold consumption, indicating that almost all the KAuCl₄ has been consumed for the growth of Au nanodots (Appendix 1.2).

As a first conclusion, we discussed here the effect of the exposure time on the photodeposition process of gold on TiO₂. The gold growth is very fast. It is completed in less than 4 min of exposure time for an applied power of 56.1 mW. Moreover, as we shall show later on, the Au size can be predicted from our modeling, indicating that almost all the quantity of the metallic precursor has been used for the Au deposition.

3.3.2 Variation of the Au precursor concentration

In a second step, we investigated the effect of the reactant concentration on the photodeposition, starting with the variation of the concentration of KAuCl₄. All the other experimental parameters were fixed: [TiO₂] = 5.5 mM, 56.1 mW applied power, 50 vol.% methanol as hole scavenger, the mixture was adjusted at pH 3.3 and 4 min exposure

time was adopted to ensure a complete deposition. The TEM images and data of Au-TiO₂ NPs obtained for three different KAuCl₄ concentrations are shown in **Figure 3.8** and **Table 3.3**.

The Au NDs size becomes bigger with increasing the KAuCl₄ concentration (Figure 3.9a), and so does the size distribution. In addition, the NHDs yield slightly increases from 40% to 50% (**Table 3.3**). Moreover, the Au size is very close to the theoretical value. However, the Au-TiO₂ NHDs yield does not increase much and is still far from our expectations.

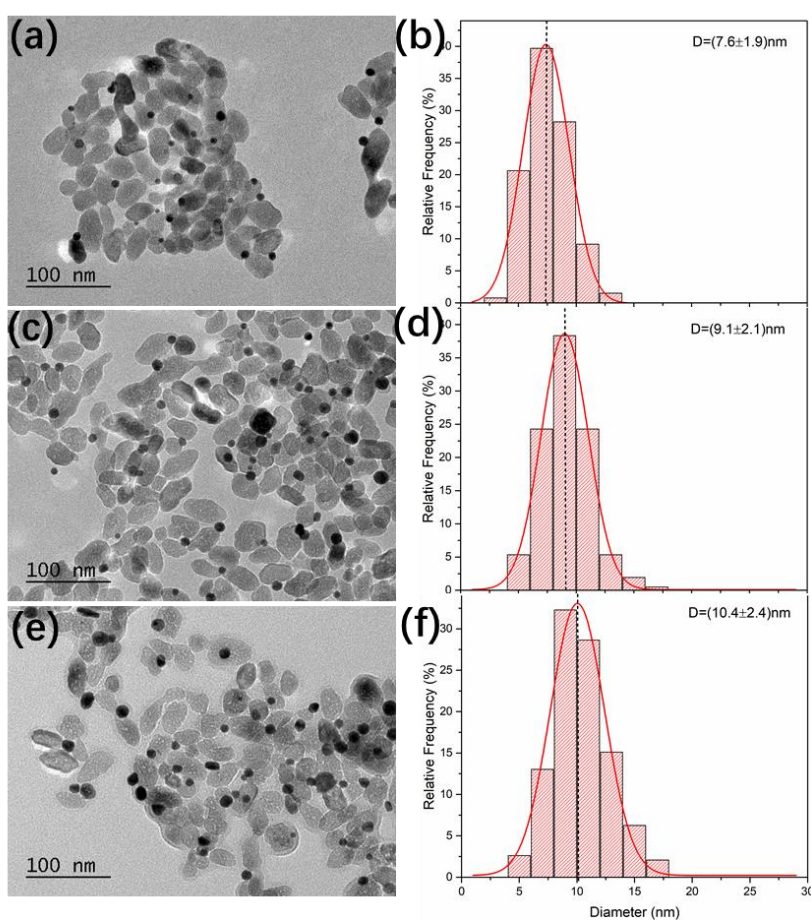


Figure 3.8 TEM images of Au-TiO₂ NHDs synthesized for different KAuCl₄ concentrations, (a) 0.125 mM, (c) 0.25 mM, (e) 0.5 mM and their corresponding size distribution in (b), (d) and (f), respectively. Experimental conditions are: [TiO₂] = 5.5 mM, Power = 56.1 mW, exposure time is 4 min, 50 vol.% methanol as hole scavenger.

Table 3.3 Data of Au size and yield of Au-TiO₂ NHDs made in the cuvette setup at different KAuCl₄ concentrations. Experimental conditions are: [TiO₂] = 5.5 mM, Power = 56.1 mW, exposure time is 4 min, 50 vol.% methanol as a hole scavenger.

[KAuCl ₄] (mM)	Au diameter (SD) (nm)	NHDs yield (%)	Predicted Au diameter(nm)
0.125	7.6(1.9)	40	8.0
0.25	9.4(2.5)	46	9.6
0.5	10.7(2.8)	50	11.8

UV-vis absorption spectroscopy was also performed to analyze the optical properties of the Au-TiO₂ NPs (**Figure 3.9b**). The SPR shifts from 530 to 550 nm exhibiting a redshift when increasing the precursor concentration. This is expected because of the increasing size of the Au NDs (**Figure 3.8**).

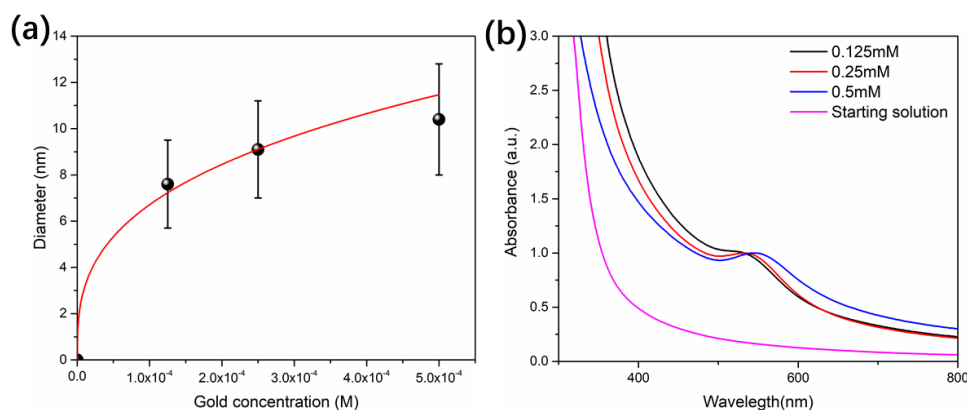


Figure 3.9 (a) Variation of Au-TiO₂ NHDs size obtained at different KAuCl₄ concentrations and the red curve is a fit based on the modeling described below (part 3.4). (b) UV-vis spectra of Au-TiO₂ NHDs made using different KAuCl₄ concentrations. Experimental conditions are: power = 56.1 mW, exposure time 4 min, [TiO₂] = 5.5 mM, 50 vol. % methanol as a hole scavenger.

3.3.3 Variation of KAuCl₄ content at different concentrations of TiO₂

Up to now, the maximum NHDs yield has been around 50 % when varying either the Au precursor on the one hand or the beam intensity and exposure time, on the other hand, we, therefore, undertook a systematic variation of the concentration of TiO₂ the other reagent.

Consequently, we tried to lower the concentration of TiO₂ (1.1 mM) keeping the concentration of KAuCl₄ at 0.5 mM (this not only plays a role in the ratio between gold and TiO₂ but also in the number of TiO₂ NPs present in the solution). The TEM characterization was conducted to check the size, size distribution of the Au NDs, and the yield of Au-TiO₂ NHDs as illustrated in **Figure 3.10**.

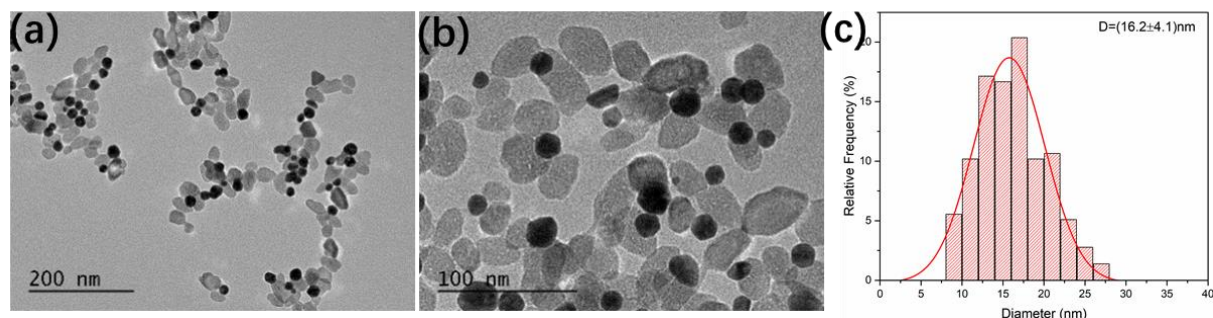


Figure 3.10 TEM images of Au-TiO₂ NHDs (a, b) and their size distribution in (c). Experimental conditions are: [TiO₂] = 1.1 mM, [KAuCl₄] = 0.5 mM, Power = 56.1 mW, exposure time 4 min, 50 vol.% methanol as a hole scavenger. To be compared to Figure 3.8e.

Table 3.4 Data concerning Au size and yield of Au-TiO₂ NHDs synthesized using different TiO₂ concentrations. Experimental conditions are: [KAuCl₄] = 0.5 mM, Power = 56.1 mW, exposure time 4 min, 50 vol.% methanol as a hole scavenger.

[TiO ₂], (mM)	[KAuCl ₄], (mM)	Au diameter (SD) (nm)	NHDs yield (%)
5.5	0.5	10.4(2.4)	48
1.1	0.5	16.2(4.1)	76

When the concentration of TiO₂ is decreased to 1.1 mM while [KAuCl₄] is kept at 0.5 mM as before, the size of the Au NDs and the NHDs yield both significantly increase, from 48% to 76 % for the yield. Based on this observation, the effect of KAuCl₄ concentration on the photodeposition at low concentrations of TiO₂ (1.1, 0.55, 0.1 mM) was studied.

a. [TiO₂] = 1.1 mM

Here, we fix the concentration of TiO₂ to 1.1 mM and vary the KAuCl₄ concentrations from 0.05 mM to 0.5 mM. The TEM characterization was performed to check the size of Au NDs on TiO₂, and its variation with the precursor concentration, is shown in **Figure 3.11**, **Figure 3.12(a)**, and **Table 3.5**. The size of Au NDs gradually increases with the KAuCl₄ concentration. Meanwhile, the width of the size distribution increases also while the relative width $\Delta D/D = 22, 23, 25, 27, 30,$ and 25% , respectively, weakly increases. Some of the Au particles also lose their regular spherical shapes when their size reaches 20-25 nm. Overall, the Au-TiO₂ NHDs yield shows a stable trend growing from 32 % to 80 % when the KAuCl₄ concentration varies from 0.05 to 0.5 mM (**Figure 3.12 (c)**).

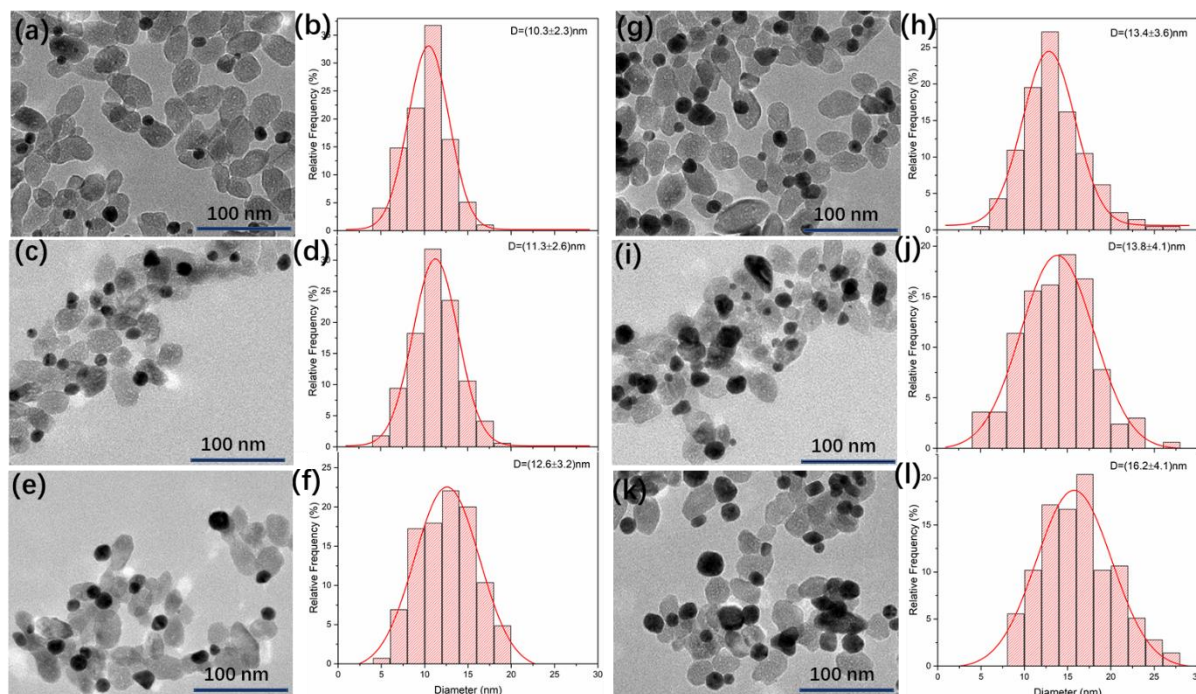


Figure 3.11 TEM images of Au-TiO₂ NHDs synthesized at different KAuCl₄ concentrations, (a) 0.05 mM, (c) 0.1 mM, (e) 0.2 mM, (g) 0.25 mM, (i) 0.4 mM, (k) 0.5 mM and their corresponding size distribution in (b), (d), (f), (h), (j) and (l), respectively. Experimental conditions are: [TiO₂] = 1.1 mM, Power = 56.1 mW, exposure time is 4 min, 50 vol.% methanol as a hole scavenger.

Table 3.5 Data of Au size and yield of Au-TiO₂ NHDs synthesized at different KAuCl₄ concentrations. Experimental conditions are: [TiO₂] = 1.1 mM, Power = 56.1 mW, exposure time is 4 min, 50 vol.% methanol as a hole scavenger. Detailed calculation of theoretical value is in Appendix 1.2.

[KAuCl ₄] (mM)	Au diameter (SD) (nm)	NHDs yield(%)	Predicted Au diameter (nm)
0.05	10.3(2.3)	32	10.9
0.1	11.3(2.6)	41	12.4
0.2	12.6(3.2)	64	13.7
0.25	13.4(3.6)	71	14.3
0.4	13.8(4.1)	76	16.3
0.5	16.2(4.1)	80	17.3

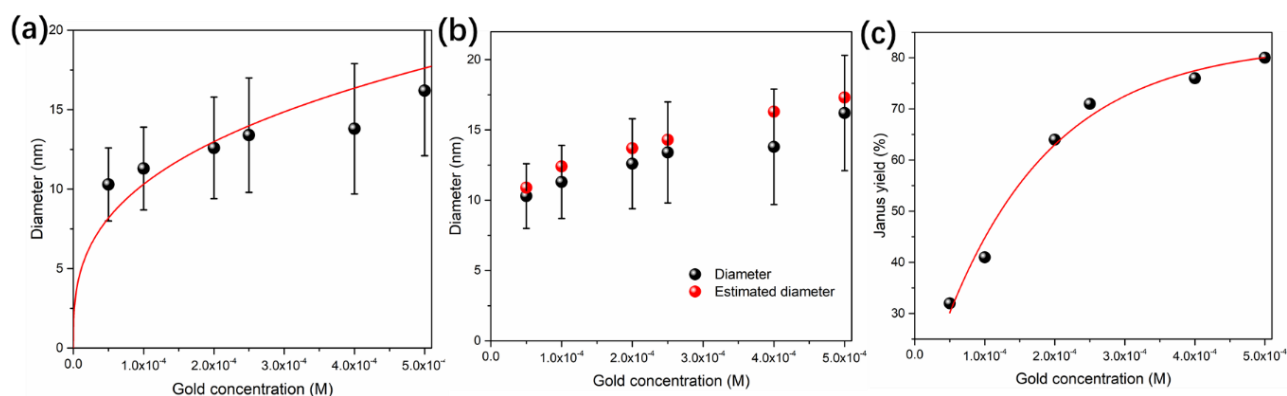


Figure 3.12 (a) Variation of Au size with the KAuCl₄ concentration (the red curve is a fit according to the modeling described below, 3.4 part) and (b) comparison with the predicted values; (c) corresponding NHDs yield when varying the KAuCl₄ concentration (the red curve is a guide for eyes). Experimental conditions are: [TiO₂] = 1.1 mM, Power = 56.1 mW, 50 vol. % methanol as a hole scavenger.

As shown in **Figure 3.12 (b)**, the Au NDs size is always a little bit smaller but quite close to the theoretical value, which is deduced by the measured NHDs yield for each experiment. Thus, it implies that our measurement of Au NDs size and calculation of NHDs yield are relatively accurate.

b. [TiO₂] = 0.55 mM

Based on the above experiments, the TiO₂ concentration was further reduced to

0.55 mM while continuing to vary the concentration of KAuCl₄ from 0.05 to 0.5 mM. The TEM images and data are shown in **Figure 3.13**, **Figure 3.14**, and **Table 3.6**.

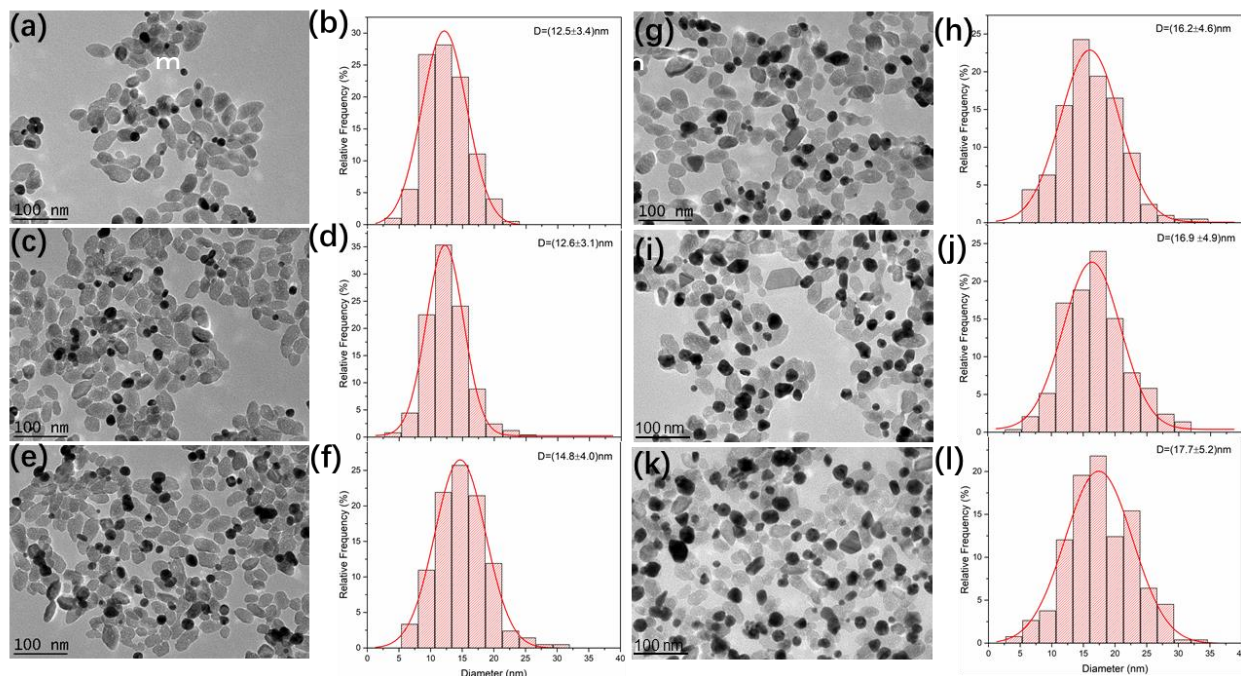


Figure 3.13 TEM images of Au-TiO₂ NHDs synthesized at different KAuCl₄ concentration, (a) 0.05 mM, (c) 0.08 mM, (e) 0.12 mM, (g) 0.18 mM, (i) 0.25 mM, (k) 0.35 mM and their corresponding size distribution in (b), (d), (f), (h), (j) and (l), respectively. Experimental conditions are: [TiO₂] = 0.55 mM, Power = 56.1 mW, exposure time 4 min, 50 vol.% methanol as a hole scavenger.

Table 3.6 Data of Au size and yield of Au-TiO₂ NHDs synthesized at different KAuCl₄ concentrations. Experimental conditions are: [TiO₂] = 0.55 mM, Power = 56.1 mW, exposure time 4 min, 50 vol.% methanol as a hole scavenger. Theoretical value calculation is Appendix 1.2.)

[KAuCl ₄] (mM)	Au diameter (SD) (nm)	NHDs yield (%)	Predicted Au diam. (nm)
0.05	12.5(3.4)	30	14.0
0.08	12.6(3.1)	35	15.9
0.12	14.8(4)	50	15.8
0.18	16.2(4.6)	65	16.6
0.25	16.9(4.9)	71	17.9
0.35	17.7(5.2)	100	17.9
0.5	17.9(6.3)	>100 (multi dots)	/

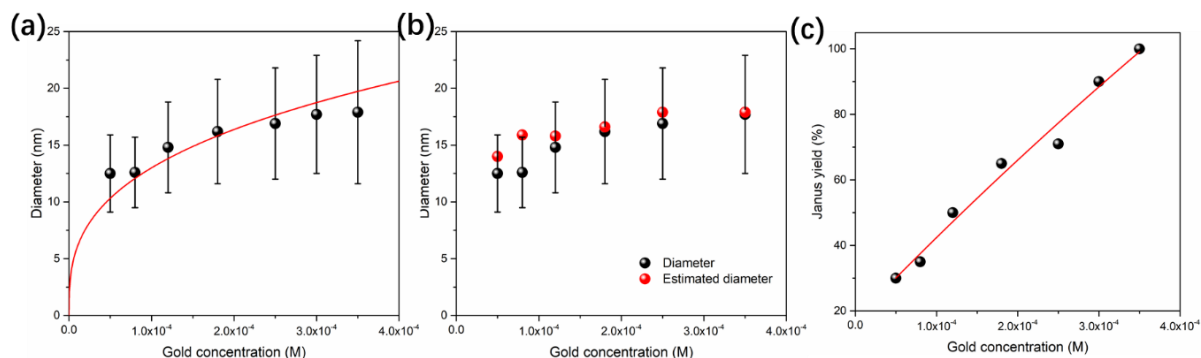


Figure 3.14 (a) Variation of the Au size with various KAuCl₄ concentrations (the red curve is a fit according to the modeling described below, part 3.4); (b) comparison to the predicted size; (c) Yield of Au-TiO₂ NHDs synthesized at different KAuCl₄ concentrations (the red curve is a guide for the eyes). Experimental conditions are: [TiO₂] = 0.55 mM, Power = 56.1 mW, exposure time 4 min, 50 vol.% methanol as a hole scavenger.

As shown in **Table 3.6** and **Figure 3.14**, the Au ND size gradually increases from 12.5 to 17.9 nm with the KAuCl₄ concentration, and so does the size distribution with the relative width $\Delta D/D = 27, 25, 27, 28, 29, 29,$ and 35%, respectively. In addition, the NHDs yield increases significantly with KAuCl₄ content. When the KAuCl₄ concentration is 0.35 mM, the yield already reached 100 % while it is around 30 % when KAuCl₄ is 0.05 mM. Finally, secondary nucleation starts to emerge on TiO₂ when KAuCl₄ reaches 0.5 mM, and we observe some TiO₂ particles with two Au NDs. The Au size nonetheless remains very close to the predicted one as shown in **Figure 3.14** as already illustrated for the TiO₂ concentration of 1.1 mM.

c. [TiO₂] = 0.1 mM

We finally tried a very low concentration of TiO₂ (0.1 mM) and varied the KAuCl₄ concentration: 0.02 mM, 0.05 mM and 0.1 mM. The TEM images and data are shown in **Figure 3.15**, **Figure 3.16**, and **Table 3.7**.

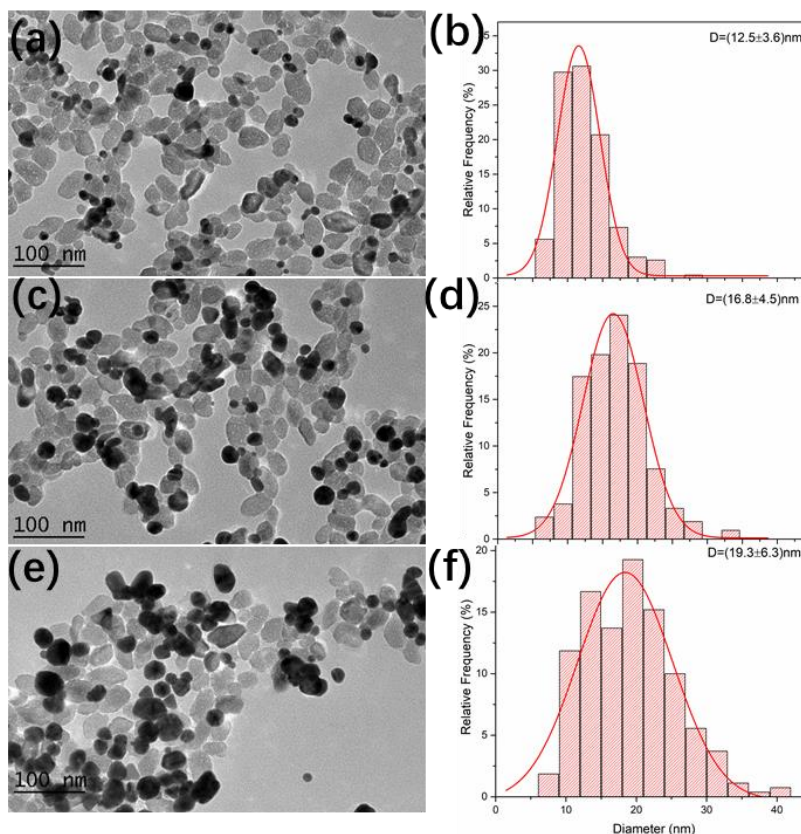


Figure 3.15 TEM images of Au-TiO₂ NHDs synthesized at different KAuCl₄ concentrations, (a) 0.02 mM, (c) 0.05 mM, (e) 0.1 mM and their corresponding size distribution in (b), (d), and (f) respectively. Experimental conditions are: [TiO₂] = 0.1 mM, Power = 56.1 mW, exposure time is 4 min, 50 vol. % methanol as a hole scavenger.

Table 3.7 Data of Au NDs size and NHDs Au-TiO₂ yields made at different KAuCl₄ concentrations. Experimental conditions are: [TiO₂] = 0.1 mM, Power = 56.1 mW, exposure time is 4 min, 50 vol. % methanol as a hole scavenger. Theoretical value calculation is in Appendix 1.2.

[KAuCl ₄] (mM)	Au diameter (SD) (nm)	NHDs yield (%)	Predicted Au diameter(nm)
0.02	12.5(3.6)	46	15.8
0.05	16.8(4.5)	57	19.9
0.1	19.3(6.3)	71	23.3

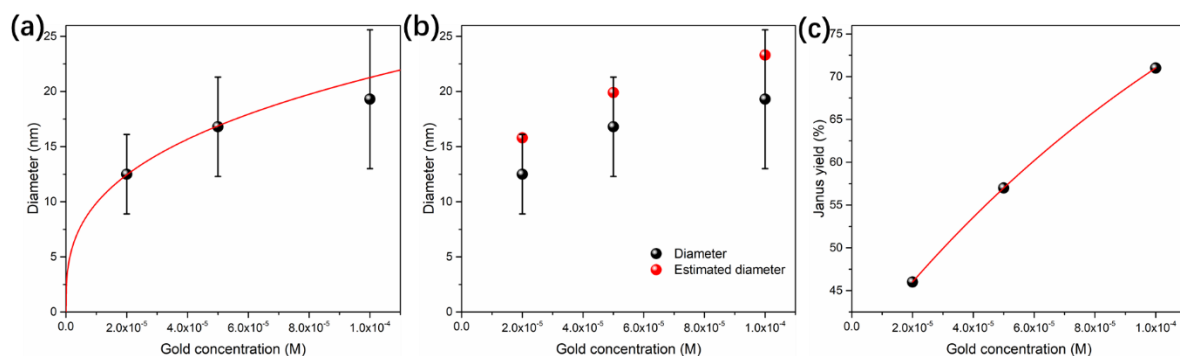


Figure 3.16 (a) Variation of Au NDs size with various KAuCl₄ concentrations (the red curve is a fit according to the modeling described below, part 3.4); (b) Au size and theoretical size (c) Yield of Au-TiO₂ NHDs synthesized at different KAuCl₄ concentrations (the red curve is a guide for the eyes). Experimental conditions are: [TiO₂] = 0.1 mM, Power = 56.1 mW, exposure time = 4 min, 50 vol.% methanol as a hole scavenger.

It appears from **Table 3.7** that when the KAuCl₄ concentration is 0.1 mM, the Au-TiO₂ NHDs yield is 71% and the diameter of Au ND is very large (19.3 nm) with a none spherical morphology. Moreover, we can observe a few free Au NPs on the TEM images (**Figure 3.15e**) which probably detached from the TiO₂ during the stirring of the photodeposition process. Nonetheless, the size of Au NDs and the NHDs yield both show a stable upward trend (**Figure 3.16**).

Eventually, the Au-TiO₂ NHDs yields, as a function of KAuCl₄ concentration at all the considered TiO₂ concentrations, are summarized in **Figure 3.17**. The lower concentration of TiO₂ NPs, the faster the growth of the Au-TiO₂ NHDs and the higher the yield when increasing the concentration of KAuCl₄. When the TiO₂ concentration is 5.5 mM, the NHDs yield increases gradually up to a plateau of around 50%. TiO₂ and KAuCl₄ concentrations both have a big influence on the NHDs yield, going up to 100% with each TiO₂ NP decorated with a single Au ND.

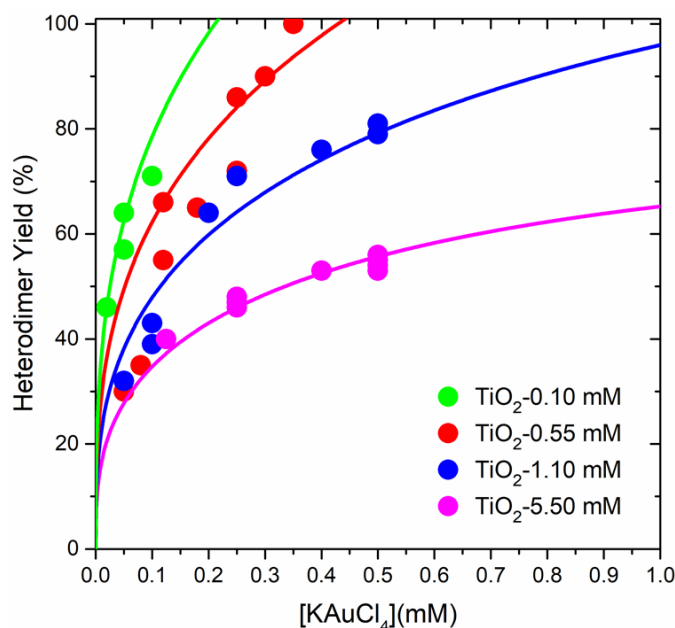


Figure 3.17 NHDs Au-TiO₂ yields variation with the KAuCl₄ concentration at different TiO₂ concentrations. The curves are guides for the eyes.

In a short conclusion, we studied the effect of the TiO₂ NPs concentration on the Au photodeposition. We reached our first objective and determined the conditions to increase the yield of Janus NPs. The Au-TiO₂ NHDs yield can be improved by increasing the metallic precursor and lowering the concentration of substrate (TiO₂).

3.3.4 Variation of the exposure time at varying beam intensities

The effect of laser power on photodeposition is also an important issue. Since in all of the previous experiments, the photodeposition was performed with a 56.1 mW applied power, both a lower (40 mW) and a higher (80 mW) powers are investigated in this section. For each power, the exposure time was varied between 2 and 16 min to study the growth of Au NDs while the other parameters were as follows: $[TiO_2] = 2.3$ mM, $[KAuCl_4] = 0.4$ mM, 50 vol.% methanol as a hole scavenger.

The TEM images and size distributions of Au NDs are illustrated in **Figures 3.18** (40 mW) and 3.20 (80 mW).

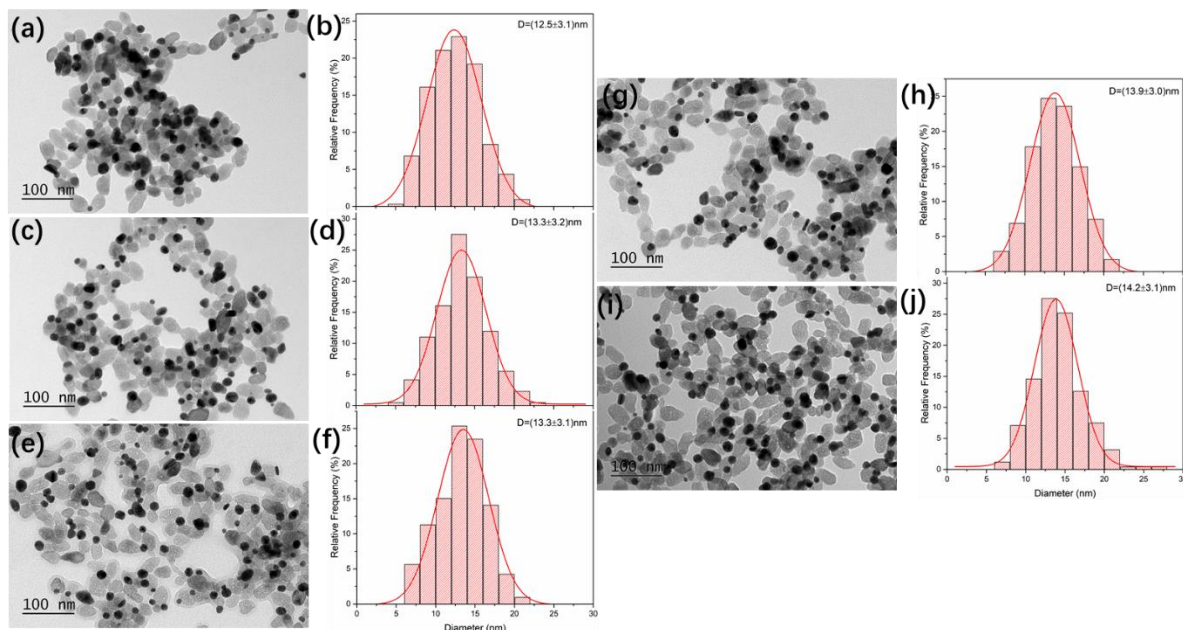


Figure 3.18 TEM images of Au-TiO₂ NHDs synthesized at different exposure times, (a) 2 min, (c) 4 min, (e) 6 min, (g) 8 min, (i) 16 min and their corresponding size distribution in (b), (d), (f), (h) and (j), respectively. Experimental conditions are: $[TiO_2] = 2.3 \text{ mM}$, $[KAuCl_4] = 0.4 \text{ mM}$, Applied Power = 40 mW, 50 vol.% methanol as a hole scavenger.

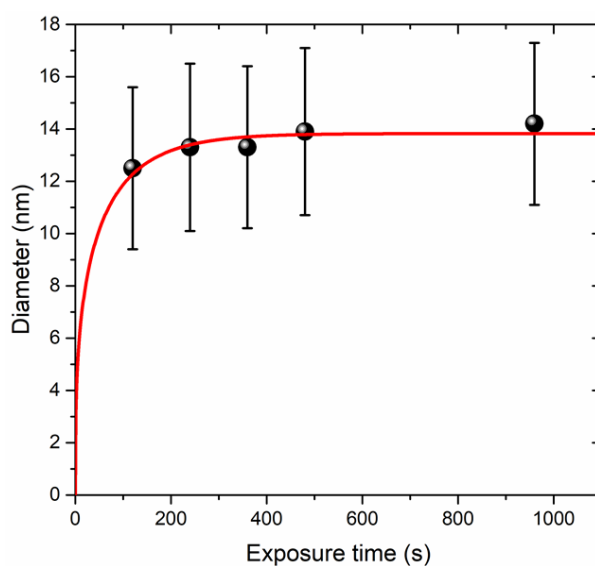


Figure 3.19 Variation of Au NDs size with various exposure times for an applied power of 40 mW. The red curve is a fit according to the modeling described below, part 3.4. Experimental conditions are: $[TiO_2] = 2.3 \text{ mM}$, $[KAuCl_4] = 0.4 \text{ mM}$, Applied Power = 40 mW, 50 vol.% methanol as a hole scavenger.

As shown in **Figure 3.18**, the diameter of Au is already 12.5 nm when the exposure time is 2 min. After that, the diameter gently increases to 13.3 nm after 4 min irradiation

(Figure 3.19), and then remains almost constant suggesting that once again the Au growth is completed within 4 min exposure time.

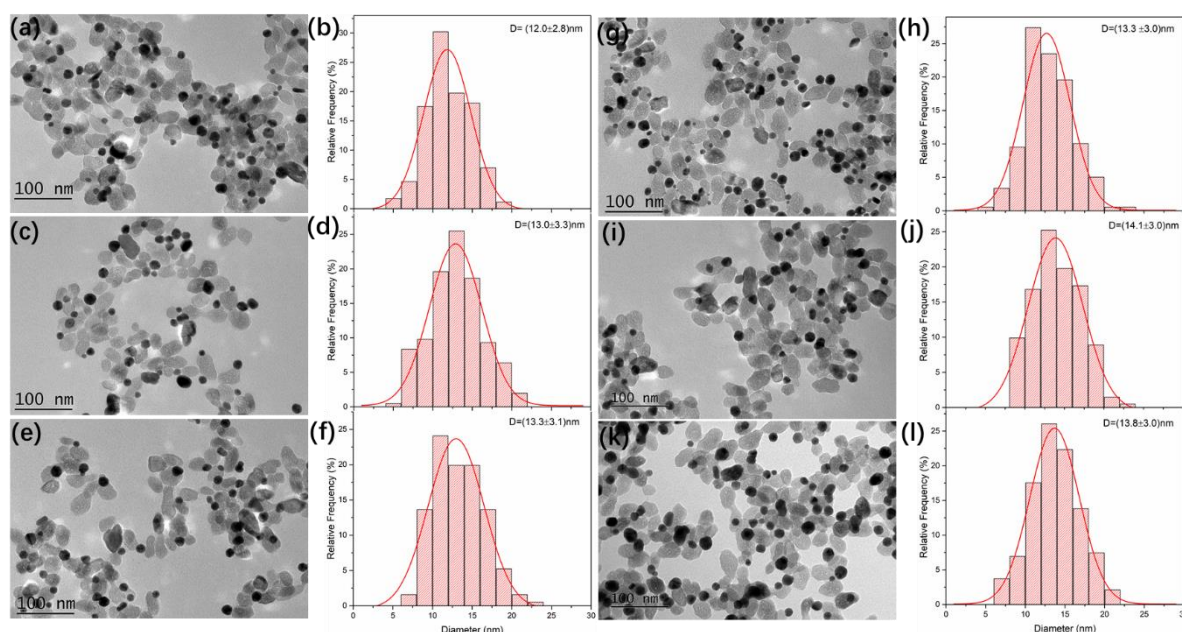


Figure 3.20 TEM images of NHDs Au-TiO₂ synthesized at different exposure times, (a) 1 min, (c) 2 min, (e) 4 min, (g) 6 min, (i) 8 min, (k) 16 min and their corresponding size distribution in (b), (d), (f), (h), (j) and (l), respectively. Experimental conditions are: [TiO₂] = 2.3 mM, [KAuCl₄] = 0.4 mM, Applied Power = 80 mW, 50 vol.% methanol as a hole scavenger.

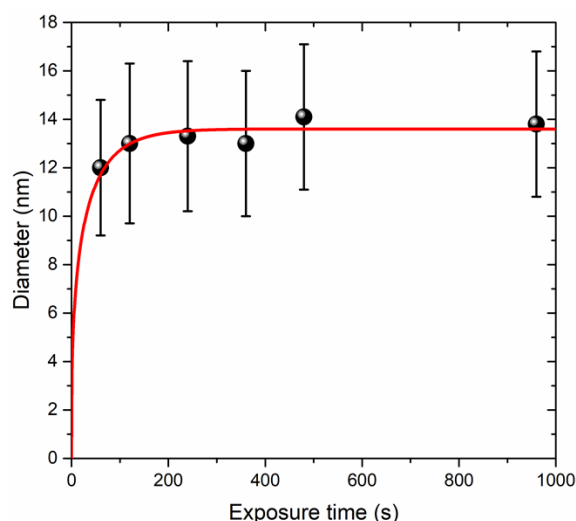


Figure 3.21 Variation of Au NDs size with various exposure times for an applied power of 80 mW. The red curve is a fit according to the modeling described below, part 3.4; Experimental conditions are: [TiO₂] = 2.3 mM, [KAuCl₄] = 0.4 mM, Applied Power = 80 mW, 50 vol.% methanol as a hole scavenger.

When the higher power (80 mW) is applied, the diameter of Au is already 12 nm

after an exposure time of 1 min. It increases gradually to 13.0 nm with 2 min irradiation before saturating, as shown in **Figure 3.21**. The Au growth completion occurred earlier than that observed at 40 mW.

The variation of the Au NDs diameter, as well as the Au-TiO₂ NHDs yield with various exposure times, are shown in **Table 3.8**. The NHDs yield is very stable, around 70% likely because the TiO₂ concentration is 2.3 mM, *i.e.* between 50-55% for 5.5 mM and 80% for 1.1 mM. Moreover, the diameters at completion are very close to the predicted values.

Table 3.8 Data of Au size and yields of Au-TiO₂ NHDs synthesized at different powers and exposure times. Experimental conditions are: [TiO₂] = 2.3 mM, [KAuCl₄] = 0.4 mM, 50 vol. % methanol as a hole scavenger. Theoretical value calculation is in Appendix 1.2.

Applied power(mW)	Exposure time (min)	Au diameter (SD)(nm)	NHDs yield (%)	Predicted Au diameter(nm)
40	2	12.5(3.1)	71	14.0
	4	13.3(3.2)	71	14.0
	6	13.3(3.1)	70	14.1
	8	13.9(3.0)	64	14.5
	16	14.2(3.1)	65	14.4
80	1	12.0(2.8)	64	14.5
	2	13.0(3.3)	66	14.3
	4	13.3(3.1)	65	14.4
	6	13.3(3.0)	70	14.0
	8	14.1(3.0)	73	13.9
	16	13.8(3.0)	72	13.9

As a final partial conclusion, the laser power has indeed an influence on the gold growth process. An increase in power reduces the time to completion. Nonetheless, the size of Au NDs obtained at the completion is the same whatever the power.

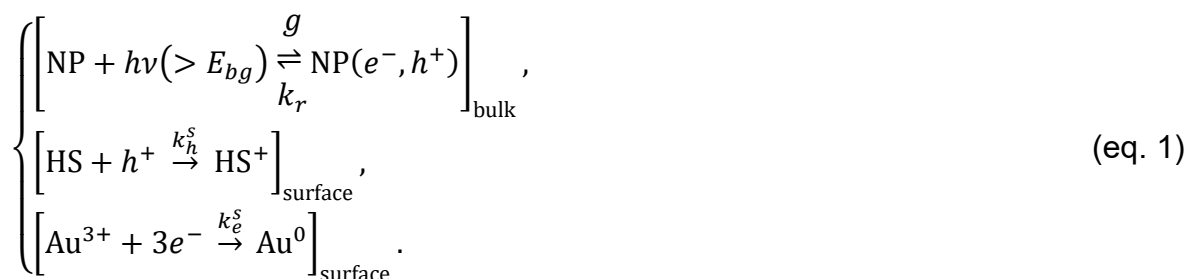
3.4 Mechanism of Au NDs growth onto TiO₂ NPs

3.4.1 Photochemical reaction scheme

The development of a growth prediction model is based on the physical processes involved in the photodeposition as follows:

- (a) Light absorption by TiO₂ induces the production of electron-hole pairs in the bulk and at the surface of the TiO₂ particle.
- (b) Electrons may recombine with holes, be trapped on defects, and/or reach the surface to reduce the metal ions at the surface of TiO₂; the same may happen for the holes in TiO₂ with oxidation of a hole scavenger at the surface of TiO₂.
- (c) Reduction of Au³⁺ ions produces Au⁰ atoms and beyond a certain amount of Au⁰ atoms, an Au⁰ cluster is nucleated and grows at the surface of TiO₂ as a function of (i) the production of electrons related to the laser absorption and intensity, (ii) the Au³⁺ concentration and (iii) the exposure time.

The chemical reactions are the following set of equations:



On the one hand, electrons and holes are produced in bulk TiO₂ NPs by optical absorption within the bandgap (g) and may recombine at a bulk rate k_r . On the other hand, the oxidation of the hole scavenger (HS) with a surface rate k_h^s and the reduction of the metal ions with a surface rate k_e^s (exponent “s” to indicate the surface) just take place at the TiO₂ surface with adsorbed metal ions and hole scavenger (usually methanol) coming from the bulk solution. We assume that:

- (1) The diffusion of electrons and holes inside the TiO₂ NPs can be confidently neglected in the reaction-diffusion equations since equilibration times for electron and hole concentrations are very short (due to the nanometric size of the TiO₂ NPs)

compared to the time scales of growth experiments by photodeposition.

(2) The deposition Au@TiO₂ is pseudo-first-order, as already demonstrated experimentally in Bai's work³³.

(3) Methanol always remains in excess, then we can assume $[HS](t) = cte$.

We use the following notations used in the literature.³⁹ For a reagent R adsorbed at the surface of TiO₂, $\{R\}$ expresses surface concentrations in mole/m² (mole/unit catalyst surface). As R is initially present in the bulk solution, this surface concentration can be related to its corresponding volume concentration $[R]_{ads}$ in mole/l using the specific surface area of the catalysts S_{sa} expressed in m²/g and obtained by BET, and q expressed in g/L is the fixed TiO₂ load of the solution, so that:

$$[R]_{ads} = qS_{sa}\{R\}.$$

As electrons e and holes h are, on the contrary, produced in the bulk TiO₂, their concentrations at the surface of TiO₂ are not related to any adsorption mechanism nor to the load q , but to its density ρ_{TiO_2} so that:

$$[e, h] = \rho_{TiO_2}S_{sa}\{e, h\}.$$

Then, the basic equations are described by:

$$\begin{cases} \frac{d[e]}{dt} = (g - k_r[e][h])_{bulk} - k_e^s\{e\}\{Au^{3+}\} \\ \frac{d[h]}{dt} = (g - k_r[e][h])_{bulk} - k_h^s\{h\}\{HS\} \\ \frac{d[HS^+]}{dt} = k_h^s\{h\}\{HS\} \\ \frac{d[Au^0]}{dt} = k_e^s\{e\}\{Au^{3+}\} \end{cases} \quad (\text{eq. 2})$$

(1) As the surface concentrations $\{R\}$ are expressed in mole/m², then the dimension of the surface rates k^s is $k^s: \frac{l}{mole \cdot s} \cdot \left(\frac{m^2}{g} \times \frac{g}{l}\right)^2$, corresponding to a bulk reaction rate k in M⁻¹.s⁻¹ divided by a surface term, and as electrons and holes are produced in the bulk TiO₂ we finally get $k_{e,h}^s = k_{e,h}q\rho_{TiO_2}S_{sa}^2$ that relates the surface reaction rate to an equivalent volume reaction rate.

(2) g is the so-called source term due to the light absorption by the NPs. For a linear excitation in intensity: $g = \frac{\sigma_{abs}[NP]I}{\hbar\omega}$, where $[NP]$ is the concentration of TiO₂ NPs

expressed in mol/L , $\hbar\omega$ is the photon energy, I is the beam intensity and σ_{abs} (in m^2) is the absorption cross-section of the NPs; σ_{abs} is calculated by assuming that the NPs eccentricity is sufficiently small to assimilate the NPs to spheres.⁴⁰

For spherical Rayleigh NPs ($r \ll \lambda_0$), $\sigma_{abs} = \frac{24\pi^2 n_m r^3}{\lambda_0} \frac{\varepsilon_2 \varepsilon_m}{(\varepsilon_1 + 2\varepsilon_m)^2 + \varepsilon_2^2}$, where r is the radius of the spherical particle, ε_1 and ε_2 are the real and imaginary components of the dielectric constant and n_m the index of refraction of the solvent (assumed as water). On the one hand, for $\lambda_0 = 364 \text{ nm}$ and $T = 25^\circ\text{C}$, we use the wavelength dependence of refractive indices from the following website (<https://refractiveindex.info/>)

TiO₂ : $n=2.8877$ $\varepsilon_1=8.3386$

TiO₂ : $k=0.019701$ $\varepsilon_2=0.11378$

Water: $n_m=1.3419$ $\varepsilon_m=1.8006$ ($k=0$ assumed as $k=5 \times 10^{-9}$)

On the other hand, the volume of an ellipsoidal TiO₂ NP is:

(1) TiO₂ NPs from the Present work: $v = 4/3 \times \pi \times (11 \times 11 \times 18) \text{ nm}^3 = 9.123 \times 10^{-24} \text{ m}^3$ (equivalent 'sphere radius' $r=12.96 \text{ nm}$ neglecting eccentricity). Then the absorption cross-section of a TiO₂ NP is $(\sigma_{abs})_{TiO_2} = 2.7330 \times 10^{-18} \text{ m}^2$ and using $\hbar\omega = \frac{hc}{\lambda} = 6.62 \times 10^{-34} \times 3 \times 10^8 / 0.364 \times 10^{-6} = 5.45 \times 10^{-19} \text{ J}$, we find $g = 5.0015 \times [NP]I$ in M/s.

(2) TiO₂ NPs from Work performed using a solution flowing in a microchannel: $v = 4/3 \times \pi \times (12.5 \times 12.5 \times 20) \text{ nm}^3 = 1.309 \times 10^{-23} \text{ m}^3$ (equivalent 'sphere radius' $r=14.62 \text{ nm}$ neglecting eccentricity). Then the absorption cross-section of a TiO₂ NP is $(\sigma_{abs})_{TiO_2} = 3.921 \times 10^{-18} \text{ m}^2$ and using $\hbar\omega = \frac{hc}{\lambda} = 6.62 \times 10^{-34} \times 3 \times 10^8 / (0.364 \times 10^{-6}) = 5.45 \times 10^{-19} \text{ J}$, we find $g = 7.1951 \times [NP]I$ in M/s.

(3) For bare TiO₂: the recombination value, determined by the fit of the silver NPs growth data in a microchannel³³ at very high intensity, is: $(k_r)_{\mu c} = (1.04 \pm 0.06) 10^9 \text{ M}^{-1} \text{ s}^{-1}$.

(4) For bare TiO₂ data, the reaction rate for hole scavenging by methanol is $k_h = 1.4 \times 10^9 \text{ M}^{-1} \text{ s}^{-1}$ from reference.⁴¹ And from the fit of the gold data at very high intensity in a microchannel³³ the reaction rate for gold ion reduction is $(k_e)_{\mu c} =$

$$(4.45 \pm 0.7) \times 10^4 M^{-1}s^{-1}.$$

3.4.2 Growth law

Bai and coauthors³³ synthesized metal@titanium oxide NHDs by laser-driven photodeposition in a flowing solution in a microchannel and developed a model to describe this situation. They assumed that the Au nanodots (NDs) had a spherical cap shape and that their late-stage growth on a TiO₂ NP was triggered by a flux of gold atoms at the surface due to the field gradient effect induced by and directed toward this metallic Au ND. Therefore, the total flux $\Phi(t)$ of gold atoms, produced at the surface of the TiO₂ NP, at the perimeter of the Au ND was proportional to the photoproduction rate of gold atoms $d[Au^0]/dt$.

On the one hand, $\Phi(t) = [v_{Au}/(Y[NP])] d[Au^0]/dt$, where v_{Au} is the volume of a gold atom, Y is the NHDs yield, and thus $Y[NP]$ is the number of TiO₂ NPs that are truly disymmetrized by photodeposition. On the other hand, the mass conservation imposes that $\Phi(t) = dV/dt = (X/8)D^2(dD/dt)$, where X is a dimensionless factor related to the contact angle of the gold NDs on the TiO₂ NPs, and D is the measured diameter of Au NDs. So $(X/8)D^2(dD/dt) = [v_{Au}/(Y[NP])] d[Au^0]/dt$, and finally $D^3(t) = (24/X)[v_{Au}/(Y[NP])][Au^0](t)$, where $t = 0$ s corresponds to the time at which the laser exposure is turned on, $[Au^0](t = 0) = 0$, and where the nucleation diameter $D_c = D(t = 0)$ is neglected since experiments are performed over a long exposure time.

For Au ND on a TiO₂ NP, the contact angle is 140° which is larger than 90° and the real diameter D of the Au ND is measured experimentally. In this case, the volume of a spherical cap is given by $V = \pi D^3 \kappa(\theta)/8$ where $\kappa(\theta) = (2/3 - \cos\theta + 1/3 \cos^3\theta)$. So $\frac{dV}{dt} = \frac{3}{8} \pi \kappa(\theta) D^2 \frac{dD}{dt}$ and thus $X = 3\pi \kappa(\theta)$. This calculation is based on reference 42.⁴² Finally, the growth of gold NDs onto TiO₂ NPs is described by equation 3:

$$D^3(t) = \frac{8}{\pi \kappa(\theta)} \frac{v_{Au}}{Y[NP]} [Au^0](t) \quad (\text{eq. 3})$$

3.4.3 Adsorption at the surface of TiO₂

Metal deposition on TiO₂ is performed in an aqueous solution so that the hole scavenger HS (methanol in our case) and the metal ions should adsorb/react easily at the surface of TiO₂ NPs. This is a complex interface problem still under debate, in particular concerning heterogeneous catalysis.⁴³ This adsorption may have a chemical (chemisorption), a physical (physisorption), or a mixed origin.⁴⁴

3.4.3.1 Chemisorption at the surface of TiO₂

Chemisorption originally means (Langmuir) that adsorbed molecules are held to the surface by covalent or nearly-covalent bonds. The adsorption of methanol⁴⁵ and Au³⁺ ions⁴⁶ on TiO₂ has been described in the literature using the Langmuir-Hinshelwood isotherm formalism (chemisorption case). The reaction scheme, including the adsorption and a subsequent reaction, for a reagent R (in our case HS and Au³⁺) in the solution, is given by:



Where k_1 and k_{-1} are the rates of adsorption and desorption at the interface of the TiO₂ NPs. We suppose that adsorption and desorption are much faster than any subsequent reaction so we can look at the first reaction $R(bulk) \xrightleftharpoons[k_{-1}]{k_1} R(ads)$ almost independently.

Then, if θ designs the surface coverage of reactant, $\theta = \frac{\{R\}_{ads}}{\{R\}_{ads}^{Max}}$ or $\theta = \{R\}_{ads} \frac{N_A}{n_R/m^2}$, where n_R/m^2 represents the maximum number of R that can be adsorbed to the surface of TiO₂, the dynamics of this adsorption reaction can be written as:

$$\frac{\partial \theta}{\partial t} = k_1 [R]_{bulk} (1 - \theta) - k_{-1} \theta \quad (\text{eq. 5})$$

And since this reaction is assumed to be very fast, we get at the pseudo equilibrium

$$\left(\frac{\partial [R]_{ads}}{\partial t} = 0\right):$$

$$\theta = \frac{(k_1/k_{-1})[R]_{bulk}}{1+(k_1/k_{-1})[R]_{bulk}} \equiv \frac{K_{ads}[R]_{bulk}}{1+K_{ads}[R]_{bulk}}, \text{ where } K_{ads} = (k_1/k_{-1}) \text{ is the equilibrium constant}$$

for the overall adsorption process.

Then $\{R\}_{ads} = \theta \frac{n_R/m^2}{N_A} = \frac{n_R/m^2}{N_A} \frac{K_{ads}[R]_{bulk}}{1+K_{ads}[R]_{bulk}}$, and we can deduce the concentration $[R]_{ads}$ at the surface of the TiO₂ NPs from $[R]_{ads} = qS_{sa}\{R\}_{ads}$. We set $C_T = \frac{n_R/m^2}{N_A} \times q \times S_{sa}$, as defined by Clarizia⁴⁷. For the chemisorption of a single species R , either HS or Au³⁺ can be deduced from their bulk values $[Au^{3+}]_{bulk}$ and $[HS]_{bulk}$ using a Langmuir-Hinshelwood type equation:

$$\begin{cases} [Au^{3+}]_{ads} = (C_T)_{Au} \frac{K_{Au}[Au^{3+}]_{bulk}}{1 + K_{Au}[Au^{3+}]_{bulk}} \\ [HS]_{ads} = (C_T)_{HS} \frac{K_{HS}[HS]_{bulk}}{1 + K_{HS}[HS]_{bulk}} \end{cases} \quad (\text{eq. 6})$$

where K_{Au} and K_{HS} are the Au³⁺ and HS adsorption equilibrium constants, and C_T is the highest concentration of active sites for Au³⁺ and HS respective adsorptions at the TiO₂ surface. C_T is also written as $C_T = q \cdot N_R$, where q is the TiO₂ loading of the solution, and $N_{Au^{3+}}$ and N_{HS} are the respective total numbers of moles of active sites per unit mass of TiO₂ in *mol/g* which is calculated from the maximum number of adsorbed ions and molecules per unit area ($n_{Au^{3+}}/nm^2$ and n_{HS}/nm^2).

Nonetheless, if the adsorptions of HS and Au³⁺ compete in surface covering, we may need to take into account the two adsorptions together. Performing the same calculation with two species, we obtain the following set of equations⁴⁴:

$$\begin{cases} [Au^{3+}]_{ads} = (C_T)_{Au} \frac{K_{Au}[Au^{3+}]_{bulk}}{1 + K_{Au}[Au^{3+}]_{bulk} + K_{HS}[HS]_{bulk}} & (\text{eq.7 a}) \\ [HS]_{ads} = (C_T)_{HS} \frac{K_{HS}[HS]_{bulk}}{1 + K_{Au}[Au^{3+}]_{bulk} + K_{HS}[HS]_{bulk}} & (\text{eq.7 b}) \end{cases}$$

3.4.3.1.1 Load q and number of TiO₂ NPs

Growth investigations not only require the concentration of TiO₂ NPs, $[NP]$, but also

its molar concentration, $[TiO_2]$, because the adsorption was taken into account. To switch from one to the other, we use the load q in TiO₂: $q = [TiO_2]M_{TiO_2} = N\rho_{TiO_2}v_{NP} = [NP]N_A\rho_{TiO_2}v_{NP}$ where N_A is the Avogadro number and v_{NP} is the volume of a TiO₂ NP calculated above. So $[NP] = \frac{M_{TiO_2}}{N_A\rho_{TiO_2}v_{NP}}[TiO_2]$.

The volume of an ellipsoidal TiO₂ NP used in the cuvette setup (present work) and microchannel setup is:

$$(1) \text{ Present work: } v = 4/3 \times \pi \times (11 \times 11 \times 18) \text{ nm}^3 = 9.123 \times 10^{-24} \text{ m}^3.$$

$$(2) \text{ Microchannel: } v = 4/3 \times \pi \times (12.5 \times 12.5 \times 20) \text{ nm}^3 = 1.309 \times 10^{-23} \text{ m}^3.$$

Since $M_{TiO_2} = 79.8658 \text{ g/M}$, $\rho_{TiO_2} = 3.9 \text{ g/cm}^3$, the concentrations of TiO₂ NPs in the two conditions are:

$$(1) \text{ Present work: } [NP] = \frac{M_{TiO_2}}{N_A m_{NP}} [TiO_2] = 3.73 \times 10^{-6} [TiO_2]$$

$$(2) \text{ Microchannel: } [NP] = \frac{M_{TiO_2}}{N_A m_{NP}} [TiO_2] = 2.60 \times 10^{-6} [TiO_2].$$

3.4.3.1.2 Concentration of hole scavengers at the surface of TiO₂

Matthews *et al.*⁴⁸ measured on bare TiO₂: $(K_{HS})_{Matthews} = 14 \text{ l} \cdot \text{g}^{-1} \equiv 1118.1 \text{ M}^{-1}$. Measurements of N_{HS} , corresponding to the highest number of OH sites, reported in the literature for TiO₂-P25 are $N_{HS} = 2.74 \times 10^{-4} \text{ mol/g}$ from reference⁴⁹ and $N_{HS} = 3.98 \times 10^{-4} \text{ mol/g}$ for TiO₂-P25 from reference⁴⁵. Since these two values are very close, we will consider their mean value $N_{HS} = (3.36 \pm 0.62) \times 10^{-4} \text{ mol/g}$.

Using an initial bulk methanol concentration $[HS] = 12.34 \text{ M}$, we find that $K_{HS}[HS]_{bulk} \gg 1$. Moreover, considering our experimental conditions, $K_{Au}[Au^{3+}]_{bulk} \ll 1$ as illustrated below, according to eq.7 we finally get:

$$[HS]_{ads} = (C_T)_{HS} \frac{K_{HS}[HS]_{bulk}}{1 + K_{Au}[Au^{3+}]_{bulk} + K_{HS}[HS]_{bulk}} \approx (C_T)_{HS} = qN_{HS} = [TiO_2]M_{TiO_2}N_{HS}, \text{ which}$$

becomes independent of the adsorption constants and bulk concentrations, meaning that the surface of the TiO₂ NPs is saturated. Using our typical TiO₂ load $q = [TiO_2]M_{TiO_2} = 0.439 \text{ g/L}$ ($[TiO_2] = 5.5 \times 10^{-3} \text{ M}$) and $N_{HS} = 3.36 \times 10^{-4} \text{ mol/g}$, we deduce: $[HS]_{ads} = qN_{HS} = (1.475 \pm 0.272) \times 10^{-4} \text{ M}$.

3.4.3.1.3 Concentration of gold ions at the surface of TiO₂

Soejima *et al.*⁴⁶ investigated the adsorption isotherm of Au(III) (from HAuCl₄) on TiO₂ anatase with a specific surface area is 8.1 m².g⁻¹. A fit of their data using a Langmuir-Hinshelwood-type model for adsorption:

$$\Gamma(\text{ions}/\text{nm}^2) = \Gamma_{\infty} \frac{K_{Au}[Au^{3+}]_{Bulk}}{(1+K_{Au}[Au^{3+}]_{Bulk})}$$

Gives $K_{Au} = (250 \pm 100)M^{-1}$ for the adsorption equilibrium constant and $\Gamma_{\infty} = (2.11 \pm 0.37) \text{ ions}/\text{nm}^2$ for the maximum number of active sites for Au³⁺ adsorption at the surface of the used TiO₂.

We described the concentration of Au(III) adsorbed at the surface of TiO₂ in eq.7a:

$$[Au^{3+}]_{ads} = (C_T)_{Au} \frac{K_{Au}[Au^{3+}]_{bulk}}{1 + K_{Au}[Au^{3+}]_{bulk} + K_{HS}[HS]_{bulk}}$$

With $(C_T)_{Au} = q \times N_{Au}$ where q (g/L) is the fixed TiO₂ load of the solution and N_{Au} is the maximum moles of active sites per unit mass of TiO₂ (mol/g). Considering our experiments (specific surface area of 46.7 m²/g), if we use Soejima's adsorption $K_{Au} = (250 \pm 100)M^{-1}$ and a maximum number of active sites for Au³⁺ adsorption at the surface of TiO₂ $\Gamma_{\infty} = (2.11 \pm 0.37) \text{ ions}/\text{nm}^2$, then $N_{Au} = (1.64 \pm 0.29) \times 10^{-4} \text{ mole}/\text{g}$ and for our typical load $q = 0.439 \text{ g}/\text{L}$, we finally get: $(C_T)_{Au} = q \times N_{Au} = (7.19 \pm 1.26) \times 10^{-5} M$.

This competitive adsorption shows that the adsorption of gold ions $[Au^{3+}]_{ads}$ is significantly reduced due to the $K_{HS}[HS]_{bulk}$ term, typically by a factor 10⁴ in our experimental conditions. Then, the efficiency of the photodeposition should be very weak, contrary to observations. Then, since (i) the competitive adsorption is not always demonstrated and (ii) the photodeposition by lasers in our experimental conditions is quite efficient, we shall continue in the following to consider the adsorption of reactants as independent of each other, so that $[Au^{3+}]_{ads} = (C_T)_{Au} \frac{K_{Au}[Au^{3+}]_{bulk}}{1+K_{Au}[Au^{3+}]_{bulk}}$ and considering $K_{Au}[Au^{3+}]_{bulk} \ll 1$, we finally consider $[Au^{3+}]_{ads} \approx (C_T)_{Au}K_{Au}[Au^{3+}]_{bulk}$.

3.4.3.2 Physisorption at the surface of TiO₂ (The Eley-Rideal mechanism)

Physisorption originally means that the adsorption is weak in the sense that molecules are held to the surface by van der Waals interactions. So, if a reagent R , in our case methanol or gold ions, is not specifically adsorbed onto the substrate in the dark, in our case TiO₂ anatase, it is assumed that $[R]_{ads} \propto [R]_{bulk}$ at least at low $[R]_{bulk}$.

Concerning the adsorption of MeOH on TiO₂, the recent critical review by Mills⁴³ came back on the interpretation in terms of L-H isotherm and showed that chemisorption was not so well established. They suggested that the interaction of R with the surface could be weak and non-specific, so $[R]_{ads} \propto [R]_{bulk}$. They cited examples⁵⁰ of R that could fall into this category: aliphatic alcohols (MeOH, EtOH, PrOH), chlorinated solvents (chloroform), and usually PhOH and 4-chlorophenol. In contrast, examples of R such as carboxylic acids can chemisorb onto the surface of the TiO₂: formic acid (FA), acetic acid (AA), and several aromatic carboxylic acids. In these latter examples, a Langmuir adsorption isotherm is invariably used to describe the binding of R to the titania surface. Then, it seems that eventually, the adsorption of MeOH onto TiO₂ belongs to the physisorption case.

In physisorption, data are interpreted differently.⁵¹⁻⁵² The reaction scheme is described by the following equation:



In this description, the absorption of light by the surface of the photocatalyst gives excited states of surface sites S^* , which are determined by the absorption of surface-active centers S . The decay of these active centers down to the ground-state S is assumed to be spontaneous (we add stimulated emission) and occurs through first-

order kinetics. The reaction of reactant molecules R with S*, to produce R_{ads} at the surface, occurs via second-order kinetics.

If we consider the first surface reaction as much faster than the second one (excitation processes are often faster than reaction ones), then we can use the formalism of a two-level system, with absorption (W), stimulated (W) and spontaneous ($1/\tau$) emissions, and deduce:

$$\frac{\partial\{S^*\}}{\partial t} = W(\{S\} - \{S^*\}) - \frac{\{S^*\}}{\tau}$$

Where $\{S\}$ is expressed in $mole/m^2$; $W = \frac{\sigma I}{\hbar\omega}$ is the probability of transition and τ is the lifetime of the excited surface state. Here, σ is the absorption cross-section of surface-active states and I is the beam intensity. Also, the finite-size effects of the NPs tell us that $\{S^*\} + \{S\} = \{S\}_0$, the total number of sites. Then $\{S\} - \{S^*\} = \{S\}_0 - 2\{S^*\}$ so that $\frac{\partial\{S^*\}}{\partial t} = W(\{S\}_0 - 2\{S^*\}) - \frac{\{S^*\}}{\tau}$.

At the steady-state, we get $\tau W\{S\}_0 = (1 + 2\tau W)\{S^*\}$, and $\{S^*\} = \frac{\tau W}{1+2\tau W}\{S\}_0$. We also deduce $\{S\} = \{S\}_0 - \{S^*\} = \frac{1+\tau W}{1+2\tau W}\{S\}_0$.

As $\tau W = \frac{\tau\sigma I}{\hbar\omega}$, one can define a surface saturation intensity $I_S = \frac{\hbar\omega}{\sigma\tau}$ from which we deduce $W\tau = \frac{I}{I_S}$.

To switch to a chemical reaction rate notation, we note:

$$\frac{\partial\{S^*\}}{\partial t} = W(\{S\} - \{S^*\}) - \frac{\{S^*\}}{\tau} = W\{S\} - \frac{1+W\tau}{\tau}\{S^*\} \equiv k_{\uparrow}\{S\} - k_{\downarrow}\{S^*\} \text{ so that}$$

$$k_{\uparrow} = W = \frac{1}{\tau} \frac{I}{I_S} \text{ and } k_{\downarrow} = \frac{1+W\tau}{\tau} = \frac{1}{\tau} \left(1 + \frac{I}{I_S}\right), \text{ and } \frac{k_{\uparrow}}{k_{\downarrow}} = \frac{W\tau}{1+W\tau} = \frac{I/I_S}{1+I/I_S}; \text{ we deduce } \frac{\{S^*\}}{\{S\}} = \frac{\tau W}{1+\tau W} = \frac{k_{\uparrow}}{k_{\downarrow}}.$$

Even if the excitation stage is much faster than the reactive one, allowing the determination of the ratio $\frac{k_{\uparrow}}{k_{\downarrow}}$ at the steady-state, the two stages of the reaction remain coupled so that the two equations need to be eventually solved together:

$$\begin{cases} \frac{\partial\{S^*\}}{\partial t} = k_{\uparrow}\{S\} - k_{\downarrow}\{S^*\} - k_{ads}\{S^*\}[R]_{bulk} \\ \frac{\partial\{R\}}{\partial t} = k_{ads}\{S^*\}[R]_{bulk} - k_{des}\{R\} \end{cases} \quad (\text{eq.9})$$

with k_{ads} is in $M^{-1} \cdot s^{-1}$, k_{des} in s^{-1} , and $\{R\}$ in mol/m^2 . Assuming stationarity for the population of excited surface states ($d\{S^*\}/dt = 0$), we get from the first equation:

$$\{S^*\} = \left(\frac{k_{\uparrow}}{k_{\downarrow} + k_{ads}[R]_{bulk}} \right) \{S\}, \text{ so that:}$$

$$\frac{\partial\{R\}}{\partial t} = k_{ads} \left(\frac{k_{\uparrow}}{k_{\downarrow} + k_{ads}[R]_{bulk}} \right) \{S\}[R]_{bulk} - k_{des}\{R\}$$

This equation rate corresponds to the Eley-Rideal type formulation in Emeline's paper⁵¹ when desorption ($k_{des} = 0$) is neglected. Moreover, the conservation of the total number of surface sites tells us that $\{S^*\} + \{S\} = \{S\}_0$ the maximum number per nanoparticle of TiO₂. If we continue to assume that excitation and relaxation remain the fastest processes, then the conservation condition $\{S^*\} + \{S\} = \{S\}_0$ can be written as $\left(\frac{k_{\uparrow}}{k_{\downarrow}} + 1 \right) \{S\} \approx \{S\}_0$ and leads to $\{S\} \approx \frac{\{S\}_0}{\left(1 + \frac{k_{\uparrow}}{k_{\downarrow}} \right)}$.

$$\text{We deduce } \frac{\partial\{R\}}{\partial t} = k_{ads} \left(\frac{k_{\uparrow}}{k_{\downarrow} + k_{ads}[R]_{bulk}} \right) \frac{\{S\}_0}{\left(1 + \frac{k_{\uparrow}}{k_{\downarrow}} \right)} [R]_{bulk} - k_{des}\{R\}$$

Interested in the adsorbed concentration in stationary conditions $[R]_{ads}$, we finally get:

$$\{R\} = \frac{k_{ads}}{k_{des}} \left(\frac{k_{\uparrow}}{k_{\downarrow} + k_{ads}[R]_{bulk}} \right) \frac{\{S\}_0}{\left(1 + \frac{k_{\uparrow}}{k_{\downarrow}} \right)} [R]_{bulk} = \frac{k_{\uparrow}\{S\}_0}{k_{des}} \frac{1}{\left(1 + \frac{k_{\uparrow}}{k_{\downarrow}} \right)} \left(\frac{(k_{ads}/k_{\downarrow})[R]_{bulk}}{1 + (k_{ads}/k_{\downarrow})[R]_{bulk}} \right), \text{ and}$$

$$[R]_{ads} = \frac{k_{ads}}{k_{des}} \left(\frac{k_{\uparrow}}{k_{\downarrow} + k_{ads}[R]_{bulk}} \right) \frac{\{S\}_0 \times S_{sa} \times q}{\left(1 + \frac{k_{\uparrow}}{k_{\downarrow}} \right)} [R]_{bulk} = C_T \frac{k_{\uparrow}}{k_{des}} \frac{1}{\left(1 + \frac{k_{\uparrow}}{k_{\downarrow}} \right)} \left(\frac{(k_{ads}/k_{\downarrow})[R]_{bulk}}{1 + (k_{ads}/k_{\downarrow})[R]_{bulk}} \right)$$

Where we set $C_T = \{S\}_0 \times S_{sa} \times q$.

This equation shows an L-H form. Nonetheless, the physical meaning of the new 'adsorption' constant k_{ads}/k_{\downarrow} is entirely different from the sense given in the L-H kinetic treatment by chemisorption since the parameter $1/k_{\downarrow}$ reflects the lifetime of the surface-active center S^* , whereas the L-H reverse constant $1/k_{-1}$ denotes the lifetime of molecules R at the surface in an adsorbed state R_{ads} .

In conclusion, considering our experimental conditions:

- (i) For MeOH: chemisorption leads to $[HS]_{ads} \approx (C_T)_{HS}$, and physisorption to $[HS]_{ads} \approx K [HS]_{bulk}$ where $K' = \left(C_T \frac{k_{ads}}{k_{des}} \right)_{HS} \frac{I/I_s}{1+2I/I_s}$ is a function of the beam intensity when $(k_{ads}/k_{\downarrow})[MeOH]_{bulk} \ll 1$,
- (ii) For Au³⁺: chemisorption leads to $[Au^{3+}]_{ads} \approx K[Au^{3+}]_{bulk}$ with $K = C_T K_{Au}$, and

physisorption to $[Au^{3+}]_{ads} \approx C_T \frac{k_{ads}}{k_{des}} \frac{I/I_S}{1+2I/I_S} [Au^{3+}]_{bulk}$ so that $K = \left(C_T \frac{k_{ads}}{k_{des}} \right)_{Au} \frac{I/I_S}{1+2I/I_S}$ which is an increasing function of the beam intensity.

Comparison with experimental data should tell us which adsorption mechanism is compatible with all the experiments, and beam intensity tests should discriminate since the dependence in I is completely different for chemisorption and physisorption.

3.4.4 Calculation of the Au⁰ concentration produced by photoreduction for the growth of a gold ND

3.4.4.1 Set-up of the equations

As already described by eq. 2, these chemical reactions are:

$$\left\{ \begin{array}{l} \frac{d[e]}{dt} = (g - k_r[e][h])_{bulk} - k_e^s\{e\}\{Au^{3+}\} \\ \frac{d[h]}{dt} = (g - k_r[e][h])_{bulk} - k_h^s\{h\}\{HS\} \\ \frac{d[HS^+]}{dt} = k_h^s\{h\}\{HS\} \\ \frac{d[Au^0]}{dt} = k_e^s\{e\}\{Au^{3+}\} \end{array} \right. \quad (\text{eq. 2})$$

With $[R]_{ads} = qS_{sa}\{R\}$, $[e, h] = \rho_{TiO_2}S_{sa}\{e, h\}$ and $k_{e,h}^s = k_{e,h}q\rho_{TiO_2}S_{sa}^2$.

To solve the chemical reduction process, we assume a charge equilibration at growth time scales so that $d[e]/dt = d[h]/dt$. Then $k_e^s\{e\}\{Au^{3+}\} = k_h^s\{h\}\{HS\}$.

Using the above definitions, we deduce $k_e[e][Au^{3+}]_{ads} = k_h[h][HS]_{ads}$ and finally,

$$[h] = \frac{k_e[e][Au^{3+}]_{ads}}{k_h[HS]_{ads}}.$$

Then $\frac{d[e]}{dt} = (g - k_r[e][h])_{bulk} - k_e^s\{e\}\{Au^{3+}\}$ becomes:

$$\frac{d[e]}{dt} = g - k_e[Au^{3+}]_{ads}[e] \left[\frac{k_r}{k_h[HS]_{ads}}[e] + 1 \right] \quad (\text{eq. 10})$$

Assuming the high-field condition $\frac{k_r}{k_h[HS]_{ads}}[e] \gg 1$ already used in laser-driven photodeposition experiments in microchannels, the electron production is described

$$\text{by } \frac{d[e]}{dt} \approx g - \frac{k_r k_e [Au^{3+}]_{ads}}{k_h [HS]_{ads}} [e]^2.$$

This equation, coupled with those for the gold ions variation and gold production,

$-\frac{d[Au^{3+}]}{dt} = \frac{d[Au^0]}{dt} = k_e^s \{e\} \{Au^{3+}\}$, cannot be solved analytically when $[Au^{3+}](t)$ varies with time because we need to take into account the temporal behaviors of the second-order terms $[e]^2(t)$ and $\{e\}(t) \cdot \{Au^{3+}\}(t)$.

So, we propose a simpler and already improved route by assuming that the stationary electron concentration $[e]_{sta}$ is reached at a time scale much smaller than that of the growth so that $[e]$ is continuously stationary (when looking at the growth time scale $[e] \approx [e]_{sta}$, see Bai *et al.*³³); this condition is quite reasonable since it means that $[e]$ ‘instantaneously’ adapts to the ‘slow’ variations of $[Au^{3+}]_{ads}(t)$ related to the consumption and the production of gold NDs.

This stationary solution $d[e]_{sta}/dt \approx 0$, valid in the high field condition of laser

$$\text{deposition, leads to } [e]_{sta} = \sqrt{\frac{k_h [HS]_{ads} g}{k_r k_e [Au^{3+}]_{ads}}}$$

Then we need to solve:

$$-\frac{d[Au^{3+}]}{dt} = \frac{d[Au^0]}{dt} \approx k_e^s \{e\}_{sta} \{Au^{3+}\}$$

At first:

$$\frac{d[Au^{3+}]}{dt} = -k_e^s \{e\}_{sta} \{Au^{3+}\}, \text{ leading to:}$$

$$\frac{d[Au^{3+}]}{dt} = -\sqrt{\frac{k_e k_h [HS]_{ads} g}{k_r}} \cdot \sqrt{[Au^{3+}]_{ads}}$$

In the *chemisorption* case, the adsorption at the surface of TiO₂ is expected to be compatible with a Langmuir-Hinshelwood-type model. Considering our experimental conditions, $K_{Au} [Au^{3+}]_{bulk} \ll 1$ and finally: $[Au^{3+}]_{ads} \approx (C_T)_{Au} K_{Au} [Au^{3+}]_{bulk}$.

In the *physisorption* case, with $(k_{ads}/k_d)[Au^{3+}]_{bulk} \ll 1$, we obtain: $[Au^{3+}]_{ads} \approx (C_T)_{Au} \left(\frac{k_{ads}}{k_{des}}\right)_{Au} \frac{1/I_S}{1+2I/I_S} [Au^{3+}]_{bulk}$.

So, at low gold ion concentration, $[Au^{3+}]_{ads} \approx K [Au^{3+}]_{bulk}$, where the proportionality

constant is $K = (C_T)_{Au} K_{Au}$ (chemisorption), or $K = (C_T)_{Au} \left(\frac{k_{ads}}{k_{des}} \right)_{Au} \frac{I/I_S}{1+I/I_S}$ (physisorption). Consequently,

$$\frac{d[Au^{3+}]}{dt} = -\sqrt{\frac{k_e k_h [HS]_{ads} g}{k_r}} \cdot \sqrt{[Au^{3+}]_{ads}} \approx -\sqrt{\frac{k_e k_h [HS]_{ads} g}{k_r}} \cdot \sqrt{K} \sqrt{[Au^{3+}]}$$

and, the solution is:

$$\sqrt{[Au^{3+}]}(t) = \sqrt{[Au^{3+}]_0} \left[1 - \frac{1}{2} \sqrt{\frac{k_e k_h [HS]_{ads}}{k_r} \cdot \frac{K}{[Au^{3+}]_0} \cdot g \cdot t} \right]$$

by using the initial condition $[Au^{3+}](t = 0) = [Au^{3+}]_0$ at $t = 0$.

Then we can set a time scale $\tau = \sqrt{\frac{k_r}{k_e k_h [HS]_{ads} g} \frac{[Au^{3+}]_0}{K}}$ so that:

$$[Au^{3+}](t) = [Au^{3+}]_0 \left(1 - \frac{t}{2\tau} \right)^2.$$

Accordingly, in a second step:

$$\frac{d[Au^0]}{dt} = k_e^s \{e\}_{sta} \{Au^{3+}\} \approx \sqrt{\frac{k_e k_h [HS]_{ads} g}{k_r}} \cdot \sqrt{K} \sqrt{[Au^{3+}]},$$

which can be written:

$$\frac{d[Au^0]}{dt} \approx \frac{1}{\tau} \cdot \left| 1 - \frac{t}{2\tau} \right|$$

$$\text{We deduce: } [Au^0](t \leq 2\tau) = [Au^{3+}]_0 \frac{t}{\tau} \cdot \left| 1 - \frac{t}{4\tau} \right|$$

However, if we assume a total consumption of $[Au^{3+}]_0$ at completion, $[Au^{3+}]_{ads}(t \rightarrow \infty) = 0$, then $[e]_{sta}$ should grow and diverge ($[e]_{sta} \rightarrow \infty$ if $[Au^{3+}]_{ads} \rightarrow 0$), which is not physically possible because (i) $[e]$ must remain finite in finite-size NPs and (ii) nonlinear effects may emerge at large $[e]_{sta}$, including the Auger effect and others, that prevent divergence of $[e]_{sta}$. In our linear model of excitation, $[e]_{sta}$ should then saturate to a value $[e]_{max} = \sqrt{g_{sat}/k_r}$, where g_{sat} corresponds to the saturation value at large intensities; for a two-level system it can be shown that $g_{sat} = \frac{N_{APTiO_2} v_{NP}}{M_{TiO_2}} \cdot \frac{[NP]}{2\tau}$.

Therefore, there is an exposure time t^* , corresponding to the concentration $[Au^{3+}](t = t^*)$ beyond which $[e]_{sta} = [e]_{max}$ and for which the electron production is no more dependent of $[Au^{3+}](t = t^*)$.

Then for $t > t^*$ we need to solve:

$$-\frac{d[Au^{3+}]}{dt} = \frac{d[Au^0]}{dt} = k_e^s \{e\}_{max} \{Au^{3+}\}$$

At first:

$$\frac{d[Au^{3+}]}{dt} = -k_e^s \{e\}_{max} \{Au^{3+}\} = -k_e [Au^{3+}]_{ads} [e]_{max} \quad \text{with} \quad [e]_{max} = \sqrt{\frac{g_{sat}}{k_r}} \quad \text{and}$$

$$[Au^{3+}]_{ads} \approx K[Au^{3+}]_{bulk},$$

$$\text{So } \frac{d[Au^{3+}]}{dt} = -k_e [e]_{max} K[Au^{3+}].$$

$$\text{Finally, } [Au^{3+}](t \geq t^*) = [Au^{3+}]^* \cdot \exp[-k_e [e]_{max} K \cdot (t - t^*)].$$

Accordingly,

$$\frac{d[Au^0]}{dt} = k_e^s \{e\}_{max} \{Au^{3+}\} = k_e [e]_{max} K[Au^{3+}](t \geq t^*), \text{ so that}$$

$$\frac{d[Au^0]}{dt} = k_e [e]_{max} K[Au^{3+}]^* \cdot \exp[-k_e [e]_{max} K \cdot (t - t^*)]$$

Using $[Au^0](t = t^*) = [Au^0]^*$, we deduce

$$[Au^0](t \geq t^*) = [Au^0]^* + [Au^{3+}]^* \cdot [1 - \exp[-k_e [e]_{max} K \cdot (t - t^*)]] \quad (\text{eq. 11})$$

This eq.11 suggests that the gold production should saturate exponentially.

3.4.4.2 Conclusion

Based on the set-up of equations in the previous part (3.4.4.1), we can get the following conclusions:

$$1) [Au^0](t \leq 2\tau) = [Au^{3+}]_0 \frac{t}{\tau} \cdot \left| 1 - \frac{t}{4\tau} \right|, \text{ where } \tau = \sqrt{\frac{k_r}{k_e k_h [HS]_{ads} g} \frac{[Au^{3+}]_0}{K}}$$

This equation indicates that the gold production is a linear variation of $[Au^0]$ followed by a parabolic crossover towards saturation.

We can note that $[Au^0](t \ll 4\tau) \approx [Au^{3+}]_0 \frac{t}{\tau}$, so:

$$[Au^0](t \ll 4\tau) \approx \sqrt{\frac{k_e k_h [HS]_{ads} \cdot K[Au^{3+}]_0 \cdot g \cdot t}{k_r}}$$

This allows retrieving the 1/3 growth regime in the microchannel configuration at a high field observed by Bai *et al.*,³³ so that the present result generalizes the previous one when the gold ion concentration cannot anymore be considered constant (long time exposure in finite volume for instance). Conversely, the model shows that $[Au^0](t)$ reaches a maximum at $t = 2\tau$ that can be considered as the characteristic time at which completion is almost completed.

$$2) [Au^0](t \geq t^*) = [Au^0](t = t^*) + [Au^{3+}]^* \cdot [1 - \exp[-k_e [e]_{max} K \cdot (t - t^*)]]$$

This equation indicates that the gold production should saturate exponentially.

In section 3.4.2, we have described the growth of gold NDs onto TiO₂ NPs by eq. 3,

$$D^3(t) = \frac{8}{\pi\kappa(\theta)} \frac{v_{Au}}{Y[NP]} [Au^0](t).$$

To verify these predicted behaviors using ‘late-stage’ growth data of a single gold ND growth onto a TiO₂ NP, we need to plot

$$D(t) = \left(\frac{8}{\pi\kappa(\theta)} \frac{v_{Au}}{Y[NP]} \right)^{1/3} [Au^0](t)^{1/3}, \quad \text{where } [Au^0](t) = [Au^{3+}]_0 \cdot f(t/\tau) \text{ and } f(t/\tau \rightarrow$$

$\infty) = 1$, we finally get

$$D(t) = \left(\frac{[Au^{3+}]_0}{Y[NP]} \right)^{1/3} \left[\frac{8v_{Au}}{\pi\kappa(\theta)} \cdot f(t/\tau) \right]^{1/3} \quad (\text{eq. 12})$$

$$\text{where } \tau = \sqrt{\frac{k_r}{k_e k_h [HS]_{ads} g} \frac{[Au^{3+}]_0}{K}}.$$

For pure Chemisorption:

$$\frac{t}{\tau} \propto \sqrt{\frac{[HS]_0 [NP] I}{[Au^{3+}]_0}} \cdot t.$$

For pure Physisorption:

$$\frac{t}{\tau} \propto \sqrt{\frac{[HS]_0 [NP] I}{[Au^{3+}]_0}} \cdot \left(\frac{I/I_S}{1+2I/I_S} \right) \cdot t.$$

3.4.5 Growth Analysis-Global

3.4.5.1 Variation in exposure time at a varying gold concentration

For these experiments, the TiO₂ concentration is fixed to, $[TiO_2] = 5.5 \times 10^{-3}$ M, leading to $[NP] = 3.73 \times 10^{-6} \times [TiO_2] = 2.052 \times 10^{-8}$ M, and two concentrations $[Au^{3+}]_0$ are used: 0.25 and 0.5 mM. We choose a power (P) of 56.1 mW so that, the beam intensity inside the cuvette is $I = \frac{2P}{\pi r^2} = 142.86 \text{ mW/cm}^2$, where $r = 0.5$ nm is the radius of the laser beam.

The expected growth law of the Au ND is described by eq.12,

$$D(t) = \left(\frac{[Au^{3+}]_0}{Y[NP]} \right)^{1/3} \left[\frac{8v_{Au}}{\pi\kappa(\theta)} \cdot f(t/\tau) \right]^{1/3} \quad (\text{eq.12})$$

For pure Chemisorption: $\frac{t}{\tau} \propto \sqrt{\frac{[HS]_0[NP]I}{[Au^{3+}]_0}} \cdot t.$

For pure Physisorption: $\frac{t}{\tau} \propto \sqrt{\frac{[HS]_0[NP]I}{[Au^{3+}]_0}} \cdot \left(\frac{I/I_S}{1+2I/I_S} \right) \cdot t.$

Thus, the expected growth law is: $D(t) \sim [f(t/\tau)]^{1/3}$ with $\tau = cte$, which exhibits a $D(t) \sim (t/\tau)^{1/3}$ at the early stage followed by an exponential saturation to $D_\infty = \left(\frac{8}{\pi\kappa(\theta)} \frac{v_{Au}}{\bar{Y}} \frac{[Au^{3+}]_0}{[NP]} \right)^{1/3}$ where $\kappa(\theta) = (2/3 - \cos\theta + 1/3 \cos^3\theta)$ and $\theta = 140^\circ$ is the contact angle of Au ND on TiO₂ NPs, v_{Au} is the volume of a gold atom. Finally, we get

$$D_\infty = \left(\frac{8}{\pi\kappa(\theta)} \frac{v_{Au}}{\bar{Y}} \frac{[Au^{3+}]_0}{[NP]} \right)^{1/3} = \left[\frac{8}{\pi\kappa(\theta)} \frac{M_{Au}}{N_{A}\rho_{Au}} \frac{[Au^{3+}]_0}{\bar{Y}[NP]} \right]^{1/3} = 3.2285 \times 10^{-1} \times \left(\frac{[Au^{3+}]_0}{Y[NP]} \right)^{1/3} \text{ nm}.$$

Data and fits are shown in **Figure 3.22**.

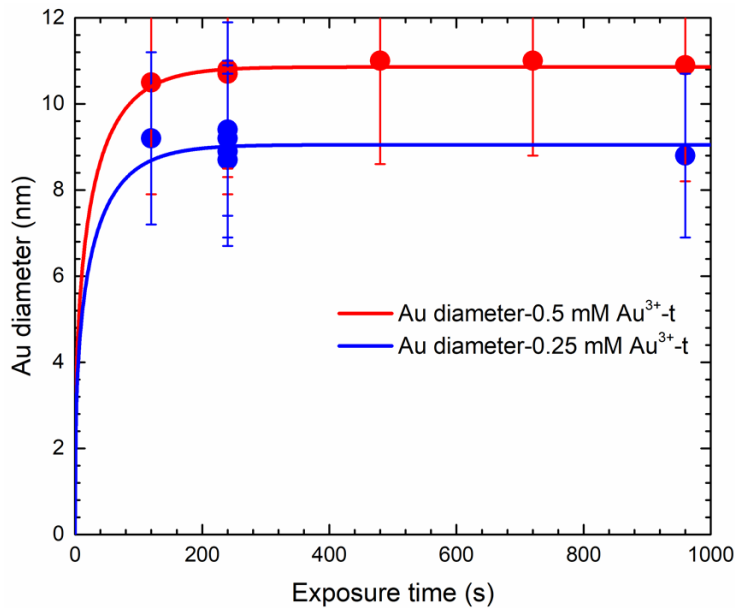


Figure 3.22 Variation of Au ND size with exposure time when the applied power is 56.1 mW. Refer to figures 3.4a and 3.7.

Experiments do not show a real dynamic behavior. This is likely because the photodeposition dynamics are very fast so experiments should also be performed at time exposures shorter than 3 min, which is not experimentally easy.

Nonetheless, from the fitting we get the final values of the Au ND diameter at completion: $D_\infty(0.25 \text{ mM}) = 9.1 \text{ nm}$ and $D_\infty(0.5 \text{ mM}) = 10.9 \text{ nm}$.

In addition, the theoretical expectation for the Au ND diameter at completion by

$$D_{\infty} = \left(\frac{8}{\pi\kappa(\theta)} \frac{\nu_{Au}}{\bar{Y}} \frac{[Au^{3+}]_0}{[NP]} \right)^{1/3} \text{ with an average yield } \bar{Y} = 50.4 \% \text{ is: } D_{\infty}(0.25 \text{ mM}) = 3.2285 \times 10^{-1} \times \left(\frac{0.25 \times 10^{-3}}{0.5044 \times 2.052 \times 10^{-8}} \right)^{1/3} = 9.3 \text{ nm} \quad \text{and} \quad D_{\infty}(0.5 \text{ mM}) = 3.2285 \times 10^{-1} \left(\frac{0.5 \times 10^{-3}}{0.5044 \times 2.052 \times 10^{-8}} \right)^{1/3} = 11.8 \text{ nm}.$$

The D_{∞} obtained by fitting is in fairly good agreement with theoretical expectation expectations.

3.4.5.2 Variation of exposure times for different beam intensities

These experiments are performed at a different concentration $[TiO_2] = 2.34 \times 10^{-3} \text{ M}$, leading to $[NP] = 3.73 \times 10^{-6} \times [TiO_2] = 8.724 \times 10^{-9} \text{ M}$, and for $[Au^{3+}]_0 = 0.4 \times 10^{-3} \text{ M}$. Three experiments were performed at varying exposure times, one at $I = 101.86 \text{ mW/cm}^2$ ($P = 40 \text{ mW}$) and two others at $I = 203.72 \text{ mW/cm}^2$ ($P = 80 \text{ mW}$) (§ 3.3.4). This choice was motivated by using the largest intensity range that belongs to the high field condition while ensuring the condition $I \ll I_s$ to check the beam intensity dependence of the growth. The expected growth behavior is the same as before (section 3.4.5.1): $D(t) \sim [f(t/\tau)]^{1/3}$ with $\tau = cte$ which exhibits a $D(t) \sim (t/\tau)^{1/3}$ at the early stage followed by an exponential saturation to $D_{\infty} = \left(\frac{8}{\pi\kappa(\theta)} \frac{\nu_{Au}}{\bar{Y}} \frac{[Au^{3+}]_0}{[NP]} \right)^{1/3} = 3.2285 \times 10^{-1} \times \left(\frac{[Au^{3+}]_0}{\bar{Y}[NP]} \right)^{1/3} \text{ nm}$ with $\bar{Y} = 68.4 \%$. Data and fits are shown in **Figure 3.23**.

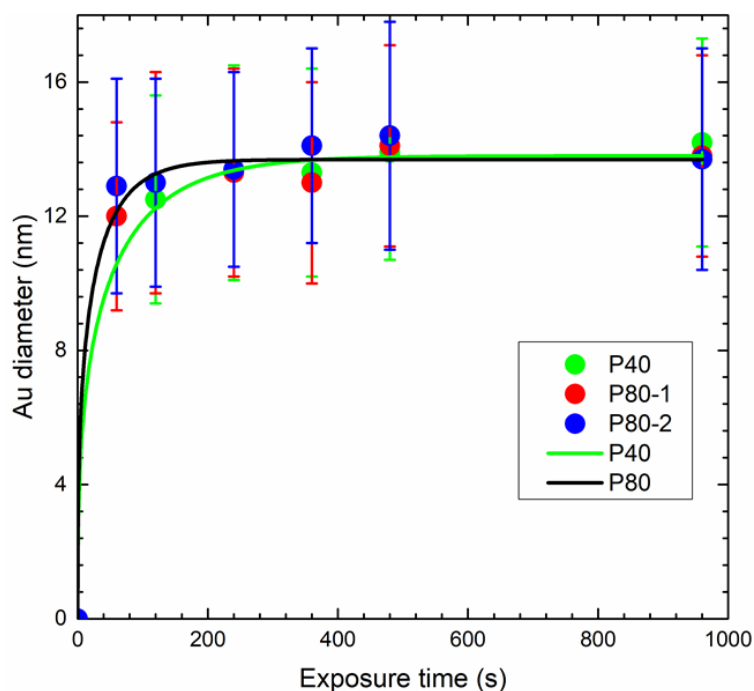


Figure 3.23 Variation of the Au NDs size with the exposure time when the applied powers are 40 and 80 mW respectively.

Even if the measurement started at 2 min exposure, experiments still show a weak dynamic behavior. Moreover, it appears, as expected, that the weaker the beam intensity, the slower the dynamics. Finally, D_{∞} is nearly the same, as also expected, as it is independent of the beam intensity. The final values of the Au ND diameter at the completion $D_{\infty}(0.1 W/cm^2) = 13.9 nm$ and $D_{\infty}(0.2 W/cm^2) = 13.7 nm$ as compared to the prediction $D_{\infty} = 3.2285 \times 10^{-1} \times \left(\frac{0.4 \times 10^{-3}}{0.6841 \times 8.724 \times 10^{-9}} \right)^{1/3} = 13.1 nm$ show a reasonably good agreement with expectations.

3.4.5.3 Variation in gold ion concentration for varying TiO₂ NPs concentrations

Four different TiO₂ concentrations were used to investigate the effects of gold ions on deposition. $[TiO_2] = 0.1, 0.55, 1.1, 5.5 mM$ and $[NP] = 3.73 \times 10^{-6} \times [TiO_2]$. The beam intensity inside the cell is $I = 142.86 mW/cm^2$ ($P = 56.1 mW$) and the exposure time t is set to 4 min (§ 3.3.3). The respective mean yields \bar{Y} are: $\bar{Y} = 59.5\%$ ($[TiO_2] = 0.1 mM$), $\bar{Y} = 62.9\%$ ($[TiO_2] = 0.55 mM$), $\bar{Y} = 60.6\%$ ($[TiO_2] = 1.1 mM$) and $\bar{Y} =$

49.9 % ($[TiO_2] = 5.5 \text{ mM}$). The expected dynamics are $D([Au^{3+}]_0) \sim [Au^{3+}]_0^{1/3} f(t/\tau)$ with $\frac{t}{\tau} \propto [Au^{3+}]_0^{-1/2}$ (both for pure chemisorption and physisorption). Nonetheless, as all these experiments are performed at an exposure time $t = 4 \text{ min}$, and as experiments in time exposure show that completion is almost reached at 4 min, we can simply assume that growth is almost completed.

As shown in eq. 12, $D(t) = \left(\frac{[Au^{3+}]_0}{Y[NP]} \right)^{1/3} \left[\frac{8v_{Au}}{\pi\kappa(\theta)} \cdot f(t/\tau) \right]^{1/3}$. Since $f(t/\tau) \approx 1$ at long time exposure, $D(t) \approx D_\infty = \left(\frac{8}{\pi\kappa(\theta)} \frac{v_{Au}}{Y} \frac{[Au^{3+}]_0}{[NP]} \right)^{1/3}$. The expected behavior is thus, $D([Au^{3+}]_0) \sim [Au^{3+}]_0^{1/3}$. Data and fits are shown in **Figure 3.24**.

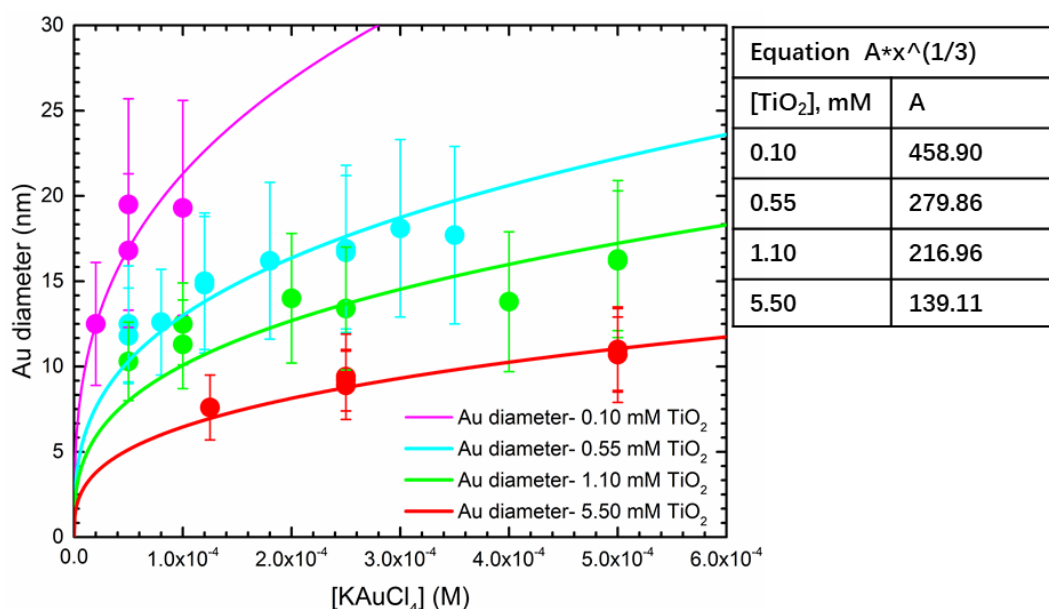


Figure 3.24 Variation of Au NDs size with the gold ion concentration for varying TiO₂ NPs concentrations. The results of fitting are shown in the Excel on the right.

This expectation of an almost stationary behavior is quite well retrieved even if one correlation is a bit weak. The plot of the amplitudes $A = \left(\frac{8}{\pi\kappa(\theta)} \frac{v_{Au}}{Y} \frac{1}{[NP]} \right)^{1/3}$ versus $[NP]$ gives the following result in **Figure 3.25** (errors bars correspond to the standard deviations given by the fit in **Figure 3.24**).

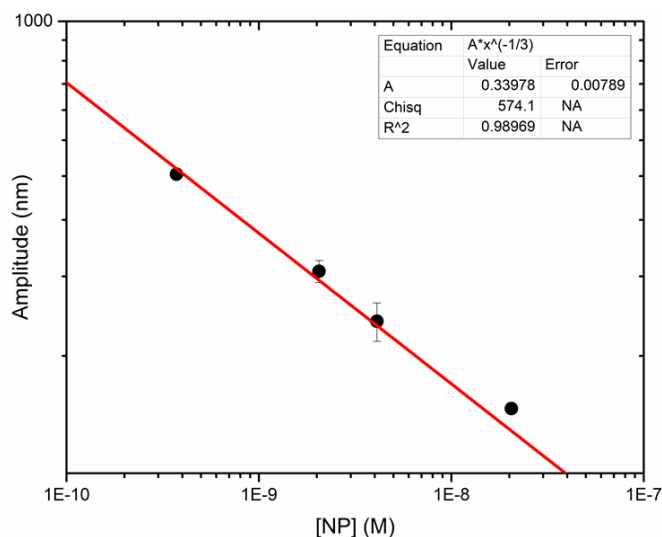


Figure 3.25 Variation of the amplitudes A determined by fitting in Figure 3.24 with the TiO₂ NPs concentrations in log-log representation.

This amplitude behavior is totally coherent with an expected behavior $\left(\frac{8}{\pi\kappa(\theta)} \frac{\nu_{Au}}{Y} \frac{1}{[NP]}\right)^{1/3}$ as a power-law fit gives an exponent -1/3. The fitted amplitude A is 0.34 which should also be given by $\left(\frac{8}{\pi\kappa(\theta)} \frac{\nu_{Au}}{Y}\right)^{1/3}$. With an average yield $\bar{Y} = 58.4$ for these four experiments, we predict $\left(\frac{8}{\pi\kappa(\theta)} \frac{\nu_{Au}}{Y}\right)^{1/3}$ is 0.39, showing again the closeness to the experimental value 0.34 deduced from the fit and the robustness of experiments versus completion predictions given by the model.

3.4.5.4 Variation in gold ion concentration for multi-addition

Since we were interested in investigating the maximum Au ND size reachable for application purposes, we also performed some deposition experiments by adding the gold ions in a two-step procedure and each photodeposition was performed in 4 min. The experiments are described in chapter 5.3.2 and detailed experimental conditions are: $[TiO_2] = 5.5 \text{ mM}$ and $[NP] = 3.73 \times 10^{-6} \times [TiO_2] = 2.052 \times 10^{-8} \text{ M}$. The beam intensity inside the cell is $I = 142.86 \text{ mW/cm}^2$, exposure time is $t = 2 \times 4 = 8 \text{ min}$, and the mean experimental yield is $\bar{Y} = 49.7 \%$. The expected behavior is: $D([Au^{3+}]_0) \sim [Au^{3+}]_0^{1/3} f(t/\tau)$ with $\frac{t}{\tau} \propto [Au^{3+}]_0^{-1/2}$, and more likely $D(t) \approx D_\infty =$

$\left(\frac{8}{\pi\kappa(\theta)} \frac{\nu_{Au}}{Y} \frac{[Au^{3+}]_0}{[NP]}\right)^{1/3}$ with a total of exposure time $t = 8 \text{ min}$, so that $D([Au^{3+}]_0) \sim [Au^{3+}]_0^{1/3}$. We performed a fit of these two behaviors and the result is shown in **Figure 3.26**.

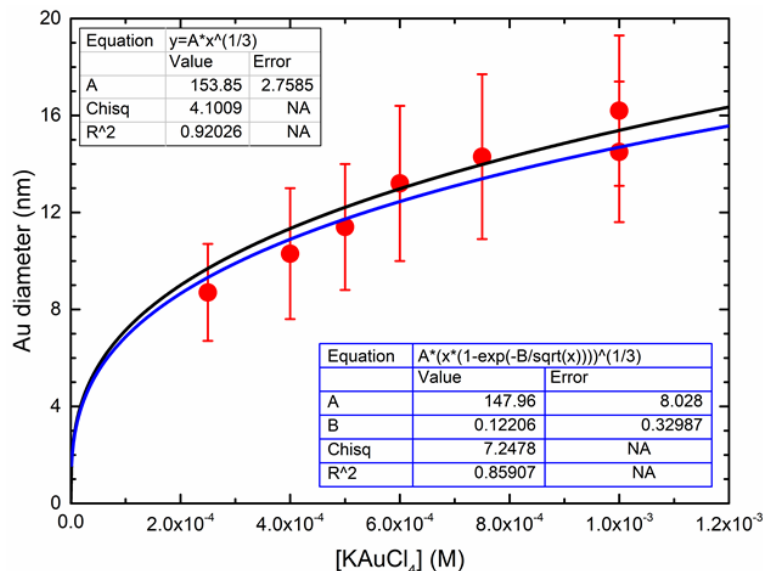


Figure 3.26 Variation of the Au ND size with gold ion concentration by multi-addition.

The two types of fitting (dynamic and stationary) are presented and coherently describe the data variations. Nonetheless, since completion at 4 min was an assumption, we can now confidently consider that completion is reached after 8 min

so that $D(t) \approx D_{\infty} = \left(\frac{8}{\pi\kappa(\theta)} \frac{\nu_{Au}}{Y} \frac{[Au^{3+}]_0}{[NP]}\right)^{1/3}$.

The stationary fit gives $D_{\infty} = \left(\frac{8\nu_{Au}}{\pi\kappa(\theta)[NP]Y}\right)^{1/3} [Au^{3+}]_0^{1/3} = 153.85 \cdot [Au^{3+}]_0^{1/3}$. Using the mean yield $\bar{Y} = 49.7\%$, we finally find $\left(\frac{8\nu_{Au}}{\pi\kappa(\theta)}\right)^{1/3} = 0.33$ very close to the theoretical value of 0.32; with the dynamic fit $D_{\infty} = \left(\frac{8\nu_{Au}}{\pi\kappa(\theta)[NP]Y}\right)^{1/3} [Au^{3+}]_0^{1/3} = 147.96 \cdot [Au^{3+}]_0^{1/3}$, leading to $\left(\frac{8\nu_{Au}}{\pi\kappa(\theta)}\right)^{1/3} = 0.32$ is the same as the prediction.

3.4.5.5 Varying both gold ion concentration and TiO₂ NPs concentrations

The Au ND diameter is related to both gold ions and TiO₂ NPs concentrations. Assembling these two parameters, the expected dynamics is given by:

$$D([Au^{3+}]_0) \sim \left(\frac{[Au^{3+}]_0}{Y[NP]} \right)^{1/3} f(t/\tau) \text{ with } t = Cte \text{ and } \frac{t}{\tau} \propto \sqrt{\frac{[HS]_0[NP]I}{[Au^{3+}]_0}} \cdot t \text{ (pure chemisorption)}$$

$$\text{or } \frac{t}{\tau} \propto \sqrt{\frac{[HS]_0[NP]I}{[Au^{3+}]_0}} \cdot \left(\frac{I/I_S}{1+2I/I_S} \right) \cdot t \text{ (pure Physisorption).}$$

Then, considering previous experiments performed at $I = 142.86 \text{ mW/cm}^2$ ($P = 56.1 \text{ mW}$), $D(t)$ is solely a function of $\frac{[Au^{3+}]_0}{[NP]}$ for both the amplitude and the characteristic time as shown in **Figure 3.27**.

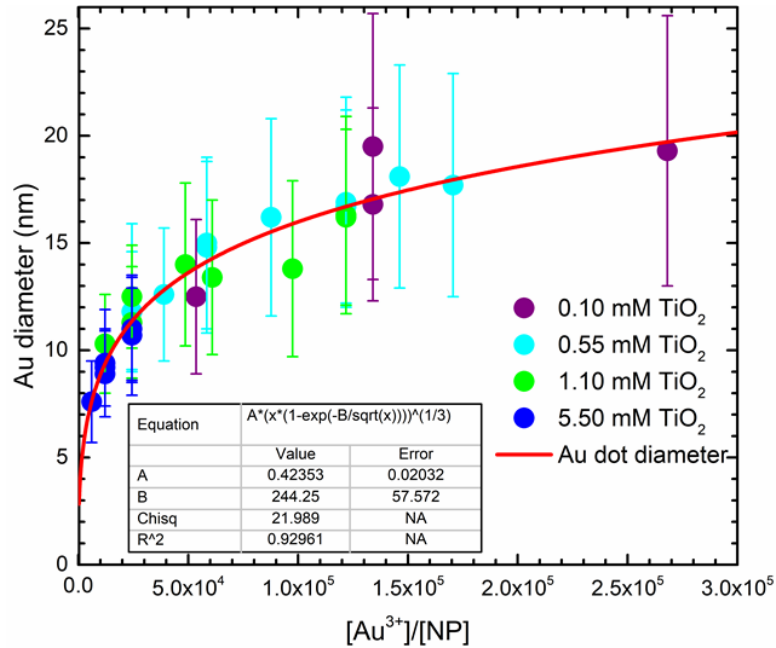


Figure 3.27 Variation of the Au ND size with both gold ion concentration and TiO₂ NPs concentrations.

Data obtained for different TiO₂ NPs and gold ion concentrations match perfectly with the fit of the predicted dynamics. From the fitting, we deduce $A = \left(\frac{8}{\pi\kappa(\theta)} \frac{v_{Au}}{Y} \right)^{1/3} = 0.42$. And considering an average yield $\bar{Y} = 58.4\%$ for the four different [NP] experiments, we finally get $\left(\frac{8v_{Au}}{\pi\kappa(\theta)} \right)^{1/3} = 0.35$, once again close to the theoretical value of 0.32.

3.4.5.6 First scaling analysis

Full scaling will confirm the adsorption mechanism of MeOH and Au³⁺ on TiO₂ anatase.

We have concluded the growth model in the 3.4.4.2 section as below,

$$\left(\frac{[NP]}{[Au^{3+}]_0}\right)^{1/3} D(t) = \left[\frac{8\nu_{Au}}{\pi\kappa(\theta)Y} \cdot f(t/\tau)\right]^{1/3} \text{ where } f(t/\tau \rightarrow \infty) = 1, \text{ and}$$

$$(i) \quad \text{for pure chemisorption: } \frac{t}{\tau} \propto \sqrt{\frac{[HS]_0[NP]I}{[Au^{3+}]_0}} \cdot t \text{ and}$$

$$(ii) \quad \text{for pure physisorption: } \frac{t}{\tau} \propto \sqrt{\frac{[HS]_0[NP]I}{[Au^{3+}]_0}} \cdot \left(\frac{I/I_S}{1+2I/I_S}\right) \cdot t.$$

Since numerous reaction rates are missing, we should plot $\left(\frac{[NP]}{[Au^{3+}]_0}\right)^{1/3} D(t)$ as a function of $\sqrt{\frac{[MeOH]_0[NP]I}{[Au^{3+}]_0}} \cdot \frac{1}{2} \left(\frac{2I/I_S}{1+2I/I_S}\right) \cdot t \propto \frac{t}{\tau}$ to see whether or not we have the emergence of a full scaling of the data sets. The difficulty is that we do not know I_S , we just suspect $0.2 \text{ W/cm}^2 \ll I_S \ll 100 \text{ W/cm}^2$, the latter value corresponding to the mean intensity previously used in the photodeposition experiments performed in a microchannel. Fortunately, we have enough data at a fixed beam intensity (most cuvette experiments were performed at $I = 0.14 \text{ W/cm}^2$ so that we can already check a scaling based on time and concentration variations). Since these data will eventually be compared to those obtained in microchannel experiments for which the condition

$I \gg I_S$ is verified, we choose $\left(\frac{t}{\tau}\right)_{I \gg I_S} \propto \sqrt{\frac{[MeOH]_0[NP]I}{[Au^{3+}]_0}} \cdot \frac{1}{2} \cdot t$ as the rescaled time.

Then, we plot $\left(\frac{[NP]}{[Au^{3+}]_0}\right)^{1/3} D(t)$ as a function of $\sqrt{\frac{[MeOH]_0[NP]I}{[Au^{3+}]_0}} \cdot \frac{1}{2} \cdot t \propto \left(\frac{t}{\tau}\right)_{I \gg I_S}$ for the whole set of data obtained at $I = 0.14 \text{ W/cm}^2$, thus generalizing what we had already done for the variation of the diameter as a function of $\frac{[Au^{3+}]_0}{[NP]}$ at constant $[MeOH]_0$. The result of the fit is shown in **Figure 3.28**.

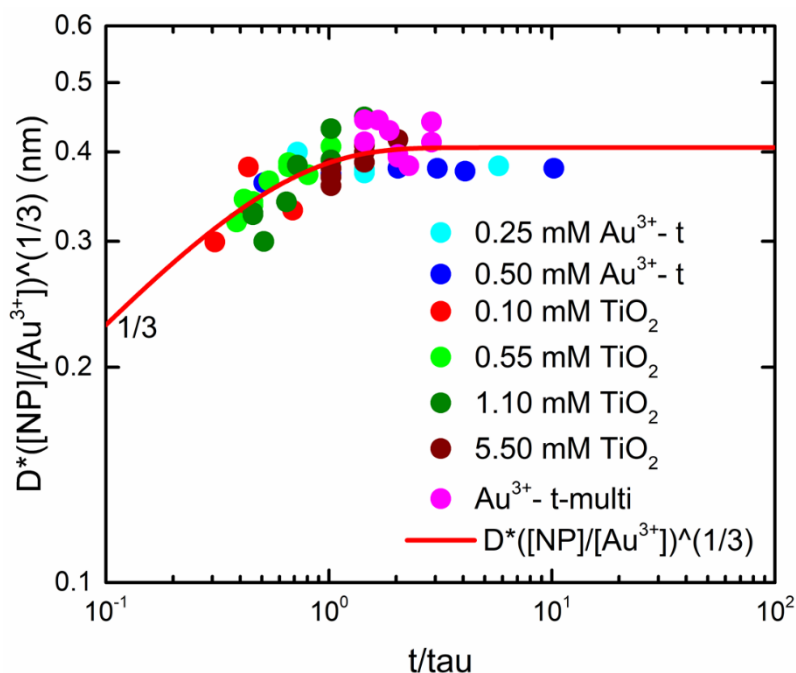


Figure 3.28 Plot of the Au ND diameter $D([NP]/Au^{3+})^{1/3}$ as a function of the rescaled high field time $\left(\frac{t}{\tau}\right)_{I \gg I_S} \propto \sqrt{\frac{[MeOH]_0 [NP] I}{[Au^{3+}]_0}} \cdot \frac{1}{2} \cdot t$ obtained under various conditions. when varying the exposure times (Figure 3.22 and Figure 3.23), and the gold ions concentration (Figure 3.24 and 3.26).

Growth data in $[NP]$, $[Au^{3+}]_0$, and time, do perfectly collapse with the model predictions at constant beam intensity. The whole fit gives $D_\infty \left(\frac{[NP]}{[Au^{3+}]_0}\right)^{1/3} = 0.41$. As $D_\infty \left(\frac{[NP]}{[Au^{3+}]_0}\right)^{1/3} = \left(\frac{8v_{Au}}{\pi\kappa(\theta)Y}\right)^{1/3}$ and the mean yield for the whole data set is $\bar{Y} = 54\%$, we find $\left(\frac{8v_{Au}}{\pi\kappa(\theta)}\right)^{1/3} = 0.33$ in very good agreement with the theoretical value of 0.32.

This curve demonstrates the late-stage convergence of the gold diameter towards a final value that behaves as $D_\infty \propto \left(\frac{[Au^{3+}]_0}{Y[NP]}\right)^{1/3} nm$, where $Y[NP]$ represents the concentration of NHDs. Moreover, the quantitative agreement with the predicted value is demonstrated so that we can even predict $D_\infty = \left(\frac{8v_{Au}}{\pi\kappa(\theta)}\right)^{1/3} \cdot \left(\frac{[Au^{3+}]_0}{Y[NP]}\right)^{1/3} = 3.2285 \times 10^{-1} \times \left(\frac{[Au^{3+}]_0}{Y[NP]}\right)^{1/3} nm$.

3.4.5.7 Chemisorption or physisorption: experiments in beam intensity

We still have to demonstrate which adsorption mechanism is responsible for the

single Au nanodot deposition on the bare TiO₂ nanoparticles. We have the following predicted scaling

$$\left(\frac{[NP]}{[Au^{3+}]_0}\right)^{1/3} D(t) = \left[\frac{8\nu_{Au}}{\pi\kappa(\theta)Y} \cdot f(t/\tau)\right]^{1/3} \text{ where } f(t/\tau \rightarrow \infty) = 1, \text{ and}$$

$$(i) \quad \text{for pure Chemisorption: } \frac{t}{\tau} \propto \sqrt{\frac{[HS]_0[NP]I}{[Au^{3+}]_0}} \cdot t \text{ or,}$$

$$(ii) \quad \text{for pure Physisorption: } \frac{t}{\tau} \propto \sqrt{\frac{[HS]_0[NP]I}{[Au^{3+}]_0}} \cdot \left(\frac{I/I_S}{1+2I/I_S}\right) \cdot t.$$

So, the beam intensity experiments should discriminate them if experiments are performed at $I/I_S \ll 1$ where an intensity variation $\left(\frac{I/I_S}{1+2I/I_S}\right) \approx I/I_S$ should be observed, while saturation is expected $\left(\frac{I/I_S}{1+2I/I_S}\right) \approx \frac{1}{2}$ for $I/I_S \gg 1$.

Curves plotting the variation of the diameter with $\left(\frac{t}{\tau}\right)_{I \gg I_S} \propto \sqrt{\frac{[MeOH]_0[NP]I}{[Au^{3+}]_0}} \cdot \frac{1}{2} \cdot t$ assuming $\left(\frac{t}{\tau}\right)_{I \gg I_S}$ and a pure Chemisorption mechanism obtained at different beam intensities should all collapse together because they are independent of $\left(\frac{I/I_S}{1+2I/I_S}\right)$. Conversely, when plotting the diameter as a function of $\left(\frac{t}{\tau}\right)_{I \gg I_S}$ in the presence of physisorption, data will be overestimated by a factor $\left(\frac{1+2I/I_S}{I/I_S}\right)$ and thus artificially shifted toward a larger $\left(\frac{t}{\tau}\right)_{I \gg I_S}$. The plot is shown in **Figure 3.29**.

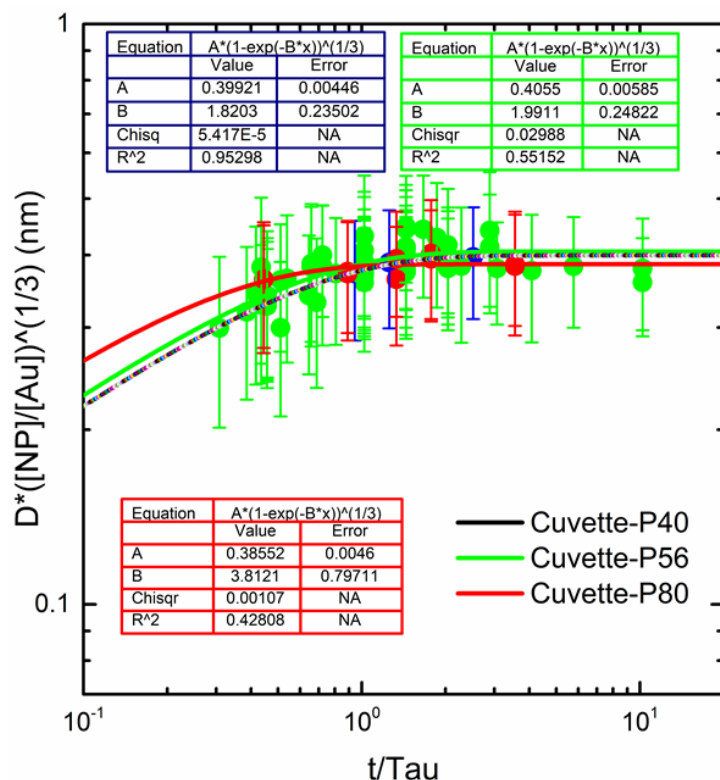


Figure 3.29 Plot of the variation of Au ND diameter $D([NP]/Au^{3+})^{1/3}$ as a function of the rescaled time $\left(\frac{t}{\tau}\right)_{I \gg I_S} \propto \sqrt{\frac{[MeOH]_0[NP]I}{[Au^{3+}]_0}} \cdot \frac{1}{2} \cdot t$ obtained for various powers.

Data in intensity clearly do not merge when rescaled according to the very high field time scale $\left(\frac{t}{\tau}\right)_{I \gg I_S} \propto \sqrt{\frac{[MeOH]_0[NP]I}{[Au^{3+}]_0}} \cdot \frac{1}{2} \cdot t$. Then, the chemisorption should definitively be eliminated as a mechanism of adsorption for the photoreduction of gold ions. Then, we now need to check quantitatively if physisorption can explain these observations.

3.4.5.8 Physisorption mechanism for both cuvette and microchannel experiments

The differences between the cuvette and the microchannels experiments are (i) much longer exposure times (2-32 min vs. <1 s), (ii) much lower beam intensities (0.1-0.2 vs 50-400 W/cm²) in the cuvette versus microchannel. Item (i) gives access to the gold growth toward completion in the cuvette experiments while such a regime is not accessible when using a solution flowing in a microchannel. Item (ii) has a strong influence since the physisorption is driven by the intensity, varying linearly at low

intensities (cuvette) and reaching a constant value at large ones (microchannel). We expect:

$$\left(\frac{[NP]}{[Au^{3+}]_0}\right)^{1/3} D(t) = \left[\frac{8v_{Au}}{\pi\kappa(\theta)Y} \cdot f(t/\tau)\right]^{1/3} \text{ where } f(t/\tau \rightarrow \infty) = 1$$

With the following temporal behaviors:

For experiments in microchannels ($I \gg I_S$), so that $\frac{t}{\tau} = \left(\frac{t}{\tau}\right)_{I \gg I_S} \propto \sqrt{\frac{[MeOH]_0[NP]I}{[Au^{3+}]_0}} \cdot \frac{1}{2} \cdot t$

For experiments in cuvettes ($I \ll I_S$), so that $\frac{t}{\tau} \propto \sqrt{\frac{[MeOH]_0[NP]I}{[Au^{3+}]_0}} \cdot \frac{1}{2} \cdot \left(\frac{2I/I_S}{1+2I/I_S}\right) \cdot t$

We first plot all the data sets as a function of the high field rescaled time $\left(\frac{t}{\tau}\right)_{I \gg I_S} \propto \sqrt{\frac{[MeOH]_0[NP]I}{[Au^{3+}]_0}} \cdot \frac{1}{2} \cdot t$. The fitting result is shown in **Figure 3.30**.

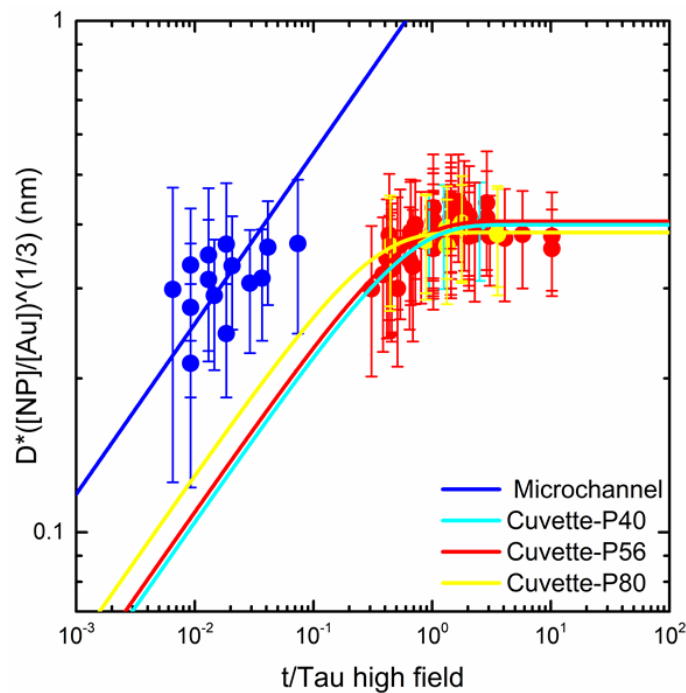


Figure 3.30 Plots of the Au ND diameter $D([NP]/Au^{3+})^{1/3}$ as a function of the rescaled time $\left(\frac{t}{\tau}\right)_{I \gg I_S} \propto \sqrt{\frac{[MeOH]_0[NP]I}{[Au^{3+}]_0}} \cdot \frac{1}{2} \cdot t$ obtained in microchannel and cuvette setups.

On this graph, it appears that the microchannel experiments are shifted toward the smallest $\frac{t}{\tau}$ values as expected. Moreover, they do not show any other beam intensity dependence than that which already appears in $\left(\frac{t}{\tau}\right)_{I \gg I_S}$ (see Bai *et al.*³³); this strongly

suggests that the microchannel experiments are indeed performed at $I \gg I_S$.

We now need to rescale these four data sets according to the physisorption mechanism by trying to find a value of I_S , compatible with the condition $I_{Cuvette} \ll I_S \ll I_{Microchannel}$, that allows merging all the high-field data sets whatever the used beam intensity and setup. A way to do that statistically consists in fitting the amplitude of the 1/3 regime of the growth laws fitted in **Figure 3.30** versus $1/I$; this is not necessary for experiments performed in microchannels as they already belong to this 1/3 power-law regime. Indeed, in the early growth regime, the plots above give us $\left(\frac{[NP]}{[Au^{3+}]_0}\right)^{1/3} D(t) = A \times \left(\frac{t}{\tau}\right)_{I \gg I_S}^{1/3}$, where $A \left(\frac{2I}{I_S}\right)$ is the expected intensity-dependent amplitude. Physisorption predicts $A \left(\frac{2I}{I_S}\right) \propto \left(\frac{2I/I_S}{1+2I/I_S}\right)^{1/3}$ where A is a constant, which can be rewritten as $A \left(\frac{2I}{I_S}\right) \propto \left(1 + \frac{I_S}{2I}\right)^{-1/3}$. In the representation below we attributed to the microchannel experiments, the mean intensity of the range of investigation, *i.e.* 200 W/cm^2 .

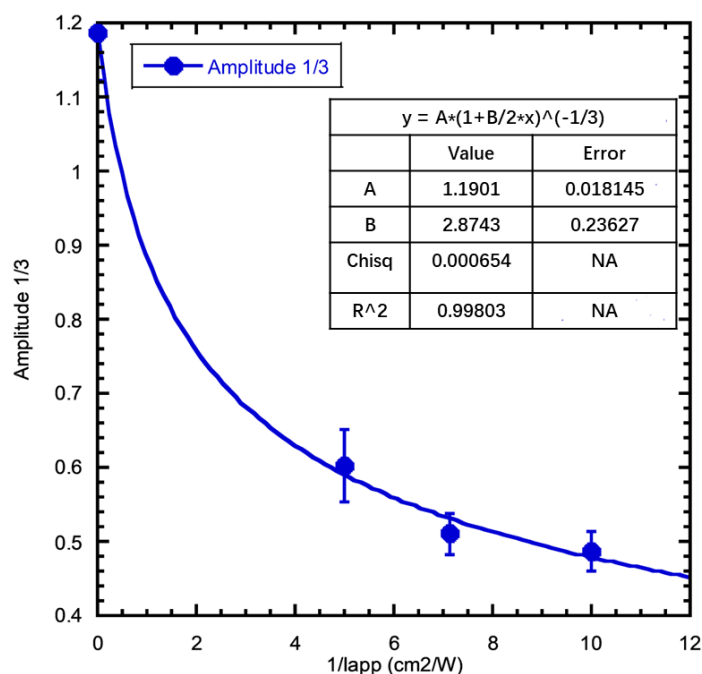


Figure 3.31 Plot of the amplitude $D([NP]/Au^{3+})^{1/3}$ as a function of the $1/I$ obtained in microchannel and cuvette setups.

The plot in **Figure 3.31** shows that the fit of the amplitude as a function of

$\left(1 + \frac{I_S}{2I}\right)^{-1/3}$ is particularly accurate. It gives B, $\bar{I}_S \approx (2.9 \pm 0.2) W/cm^2$.

Eventually, we replotted all the data sets as a function of $\frac{t}{\tau} \propto \sqrt{\frac{[MeOH]_0[NP]I}{[Au^{3+}]_0}} \cdot \frac{1}{2} \cdot \left(\frac{2I/I_S}{1+2I/I_S}\right) \cdot t$ with $I_S = 2.9 W/cm^2$ to get a total collapse of any type of Au@TiO₂ photodeposition experiment performed in high-field conditions (**Figure 3.32**).

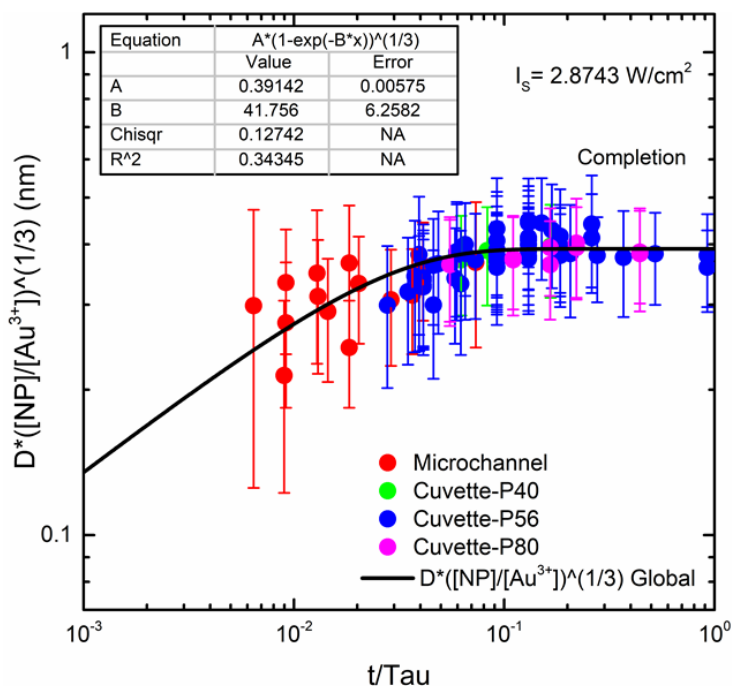


Figure 3.32 Plot of the Au ND diameter $D([NP]/[Au^{3+}])^{1/3}$ as a function of the rescaled time $\left(\frac{t}{\tau}\right) \propto \sqrt{\frac{[MeOH]_0[NP]I}{[Au^{3+}]_0}} \cdot \frac{1}{2} \cdot \left(\frac{2I/I_S}{1+2I/I_S}\right) t$ ($I_S = 2.9 W/cm^2$) obtained in microchannel and cuvette setups.

We indeed observe the collapse in the intensity of all the data sets performed in various conditions that confirms a physisorption mechanism and gives us a coherent value for I_S . This collapse allows us to figure out the whole growth dynamics of an Au ND onto TiO₂ NPs by laser deposition from the 1/3 regime (mainly observed in microchannel experiments) to the crossover toward completion in the high-field condition (shown by cuvette experiments), whatever the concentrations and the intensities.

Finally, the global fit according to the expected dynamics gives $D_{\infty} \left(\frac{[\text{NP}]}{[\text{Au}^{3+}]_0} \right)^{1/3} = 0.39152$. As $D_{\infty} \left(\frac{[\text{NP}]}{[\text{Au}^{3+}]_0} \right)^{1/3} = \left(\frac{8\nu_{\text{Au}}}{\pi\kappa(\theta)Y} \right)^{1/3}$ and the mean yield for the whole data is $\bar{Y} = 57\%$, we find $\left(\frac{8\nu_{\text{Au}}}{\pi\kappa(\theta)} \right)^{1/3} = 0.325$ in excellent agreement with the theoretical value of 0.32.

3.4.6 Conclusion of modeling

- 1) Photodeposition of metals onto TiO₂ is driven by physisorption as illustrated by the global rescaling and the fitting of the experimental gold ND growth versus concentrations and intensity.
- 2) The collapse on a master curve of short- and long-time exposure experiments, allows us to describe the entire dynamics of the growth of a gold ND onto a TiO₂ NP from the regime of exponent 1/3 up to the completion.
- 3) Beyond investigating the dynamics, completion offers us a way to predict the final size in any experimental conditions if we know the yield.

3.5 Conclusion

In this section, experiments dedicated to the photodeposition of Au nanodots onto bare TiO₂ nanoparticles were performed using a UV laser as the light source in a cuvette setup. Au-TiO₂ NHDs were obtained, and TEM and UV-vis spectroscopy were performed to characterize the Au nanodots deposited on the TiO₂ surface. The effect of the TiO₂ and gold precursor concentrations, the laser intensity I , and the exposure time on the photodeposition process were investigated. The gold ND size was well fitted with the prediction value.

We achieved all the initial objectives of this project:

- (i) a close to 100% yield of Au-TiO₂ NHDs was achieved by modifying the concentration of TiO₂ and gold precursor,
- (ii) the adsorption mechanism of methanol and gold precursor on TiO₂ during

- photodeposition was investigated. We showed that the use of a laser beam and the variation of its intensity constituted an elegant way to discriminate between chemi- and physi- sorption. It was illustrated that the photodeposition of metals onto TiO₂ was driven by physisorption by fitting the experimental data,
- (iii) by comparing experimental data obtained in microchannel and cuvette setups, the established modeling showed that all the results did collapse onto a single master curve, offering the possibility to describe the entire dynamics of the Au ND growth on TiO₂ from the 1/3 growth regime up to completion,
 - (iv) the final size of Au NDs can be accurately predicted in particular the growth completion.

3.6 References

1. Ibhaddon, A.; Fitzpatrick, P., Heterogeneous Photocatalysis: Recent Advances and Applications. *Catalysts* **2013**, *3* (1), 189-218.
2. Meng, A.; Zhang, L.; Cheng, B.; Yu, J., TiO₂-MnOx-Pt Hybrid Multiheterojunction Film Photocatalyst with Enhanced Photocatalytic CO₂-Reduction Activity. *ACS applied materials & interfaces* **2018**, *11* (6), 5581-5589.
3. Yoon, S.; Oh, K.; Liu, F.; Seo, J. H.; Somorjai, G. A.; Lee, J. H.; An, K., Specific Metal-Support Interactions between Nanoparticle Layers for Catalysts with Enhanced Methanol Oxidation Activity. *ACS Catalysis* **2018**, *8* (6), 5391-5398.
4. Veziroglu, S.; Obermann, A.-L.; Ullrich, M.; Hussain, M.; Kamp, M.; Kienle, L.; Leißner, T.; Rubahn, H.-G.; Polonskyi, O.; Strunskus, T.; Fiutowski, J.; Es-Souni, M.; Adam, J.; Faupel, F.; Aktas, O. C., Photodeposition of Au Nanoclusters for Enhanced Photocatalytic Dye Degradation over TiO₂ Thin Film. *ACS applied materials & interfaces* **2020**, *12* (13), 14983-14992.
5. Gomathi Devi, L.; Kavitha, R., A Review on Plasmonic Metal-TiO₂ Composite for Generation, Trapping, Storing and Dynamic Vectorial Transfer of Photogenerated Electrons Across the Schottky Junction in a Photocatalytic System. *Applied Surface Science* **2016**, *360*, 601-622.
6. Wenderich, K.; Mul, G., Methods, Mechanism, and Applications of Photodeposition in Photocatalysis: a review. *Chemical reviews* **2016**, *116* (23), 14587-14619.
7. Lee, Y.; Kim, E.; Park, Y.; Kim, J.; Ryu, W.; Rho, J.; Kim, K., Photodeposited Metal-Semiconductor Nanocomposites and Their Applications. *Journal of Materiomics* **2018**, *4* (2), 83-94.
8. Ayati, A.; Ahmadpour, A.; Bamoharram, F. F.; Tanhaei, B.; Manttari, M.; Sillanpaa, M., A Review on Catalytic Applications of Au/TiO₂ Nanoparticles in the Removal of Water Pollutant. *Chemosphere* **2014**, *107*, 163-174.
9. Tanaka, A.; Fuku, K.; Nishi, T.; Hashimoto, K.; Kominami, H., Functionalization of Au/TiO₂ Plasmonic Photocatalysts with Pd by Formation of a Core-Shell Structure for Effective Dechlorination of Chlorobenzene Under Irradiation of Visible Light. *The Journal of Physical Chemistry C* **2013**, *117* (33), 16983-16989.
10. Yang, G.; Ding, H.; Chen, D.; Feng, J.; Hao, Q.; Zhu, Y., Construction of Urchin-Like ZnIn₂S₄-Au-TiO₂ Heterostructure with Enhanced Activity for Photocatalytic Hydrogen Evolution. *Applied Catalysis B: Environmental* **2018**, *234*, 260-267.
11. Singh, J.; Sahu, K.; Satpati, B.; Shah, J.; Kotnala, R.; Mohapatra, S., Facile Synthesis, Structural and Optical Properties of Au-TiO₂ Plasmonic Nanohybrids for Photocatalytic Applications. *Journal of Physics and Chemistry of Solids* **2019**, *135*, 109100.
12. Feil, A. F.; Migowski, P.; Scheffer, F. R.; Pierozan, M. D.; Corsetti, R. R.; Rodrigues, M.; Pezzi, R. P.; Machado, G.; Amaral, L.; Teixeira, S. R., Growth of TiO₂ Nanotube Arrays with Simultaneous Au Nanoparticles Impregnation: Photocatalysts for Hydrogen Production. *Journal of the Brazilian Chemical Society* **2010**, *21*, 1359-1365.
13. Li, W.-C.; Comotti, M.; Schüth, F., Highly Reproducible Syntheses of Active Au/TiO₂ Catalysts for CO Oxidation by Deposition-Precipitation or Impregnation. *Journal of Catalysis* **2006**, *237* (1), 190-196.
14. Rodríguez-Martínez, C.; García-Domínguez, Á. E.; Guerrero-Robles, F.; Saavedra-Díaz, R. O.; Torres-Torres, G.; Felipe, C.; Ojeda-López, R.; Silahua-Pavón, A.; Cervantes-Urbe, A., Synthesis of

Supported Metal Nanoparticles (Au/TiO₂) by the Suspension Impregnation Method. *Journal of Composites Science* **2020**, 4 (3), 89.

15. Zanella, R.; Delannoy, L.; Louis, C., Mechanism of Deposition of Gold Precursors onto TiO₂ During the Preparation by Cation Adsorption and Deposition–Precipitation with NaOH and urea. *Applied Catalysis A: General* **2005**, 291 (1-2), 62-72.

16. Oros-Ruiz, S.; Zanella, R.; López, R.; Hernández-Gordillo, A.; Gómez, R., Photocatalytic Hydrogen Production by Water/Methanol Decomposition Using Au/TiO₂ Prepared by Deposition–Precipitation with Urea. *Journal of hazardous materials* **2013**, 263, 2-10.

17. Huang, J.; He, S.; Goodsell, J. L.; Mulcahy, J. R.; Guo, W.; Angerhofer, A.; Wei, W. D., Manipulating Atomic Structures at the Au/TiO₂ Interface for O₂ Activation. *Journal of the American Chemical Society* **2020**, 142 (14), 6456-6460.

18. Fu, C.; Li, M.; Li, H.; Li, C.; guo Wu, X.; Yang, B., Fabrication of Au Nanoparticle/TiO₂ Hybrid Films for Photoelectrocatalytic Degradation of Methyl orange. *Journal of alloys and compounds* **2017**, 692, 727-733.

19. Luo, S.; Xiao, Y.; Yang, L.; Liu, C.; Su, F.; Li, Y.; Cai, Q.; Zeng, G., Simultaneous Detoxification of Hexavalent Chromium and Acid Orange 7 by a Novel Au/TiO₂ Heterojunction Composite Nanotube Arrays. *Separation and Purification Technology* **2011**, 79 (1), 85-91.

20. Yang, Y.-F.; Sangeetha, P.; Chen, Y.-W., Au/TiO₂ Catalysts Prepared by Photo-Deposition Method for Selective CO Oxidation in H₂ Stream. *International Journal of Hydrogen Energy* **2009**, 34 (21), 8912-8920.

21. Bhardwaj, S.; Dogra, D.; Pal, B.; Singh, S., Photodeposition Time Dependant Growth, Size and Photoactivity of Ag and Cu Deposited TiO₂ Nanocatalyst under Solar Irradiation. *Solar Energy* **2019**, 194, 618-627.

22. Bamwenda, G. R.; Tsubota, S.; Nakamura, T.; Haruta, M., Photoassisted Hydrogen Production from a Water-Ethanol Solution: a Comparison of Activities of Au-TiO₂ and Pt-TiO₂. *Journal of Photochemistry and Photobiology A: Chemistry* **1995**, 89 (2), 177-189.

23. Tanaka, A.; Ogino, A.; Iwaki, M.; Hashimoto, K.; Ohnuma, A.; Amano, F.; Ohtani, B.; Kominami, H., Gold-Titanium(IV) Oxide Plasmonic Photocatalysts Prepared by a Colloid-Photodeposition Method: Correlation Between Physical Properties and Photocatalytic Activities. *Langmuir* **2012**, 28 (36), 13105-11.

24. Kenens, B.; Chamtoury, M.; Aubert, R.; Miyakawa, K.; Hayasaka, Y.; Naiki, H.; Watanabe, H.; Inose, T.; Fujita, Y.; Lu, G.; Masuhara, A.; Uji-i, H., Solvent-Induced Improvement of Au Photo-Deposition and Resulting Photo-Catalytic Efficiency of Au/TiO₂. *RSC Advances* **2016**, 6 (100), 97464-97468.

25. Iliev, V.; Tomova, D.; Bilyarska, L.; Tyuliev, G., Influence of the Size of Gold Nanoparticles Deposited on TiO₂ Upon the Photocatalytic Destruction of Oxalic Acid. *Journal of Molecular Catalysis A: Chemical* **2007**, 263 (1-2), 32-38.

26. Gartner, F.; Losse, S.; Boddien, A.; Pohl, M. M.; Denurra, S.; Junge, H.; Beller, M., Hydrogen Evolution from Water/Alcohol Mixtures: Effective in Situ Generation of an Active Au/TiO₂ Catalyst. *ChemSusChem* **2012**, 5 (3), 530-3.

27. Hidalgo, M. C.; Murcia, J. J.; Navío, J. A.; Colón, G., Photodeposition of Gold on Titanium Dioxide for Photocatalytic Phenol Oxidation. *Applied Catalysis A: General* **2011**, 397 (1-2), 112-120.

28. Deepagan, V. G.; You, D. G.; Um, W.; Ko, H.; Kwon, S.; Choi, K. Y.; Yi, G.-R.; Lee, J. Y.; Lee, D. S.; Kim, K.; Kwon, I. C.; Park, J. H., Long-Circulating Au-TiO₂ Nanocomposite as a Sonosensitizer for ROS-Mediated Eradication of Cancer. *Nano Lett.* **2016**, 16 (10), 6257-6264.

29. Zhou, X.; Qian, K.; Zhang, Y.; Li, D.; Wei, Z.; Wang, H.; Ye, R.; Liu, J.; Ye, B.; Huang, W., Tuning the Size of Photo-deposited Metal Nanoparticles via Manipulating Surface Defect Structures of TiO₂ Nanocrystals. *Chem Commun (Camb)* **2020**, *56* (13), 1964-1967.
30. Yoshida, T.; Misu, Y.; Yamamoto, M.; Tanabe, T.; Kumagai, J.; Ogawa, S.; Yagi, S., Effects of the Amount of Au Nanoparticles on the Visible Light Response of TiO₂ Photocatalysts. *Catalysis Today* **2020**, *352*, 34-38.
31. Sangeetha, P.; Chang, L.-H.; Chen, Y.-W., Preferential Oxidation of CO in H₂ Stream on Au/TiO₂ Catalysts: Effect of Preparation Method. *Industrial & engineering chemistry research* **2009**, *48* (12), 5666-5670.
32. Wang, D.; Bi, Q.; Yin, G.; Wang, P.; Huang, F.; Xie, X.; Jiang, M., Photochemical Preparation of Anatase Titania Supported Gold Catalyst for Ethanol Synthesis from CO₂ Hydrogenation. *Catal. Lett.* **2018**, *148* (1), 11-22.
33. Bai, Q.; Shupyk, I.; Vauriot, L.; Majimel, J.; Labrugere, C.; Delville, M. H.; Delville, J. P., Design of Metal@Titanium Oxide Nano-Heterodimers by Laser-Driven Photodeposition: Growth Mechanism and Modeling. *ACS Nano* **2021**, *15* (2), 2947-2961.
34. Kanie, K.; Sugimoto, T., Shape Control of Anatase TiO₂ Nanoparticles by Amino Acids in a Gel-Sol System. *Chemical Communications* **2004**, (14), 1584-1585.
35. Xu, J.; Li, L.; Yan, Y.; Wang, H.; Wang, X.; Fu, X.; Li, G., Synthesis and Photoluminescence of Well-Dispersible Anatase TiO₂ Nanoparticles. *Journal of colloid and interface science* **2008**, *318* (1), 29-34.
36. Bai, Q. Synthesis of Nano Heterodimers by Laser Photodeposition of Metal Nanodots on TiO₂ Nanoparticles. Université de Bordeaux, 2019.
37. Amendola, V.; Pilot, R.; Frasconi, M.; Maragò, O. M.; Iati, M. A., Surface Plasmon Resonance in Gold Nanoparticles: a Review. *Journal of Physics: Condensed Matter* **2017**, *29* (20), 203002.
38. Reddy, K. M.; Manorama, S. V.; Reddy, A. R., Bandgap Studies on Anatase Titanium Dioxide Nanoparticles. *Materials Chemistry and Physics* **2003**, *78* (1), 239-245.
39. Minero, C., Kinetic Analysis of Photoinduced Reactions at the Water Semiconductor Interface. *Catalysis Today* **1999**, *54* (2-3), 205-216.
40. Bohren, C. F.; Huffman, D. R., *Absorption and Scattering of Light by Small Particles*. John Wiley & Sons: 2008.
41. Dimitrijevic, N. M.; Shkrob, I. A.; Gosztola, D. J.; Rajh, T., Dynamics of Interfacial Charge Transfer to Formic Acid, Formaldehyde, and Methanol on the Surface of TiO₂ Nanoparticles and Its Role in Methane Production. *The Journal of Physical Chemistry C* **2012**, *116* (1), 878-885.
42. Henry, C. R., Growth, Structure and Morphology of Supported Metal Clusters Studied by Surface Science Techniques. *Crystal Research and Technology: Journal of Experimental and Industrial Crystallography* **1998**, *33* (7-8), 1119-1140.
43. Mills, A.; O'Rourke, C.; Moore, K., Powder Semiconductor Photocatalysis in Aqueous Solution: An Overview of Kinetics-Based Reaction Mechanisms. *Journal of Photochemistry and Photobiology A: Chemistry* **2015**, *310*, 66-105.
44. Laidler, K., *Chemical Kinetics*, 1987. *Google Scholar* **1987**, 42.
45. Mueller, R.; Kammler, H. K.; Wegner, K.; Pratsinis, S. E., OH Surface Density of SiO₂ and TiO₂ by Thermogravimetric Analysis. *Langmuir* **2003**, *19* (1), 160-165.
46. Soejima, T.; Tada, H.; Kawahara, T.; Ito, S., Formation of Au Nanoclusters on TiO₂ Surfaces by a Two-Step Method Consisting of Au (III)-Complex Chemisorption and Its Photoreduction. *Langmuir* **2002**,

18 (11), 4191-4194.

47. Clarizia, L.; Di Somma, I.; Onotri, L.; Andreatti, R.; Marotta, R., Kinetic Modeling of Hydrogen Generation Over Nano-Cu (s)/TiO₂ Catalyst Through Photoreforming of Alcohols. *Catalysis Today* **2017**, *281*, 117-123.

48. Matthews, R. W., Kinetics of Photocatalytic Oxidation of Organic Solutes Over Titanium Dioxide. *Journal of Catalysis* **1988**, *111* (2), 264-272.

49. Vohra, M.; Selimuzzaman, S.; Al-Suwaiyan, M., NH₄⁺-NH₃ Removal from Simulated Wastewater Using UV-TiO₂ Photocatalysis: Effect of Co-Pollutants and pH. *Environmental technology* **2010**, *31* (6), 641-654.

50. Monllor-Satoca, D.; Gómez, R.; González-Hidalgo, M.; Salvador, P., The "Direct-Indirect" Model: An Alternative Kinetic Approach in Heterogeneous Photocatalysis Based on the Degree of Interaction of Dissolved Pollutant Species with the Semiconductor Surface. *Catalysis Today* **2007**, *129* (1-2), 247-255.

51. Emeline, A.; Ryabchuk, V.; Serpone, N., Dogmas and Misconceptions in Heterogeneous Photocatalysis. Some Enlightened Reflections. *The Journal of Physical Chemistry B* **2005**, *109* (39), 18515-18521.

52. Dolgikh, Y. K.; Ryabchuk, V.; Basov, L.; Grenishin, S., Photoinduced Oxygen Adsorption of AgBr Crystals at 77 K. *Reaction Kinetics and Catalysis Letters* **1986**, *32* (1), 45-50.

Chapter 4

Photodeposition of Ag, and Pd Nanodots on TiO₂ Nanoparticles

Table of contents

Chapter 4.....	131
Photodeposition of Ag, and Pd Nanodots on TiO ₂ Nanoparticles.....	131
4.1 Introduction to the photodeposition of Ag NDs on TiO ₂ NPs.....	135
4.1.1 Experimental method.....	138
4.1.2 Results and discussion.....	138
4.1.3.1 The effects of the hole scavenger on Ag photodeposition.....	139
4.1.3.2 The effects of the exposure time on Ag photodeposition.....	140
4.1.3.3 The effects of the laser power on the Ag photodeposition.....	143
4.1.3.4 The effects of PVP on the Ag photodeposition.....	146
4.1.3.5 Different silver precursors.....	147
4.1.4 Conclusion.....	150
4.2 Introduction to the photodeposition of Pd NDs on TiO ₂ NPs.....	150
4.2.1 Experiment method.....	152
4.2.2 Result and discussion.....	153
4.2.2.1 The effects of the hole scavenger on the Pd photodeposition.....	153
4.2.2.2 The respective influence of HNO ₃ and HCl on the Pd photodeposition.....	154
4.2.2.3 The effects of the metal precursor on the Pd photodeposition.....	156
4.2.2.4 The effects of the exposure time on the Pd photodeposition.....	158
4.2.2.5 The effects of TiO ₂ and Pd ²⁺ concentrations on the Pd photodeposition ..	160
4.2.3 Conclusion.....	163
4.3 Laser deposition of Pd and Ag NDs onto TiO ₂ NPs in the cuvette and microchannel setups from growth to completion.....	164
4.3.1 Overall analysis of the experiments on Silver photodeposition.....	168
4.3.2 Overall analysis of the experiments on Palladium photodeposition.....	172
4.4 Conclusion.....	177
4.5 References.....	179

4.1 Introduction to the photodeposition of Ag NDs on TiO₂ NPs

The noble metal, Ag, is a promising candidate for extensive applications because of its low cost, inherent antibacterial activity, and simple preparation methods. Among hybrid metal-semiconductor systems, Ag-TiO₂ nanoparticles have attracted substantial attention because they combine the advantages of silver, a nontoxic, remarkable catalytic metal with size- and shape-dependent optical properties, and TiO₂, a photoactive and low-cost semiconductor material. Ag has been introduced onto the TiO₂ surface in different ways including physical vapor deposition¹, chemical reduction², deposition-precipitation,³ and photo-deposition methods.⁴⁻⁵

Photodeposition is one of the simplest methods to synthesize noble metal/semiconductor nanocomposites. In contrast to most other methods that require high temperatures, additional redox agents, or multi-step processing, the photo-induced reduction requires only the irradiation of a light source. Furthermore, the size of metal NPs can be controlled by adjusting the concentration of precursor, irradiating time, and irradiating power.

In 1971, Fleischauer *et al.*⁶ proposed a simple reaction scheme for the photoreduction of Ag⁺ ions on both TiO₂ and ZnO surfaces. They assumed an electron transfer from the conduction band, under flat band conditions, to the adsorbed Ag⁺ ions, without the intervention of the deep-trapped electron states. Then, in 1981, Hada *et al.*⁷ studied the reduction of Ag⁺ by irradiation with a 365 nm light on TiO₂ single-crystal surface in aqueous solutions containing AgNO₃. They proposed that some conduction-band electrons, produced in the TiO₂ by irradiation, transferred to the Ag⁺ adsorbed on the TiO₂ surface. Afterward, Ohtani and co-workers⁸⁻⁹ suggested that the significant pH dependence of the photocatalytic activity of TiO₂ suspended in AgNO₃ solution was correlated with the pH-dependent adsorption of Ag⁺ on the TiO₂ surface. They inferred the involvement of Ag-O-Ti surface states formed by the “chemisorption” of Ag⁺ at specific active sites on the TiO₂ surface. The initial studies on Ag

photodeposition on semiconductors mainly focused on mechanisms but rarely involved morphology, distribution, or size of Ag nanodots (NDs) which, however, play a significant role in photocatalytic activity.

Chen and coworkers¹⁰ synthesized silver-decorated TiO₂ nanoparticles (NPs) (Ag@TiO₂) by photoreduction of Ag⁺ species in an EG-ethanol solution in the presence of TiO₂ (P25) NPs. Ag nanoclusters (NCs) with a size range of 1 to 3 nm were uniformly anchored on the surface of the TiO₂ NPs, and the distribution densities of Ag NCs increased with increasing amounts of Ag⁺. When degrading Rhodamine B under visible light, they found that the photocatalytic activity of the as-synthesized Ag@TiO₂ nanocomposites depended on the Ag-loading density. Ag@TiO₂ photocatalysts with ~1% Ag NCs exhibited the best photocatalytic performance with a high-rate constant. In addition, Aulakh *et al.*,¹¹ using a Hg arc light source, reported the deposition of Ag on commercially available P25-TiO₂ in an aqueous solution with 2-propanol as a hole scavenger. They found that Ag NPs size, distribution, and oxidation state also depended on the deposition time.

Photodeposition was also performed in organic media containing TiO₂ particles capped with ligands. Dinh *et al.*¹² reported a facile photodeposition technique to deposit, in toluene, Ag clusters on TiO₂ particles capped with oleic acid. Their method was used to control both the population of Ag clusters by tuning the amount of oleic acid added to the synthesis solution and their size by the irradiation time. The obtained hybrid Ag-TiO₂ hybrid particles exhibited very high performance in photocatalytic degradation of Methyl blue. Lu and co-authors¹³ reported the synthesis of Ag-TiO₂ nanorod composites, with a single Ag ND attached to one anatase TiO₂ nanorod capped by oleic acid. They precisely controlled the size of the Ag ND deposited on the TiO₂ nanorods, by varying either the irradiation time or the amount of alcohol additive. They suggested that the formation of such unique hybrid structures could be attributed to an interesting photoinduced ripening process, in which the photogenerated oxidative species dissolved small Ag clusters. The photoexcited electrons could then

reduce the ions again and redeposit them back onto a larger and more stable Ag particle (as shown in **Figure 4.1**). These two studies were performed in nonpolar solvent (toluene) using hydrophobic surfactant-capped TiO₂ NPs.

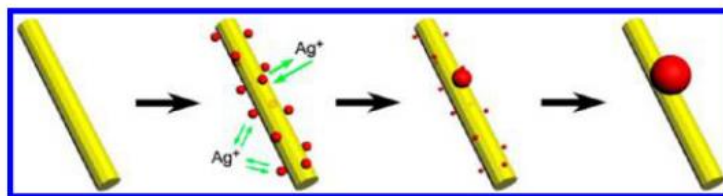


Figure 4.1 The scheme of the proposed formation mechanism of Ag-TiO₂ nanorod composites.¹³

These studies have shown successful synthesis of heterodimer structures with noble metal and TiO₂, but the synthesis was carried out in nonaqueous media. More importantly, the organic ligands employed may affect the optical properties of the particles. Another serious limitation is that stabilizers can lead to loss of catalytic activity to a great extent because they can block many active sites.

In most papers, a UV lamp is commonly used as a light source for photoreduction.^{10, 13-16} However, the exposure time for the photodeposition process using such UV lamps can take hours because of power intensity limitations, and loaded metallic dots usually have a small size, typically < 3 nm.^{10, 17-18} It is then very challenging to study the effects of the metal size and shape on the photocatalytic properties of products, and first to have a control on these metal size and shape.

This is why, in this chapter, photodepositions of Ag particles on TiO₂ will be performed in aqueous solutions with a high-energy UV laser as a light source. The investigation of the growth of Ag will be performed by controlling exposure time, and laser intensities. Two metal precursors, AgNO₃ and the so-called Tollens' reagent ([Ag(NH₃)₂]OH) will be used. The effects of methanol and sodium formate as hole scavengers on the Ag deposition will be studied. The role of ligand, PVP, on the deposition will be discussed. Modeling of the data will also be performed.

4.1.2 Experimental method

Almost the same method as for the Au deposition was used, the pH 3.3 nitric acid solution containing TiO₂ substrate, hole scavengers (methanol or HCOONa), and silver precursor (AgNO₃) is bubbled with Ar for around 10 min. The laser exposure area is designed to be circular of 1 cm in diameter, thus the 1 mL of reaction solution present in a 1 cm-wide PMMA cuvette can be fully exposed to laser light. The cuvette is capped, and the solution is continuously stirred at a speed of 300 rpm by a magnetic stirrer. We adjust the power and exposure time according to the experimental needs. All experiments are performed at room temperature.

In addition to AgNO₃, we also tried the Tollens' reagent as a silver precursor to investigate photodeposition in a basic solution. The preparation of the Tollens' reagent was performed as follows:¹⁹ 520 μ L aqueous ammonia (30%) was added into 500 μ L AgNO₃ solution (0.5 M), followed by 325 μ L of NaOH solution (3 M). Water was added to reach a final volume of 25 mL. This stock solution contained about 10 mM of [Ag(NH₃)₂]OH and 0.4 mM free NH₃·H₂O, pH = 11.5.

The TEM grid preparation was the same as previously described, (see Chapter 3.2.2 for more details). The size distribution and yields were estimated on an average of at least 300 TiO₂ NPs.

4.1.3 Results and discussion

Previously, Bai *et al.*,⁵ in our group reported on the synthesis of Ag-TiO₂ nanoheterodimers (NHDs) by laser-driven photodeposition in a microfluidic setup. This microfluidic setup allows working at a very high beam intensity (430 W/cm²) by setting a very small beam waist. This resulted in the formation of Ag NDs with a diameter larger than 14 nm in less than a second. They synthesized high-quality Ag-TiO₂ NHDs and built a growth model. However, the flow of the solution within the microchannel prevented investigations of the late-stage growth of the metal NDs.

In this chapter, we planned to synthesize the Ag-TiO₂ NHDs by photodeposition in

a cuvette setup to reduce the photon flux and thus slow down the reaction rate. The effects of numerous parameters, e.g., hole scavenger (HS), exposure time, laser intensity, and nature of the precursor on the photodeposition process were investigated in detail. In addition, we also performed some deposition in the presence of PVP used as a colloidal stabilizing agent.

4.1.3.1 The effects of the hole scavenger on Ag photodeposition

Here we checked the role of different hole scavengers (methanol, and HCOONa). We chose to keep all the other parameters identical and as follows, [TiO₂] = 5.5 mM, [Ag⁺] = 2 mM, pH = 3.3, exposure time is 320 s and applied power is 28.05 mW. The effect of the hole scavenger, either methanol (50 vol. %) or HCOONa (2 mM) is investigated. The TEM images and the size distributions of Ag NDs are shown in **Figure 4.2**.

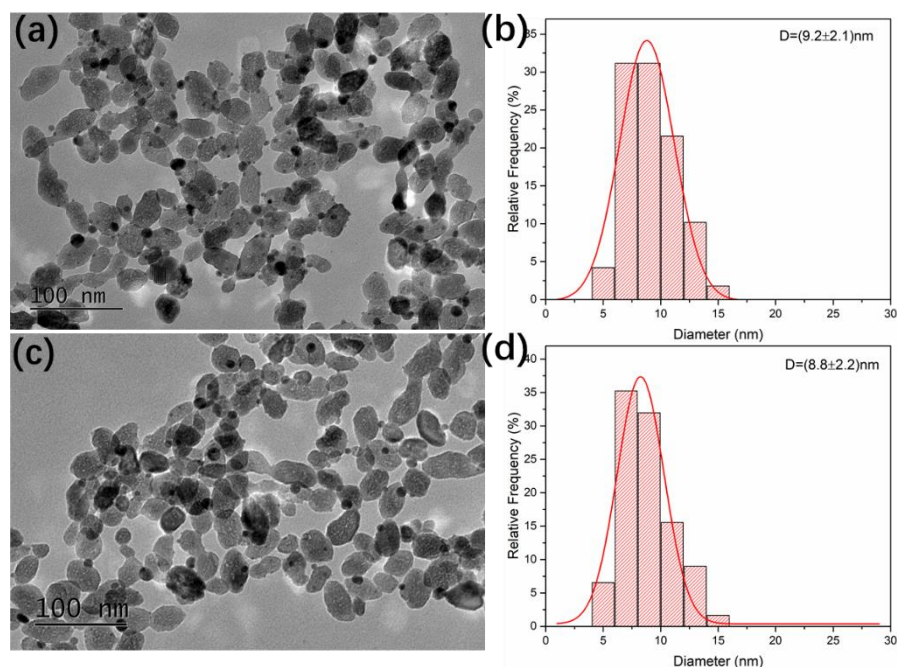


Figure 4.2 TEM images of Ag-TiO₂ NHDs synthesized using different hole scavengers. (a) methanol, (c) HCOONa and their corresponding size distributions (b, d). Note that the size of tiny dots (< 5 nm) is not taken into account in the histogram.

With methanol or HCOONa as hole scavengers, the size of Ag NDs is identical, around 9 nm, and the yields are 37% and 41%, respectively. The difference in hole scavenging comes from the silver particle distributions. In the case of methanol, in addition to the large silver ND (9 nm), much tinier Ag nanodots with a size ranging from 1 to 4 nm appear on the TiO₂ NPs, resulting in a bi-modal distribution of the silver particles. However, when HCOONa is used, most of the structures are of the heterodimer type, with one Ag ND per TiO₂ NP, although there are a few smaller Ag NDs. HCOONa is a more reliable choice for a single dot Ag deposition, while 50 vol. % methanol seems excessive here though it is effective when depositing Au in chapter 3.

In a short conclusion, in the chosen conditions, 37% and 41% of TiO₂ NPs were decorated with Ag particles ($D > 5$ nm) using methanol or HCOONa as hole scavengers, respectively. However, there are some tiny Ag NDs deposited on the TiO₂ surface which is detrimental for synthesizing Ag-TiO₂ NHDs in the case of methanol as a hole scavenger. In contrast, the result is better when using HCOONa as the hole scavenger.

4.1.3.2 The effects of the exposure time on Ag photodeposition

Here we used HCOONa as a hole scavenger and fixed the applied power at 56.1 mW, [AgNO₃] = 2 mM and [HCOONa] = 2 mM, and varied the exposure time. The TEM results concerning the resulting Ag-TiO₂ NHDs are illustrated in **Figure 4.3**.

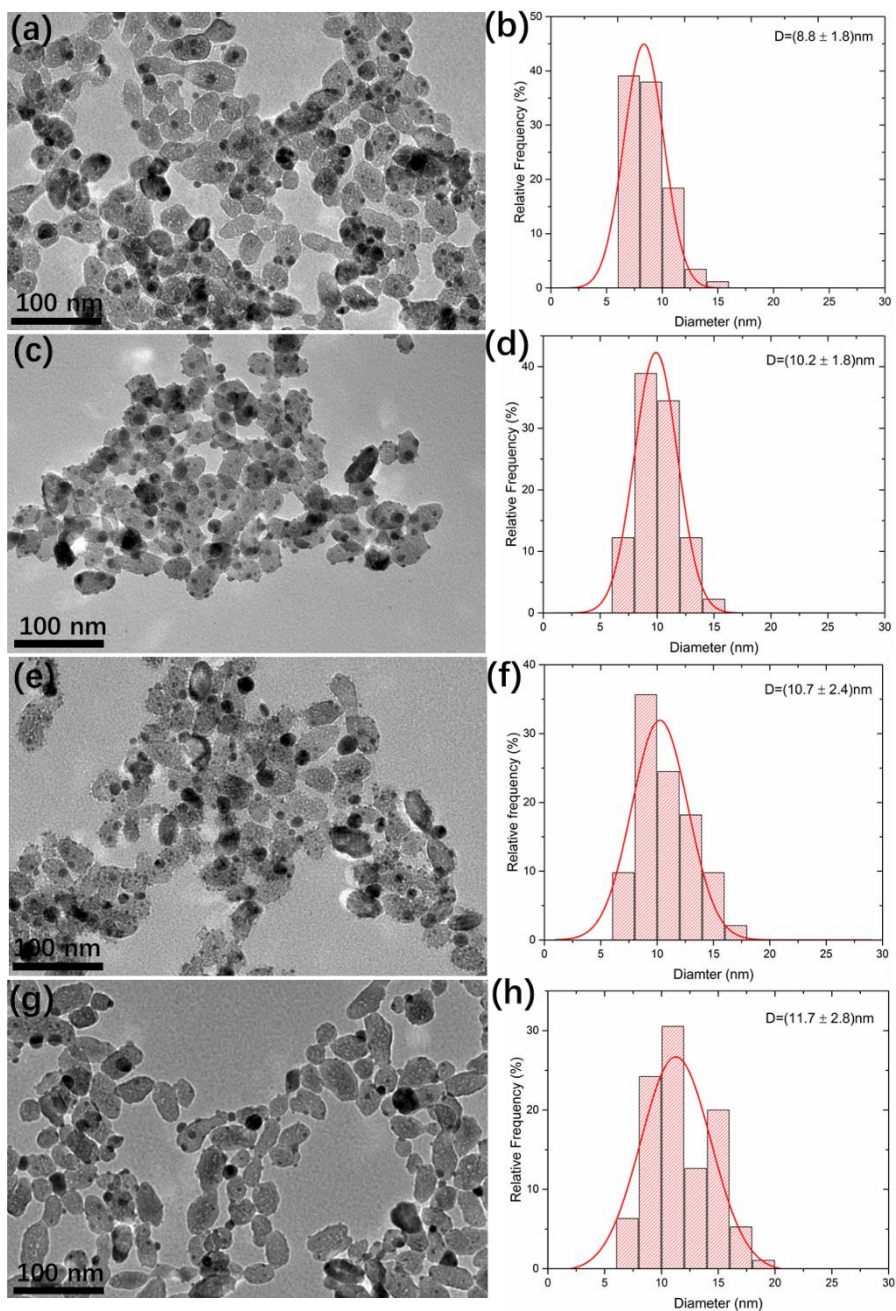


Figure 4.3 TEM images and size distributions of Ag-TiO₂ NHDs synthesized at different exposure times. (a) 160 s, (c) 400 s, (e) 800 s and (g) 1200 s and their corresponding size distribution (b, d, f and h). Experimental conditions: [TiO₂] = 5.5 mM, [AgNO₃] = 2 mM, hole scavenger [HCOONa] = 2 mM, applied power is 56.1 mW.

The variation of the Ag diameter, as well as the NHDs yield with various exposure times and the expected diameters when assuming a yield of 100% for comparison, are shown in **Table 4.1** and **Figure 4.4 (a)**.

Table 4.1 Data of Ag size prepared at different exposure times. ^a Size of tiny dots (<5 nm) is not taken into account. ^b The proportion of TiO₂ particles decorated with Ag nanodot of diameter larger than 5 nm. ^c The value is calculated assuming the NHDs yield of Ag-TiO₂ is 100% and 100% of the AgNO₃ is consumed (see Appendix 1.3). Experimental conditions: [TiO₂] = 5.5 mM, [AgNO₃] = 2 mM, hole scavenger [HCOONa] = 2 mM, applied power is 56.1 mW.

Power (mW)	Exposure time(s)	Ag diam. (SD) (nm) ^a	NHDs yield (%) ^b	Expected Ag diam. (nm) ^c
56.1	160	8.8(1.8)	12	15
56.1	400	10.2(1.8)	20	15
56.1	800	10.7(2.4)	38	15
56.1	1200	11.7(2.8)	25	15

The diameter of the Ag NDs increases with increasing exposure times. However, there are plenty of tiny Ag particles (< 5 nm) on each TiO₂ and the NHDs yields are all very low. For a long exposure time of 1200 s, it seems the number of tiny particles tends to decrease again as compared to shorter times which suggests a ripening process.¹²

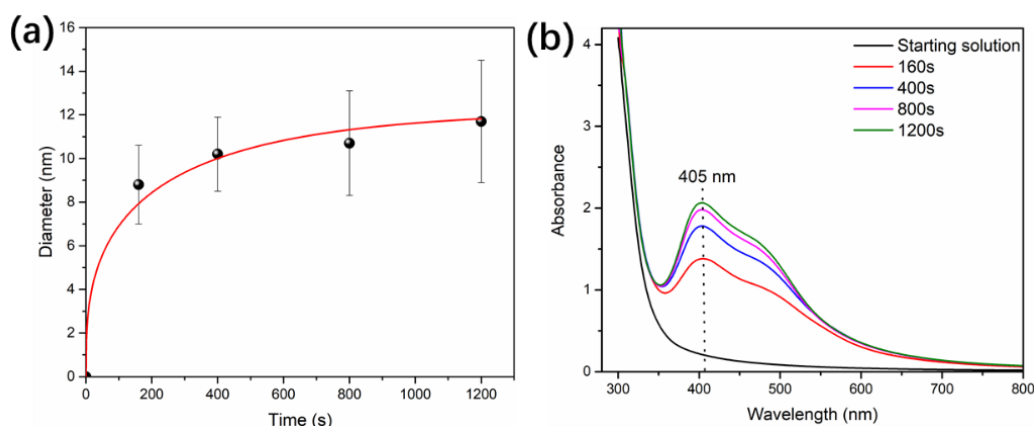


Figure 4.4 (a) Variation of the Ag NDs size with the exposure time. (b) UV-vis spectra of Ag-TiO₂ at different exposure times. The starting solution is the reaction solution before illumination by laser. Experimental conditions: [TiO₂] = 5.5 mM, [AgNO₃] = 2 mM, hole scavenger [HCOONa] = 2 mM, applied power is 56.1 mW.

The UV-vis spectroscopy (**Figure 4.4 (b)**) shows a characteristic band centered at 405 nm corresponding to the surface plasmon resonance of Ag NDs; and its intensity becomes more pronounced with the exposure time, indicating that Ag NDs are formed during the photodeposition process.

In addition to this major band at 405 nm, there is a broad shoulder in the range of

450–500 nm; some authors ascribed this to the near-field coupling between the adjacent Ag particles on each TiO₂ particle (when they are present).^{12, 20} It can also simply be attributed to the contribution of bigger Ag NDs, also illustrated by the increase of the size distribution, as shown in the histograms in **Figure 4.3**.

To conclude, the Ag size increases with the exposure time while the number of small Ag NDs decreases possibly resulting from a ripening process. The UV-vis spectra confirm the presence of Ag particles after photodeposition. Moreover, Bai⁵ performed other XPS and HRTEM characterizations in their work and confirmed the formation of metallic Ag. We did not estimate the necessity to redo these experiments.

4.1.3.3 The effects of the laser power on the Ag photodeposition

Here we turn to the effect of the laser power on the photodeposition of Ag on the TiO₂ surface. From the above results, we did not get nice results (low yield, multi Ag dots) whatever the power (28.05 mW or 56.1 mW). Since we have mentioned that Bai *et al.*⁵ obtained high yields of NHDs using a microfluidic setup with very high power intensity I (50–400 W/cm²), we undertook to vary the applied powers from 88 to 180 mW ($I = 0.22 - 0.46$ W/cm²), where 180 mW is close to the maximum power available with our laser for the cuvette setup. The exposure time was fixed at 4 min (240 s). The TEM results of Ag-TiO₂ are shown in **Figure 4.5**.

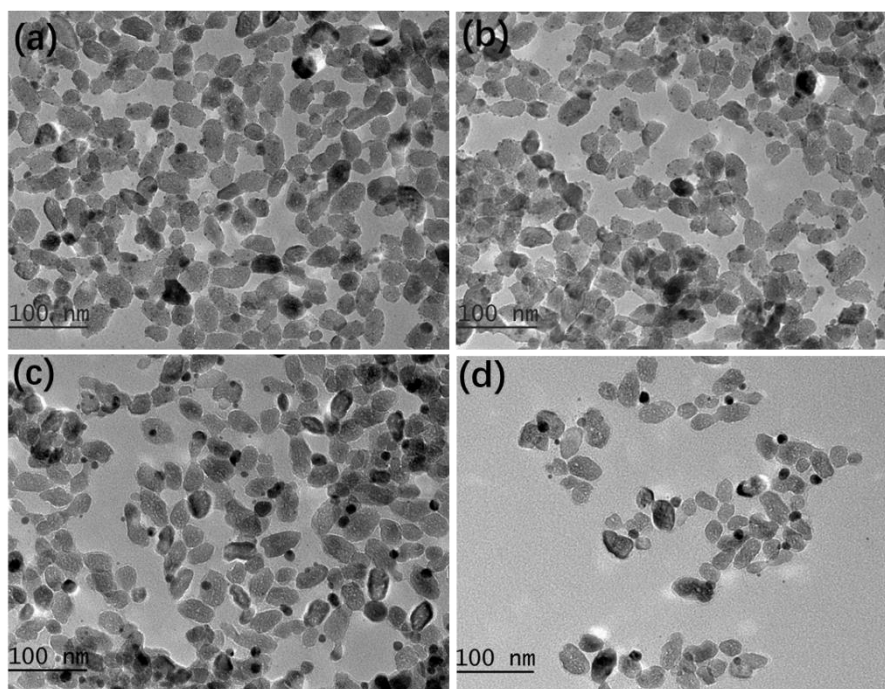


Figure 4.5 TEM images of Ag-TiO₂ NHDs synthesized at different applied powers. (a) 88 mW, (b) 100 mW, (c) 140 mW and (d) 180 mW. Experimental conditions: [TiO₂] = 5.5 mM, [AgNO₃] = 0.5 mM, 50 vol.% methanol as a hole scavenger, exposure time of 4 min.

For applied powers of 88 or 100 mW, there are many tiny NDs on each TiO₂ particle, and a few Ag particles larger than 5 nm are present. These tiny Ag NDs decreased significantly while a single big Ag particle per TiO₂ appeared for powers of either 140 or 180 mW. The mean diameter of Ag was 10.5 (2.1) and 11.1 (2.1) nm at 140 and 180 mW with 38% and 31% yields, respectively. High powers of 140 and 180 mW can more efficiently generate electrons in a short time and promote the formation of big Ag particles. As mentioned in part 4.1.3.1, 50 vol % methanol is excessive for Ag deposition resulting in multi Ag nanodots. However, when the light intensity is very high, a large number of electrons are generated instantly, and the Ag NPs will grow quickly avoiding the multi-site nucleation.

As shown in chapter 3, paragraph 3.3.3, the NHDs yield can be significantly improved by decreasing the concentration of TiO₂. Thus, we reduced the concentration of TiO₂ 5 times, from 5.5 to 1.1 mM, and varied the exposure times while fixing the other parameters. Results based on TEM data are shown in **Figure 4.6** and **Table 4.2**.

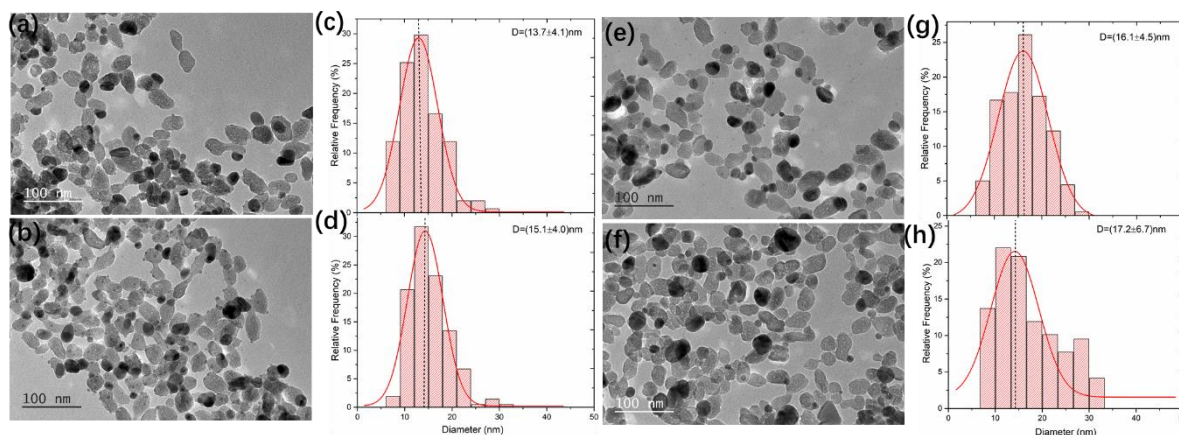


Figure 4.6 TEM images and size distributions of Ag-TiO₂ synthesized at different exposure times. (a) 4 min, (b) 8 min and (e) 16 min and (f) 64 min and their corresponding size distributions (c, d, g and h). Experimental conditions: [TiO₂] = 1.1 mM, [AgNO₃] = 0.5 mM, 50 vol.% methanol as a hole scavenger, applied power of 56.1 mW.

For exposure times of 4 and 8 min, it is clear that there are some tiny Ag particles on the TiO₂ as indicated in TEM images (**Figure 4.6**). Most of the tiny particles disappeared with increasing time up to 64 min. Moreover, the diameter of the Ag particles increased gradually from 13.7 to 17.2 nm with a similar NHDs yield (~ 40%). This phenomenon could be explained by a ripening process with the tiny particles being consumed to form the big particles along with the exposure time. Lu *et al.*¹³ have synthesized Ag-TiO₂ nanorod composites, each of which containing a single Ag nanoparticle attached to one TiO₂ nanorod and they suggested that the formation of such unique hybrid structures could be attributed to the photoinduced ripening process, in which the photogenerated oxidative species dissolved the small Ag particles and then the photoexcited electrons reduced the ions and redeposited them back onto a larger and more stable Ag ND.

Table 4.2 Data of Ag size and NHDs yield of Ag-TiO₂ prepared at different exposure times.

Power (mW)	Illumination time (min)	Ag diam. (SD) (nm)	NHDs yield (%)	Estimated Ag diam. (nm) ^a
56.1	4	13.7(4.1)	42	21.4
56.1	8	15.1(4.0)	41	21.6
56.1	16	16.1(4.5)	46	20.8
56.1	32	17.2(5.4)	42	21.4
56.1	64	17.2(6.7)	40	21.8

^a The value is calculated based on the NHDs yield of Ag-TiO₂ obtained by experiments and the assumption that the AgNO₃ is 100% consumed (see Appendix 1.3).

The NHDs yield is still low even if we work with a lower concentration of TiO₂. In addition, as shown in **Figure 4.7**, the Ag NDs diameter grows between 0 and 16 min and reaches a plateau with a stable diameter (~ 17 nm) which corresponds more or less to the theoretical value (21 nm) given the SD and the large size distribution (**Figure 4.6**).

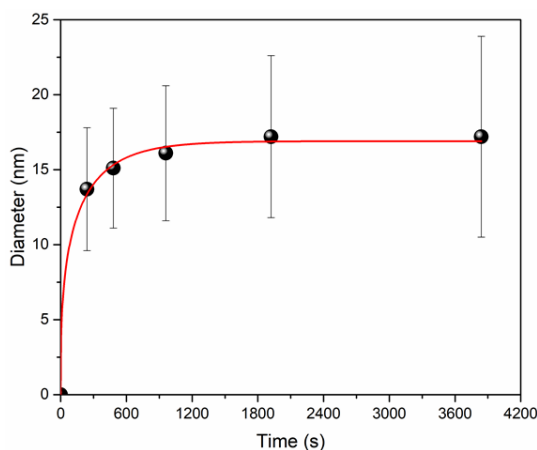


Figure 4.7 Size of Ag nanodots on TiO₂ under different exposure times. The red curve is a fit according to the modeling described below. Experimental conditions: [TiO₂] = 1.1 mM, [AgNO₃] = 0.5 mM, 50 vol.% methanol as a hole scavenger, applied power of 56.1 mW.

4.1.3.4 The effects of PVP on the Ag photodeposition

It is well known that ligands are sometimes necessary to stabilize nanoparticles in a colloidal state during their synthesis. Here, Polyvinylpyrrolidone (PVP) is used as a stabilizer in the photodeposition of Ag NDs on the surface of TiO₂. The effects of PVP on the photodeposition are studied while depositing Ag NDs with and without PVP. The results are shown in **Figure 4.8**.

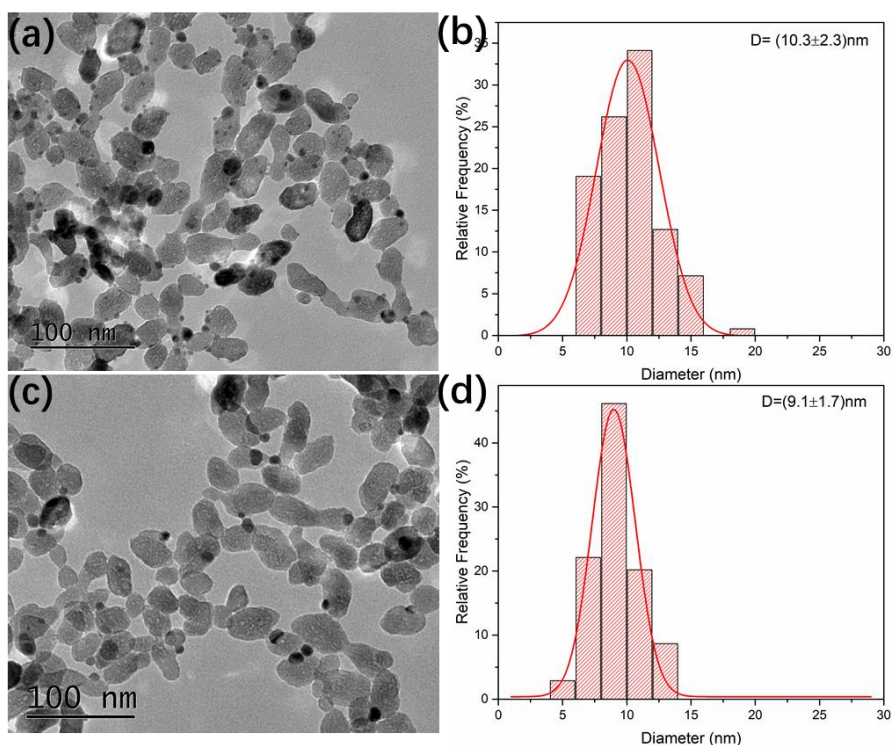


Figure 4.8 TEM images and size distributions of Ag-TiO₂ NHDs synthesized without (a) and with (c) PVP and their corresponding size distributions (b and d). Experimental conditions: [TiO₂] = 5.5 mM, [AgNO₃] = 2 mM, [PVP, 55k] = 1mg/mL, 50 vol.% methanol as a hole scavenger, applied power of 56.1 mW, exposure time of 4 min. Note that the size of tiny dots (< 5 nm) is not taken into account in the histogram.

As we can see in **Figure 4.8**, in the presence of PVP, the size of the Ag NDs (9.1 nm) is smaller than that of the NDs without PVP (11.3 nm), while their yields are very close with 37% and 39%, respectively. The obvious advantage of PVP is the absence of tiny silver NDs on the TiO₂ surface. PVP then exhibits a protective and stabilizing effect and leads to the homogenous formation of Ag particles on the surface of TiO₂. More experiments are needed to understand the influence of this stabilizer.

4.1.3.5 Different silver precursors

In previous experiments, we conducted the photodeposition in acidic media (pH 3.3) so that the TiO₂ was partially positively charged (TiO₂ ZPC 6.5) and colloidally stable. However, the silver precursor we used, Ag⁺, is also positively charged which is not beneficial for its sorption on the surface of TiO₂ considering the fundamental state with

no illumination.

On the other hand, the so-called Tollens' reagent, with a chemical formula $\text{Ag}(\text{NH}_3)_2\text{OH}$, is an alkaline solution of ammoniacal silver nitrate used to test the presence of aldehydes. This reagent consists of a solution of silver nitrate, ammonia, and some sodium hydroxide (to maintain a basic pH of the reagent solution). Silver ions in the presence of hydroxide ions come out of the solution as a brown precipitate of silver oxide, Ag_2O . This precipitate dissolves in aqueous ammonia, forming the diamine silver(I) ion, $[\text{Ag}(\text{NH}_3)_2]^+$. In this section, this Tollens' reagent was used as a silver precursor and photodeposition experiments were performed in basic conditions.

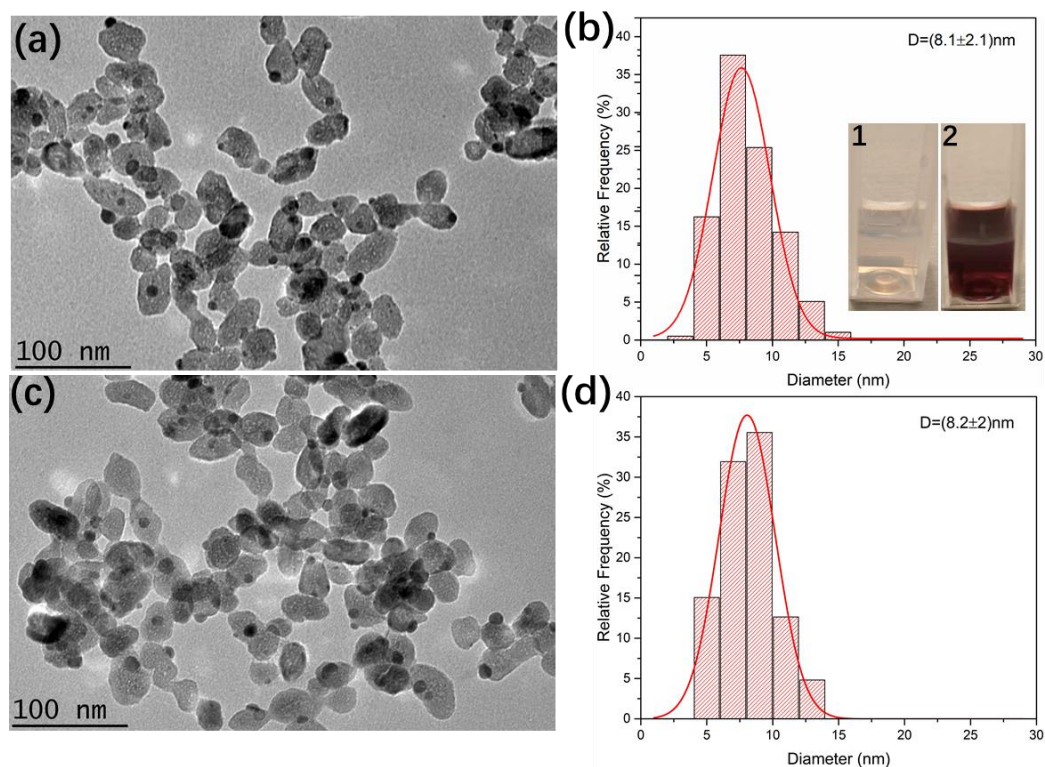


Figure 4.9 TEM images and size distributions of Ag-TiO₂ synthesized using the Tollens' reagent with HCOONa (a) and H₂O (c) as hole scavengers and their corresponding size distributions (b and d). The inserted photos 1 and 2 show the reaction solution before and after the photodeposition process. Experimental conditions: $[\text{TiO}_2] = 5.5 \text{ mM}$, $[\text{Ag}^+] = 0.5 \text{ mM}$, $[\text{HCOONa}]$ is 0 or 0.5 mM, applied power of 56.1 mW, exposure time of 4 min.

The detailed recipe to prepare the Tollens' reagent is given in the experimental section (4.1.2). The pH of the mixture solution containing H₂O, HCOONa, and Tollens' reagent is around 11.5. Under this basic condition, the opposite charges of the TiO₂

surface and $[\text{Ag}(\text{NH}_3)_2]^+$, are beneficial for the ion Ag^+ adsorption on the TiO₂ surface thanks to Coulombic attractions. The mixture solution (H₂O, Tollens' reagent, and methanol) changed immediately from colorless to grey when we tried to use methanol as a hole scavenger, which confirmed that $[\text{Ag}(\text{NH}_3)_2]^+$ ions were more than easily reduced to Ag in this condition. Thus, methanol was discarded. The photodeposition results were compared for HCOONa and H₂O itself as hole scavengers, as shown in **Figure 4.9**. The formation of the silver NPs was preliminarily confirmed by the change of color of the reaction solution (photos 1 and 2) from colorless to deep red.²¹⁻²² Whatever the hole scavenger, HCOONa, or H₂O, the Ag NDs diameters and Ag-TiO₂ NHDs yields were very close: 8.1 and 8.2 nm, 58 and 61% respectively. Nonetheless, the NHDs yield (61%) was significantly improved using the Tollens' reagent compared to AgNO₃ (41%).

To further improve the NHDs yield, the concentration of TiO₂ was reduced to 1.1 mM. The NHDs yield of Ag-TiO₂ (TiO₂ particles decorated with Ag NDs of diameter larger than 5 nm) was improved to 90% (**Figure 4.10**), however, there were also tiny Ag NDs located on the surface of TiO₂. They may be explained by the fact that in this experiment we not only changed the silver precursor nature but also the ratio between the TiO₂ and silver (5 times higher than in the case of **Figure 4.9**). The additional introduction of some PVP might also help prevent this secondary nucleation. These are new tracks for future experiments.

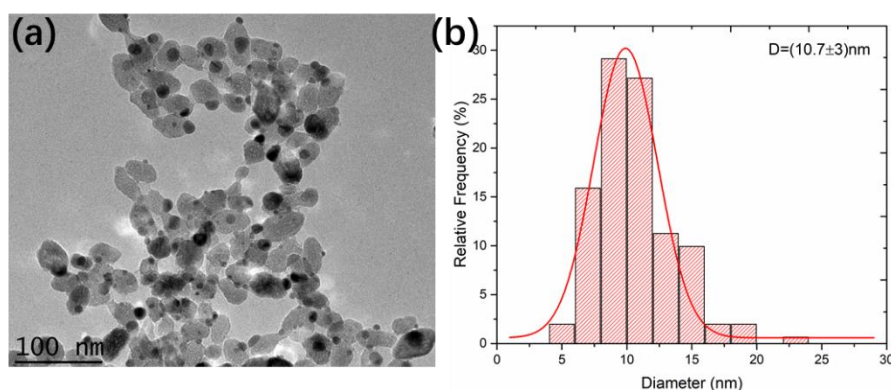


Figure 4.10 TEM image (a) and size distributions (b) of Ag-TiO₂ synthesized using the Tollens' reagent. Experimental conditions: $[\text{TiO}_2] = 1.1 \text{ mM}$, $[\text{Ag}^+] = 0.5 \text{ mM}$, applied power of 56.1 mW, exposure time of 4 min.

In conclusion, the charge properties of precursors and substates affect the nucleation and growth of noble metal nanoparticles. Opposing charged Ag precursor and TiO₂ NPs is favorable to the photodeposition. On this basis, more experiments and investigations should be conducted in the future.

4.1.4 Conclusion

In this section, experiments on the photodeposition of Ag nanodots on TiO₂ were performed using a UV laser as a light source in a cuvette setup. The effects of hole scavengers, power, exposure time, PVP, and precursors on the photodeposition were studied. TEM and UV-vis spectroscopy characterizations were conducted to check the existence, size, and distribution of the Ag nanodots on the surface of TiO₂. Higher precursor concentration seems to produce tiny Ag nanodots besides the main one on the surface of TiO₂. The addition of PVP leads to the suppression of this effect and the homogenous formation of a single Ag ND per TiO₂ and prevents the formation of tiny Ag particles. The photodeposition of Ag nanoparticles is closely related to the surface charge of TiO₂ and silver precursors.

4.2 Introduction to the photodeposition of Pd NDs on TiO₂ NPs

Among noble metals used to enhance photocatalytic activity under visible irradiation Ag and Au have been the most extensively studied since they exhibit Localized Surface Plasmon Resonance (LSPR) in the visible range of the spectrum. Despite their lower optical efficiency in the visible region, Pd NPs have surprisingly shown some extraordinary plasmonic properties, such as refractive index sensitivity or absorption capacity which are better than those of Au or Ag equivalents.²³⁻²⁴ Moreover, Pd as a plasmonic material shows other better properties than Au and Ag, for instance,

higher stability at elevated temperatures²⁵⁻²⁶ making it more suitable for certain applications. Palladium has been widely used as a catalyst in a wide variety of reactions, particularly in organic synthesis; for instance, Pd is the best catalyst for C-C bond formation reactions which are essential in pharmaceutical and agricultural industries.²⁷⁻²⁸ In addition, it has an extraordinary ability to reversibly absorb hydrogen in large quantities even under ambient conditions and has been applied in many hydrogen technologies including hydrogen purification, storage, and detection as well as fuel cells.²⁹⁻³¹

Intensive research efforts have been devoted to the decoration of noble metals onto the TiO₂ surface. Ag-TiO₂, Au-TiO₂, Pt-TiO₂ nanocomposite catalysts prepared using photodeposition methods are reported.^{12, 32-35} However, there are not so many reports on the photodeposition of Pd on TiO₂ particles.³⁶ The catalytic activity of the Pd-TiO₂ catalyst depends on both the Pd crystal size and the distribution of the nanodots, which are closely related to the photodeposition conditions including hole scavenger, precursor, and irradiation light.

Palladium chloride (PdCl₂) and disodium tetrachloropalladate (Na₂PdCl₄) are commonly used as precursors for the photodeposition of palladium in many reports. Since PdCl₂ is insoluble in water, it needs to be dissolved into a certain amount of concentrated hydrochloric acid, while Na₂PdCl₄ has good solubility in water. The different forms of the palladium chloride aqua complexes, [PdCl_n(H₂O)_{4-n}]²⁻ⁿ (n = 0- 4) exhibit different stabilities and reactivities, which are strongly dependent on both pH and pCl.³⁷⁻³⁹ In Leong's study,⁴⁰ Pd/TiO₂ nanocomposites synthesized by photodeposition under sunlight with Na₂PdCl₄ as a precursor had Pd particles with a spherical size ranging from 17 to 29 nm. Tian *et al.*⁴¹ adopted PdCl₂ as a precursor to load Pd particles on TiO₂ nanowires and got ultra-small Pd clusters (1.3 nm) highly dispersed on the surface of TiO₂. The effects of the different palladium precursors on photodeposition have not yet been reported probably because of the complexity of palladium chloride aqua complexes, it then needs to be studied.

The role of different hole scavengers on the Pd photodeposition has been studied

and reported.⁴²⁻⁴³ Dadsetan and co-authors⁴² studied the effects of different organic alcohols (methanol, ethanol, ethylene glycol, and 1-propanol) as sacrificial electron donors on the photodeposition of Pd on TiO₂. They suggested that alcohols with low carbon numbers and molar weights resulted in higher reduction rates of Pd and the highest rate was obtained with methanol.

UV lamps were commonly used as light sources for Pd photodeposition.⁴⁴⁻⁴⁶ Bai *et al.*⁴⁵ successfully deposited Pd nanoparticles on the (101) facets of flower-like anatase TiO₂ with high-activity (001) facets using ethanol as a hole scavenger in the presence of UV light irradiation by a Xenon lamp. The Pd/TiO₂ nanocomposite catalysts showed excellent photocatalytic activity for the bisphenol A degradation compared to bare TiO₂ under both UV and visible light irradiations. This was attributed to the low recombination rate of the photogenerated electrons and holes.

Although we know that the catalytic activity of Pd-TiO₂ catalysts strongly depends on the size and distribution of the Pd dots, there are few studies on the growth and morphology evolution of these Pd NDs on TiO₂ under a confined intensity and exposure time.

In this chapter, unlike in the references mentioned above,^{41-42, 44} the photodeposition of Pd NDs on TiO₂ is performed using a UV laser as a light source. The investigation of the growth of Pd will be undertaken under controlled exposure time and precursor concentration. Two metal precursors, Na₂PdCl₄ and PdCl₂ will be used and compared. The effects of methanol and H₂O as hole scavengers on the Pd photodeposition will be studied. In addition, the precise control of the Pd size can be performed according to modeling of the Pd growth which has been missing up to now.

4.2.1 Experiment method

The experimental procedures for the Pd photodeposition are the same as those for Au and Ag photodepositions. Methanol and water are used as hole scavengers, and Na₂PdCl₄ or PdCl₂ are adopted as precursors. The PdCl₂ solution (10 mM) was prepared by dissolving PdCl₂ into a pH 2 aqueous hydrochloric acid solution because

it is insoluble in water, it then becomes H₂PdCl₄. However, since this ion has a complex behavior in water depending on both pH and pCl, we choose for sake of clarity to go on mentioning the two precursors in this chapter by the formula of the commercially available products, *i.e.* Na₂PdCl₄ and PdCl₂ respectively.

The TEM grid preparation was the same as in the previous case, please see the detailed procedure in Chapter 3.2.2. The size distribution and yields were estimated on an average of at least 300 TiO₂ NPs.

4.2.2 Result and discussion

In this part, Pd-TiO₂ heterodimers were successfully synthesized by the photodeposition method. The effect of hole scavenger, media, exposure time, precursor, and concentration on the photodeposition process are investigated in detail. The experimental data are also fitted according to the growth model (see § 4.3).

4.2.2.1 The effects of the hole scavenger on the Pd photodeposition

As mentioned in the introduction, Dadsetan *et al.*⁴² suggested that alcohols with low carbon numbers and molar weights resulted in a high reduction rate of Pd on TiO₂. The highest rate of Pd photoreduction and highest dispersion percentage of Pd particles with the highest depositing amount were obtained with methanol as the sacrificial electron donors or hole scavengers.

We then used methanol as a hole scavenger and compared it with hole scavenger-free experiments where H₂O should act as such. All the other parameters remained identical except the hole scavenger and the results are shown in **Figure 4.11**.

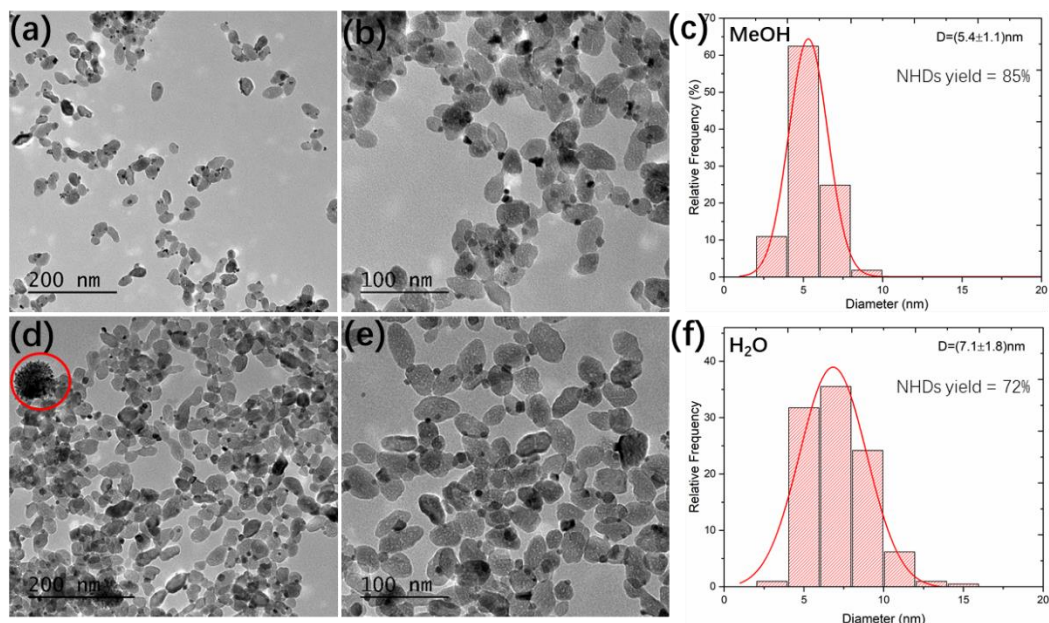


Figure 4.11 TEM images and size distributions of Pd-TiO₂ synthesized in the presence of different hole scavengers. (a, b) 50 vol.% methanol in H₂O and (d, e) H₂O and their corresponding size distributions (c and f). Experimental conditions: [TiO₂] = 5.5 mM, [Na₂PdCl₄] = 0.5 mM, exposure time of 8 min and applied power of 56.1 mW.

The TEM images (**Figure 4.11**) indicate that around 85 % and 72 % of TiO₂ particles are successfully decorated with Pd NDs either in the presence or absence of methanol. With methanol, we observe that (i) the size of Pd is smaller (5.4 nm) than in water (7.1 nm) (ii) there are multiple Pd nanodots on some of the TiO₂ particles, (iii) the starting material is completely soluble in the water/methanol mixture, while it is not the case anymore in pure water as illustrated by the remaining clusters (**Figure 11c**, red circle) on the TEM grid. Some TEM tests were performed on [Na₂PdCl₄] = 0.25 and 0.5 mM solutions to detect these clusters before UV irradiation. They were effectively found in pure water solution for [Na₂PdCl₄] = 0.5 mM but nor for [Na₂PdCl₄] = 0.25 mM.

4.2.2.2 The respective influence of HNO₃ and HCl on the Pd photodeposition

It is well known that palladium (II) forms quite stable complexes with chloride of general formula [PdCl_n(H₂O)_{4-n}]²⁻ⁿ (n = 0 - 4). The equilibria of palladium (II)

complexation are strongly dependent on pH and pCl (**Figure 4.12**).^{39, 47} When the pH is fixed, the palladium (II) complexation is only dependent on the concentration of Cl⁻ ions in the solution. Here we used a pH (3.2 ± 0.1) aqueous solution of HNO₃ or HCl as the solvent to deposit Pd on TiO₂ while fixing other parameters. [ENREF 39](#)

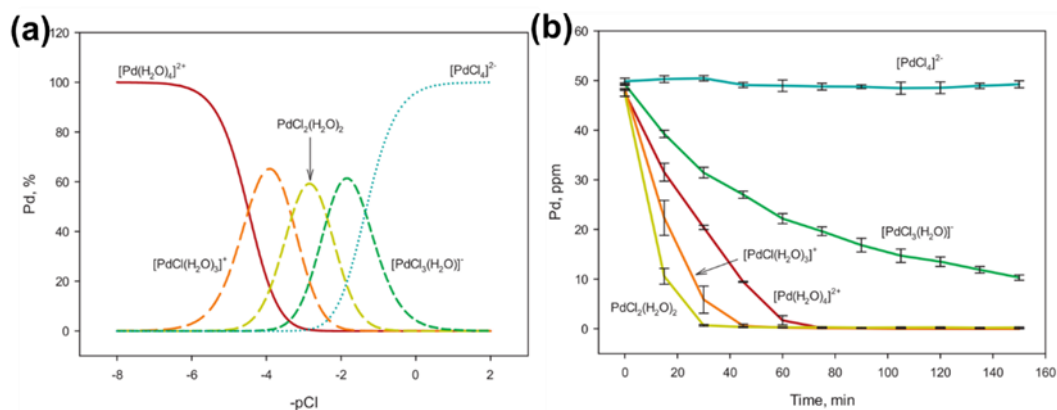


Figure 4.12 (a) Distribution of $[\text{PdCl}_n(\text{H}_2\text{O})_{4-n}]^{2-n}$ -species as a function of $-\text{pCl}$ ($\log[\text{Cl}^-]$) and (b) photocatalytic reduction trends of the $[\text{PdCl}_n(\text{H}_2\text{O})_{4-n}]^{2-n}$ system ($n = 0-4$) in the absence of an added sacrificial reducing agent. The associated legends indicate those Pd(II)-complexes present in greater abundance at a specific chloride concentration at 25°C.⁴⁷ Adapted from ref ⁴⁷

The TEM images and size distributions of the Pd NDs are shown in **Figure 4.13** and **Table 4.3**. When the reaction is performed in HCl, the size of the Pd NDs (7.8 nm) is slightly bigger than that obtained in HNO₃ (7.1 nm), while both diameters are far below the predicted value. The NHDs yields are very close, 72 % *versus* 65 %. The difference between these two different media in the photodeposition process is low, probably because the Cl⁻ introduced by HCl ultimately does not significantly change the pCl (2.58 and 2.69 respectively, **Table 4.3**). The palladium precursors are both present in the form of $[\text{PdCl}_n(\text{H}_2\text{O})_{4-n}]^{2-n}$ ($n = 2, 3$) under these two values of pCl.⁴⁷ In these conditions, PdCl₂(H₂O)₂ is the dominating species (60%) and exhibits the most efficient photocatalytic reduction rate as compared to $[\text{PdCl}(\text{H}_2\text{O})_3]^+$, $[\text{Pd}(\text{H}_2\text{O})_4]^{2+}$, $[\text{PdCl}_3(\text{H}_2\text{O})]^-$, and $[\text{PdCl}_4]^{2-}$ respectively if we refer to Kriek's work (**Figure 4.12**).⁴⁷

Table 4.3 Data concerning Pd sizes and NHDs yields of Pd-TiO₂ NHDs prepared in HNO₃ and HCl aqueous solutions. Experiment conditions are: [TiO₂] = 5.5 mM, [Na₂PdCl₄] = 0.5 mM, power 56.1mW, illumination time: 8 min. The Cl⁻ ions in HNO₃ reaction solution come from Na₂PdCl₄, and in HCl come from Na₂PdCl₄, and HCl, $pCl = -\log[Cl^-]$. The calculation of the predicted Pd size can be seen in Appendix 1.3. Pd²⁺ consumption percent is the amount of Pd²⁺ used for Pd-TiO₂ (calculation based on the yield and Pd diameter) compared to the initial Pd²⁺ precursor.

	<i>pH</i>	<i>[Cl⁻] (M)</i>	<i>pCl</i>	<i>NHDs (%)</i>	<i>Pd Size (SD) (nm)</i>	<i>Pred. Size (nm)</i>	<i>Pd²⁺ cons. (%)</i>
<i>HNO₃</i>	3.3	0.0020	2.69	72	7.1 (1.8)	10.0	36
<i>HCl</i>	3.2	0.0026	2.58	65	7.8 (1.9)	10.3	43

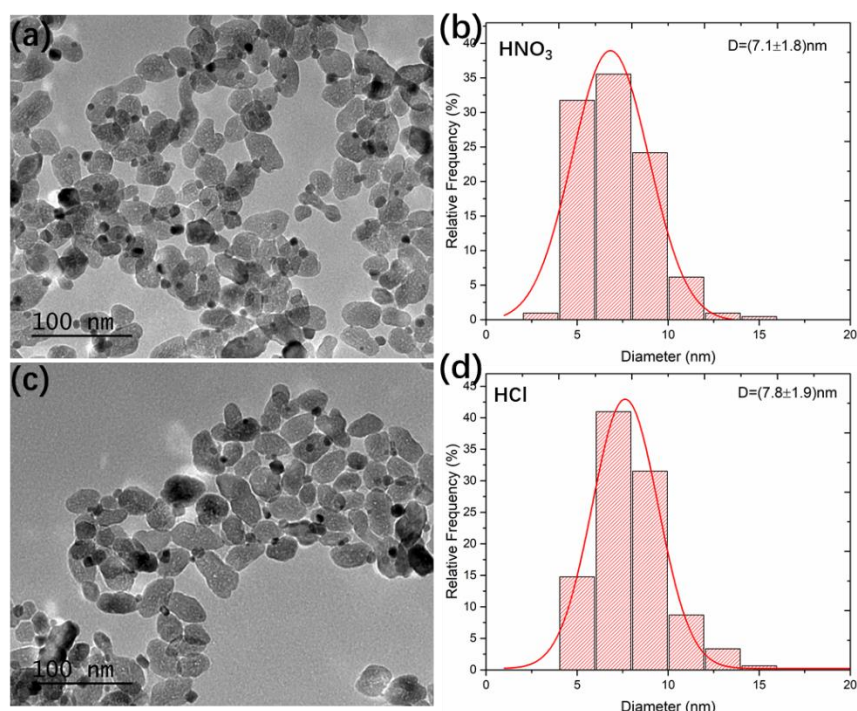


Figure 4.13 TEM images of Pd-TiO₂ synthesized in HNO₃ (a) and HCl (c) aqueous solutions and their corresponding metal size distributions (b) and (d). Experiment conditions are: [TiO₂] = 5.5 mM, [Na₂PdCl₄] = 0.5 mM, pH (3.2 ± 0.1), power: 56.1mW, illumination time: 8min.

4.2.2.3 The effects of the metal precursor on the Pd photodeposition

Here Na₂PdCl₄ and PdCl₂ are used as precursors while keeping other parameters identical. Since PdCl₂ is soluble in HCl solution and a solution containing a suitable concentration of chloride (neutral solution, for example, NaCl solution), we used an

HCl solution with a pH 3.2 value as a solvent for the photodeposition leading to an H₂PdCl₄ starting complex and its aqua derivatives. The TEM images and size distributions are shown in **Figure 4.14** and **Table 4.4**.

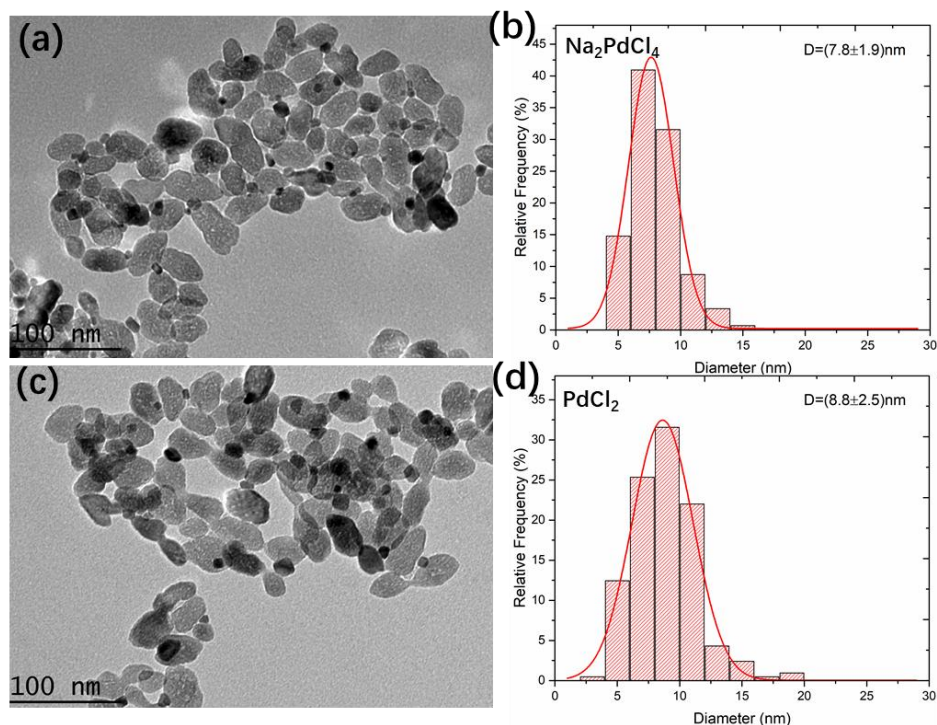


Figure 4.14 TEM images of Pd-TiO₂ synthesized with (a) Na₂PdCl₄ and (c) PdCl₂ and their corresponding metal size distributions (b) and (d). Experiment conditions are: [TiO₂] = 5.5 mM, [Pd²⁺] = 0.5 mM, pH 3.2, HCl, power: 56.1mW, illumination time: 8 min.

When using the Na₂PdCl₄ as a precursor, the size of Pd particles is smaller (7.8 nm) than with PdCl₂ as a precursor (8.8 nm). However, the NHDs yield is 65% and higher than that using PdCl₂ (50%). In addition, both Pd diameters are 2.5 nm smaller than the predicted values with 43 and 47% consumption of Na₂PdCl₄ (**Table 4.4**).

Table 4.4 Data concerning Pd sizes and NHDs yields of Pd-TiO₂ NHDs prepared with different palladium precursors. Experiment conditions are: [TiO₂] = 5.5 mM, [Pd²⁺] = 0.5 mM, power 56.1mW, illumination time: 8 min. The Cl⁻ ions come from Na₂PdCl₄ and PdCl₂ respectively, pCl = -log[Cl⁻].

	[Cl ⁻] (M)	pCl	NHDs yield (%)	Diam. of Pd (SD) (nm)	Predicted diam. (nm)	Pd ²⁺ consumption (%)
Na ₂ PdCl ₄	0.0020	2.69	65	7.8 (1.9)	10.3	43
PdCl ₂	0.0010	3.00	50	8.8 (2.5)	11.3	47

4.2.2.4 The effects of the exposure time on the Pd photodeposition

The effect of the exposure time was then investigated from 4 to 64 min while fixing the other parameters. The TEM results concerning the Pd-TiO₂ NHDs submitted to various exposure times are illustrated in **Figure 4.15**.

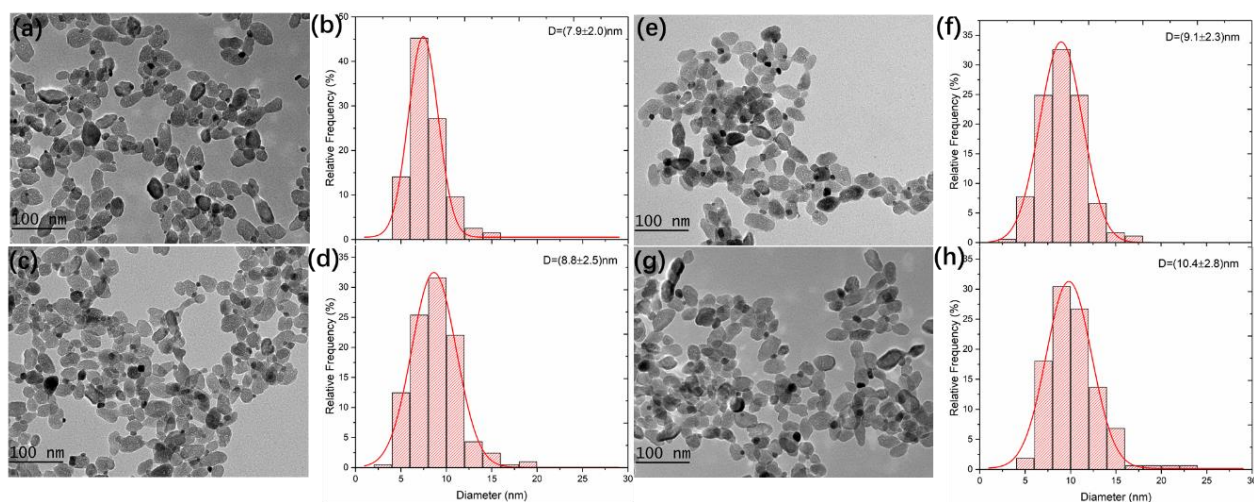


Figure 4.15 TEM images of Pd-TiO₂ synthesized at different exposure times. (a) 4 min, (c) 8 min, (e) 16 min and (g) 32 min and their corresponding size distributions (b, d, f and h). Experiment conditions are: [TiO₂] = 5.5 mM, [PdCl₂] = 0.5 mM, pH ~ 3 in HCl, power 56.1mW.

The variation of the Pd diameter, as well as the yield of Pd-TiO₂ NHDs with various exposure times, are shown in **Table 4.5** and **Figure 4.16**.

Table 4.5 Data of Pd size and NHDs yield of Pd-TiO₂ prepared at different exposure times. Experiment conditions are: [TiO₂] = 5.5 mM, [PdCl₂] = 0.5 mM, pH ~ 3 in HCl, power 56.1mW.

Exposure time (min)	Pd diameter (SD) (nm)	NHDs yield (%)	Estimated diameter (nm) ^a	Pd Pd ²⁺ consumption (%) ^b
4	7.9 (2.0)	55	11.3	38
8	8.8 (2.5)	50	11.4	47
16	9.1 (2.3)	49	11.3	51
32	10.4 (2.8)	45	11.7	70
64	11.7 (3.3)	42	11.9	93

^a The value is calculated based on the NHDs yield of Ag-TiO₂ obtained by experiments and the assumption that the Pd²⁺ is 100% consumed (see Appendix 1.3),

^b The ratio of Pd²⁺ used for Pd-TiO₂ to the initial Pd²⁺ precursor in the reaction solution. The amount of Pd²⁺ used for Pd-TiO₂ is calculated based on the yield and Pd diameter.

The size of the Pd particles increases regularly with the exposure time while the corresponding NHDs yields are stable, in the range of 42 - 50%. In addition, the difference between the measured and expected Pd diameters, becomes narrower with increasing exposure time, as expected, the largest Pd size (11.7 nm) obtained is very close to the estimated value of 11.9 nm (the longest exposure time), indicating 93% Pd²⁺ ions have been reduced.

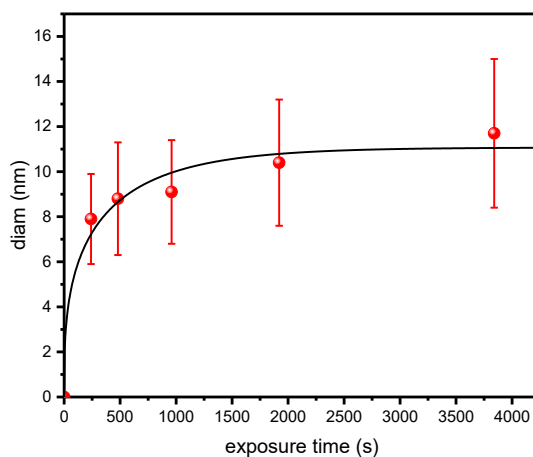


Figure 4.16 Variation of the Pd ND with the exposure time. The curve corresponds to the fit from the model, see later on in the modeling part.

4.2.2.5 The effects of TiO₂ and Pd²⁺ concentrations on the Pd photodeposition

In Chapter 3, (photodeposition of Au on TiO₂), we showed that the NHDs yield is dependent on the concentrations of TiO₂ and the metal precursor. We also varied here the concentrations of TiO₂ and PdCl₂. We first tried to decrease the concentration of TiO₂ to 2.75 mM while keeping 0.5 mM PdCl₂. We also reduced the concentration of PdCl₂ to 0.25 mM at 2.75 mM TiO₂. Finally, we kept the PdCl₂ at 0.25 mM and decreased the TiO₂ concentration to 1.1 mM. For each condition, three different exposure times, (4, 8, and 16 min) were adopted. The TEM images and size distributions are illustrated in **Figures 4.17, 4.18, and 4.19**.

a) [TiO₂] = 2.75 mM, [PdCl₂] = 0.5 mM,

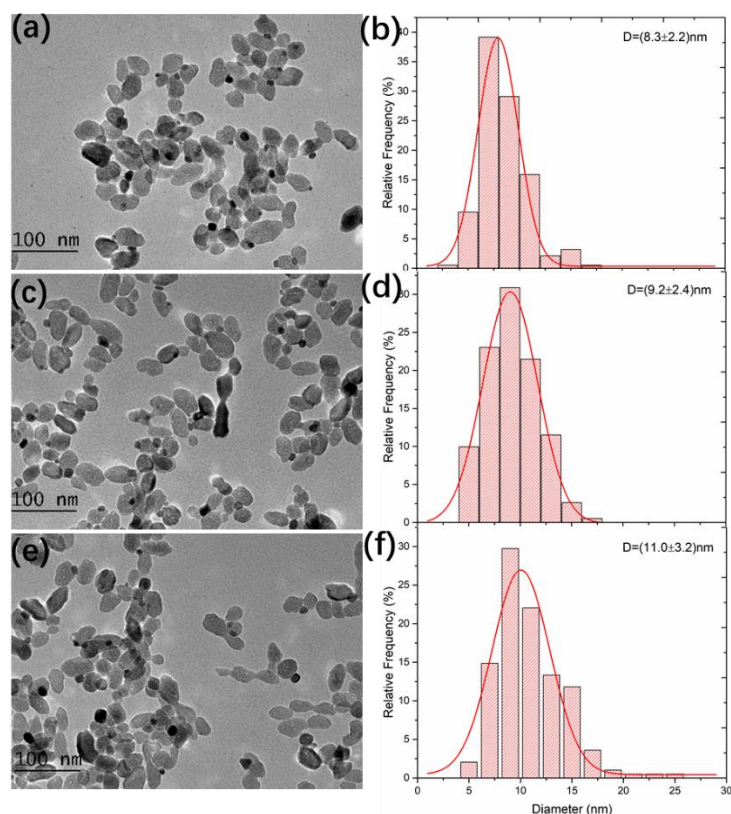


Figure 4.17 TEM images of Pd-TiO₂ synthesized at different exposure times; (a) 4 min (c) 8 min and (e) 16 min and their corresponding size distributions (b, d, f). Experimental conditions: [TiO₂] = 2.75 mM, [PdCl₂] = 0.5 mM, pH ~ 3 in HCl, power 56.1mW.

b) [TiO₂] = 2.75 mM, [PdCl₂] = 0.25 mM,

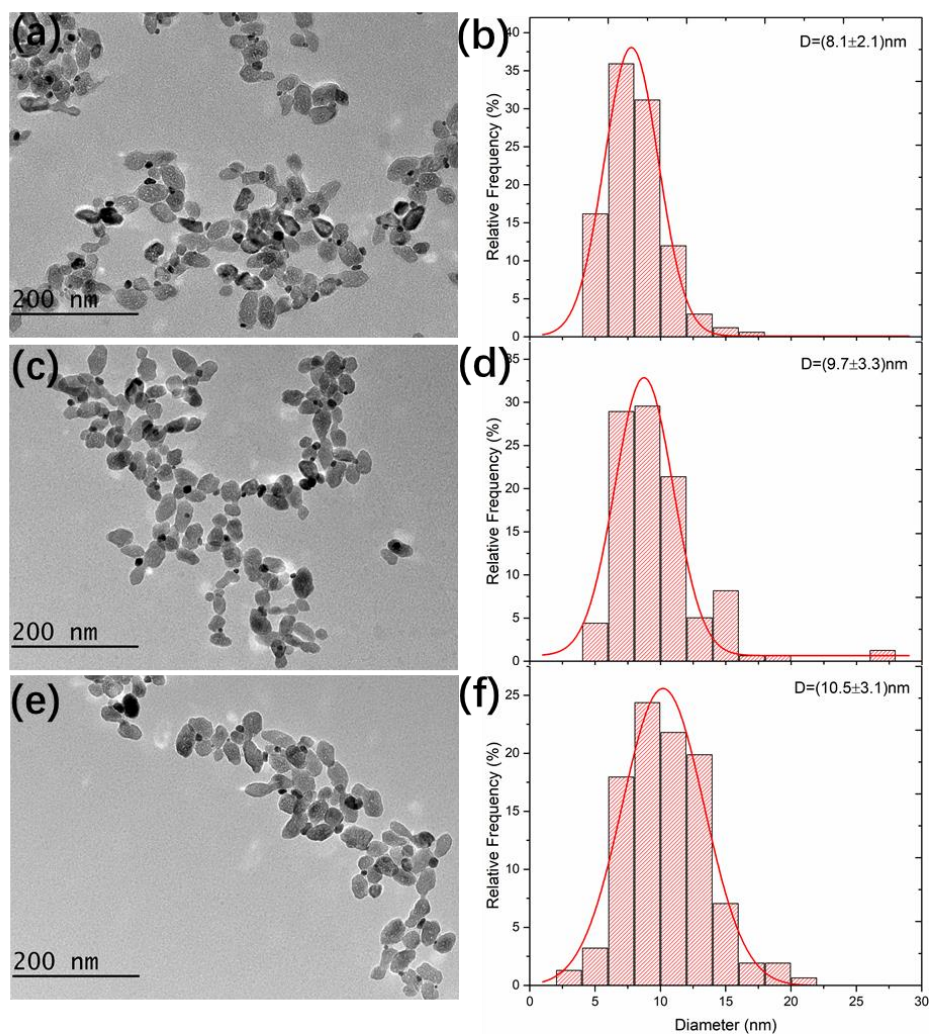


Figure 4.18 TEM images of Pd-TiO₂ synthesized at different exposure times; (a) 4 min (c) 8 min and (e) 16 min and their corresponding size distributions (b, d, f). Experimental conditions: [TiO₂] = 2.75 mM, [PdCl₂] = 0.25 mM, pH ~ 3 in HCl, power 56.1mW.

c) [TiO₂] = 1.1 mM, [PdCl₂] = 0.25 mM,

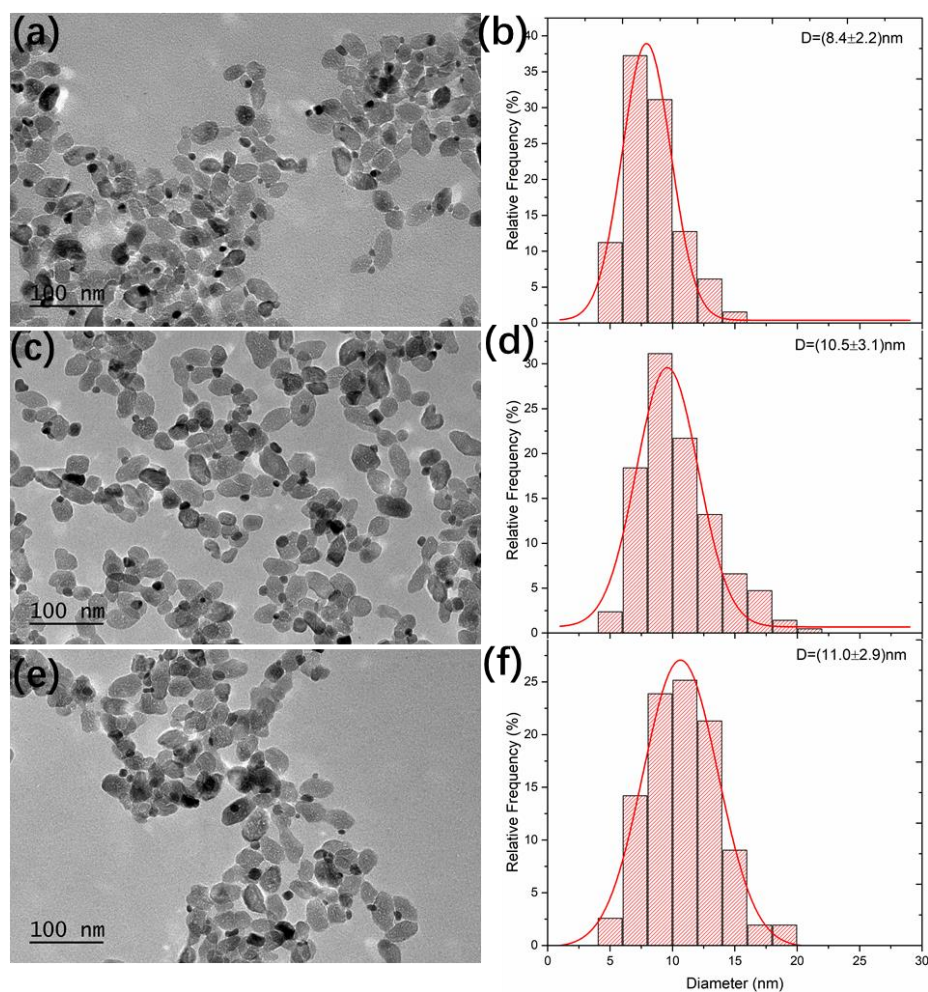


Figure 4.19 TEM images of Pd-TiO₂ synthesized at different exposure times; (a) 4 min (c) 8 min and (e) 16 min and their corresponding size distributions (b, d, f). Experimental conditions: [TiO₂] = 1.1 mM, [PdCl₂] = 0.25 mM, pH ~ 3 in HCl, power 56.1 mW.

For the different experimental conditions, the variation of the Pd diameter, the NHDs yield of Pd-TiO₂, the estimated value of Pd NDs diameter, and the consumption percentage of the palladium precursor with various exposure times, are all gathered in **Table 4.6**.

Table 4.6 Data about Pd size and NHDs yield of Pd-TiO₂ prepared at different concentrations of TiO₂, and Pd²⁺.

[TiO ₂] (mM)	[Pd ²⁺] (mM)	Exposure time (min)	Pd diam. (SD) (nm)	NHDs yield (%)	Estimated Pd diam. (nm) ^a	Pd ²⁺ consumption percent (%) ^b
2.75	0.5	4	8.3(2.2)	46	14.6	18
2.75	0.5	8	9.2(2.4)	49	14.2	26
2.75	0.5	16	11.0(3.2)	43	14.9	40
2.75	0.25	4	8.1(2.2)	45	11.7	33
2.75	0.25	8	9.7(3.3)	46	11.6	58
2.75	0.25	16	10.5(3.1)	50	11.3	80
1.1	0.25	4	8.4(2.2)	61	14.3	20
1.1	0.25	8	10.5(3.1)	63	14.1	39
1.1	0.25	16	11.0(2.9)	59	14.5	43

^a The value is calculated based on the NHDs yield of Pd-TiO₂ obtained by experiments and the assumption that the Pd²⁺ is 100% consumed (see Appendix 1.3),

^b The ratio of Pd²⁺ used for Pd-TiO₂ to the initial Pd²⁺ precursor in the reaction solution. The amount of Pd²⁺ used for Pd-TiO₂ is calculated based on the yield and Pd diameter.

Once again the size of the Pd NDs increases gradually with the exposure time under each condition. Decreasing TiO₂ for a constant PdCl₂ of 0.5 mM, shows that there is not much difference in the NHDs yield while the Pd size is getting bigger (compare with **Table 4.5**). When the concentration of TiO₂ is 2.75 mM and that of PdCl₂ decreases to 0.25 mM, the size and NHDs yield do not change, but the consumption percent of palladium precursor reaches 80% for an exposure time of 16 min. The NHDs yield increases significantly when the concentration of TiO₂ is further reduced to 1.1 mM while the PdCl₂ is 0.25 mM and only 43 % of the palladium precursor is reduced after 16 min laser irradiation. It seems that the consumption rate of PdCl₂ is related to both the concentration of TiO₂ and that of palladium precursor nature.

4.2.3 Conclusion

In this section, we investigated the photodeposition of palladium on TiO₂ by UV laser. TEM characterization confirmed the existence of metallic Pd NDs on the TiO₂ surface and the formation of Pd-TiO₂ nanoheterodimers. The effects of hole scavengers were

investigated and the results indicated methanol was too efficient and favored the formation of multi Pd NDs on the TiO₂ surface. Meanwhile, without any external hole scavengers, the photodeposition resulted in a single Pd nanodot on each TiO₂ particle. Metal precursor effects were investigated using both Na₂PdCl₄ and PdCl₂. Na₂PdCl₄ led to smaller Pd particles and higher NHDs yields than PdCl₂. The effect of the exposure time on the photodeposition was also studied. The Pd size and the consumption percent of metal precursor were gradually increased with the exposure time. The NHDs yield could also be improved by lowering TiO₂ concentrations as in the case of Au-TiO₂ NHDs. In addition, the consumption rate of PdCl₂ is related to both the concentrations of TiO₂ and palladium precursor.

4.3 Laser deposition of Pd and Ag NDs onto TiO₂ NPs in the cuvette and microchannel setups from growth to completion

Bai in his Ph.D. dissertation⁴⁸ performed a series of experiments using a laser-focused in a microchannel to analyze the growth of a single metallic ND onto TiO₂ NPs in a permanent regime. This work intended to extend these experiments using a cuvette setup and investigate the transition from growth in permanent conditions up to completion. which are typically located at the side of the rod due to their large surface areas

We shall, in the following, summarize and apply the model developed in Chapter 3 and see if it can apply to another metal of the gold column and metal of another column of the periodic table. We have:

The Growth Law

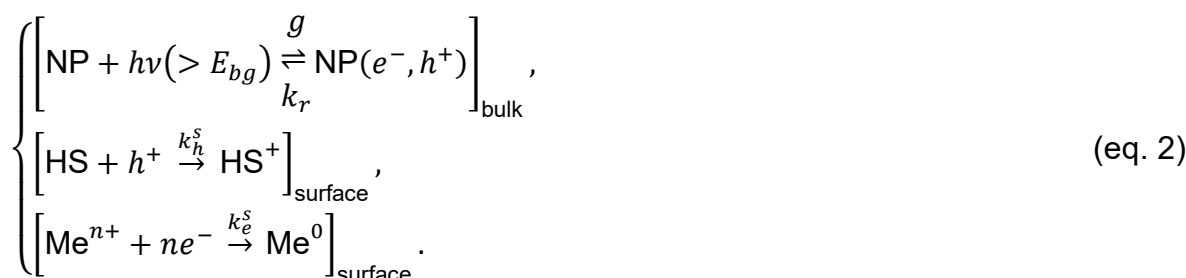
The growth model of metallic NDs (Ag, Pd) onto TiO₂ NPs is the same as for Au NDs and can be described by equation 1:

$$D^3(t) = \frac{8}{\pi\kappa(\theta)} \frac{v_{Me}}{Y[\text{NP}]} [\text{Me}^0](t) \quad (\text{eq. 1})$$

where “Me” is a generic term for metal whatever its nature. Please refer to chapter 3.4.2 for a detailed derivation process.

The Photochemical reaction scheme

The basic photochemical reaction scheme has already been illustrated in chapter 3.4.1 and the chemical reactions are the following set of equations:



Where “Me” is generically the deposited metal (Ag, n=1; Pd, n=2).

On the one hand, electrons and holes are produced in bulk TiO₂ by bulk optical absorption (rate g) and may recombine with a bulk reaction rate k_r . On the other hand, oxidation of the hole scavenger with a surface reaction rate k_h^s and reduction of metal ions with a surface reaction rate k_e^s (exponent s for surface) just occur at the surface of TiO₂ with adsorbed species arrived from the bulk solution.

We assume, as in Chapter 3, that:

- (1) The diffusion of electrons and holes inside the TiO₂ NPs can be confidently neglected in the reaction-diffusion equations since equilibration times for electron and hole concentrations are very short (due to the nanometric size of the NPs) compared to the time scales of growth experiments by photodeposition.
- (2) The deposition Me@TiO₂ is pseudo-first-order, as already demonstrated experimentally.
- (3) Methanol always remains in excess so we can assume [HS](t)=cte.

We use the same notations as those used for the description of Au@TiO₂.

- (a) For species adsorbed at the surface of TiO₂, {R} expresses reagent surface

concentrations in mole/m² (mole/unit catalyst surface). As R is initially present in the bulk solution, this surface concentration can be related to its corresponding volume concentration $[R]_{ads}$ in mole/l using the specific surface area of the catalysts S_{sa} and the load in catalyst q as $[R]_{ads} = qS_{sa}\{R\}$.

- (b) As electrons and holes are on the contrary produced in bulk TiO₂, their concentrations at the surface of TiO₂ are not related to any adsorption mechanism nor the load q , but its density ρ_{TiO_2} so that: $\{e/h\} = \frac{[e/h]}{\rho_{TiO_2}S_{sa}}$.

Then, the basic equations are described by eq 3:

$$\left\{ \begin{array}{l} \frac{d[e]}{dt} = (g - k_r[e][h])_{bulk} - k_e^s\{e\}\{Me^{n+}\} \\ \frac{d[h]}{dt} = (g - k_r[e][h])_{bulk} - k_h^s\{h\}\{HS\} \\ \frac{d[HS^+]}{dt} = k_h^s\{h\}\{HS\} \\ \frac{d[Me^0]}{dt} = k_e^s\{e\}\{Me^{n+}\} \end{array} \right. \quad (\text{eq. 3})$$

We can note as well that:

- (a) As electrons and holes are produced in bulk TiO₂, $k_{e/h}^s = k_{e/h}q\rho_{TiO_2}S_{sa}^2$ which relates the surface reaction rate to an equivalent volume reaction rate.
- (b) g is the so-called source term due to the light absorption by the NPs: $g = g_{lin} \cdot \frac{1}{1+2I/I_s^b} = \frac{\sigma_{NP}[NP]I}{\hbar\omega} \cdot \frac{1}{1+2I/I_s^b} = \frac{v_{NP}}{v_{TiO_2}} \cdot \frac{[NP]}{2\tau_b} \cdot \frac{2I/I_s^b}{1+2I/I_s^b}$ with I_s^b being a bulk saturation intensity related to the finite size of the TiO₂ NPs. As previous experiments performed in a microchannel at very high laser intensities did not show any saturation, we will assume $g \approx g_{lin} = \frac{\sigma_{abs}[NP]I}{\hbar\omega}$, where $\hbar\omega = 5.45 \cdot 10^{-19} J$ is the photon energy ($\lambda_0 = 364 nm$) and σ_{abs} is the absorption cross-section of the NPs calculated before. For the present experiments performed in a cuvette, we find $g = 5.002 \times [NP]I M/s$; while for Bai's experiments⁴⁸ performed in both microchannel and cuvette with slightly larger TiO₂ NPs we find $g = 7.195 \times [NP]I M/s$.

Physisorption is assumed at the surface of TiO₂ (Eley-Rideal-like mechanism)

We previously found (see Chapter 3) :

$$\begin{aligned} \{R\} &= \frac{k_{ads}}{k_{des}} \left(\frac{k_{\uparrow}}{k_{\downarrow} + k_{ads}[R]_{bulk}} \right) \frac{\{S\}_0}{\left(1 + \frac{k_{\uparrow}}{k_{\downarrow}}\right)} [R]_{bulk} \\ &= \frac{k_{\uparrow}\{S\}_0}{k_{des}} \frac{1}{\left(1 + \frac{k_{\uparrow}}{k_{\downarrow}}\right)} \left(\frac{(k_{ads}/k_{\downarrow})[R]_{bulk}}{1 + (k_{ads}/k_{\downarrow})[R]_{bulk}} \right) \end{aligned}$$

Leading to

$$\begin{aligned} [R]_{ads} &= \frac{k_{ads}}{k_{des}} \left(\frac{k_{\uparrow}}{k_{\downarrow} + k_{ads}[R]_{bulk}} \right) \frac{\{S\}_0 \times S_{sa} \times q}{\left(1 + \frac{k_{\uparrow}}{k_{\downarrow}}\right)} [R]_{bulk} \\ &= C_T \frac{k_{\uparrow}}{k_{des}} \frac{1}{\left(1 + \frac{k_{\uparrow}}{k_{\downarrow}}\right)} \left(\frac{(k_{ads}/k_{\downarrow})[R]_{bulk}}{1 + (k_{ads}/k_{\downarrow})[R]_{bulk}} \right) \end{aligned}$$

where $k_{\uparrow/\downarrow}$ are surface excitation/relaxation reaction rates, and $C_T = \{S\}_0 \times S_{sa} \times q$.

If $(k_{ads}/k_{\downarrow})[R]_{bulk} \ll 1$ (this is verified for [Au³⁺] and [MeOH] at the surface of TiO₂), then:

$$[R]_{ads} \approx C_T \frac{k_{ads} k_{\uparrow}}{k_{des} k_{\downarrow}} \frac{1}{\left(1 + \frac{k_{\uparrow}}{k_{\downarrow}}\right)} [R]_{bulk} = C_T \frac{k_{ads}}{k_{des}} \frac{I/I_s^s}{1+2I/I_s^s} [R]_{bulk},$$

Where I_s^s is a surface saturation intensity. Then $[R]_{ads}$ is an increasing function of the beam intensity which varies from 0 to $[R]_{ads} \approx C_T \frac{I}{I_s^s} \frac{k_{ads}}{k_{des}} [R]_{bulk}$ at $I/I_s^s \ll 1$ to an asymptotic value $[R]_{ads} \approx \frac{1}{2} C_T \frac{k_{ads}}{k_{des}} [R]_{bulk}$ which is independent of $\frac{I}{I_s^s}$ when $I/I_s^s \gg 1$.

Thus, $[R]_{ads}^{I \ll I_s^s} \approx C_T \frac{I}{I_s^s} \frac{k_{ads}}{k_{des}} [R]_{bulk}$ and $[R]_{ads}^{I \gg I_s^s} \approx C_T \frac{1}{2} \frac{k_{ads}}{k_{des}} [R]_{bulk}$ with $[R]_{ads}^{I \ll I_s^s} < [R]_{ads}^{I \gg I_s^s}$ as $[R]_{ads}$ is an increasing function of the beam intensity.

In conclusion, considering experimental conditions, we have $(k_{ads}/k_{\downarrow})[MeOH/Me]_{bulk} \ll 1$, and then $[HS]_{ads}^I \approx K'[HS]_{bulk}$ with $K' = \left(C_T \frac{k_{ads}}{k_{des}} \right)_{HS} \frac{I/I_s^s}{1+2I/I_s^s}$ and $[Me^{n+}]_{ads} \approx K[Me^{n+}]_{bulk}$ with $K = \left(C_T \frac{k_{ads}}{k_{des}} \right)_{Me} \frac{I/I_s^s}{1+2I/I_s^s}$.

Calculation of the metal concentration (Ag⁰, Pd⁰) during the growth of a metallic ND

We previously found that:

$$(1) [Me^0](t \leq 2\tau) = [Me^{n+}]_0 \frac{t}{\tau} \cdot \left| 1 - \frac{t}{4\tau} \right|, \text{ where } \tau = \sqrt{\frac{k_r}{k_e k_h [HS]_{ads} g} \frac{[Me^{n+}]_0}{K}}$$

Note that $[Me^0](t \ll 4\tau) \approx [Me^{n+}]_0 \frac{t}{\tau}$ corresponds to the permanent growth regime investigated in microchannel experiments: $[Me^0](t \ll 4\tau) \approx \sqrt{\frac{k_e k_h [HS]_{ads}}{k_r} \cdot K [Me^{n+}]_0 \cdot g \cdot t}$.

(2) This power-law growth is followed by an exponential saturation toward completion.

Finally, $D(t) = \left(\frac{8}{\pi \kappa(\theta)} \frac{\nu_{Me}}{Y[NP]} \right)^{1/3} [Me^0](t)^{1/3}$, where $[Me^0](t) = [Me^{n+}]_0 \cdot f(t/\tau)$ and $f(t/\tau \rightarrow \infty) = 1$. Then we expect:

$$D(t) = \left(\frac{[Me^{n+}]_0}{Y[NP]} \right)^{1/3} \left[\frac{8\nu_{Me}}{\pi \kappa(\theta)} \cdot f(t/\tau) \right]^{1/3} \quad (\text{eq. 4})$$

with $\frac{t}{\tau} = \sqrt{\frac{k_e k_h [HS]_0 [NP] I}{k_r [Me^{n+}]_0} \cdot \frac{\sigma_{abs}}{\hbar \omega} \cdot K' K} \cdot t$ where $K' = (C_T)_{HS} \left(\frac{k_{ads}}{k_{des}} \right)_{HS} \frac{I/I_s^s}{1+2I/I_s^s}$ and $K = (C_T)_{Au} \left(\frac{k_{ads}}{k_{des}} \right)_{Me} \frac{I/I_s^s}{1+2I/I_s^s}$ are the proportionality constants between adsorbed and bulk MeOH and metal ions at low concentrations, leading to $\frac{t}{\tau} \propto \sqrt{\frac{[HS]_0 [NP] I}{[Me^{n+}]_0} \cdot \left(\frac{I/I_s^s}{1+2I/I_s^s} \right)} \cdot t$.

4.3.1 Overall analysis of the experiments on Silver photodeposition

Firstly, We compare experiments previously performed at very high intensities in a microchannel⁴⁸ (mean intensity is 158.20 W/cm²) and a present variation in time exposure performed at lower intensity in the cuvette setup ($I = 0.14$ W/cm²).

We expect as shown by eq. 4:

$$\left(\frac{Y[NP]}{[Ag^+]_0} \right)^{1/3} D(t) = \left[\frac{8\nu_{Ag}}{\pi \kappa(\theta)} \cdot f(t/\tau) \right]^{1/3} \text{ where } f(t/\tau \rightarrow \infty) = 1, \text{ and } \frac{t}{\tau} \propto \sqrt{\frac{[NP] I}{[Ag^+]_0} \cdot \frac{1}{2} \cdot \left(\frac{2I/I_s^s}{1+2I/I_s^s} \right)} \cdot t.$$

Data are plotted versus $\left(\frac{t}{\tau}\right)_{I \gg I_s^s} \propto \sqrt{\frac{[NP]I}{[Ag^+]_0}} \cdot \frac{1}{2} \cdot t$ for comparisons between microchannel experiments, for which $I \gg I_s^s$, and the cuvette experiment for which $I \ll I_s^s$ is expected. **Figure 4.20** presents these two data sets.

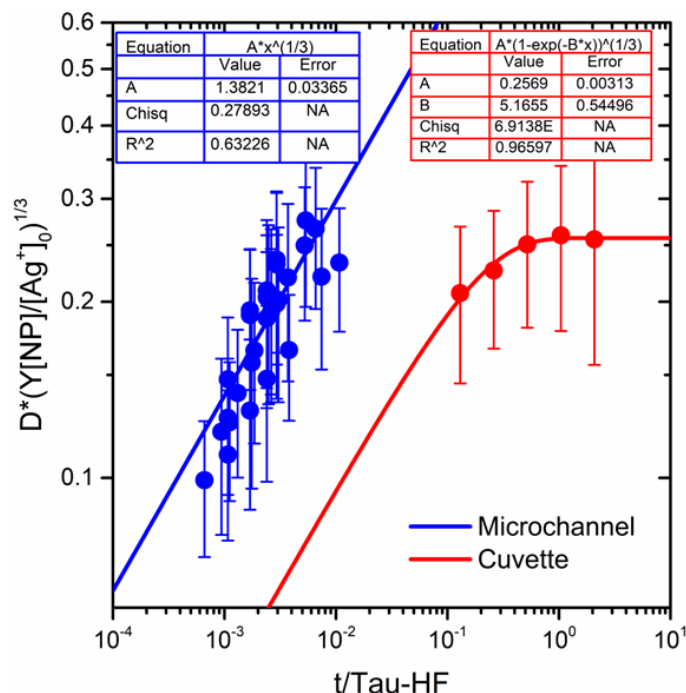


Figure 4.20 Plots of the Ag ND diameter $D(Y[NP]/[Ag^+]_0)^{1/3}$ obtained in microchannel and cuvette setups as a function of the rescaled time $\left(\frac{t}{\tau}\right)_{I \gg I_s^s} \propto \sqrt{\frac{[NP]I}{[Ag^+]_0}} \cdot \frac{1}{2} \cdot t$.

In this plot, it appears again that the microchannel experiments are shifted toward the smallest $\frac{t}{\tau}$ value as expected and already observed for gold deposition. Moreover, microchannel experiments are performed at such a high intensity that they belong to the range of $I \gg I_s^s$.

The fit of the cuvette data gives $D_\infty \left(\frac{Y[NP]}{[Ag^+]_0}\right)^{1/3} = 0.257$, which has to be compared to the expected value of $\left(\frac{8v_{Ag}}{\pi\kappa(\theta)}\right)^{1/3} = 0.324 \text{ nm}$ ($v_{Ag} = M_{Ag}/(N_A \rho_{Ag})$ with $M_{Ag} = 107.87 \text{ g}$ and $\rho_{Ag} = 10.49 \text{ g/cm}^3$, and $\kappa(\theta = 140^\circ) = 1.2829$). If the concentration of silver ions is not totally consumed at completion (which is normally not expected on bare TiO₂) or if a percentage of this concentration is deposited in a different way than

the formation of heterodimers (typically in the form of very tiny NDs difficult to observe and to measure), then the growth law should be written as $D(t) = \left(\frac{8}{\pi\kappa(\theta)} \frac{\nu_{Ag}}{Y[NP]}\right)^{1/3} [Ag^0](t)^{1/3}$, with $[Ag^0](t) = \beta \cdot [Ag^+]_0 \cdot f(t/\tau)$ and $\beta = \frac{[Ag^0]_\infty}{[Ag^+]_0}$ represents the ratio of silver present in the heterodimers at completion. Then we deduce $\beta = \frac{[Ag^0]_\infty}{[Ag^+]_0} = \frac{Y[NP]}{[Ag^+]_0} \cdot D_\infty^3 \cdot \frac{\pi\kappa(\theta)}{8\nu_{Ag}} = \left(\frac{0.257}{0.324}\right)^3 = 0.50 \pm 0.02$, showing that 50% of the initial silver ions were consumed for the production of heterodimers.

The fit of the microchannel data is: $\left(\frac{Y[NP]}{[Ag^+]_0}\right)^{1/3} D(t) = 1.382 \left(\frac{t}{\tau}\right)_{I \gg I_s}^{1/3}$

The fit of the cuvette data in the 1/3 regime gives: $\left(\frac{Y[NP]}{[Ag^+]_0}\right)^{1/3} D(t) = 0.2569 \times 5.1655^{1/3} \left(\frac{t}{\tau}\right)_{I \gg I_s}^{1/3} = 0.4441 \left(\frac{t}{\tau}\right)_{I \gg I_s}^{1/3}$ using the linear part of the red curve in Figure 4.20.

Then, considering the same value of $\left(\frac{Y[NP]}{[Ag^+]_0}\right)^{1/3} D(t)$ to measure the shift in $\left(\frac{t}{\tau}\right)$ we find $\left(\frac{t}{\tau}\right)_{I \gg I_s}^{Cuv} / \left(\frac{t}{\tau}\right)_{I \gg I_s}^{\mu C} = \left(\frac{1.3821}{0.4441}\right)^3 = 30.14$ so that, according to the model, we should get $\left(\frac{1+2I/I_s^s}{2I/I_s^s}\right) = 30.14$. We deduce $29.14 \times 2I = I_s^s$ and finally, considering $I = 0.14 \text{ W/cm}^2$ used in the cuvette experiment, we finally get $I_s^s = 8.16 \text{ W/cm}^2$. This value is 2.5 times larger than that obtained for gold deposition $\bar{I}_s^s \approx (2.9 \pm 0.2) \text{ W/cm}^2$, while both gold and silver experiments use the same amount of methanol as a hole scavenger, such a value should then be confirmed by further experiments.

Eventually, we replot the two data sets as a function of $\frac{t}{\tau} \propto \sqrt{\frac{[NP]I}{[Ag^+]_0}} \cdot \frac{1}{2} \cdot \left(\frac{2I/I_s^s}{1+2I/I_s^s}\right) \cdot t$ to get a collapse of any types of Ag@TiO₂ photodeposition experiment performed in high field conditions in the presence of methanol as a hole scavenger.

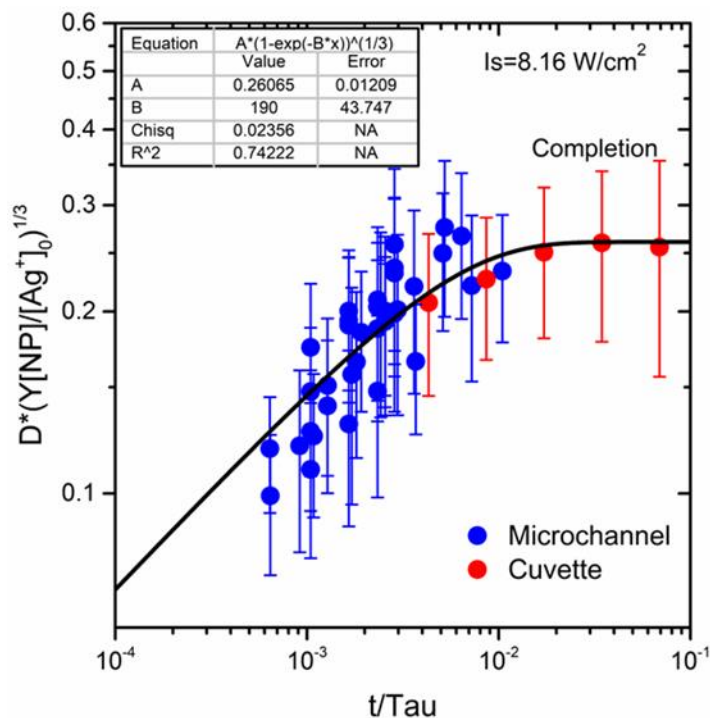


Figure 4.21 Plot of the Ag ND diameter $D(Y[NP]/[Ag^+]_0)^{1/3}$ obtained in microchannel and cuvette setups as a function of the rescaled time $\frac{t}{\tau} \propto \sqrt{\frac{[NP]I}{[Ag^+]_0}} \cdot \frac{1}{2} \cdot \left(\frac{2I/I_s^S}{1+2I/I_s^S}\right) \cdot t$ ($I_s^S = 8.16 \text{ W/cm}^2$).

We indeed observe the collapse in intensity that confirms a physisorption mechanism and gives us a qualitatively coherent value for I_s^S (condition $I_{cuvette} \ll I_s^S \ll I_{\mu C}$).

This collapse allows us to figure out the overall growth dynamics of a silver ND onto TiO₂ NPs by laser deposition from the 1/3 regime to the crossover toward completion in the high field condition, whatever the concentrations and intensities.

Finally, the whole fit according to the expected dynamics gives $D_\infty \left(\frac{Y[NP]}{[Ag^+]_0}\right)^{1/3} = 0.261$ which, compared to the expected value of 0.324 nm leads to an amount of deposited silver in the cuvette experiment of $\beta = \frac{[Ag^0]_\infty}{[Ag^+]_0} = \left(\frac{0.261}{0.324}\right)^3 = 52\%$. Further experiments in the cuvette at the largest accessible beam powers would quantitatively strengthen the observed rescaling.

4.3.2 Overall analysis of the experiments on Palladium photodeposition

The effects of the exposure time, palladium ions, and TiO₂ concentrations on Pd deposition were investigated and the experimental conditions and results are in § 4.2.2.4 and 4.2.2.5.

The expected dynamics are:

$$\left(\frac{Y[NP]}{[Pd^{2+}]_0}\right)^{1/3} D(t) = \left[\frac{8v_{Pd}}{\pi\kappa(\theta)} \cdot f(t/\tau)\right]^{1/3} \quad \text{where } f(t/\tau \rightarrow \infty) = 1, \quad \text{and } \frac{t}{\tau} \propto \sqrt{\frac{[NP]I}{[Pd^{2+}]_0}} \cdot \left(\frac{I/I_S^S}{1+2I/I_S^S}\right) \cdot t.$$

Then, we first plot $\left(\frac{[NP]}{[Pd^{2+}]_0}\right)^{1/3} D(t)$ as a function of $\sqrt{\frac{[NP]I}{[Pd^{2+}]_0}} \cdot \frac{1}{2} \cdot t \propto \left(\frac{t}{\tau}\right)_{I \gg I_S}$ for the whole set of data; this choice of $\left(\frac{t}{\tau}\right)_{I \gg I_S} \propto \sqrt{\frac{[NP]I}{[Pd^{2+}]_0}} \cdot \frac{1}{2} \cdot t$ is related to the fact that it is interesting to use the same variable for further comparisons with the microchannel experiments realized at $I \gg I_S$.

Two experiments on Pd ND growth were performed by varying separately the exposure time (**Figure 4.16**), and both palladium ion and TiO₂ concentrations (**Table 4.6**). The rescaling of these two experiments is illustrated in **Figure 4.22**.

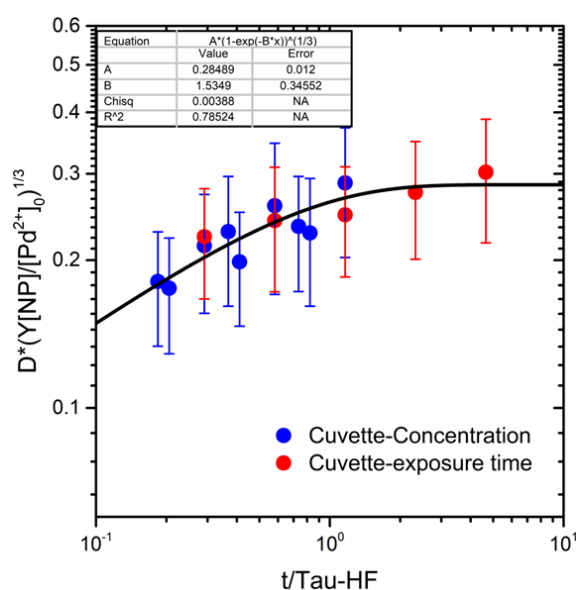


Figure 4.22 Plot of the Pd ND diameter $D(Y[NP]/[Pd^{2+}]_0)^{1/3}$ as a function of the rescaled high field

time $\left(\frac{t}{\tau}\right)_{I \gg I_S} \propto \sqrt{\frac{[NP]I}{[Pd^{2+}]_0}} \cdot \frac{1}{2} \cdot t$ obtained under various conditions when varying the exposure times (based on Figure 4.16) and the palladium ions concentration (Table 4.6).

Clearly, data variation at a given beam intensity does collapse perfectly with model predictions. The overall fit gives $D_\infty \left(\frac{Y[NP]}{[Pd^{2+}]_0}\right)^{1/3} = 0.285$, which has to be compared to the expected value of $\left(\frac{8\nu_{Pd}}{\pi\kappa(\theta)}\right)^{1/3} = 0.308 \text{ nm}$ ($\nu_{Pd} = M_{Pd}/(N_A q_{Pd})$ with $M_{Pd} = 106.42 \text{ g}$ and $q_{Pd} = 12.02 \text{ g/cm}^3$, and $\kappa(\theta = 140^\circ) = 1.2829$). Then, the ratio of palladium present in the heterodimers at completion is $\beta = \frac{[Pd^0]_\infty}{[Pd^{2+}]_0} = \left(\frac{0.285}{0.308}\right)^3 = 79\%$. This result shows that 80% of the initial palladium ions were consumed for the production of heterodimers.

Experiments with the cuvette setup were also performed at lower power of 13.88 mW;⁴⁸ the comparison with the present experiments (56.1 mW) is illustrated in **Figure 4.23**.

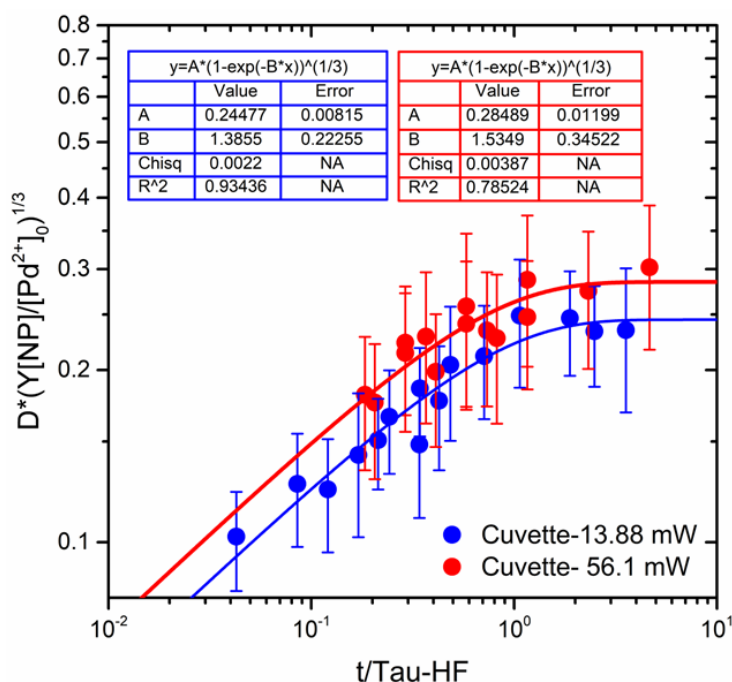


Figure 4.23 Plots of the Pd ND diameter $D(Y[NP]/[Pd^{2+}]_0)^{1/3}$ as a function of the rescaled high field

time $\left(\frac{t}{\tau}\right)_{I \gg I_S} \propto \sqrt{\frac{[NP]I}{[Pd^{2+}]_0}} \cdot \frac{1}{2} \cdot t$ for two different beam powers.

Data at 13.88 mW are shifted toward a larger $\left(\frac{t}{\tau}\right)_{I \gg I_S}$ value than that obtained in this work, as expected for experiments performed at a lower beam intensity. Nonetheless, the 13.88 mW experiment leads to an asymptotic value $D_\infty \left(\frac{Y[NP]}{[Pd^{2+}]_0}\right)^{1/3} = 0.245$, smaller than the previous one ($D_\infty \left(\frac{Y[NP]}{[Pd^{2+}]_0}\right)^{1/3} = 0.285$) for some unexplained reason, leading to an amount of palladium deposited of $\beta = \frac{[Pd^0]_\infty}{[Pd^{2+}]_0} = \left(\frac{0.245}{0.308}\right)^3 = 50\%$.

If we now compare both cuvette and microchannel experiments,

We expect:

$$\left(\frac{Y[NP]}{[Pd^{2+}]_0}\right)^{1/3} D(t) = \left[\frac{8\nu_{Pd}}{\pi\kappa(\theta)} \cdot f(t/\tau)\right]^{1/3} \text{ where } f(t/\tau \rightarrow \infty) = 1, \text{ and } \frac{t}{\tau} \propto \sqrt{\frac{[NP]I}{[Pd^{2+}]_0}} \cdot \frac{1}{2} \cdot \left(\frac{2I/I_S^S}{1+2I/I_S^S}\right) \cdot t.$$

For microchannel experiments, we have $I \gg I_S^S$ and we expect $\frac{t}{\tau} = \left(\frac{t}{\tau}\right)_{I \gg I_S^S} \propto \sqrt{\frac{[NP]I}{[Pd^{2+}]_0}} \cdot \frac{1}{2} \cdot t$. Then, we first plot all the data sets at a function of the high field rescaled time $\left(\frac{t}{\tau}\right)_{I \gg I_S^S} \propto \sqrt{\frac{[NP]I}{[Pd^{2+}]_0}} \cdot \frac{1}{2} \cdot t$. (**Figure 4.24**).

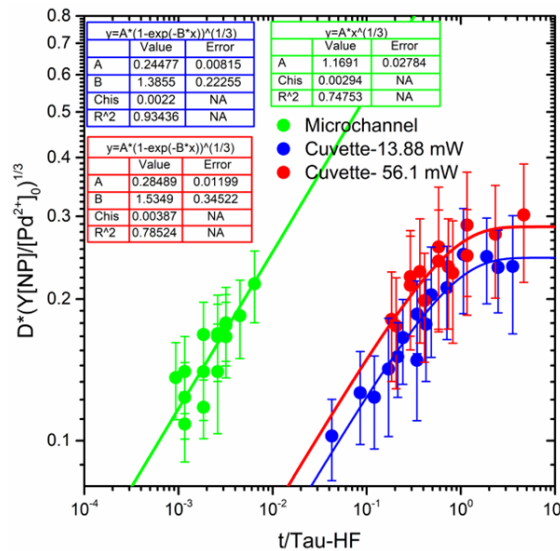


Figure 4.24 Plots of the Pd ND diameter $D \left(\frac{Y[NP]}{[Pd^{2+}]_0}\right)^{1/3}$ as a function of rescaled high-field time

$$\left(\frac{t}{\tau}\right)_{I \gg I_S} \propto \sqrt{\frac{[NP]I}{[Pd^{2+}]_0}} \cdot \frac{1}{2} \cdot t \text{ obtained in microchannel and cuvette setups.}$$

As shown in **Figure 4.24**, the microchannel experiments are again shifted toward

the smallest $\frac{t}{\tau}$ values as expected and already observed for gold (Chapter 3, **Figure 3.30**) and silver (Chapter 4, **Figure 4.20**) deposition. Moreover, microchannel experiments are performed at such a high intensity that they belong to the range of $I \gg I_s^s$.

We then need to rescale these three data sets to find a value of I_s^s , compatible with the condition $I_{Cuvette} \ll I_s^s \ll I_{\mu C}$, which allows merging all the data sets on a single curve, whatever the value of the beam intensity.

As already illustrated for Au@TiO₂, one way to do this statistically is to fit the amplitude of the 1/3 early growth regime as a function of the intensity $1/I$; the mean intensity used in microchannel experiments is 60.57 W/cm^2 . In the 1/3 growth regime; this amplitude is $A \propto \left(\frac{2I/I_s^s}{1+2I/I_s^s}\right)^{1/3} = \left(1 + \frac{I_s^s}{2} \times \frac{1}{I}\right)^{-1/3}$. Its variation with the corresponding fit is illustrated in **Figure 4.25**.

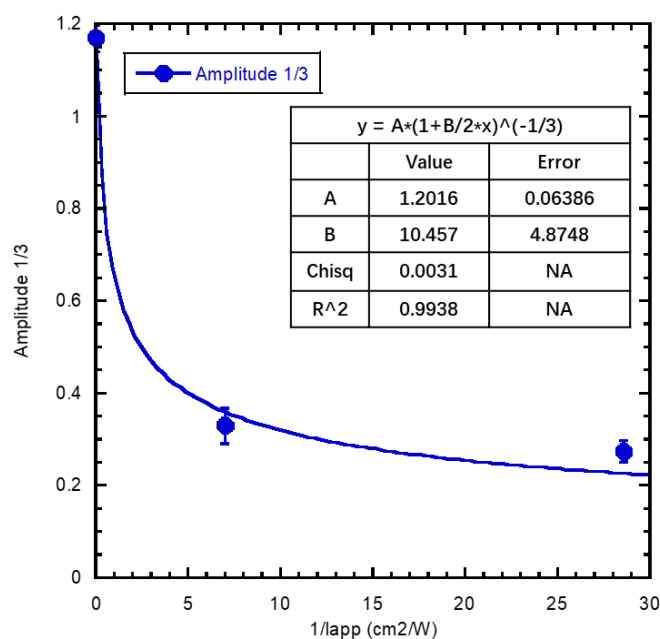


Figure 4.25 Plot of the amplitude $D(Y[NP]/[Pd^{2+}]_0)^{1/3}$ in its $\left(\frac{t}{\tau}\right)_{I \gg I_s^s}^{1/3}$ with the $1/I$ obtained in microchannel and cuvette setups.

The fit of the amplitude is reasonably accurate and gives $B = \bar{I}_s^s \approx (10.5 \pm 5) \text{ W/cm}^2$ for the mean surface saturation intensity. This value verifies the condition

$I_{Cuvette} \ll I_s^s \ll I_{\mu C}$. It is higher than those obtained for Au@TiO₂ and Ag@TiO₂ ($\bar{I}_s^s(Au) \approx (2.9 \pm 0.2) W/cm^2$, $I_s^s(Ag) = 8.16 W/cm^2$) in presence of methanol, suggesting that the lifetime τ_s of TiO₂ excited surface state and/or their absorption cross-section σ_s are smaller in presence of pure water than in presence of a water-methanol mixture ($I_s^s = \frac{\hbar\omega}{\tau_s\sigma_s}$).

Eventually, we replotted all the data sets as a function of $\frac{t}{\tau} \propto \sqrt{\frac{[NP]I}{[Pd^{2+}]_0}} \cdot \frac{1}{2} \cdot \left(\frac{2I/I_s^s}{1+2I/I_s^s}\right) \cdot t$, with $\bar{I}_s^s \approx (10.5 \pm 5) W/cm^2$, to get a total collapse of any types of Pd@TiO₂ photodeposition experiment performed in high field conditions in the absence of a dedicated hole scavenger. This collapse is illustrated in **Figure 4.26**.

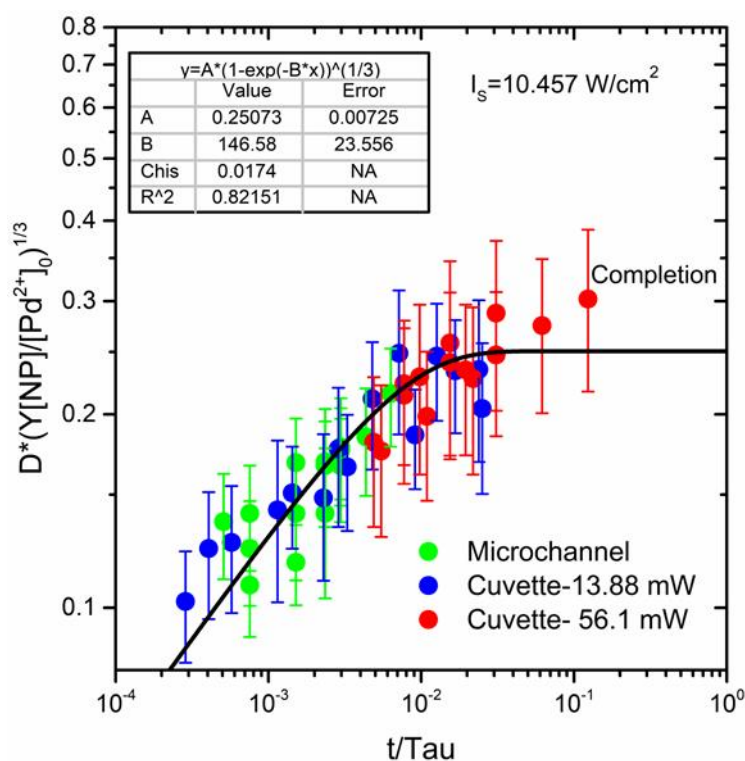


Figure 4.26 Plots of the Pd ND diameter $D(Y[NP]/[Pd^{2+}]_0)^{1/3}$ as a function of the rescaled high field time of $\frac{t}{\tau} \propto \sqrt{\frac{[NP]I}{[Pd^{2+}]_0}} \cdot \frac{1}{2} \cdot \left(\frac{2I/I_s^s}{1+2I/I_s^s}\right) \cdot t$ obtained in microchannel and cuvette setups.

We indeed observe a collapse in intensity that again confirms a physisorption mechanism of the palladium ions on the surface of TiO₂ and gives a mathematically

coherent value for I_s^S . This collapse allows us to figure out the overall growth dynamics of a Pd ND onto TiO₂ NPs by laser deposition from the 1/3 regime through the crossover toward completion in the high field condition, whatever the concentrations and intensities.

Finally, the overall fit of the expected dynamics gives $D_\infty \left(\frac{Y[\text{NP}]}{[\text{Pd}^{2+}]_0} \right)^{1/3} = 0.251$.

Then, the mean amount of palladium deposited in these experiments is: $\beta = \frac{[\text{Pd}^0]_\infty}{[\text{Pd}^{2+}]_0} =$

$\left(\frac{0.251}{0.308} \right)^3 = 54\%$, likely due to the penalty produced by the previously unexplained 50%

amount measured for a beam power of 13.88 mW.

Partial Conclusions:

- (1) Photodeposition of metals onto TiO₂ is driven by physisorption as illustrated by the overall rescaling and the fitting of the experimental gold, silver, and palladium ND growths versus concentrations and intensity.
- (2) The collapse of short and long time exposure experiments allows the description of the entire dynamics of the growth of a metallic ND onto TiO₂ NPs from the permanent regime of exponent 1/3 up to completion.
- (3) Beyond investigating the dynamics, the completion offers us a way to predict the final size in any experimental conditions if we know the yield.

4.4 Conclusion

In this chapter, we performed the photodeposition of Ag and Pd on the surface of TiO₂ with a UV laser in a cuvette setup. In the case of silver and the used conditions here, Ag particles can be deposited on the surface of TiO₂, but it is very easy to have multiple Ag tiny NDs per TiO₂ particle which is probably due to the sensitivity of silver ions that just require only one electron to form Ag. Higher precursors concentration, higher power will induce tiny Ag nanodots on the surface of TiO₂. The addition of PVP

is beneficial to the formation of Ag-TiO₂ heterodimers. Charge properties of precursors and substrates affect the nucleation and growth of noble metal nanoparticles. Oppositely charged Ag precursor and TiO₂ particles are beneficial to metal photodeposition. In the case of palladium, the Pd-TiO₂ heterodimers can be obtained easily without multiple Pd particles on TiO₂, but only in the absence of an additional hole scavenger, water playing this role.

We have also shown that we could apply for silver and palladium the model developed for gold. Then, the photodeposition of metals onto TiO₂ is driven by physisorption as illustrated by the whole rescaling and the fitting of the experimental gold, silver, and palladium ND growth versus concentrations and intensity. We illustrated that the collapse of short and long time exposure experiments allows for the description of the entire dynamics of the growth of a metallic ND onto TiO₂ NPs from the permanent regime of exponent 1/3 up to completion.

We confirm, in these two cases as well that the sorption of the ions is a physisorption process and not a chemical one as mentioned in the literature.⁸⁻⁹

4.5 References

1. Barrientos, L.; Allende, P.; Laguna-Bercero, M. Á.; Pastrían, J.; Rodríguez-Becerra, J.; Cáceres-Jensen, L., Controlled Ag-TiO₂ Heterojunction Obtained by Combining Physical Vapor Deposition and Bifunctional Surface Modifiers. *Journal of Physics and Chemistry of Solids* **2018**, *119*, 147-156.
2. Do Kim, K.; Han, D. N.; Lee, J. B.; Kim, H. T., Formation and Characterization of Ag-deposited TiO₂ Nanoparticles by Chemical Reduction Method. *Scripta materialia* **2006**, *54* (2), 143-146.
3. Kang, J.-G.; Sohn, Y., Interfacial Nature of Ag Nanoparticles Supported on TiO₂ Photocatalysts. *Journal of Materials Science* **2011**, *47* (2), 824-832.
4. Kawaguchi, T., Photo-Induced Deposition of Silver Particles on Amorphous Semiconductors. *Photo-Induced Metastability in Amorphous Semiconductors* **2003**, 182-198.
5. Bai, Q.; Shupyk, I.; Vauriot, L.; Majimel, J.; Labrugere, C.; Delville, M.-H.; Delville, J.-P., Design of Metal@Titanium Oxide Nano-Heterodimers by Laser-Driven Photodeposition: Growth Mechanism and Modeling. *ACS Nano* **2021**, *15* (2), 2947-2961.
6. Fleischauer, P. D.; Kan, H. A.; Shepard, J. R., Quantum Yields of Silver Ion Reduction on Titanium Dioxide and Zinc Oxide Single Crystals. *Journal of the American Chemical Society* **1972**, *94* (1), 283-285.
7. Hada, H.; Yonezawa, Y.; Ishino, M.; Tanemura, H., Photoreduction of Silver Ion on the Surface of Titanium Dioxide Single Crystals. *Journal of the Chemical Society, Faraday Transactions 1: Physical Chemistry in Condensed Phases* **1982**, *78* (9), 2677-2684.
8. Ohtani, B.; Okugawa, Y.; Nishimoto, S.; Kagiya, T., Photocatalytic Activity of Titania Powders Suspended in Aqueous Silver Nitrate Solution: Correlation with pH-dependent Surface Structures. *Journal of Physical Chemistry* **1987**, *91* (13), 3550-3555.
9. Ohtani, B.; Zhang, S.-W.; Handa, J.; Kajiwara, H.; Nishimoto, S.; Kagiya, T., Photocatalytic Activity Of Titanium (IV) Oxide Prepared from Titanium (IV) Tetra-2-Propoxide: Reaction in Aqueous Silver Salt Solutions. *Journal of Photochemistry and Photobiology A: Chemistry* **1992**, *64* (2), 223-230.
10. Chen, D.; Chen, Q.; Ge, L.; Yin, L.; Fan, B.; Wang, H.; Lu, H.; Xu, H.; Zhang, R.; Shao, G., Synthesis and Ag-Loading-Density-Dependent Photocatalytic Activity of Ag@TiO₂ Hybrid Nanocrystals. *Applied Surface Science* **2013**, *284*, 921-929.
11. Aulakh, M. K.; Pal, B., Solar Irradiated Selective Nitroaromatics Reduction over Plasmonic Ag-TiO₂: Deposition Time Dependent Size Growth and Oxidation State of Co-catalyst. *Chemical Engineering Journal* **2022**, *429*, 132385.
12. Dinh, C.-T.; Nguyen, T.-D.; Kleitz, F.; Do, T.-O., A New Route to Size and Population Control of Silver Clusters on Colloidal TiO₂ Nanocrystals. *ACS applied materials & interfaces* **2011**, *3* (7), 2228-2234.
13. Lu, Q.; Lu, Z.; Lu, Y.; Lv, L.; Ning, Y.; Yu, H.; Hou, Y.; Yin, Y., Photocatalytic Synthesis and Photovoltaic Application of Ag-TiO₂ Nanorod Composites. *Nano letters* **2013**, *13* (11), 5698-5702.
14. Cozzoli, P. D.; Comparelli, R.; Fanizza, E.; Curri, M. L.; Agostiano, A.; Laub, D., Photocatalytic Synthesis of Silver Nanoparticles Stabilized by TiO₂ Nanorods: A Semiconductor/Metal Nanocomposite in Homogeneous Nonpolar Solution. *Journal of the American Chemical Society* **2004**, *126* (12), 3868-

3879.

15. Guin, D.; Manorama, S. V.; Latha, J. N. L.; Singh, S., Photoreduction of Silver on Bare and Colloidal TiO₂ Nanoparticles/Nanotubes: Synthesis, Characterization, and Tested for Antibacterial Outcome. *The Journal of Physical Chemistry C* **2007**, *111* (36), 13393-13397.
16. Chan, S. C.; Barteau, M. A., Preparation of Highly Uniform Ag/TiO₂ and Au/TiO₂ Supported Nanoparticle Catalysts by Photodeposition. *Langmuir* **2005**, *21* (12), 5588-5595.
17. Carbone, L.; Jakab, A.; Khalavka, Y.; Sönnichsen, C., Light-Controlled One-Sided Growth of Large Plasmonic Gold Domains on Quantum Rods Observed on the Single Particle Level. *Nano letters* **2009**, *9* (11), 3710-3714.
18. Berr, M.; Vaneski, A.; Susha, A. S.; Rodríguez-Fernández, J.; Döblinger, M.; Jäckel, F.; Rogach, A. L.; Feldmann, J., Colloidal CdS Nanorods Decorated with Subnanometer Sized Pt Clusters for Photocatalytic Hydrogen Generation. *Appl. Phys. Lett.* **2010**, *97* (9), 093108.
19. Qi, T.; Xu, M.; Yao, Y.; Chen, W.; Xu, M.; Tang, S.; Shen, W.; Kong, D.; Cai, X.; Shi, H., Gold Nanoprism/Tollens' Reagent Complex as Plasmonic Sensor in Headspace Single-drop Microextraction for Colorimetric Detection of Formaldehyde in Food Samples Using Smartphone Readout. *Talanta* **2020**, *220*, 121388.
20. Peng, S.; Lei, C.; Ren, Y.; Cook, R. E.; Sun, Y., Plasmonic/Magnetic Bifunctional Nanoparticles. *Angewandte Chemie* **2011**, *50* (14), 3158-63.
21. Krishnaraj, C.; Jagan, E. G.; Rajasekar, S.; Selvakumar, P.; Kalaichelvan, P. T.; Mohan, N., Synthesis of Silver Nanoparticles Using Acalypha Indica Leaf Extracts and Its Antibacterial Activity Against Water Borne Pathogens. *Colloids Surf B Biointerfaces* **2010**, *76* (1), 50-6.
22. Vanaja, M.; Gnanajobitha, G.; Paulkumar, K.; Rajeshkumar, S.; Malarkodi, C.; Annadurai, G., Phytosynthesis of Silver Nanoparticles by Cissus Quadrangularis: Influence of Physicochemical Factors. *Journal of Nanostructure in Chemistry* **2013**, *3* (1).
23. De Marchi, S.; Núñez-Sánchez, S.; Bodelón, G.; Pérez-Juste, J.; Pastoriza-Santos, I., Pd Nanoparticles as a Plasmonic Material: Synthesis, Optical Properties and Applications. *Nanoscale* **2020**, *12* (46), 23424-23443.
24. Sugawa, K.; Tahara, H.; Yamashita, A.; Otsuki, J.; Sagara, T.; Harumoto, T.; Yanagida, S., Refractive Index Susceptibility of the Plasmonic Palladium Nanoparticle: Potential as the Third Plasmonic Sensing Material. *ACS Nano* **2015**, *9* (2), 1895-1904.
25. Huang, X.; Tang, S.; Liu, B.; Ren, B.; Zheng, N., Enhancing the Photothermal Stability of Plasmonic Metal Nanoplates by a Core-Shell Architecture. *Advanced materials* **2011**, *23* (30), 3420-3425.
26. Albrecht, W.; Bladt, E.; Vanrompay, H.; Smith, J. D.; Skrabalak, S. E.; Bals, S., Thermal Stability of Gold/Palladium Octopods Studied in Situ in 3D: Understanding Design Rules for Thermally Stable Metal Nanoparticles. *ACS Nano* **2019**, *13* (6), 6522-6530.
27. Hong, K.; Sajjadi, M.; Suh, J. M.; Zhang, K.; Nasrollahzadeh, M.; Jang, H. W.; Varma, R. S.; Shokouhimehr, M., Palladium Nanoparticles on Assorted Nanostructured Supports: Applications for Suzuki, Heck, and Sonogashira Cross-coupling Reactions. *ACS Applied Nano Materials* **2020**, *3* (3), 2070-2103.
28. Niakan, M.; Masteri-Farahani, M.; Karimi, S.; Shekaari, H., Hydrophilic Role of Deep Eutectic Solvents for Clean Synthesis of Biphenyls over a Magnetically Separable Pd-catalyzed Suzuki-Miyaura Coupling Reaction. *Journal of Molecular Liquids* **2021**, *324*, 115078.
29. Konda, S. K.; Chen, A., Palladium Based Nanomaterials for Enhanced Hydrogen Spillover and

- Storage. *Materials Today* **2016**, *19* (2), 100-108.
30. Niu, W.; Zhang, L.; Xu, G., Shape-controlled Synthesis of Single-Crystalline Palladium Nanocrystals. *ACS Nano* **2010**, *4* (4), 1987-1996.
31. Zhang, H.; Jin, M.; Xiong, Y.; Lim, B.; Xia, Y., Shape-Controlled Synthesis of Pd Nanocrystals and Their Catalytic Applications. *Accounts of chemical research* **2013**, *46* (8), 1783-1794.
32. Bhardwaj, S.; Dogra, D.; Pal, B.; Singh, S., Photodeposition Time Dependant Growth, Size and Photoactivity of Ag and Cu Deposited TiO₂ Nanocatalyst under Solar Irradiation. *Solar Energy* **2019**, *194*, 618-627.
33. Zhou, X.; Qian, K.; Zhang, Y.; Li, D.; Wei, Z.; Wang, H.; Ye, R.; Liu, J.; Ye, B.; Huang, W., Tuning the Size of Photo-deposited Metal Nanoparticles via Manipulating Surface Defect Structures of TiO₂ Nanocrystals. *Chem Commun (Camb)* **2020**, *56* (13), 1964-1967.
34. Veziroglu, S.; Obermann, A.-L.; Ullrich, M.; Hussain, M.; Kamp, M.; Kienle, L.; Leißner, T.; Rubahn, H.-G.; Polonskyi, O.; Strunskus, T.; Fiutowski, J.; Es-Souni, M.; Adam, J.; Faupel, F.; Aktas, O. C., Photodeposition of Au Nanoclusters for Enhanced Photocatalytic Dye Degradation over TiO₂ Thin Film. *ACS applied materials & interfaces* **2020**, *12* (13), 14983-14992.
35. Haselmann, G. M.; Baumgartner, B.; Wang, J.; Wieland, K.; Gupta, T.; Herzig, C.; Limbeck, A.; Lendl, B.; Eder, D., In situ Pt Photodeposition and Methanol Photooxidation on Pt/TiO₂: Pt-loading-dependent Photocatalytic Reaction Pathways Studied by Liquid-Phase Infrared Spectroscopy. *ACS Catalysis* **2020**, *10* (5), 2964-2977.
36. Chen, D.; Gao, H.; Yao, Y.; Zhu, L.; Zhou, X.; Peng, X.; Zhang, M., Pd Loading, Mⁿ⁺ (n=1, 2, 3) Metal Ions Doped TiO₂ Nanosheets for Enhanced Photocatalytic H₂ Production and Reaction Mechanism. *International Journal of Hydrogen Energy* **2022**, *47* (18), 10250-10260.
37. Kettemann, F.; Wuithschick, M.; Caputo, G.; Kraehnert, R.; Pinna, N.; Rademann, K.; Polte, J., Reliable Palladium Nanoparticle Syntheses in Aqueous Solution: the Importance of Understanding Precursor Chemistry and Growth Mechanism. *CrystEngComm* **2015**, *17* (8), 1865-1870.
38. Mech, K.; Żabiński, P.; Kowalik, R.; Fitzner, K., Kinetics and Mechanism of [PdCl_x(H₂O)_{4-x}]_{2-x} (x= 3, 4) Complexes Electro-reduction. *Journal of The Electrochemical Society* **2013**, *160* (10), H770.
39. Cruywagen, J.; Kriek, R., Complexation of palladium (II) with chloride and hydroxide. *Journal of Coordination Chemistry* **2007**, *60* (4), 439-447.
40. Leong, K. H.; Chu, H. Y.; Ibrahim, S.; Saravanan, P., Palladium Nanoparticles Anchored to Anatase TiO₂ for Enhanced Surface Plasmon Resonance-Stimulated, Visible-Light-driven Photocatalytic Activity. *Beilstein J Nanotechnol* **2015**, *6*, 428-37.
41. Tian, C.; Fang, H.; Chen, H.; Chen, W.; Zhou, S.; Duan, X.; Liu, X.; Yuan, Y., Photodeposition of Pd onto TiO₂ Nanowires for Aqueous-phase Selective Hydrogenation of Phenolics to Cyclohexanones. *Nanoscale* **2020**, *12* (4), 2603-2612.
42. Dadsetan, S.; Baghshahi, S.; Hadavi, S. M. M., Photodeposition of Pd Nanoparticles on TiO₂ Using Sacrificial Organic Alcohols. *Journal of the Australian Ceramic Society* **2017**, *54* (2), 383-388.
43. Jones, W.; Martin, D. J.; Caravaca, A.; Beale, A. M.; Bowker, M.; Maschmeyer, T.; Hartley, G.; Masters, A., A Comparison of Photocatalytic Reforming Reactions of Methanol and Triethanolamine with Pd Supported on Titania and Graphitic Carbon Nitride. *Applied Catalysis B: Environmental* **2019**, *240*, 373-379.
44. Fan, Q.; He, S.; Hao, L.; Liu, X.; Zhu, Y.; Xu, S.; Zhang, F., Photodeposited Pd Nanoparticles with Disordered Structure for Phenylacetylene Semihydrogenation. *Scientific reports* **2017**, *7*, 42172.
45. Bai, X.; Lv, L.; Zhang, X.; Hua, Z., Synthesis and Photocatalytic Properties of Palladium-loaded

Three Dimensional Flower-like Anatase TiO₂ with Dominant {001} Facets. *Journal of colloid and interface science* **2016**, *467*, 1-9.

46. Dadsetan, S.; Baghshahi, S.; Farshidfar, F.; Hadavi, S. M. M., Photodeposition of Pd Nanoparticles on TiO₂ Utilizing a Channel Type Quartz Reactor. *Ceramics International* **2017**, *43* (12), 9322-9326.

47. Kriek, R. J.; Mahlamvana, F., Dependency on Chloride Concentration and 'in-Sphere'oxidation of H₂O for the Effective TiO₂-Photocatalysed Electron Transfer from H₂O to [PdCl_n (H₂O)_{4-n}]²⁻ⁿ (n= 0-4) in the Absence of an Added Sacrificial Reducing Agent. *Applied Catalysis A: General* **2012**, *423*, 28-33.

48. Bai, Q. Synthesis of Nano-Heterodimers by Laser Photodeposition of Metal Nanodots on TiO₂ Nanoparticles. Université de Bordeaux, Bordeaux, 2019.

Chapter 5

Photodeposition of Au@Au, Au@Ag, and Au@Pd Core-Shell Structured Bimetallic Nanodots on TiO₂ Nanoparticles

Table of contents

Chapter 5	183
Photodeposition of Au@Au, Au@Ag, and Au@Pd Core-Shell Structured Bimetallic Nanodots on TiO ₂ Nanoparticles	183
5.1 Introduction	187
5.2 Experimental methods.....	189
5.3 Photodeposition of Au on Au-TiO ₂	190
5.3.1 Size-controlled deposition of Au on TiO ₂ nanoparticles.....	191
5.3.2 Varying the KAuCl ₄ amount added in the second step.....	193
5.3.3 Conclusion.....	197
5.4 Photodeposition of Ag on Au-TiO ₂	197
5.4.1 Photodeposition of Ag on Au-TiO ₂ without chloride ions.....	199
5.4.1.1 HCOONa as a hole scavenger.....	199
5.4.1.1.1 Varying amounts of AgNO ₃	199
5.4.1.1.2 Influence of the laser power.....	203
5.4.1.2 Methanol as hole scavenger.....	204
5.4.2 Photodeposition of Ag on Au-TiO ₂ with chloride ions.....	207
5.4.2.1 Varying exposure times and laser powers.....	207
5.4.2.2 Varying the amounts of AgNO ₃	209
5.4.2.3 Depositing Ag on Au-TiO ₂ which contains big Au particle.....	211
5.4.3 Conclusion.....	212
5.5 Photodeposition of Pd on Au-TiO ₂	213
5.5.1 Effect of the hole scavenger.....	213
5.5.2 Different Pd precursors.....	217
5.5.3 Conclusion.....	222
5.6 Conclusion.....	222
5.7 References.....	224

5.1 Introduction

It is well known that some of the noble-metal nanoclusters on semiconductors enhance visible-light absorption through the surface plasmon resonance (SPR) and detailed mechanistic aspects have been addressed in many kinds of literature.¹⁻³ However, not many studies have been conducted on more than one noble metal simultaneously to maximize the use of visible light. It has already been reported that bimetallic nanostructures in which two different metals are present in the same particle, can exhibit unique optical, catalytic, and electronic properties due to the synergistic effects of these two kinds of metal nanodots.⁴⁻⁷ To improve the conversion efficiency of solar energy, Au-Ag,⁸⁻⁹ Au-Pd,¹⁰ Ag-Cu,¹¹ Ag-Ni¹² and other bimetallic nanoparticles (BNPs) with core-shell structures have been loaded onto semiconductor materials as cocatalysts. See also the review by Li and co-authors.¹³ In these structures, light absorption, charge recombination dynamics as well as photoredox catalytic active sites can be well regulated.

Two-step photodeposition is a delicate strategy for the preparation of core-shell structured BNPs on semiconductor oxides otherwise alloyed metallic NPs are obtained as illustrated by Chen *et al.*¹⁴ In this way, the first deposited metal particles could act as a sink of photo-induced electrons, causing the site-specific reduction and deposition of the second metal on the surface of the first metal particle during the second deposition process. In 1990, Fernandez *et al.*¹⁵ studied the photocatalytic reduction of rhodium on photosensitive support (titania) already loaded with another metal (Pt). They found that the size and location of the rhodium particles depended on the reaction medium, and rhodium particles with 1-1.5 nm diameter were well distributed on free TiO₂ in water. In 2-propanol-water (20: 1, v/v), the deposition yielded rhodium particles 2-3 nm in diameter, also located almost on titania. Finally, in a basic medium, the deposition of rhodium occurred selectively on the pre-existing platinum particles. The effect of 2-propanol was mainly attributed to its hole-scavenging properties which

promoted the reduction of Rh³⁺ and the growth of rhodium particles by reducing the recombination of photo-produced charges. In an ammonia medium, the adsorption of Rh³⁺ ions on TiO₂ should be hindered by a large amount of NH₄⁺ ions, while easier hole-trapping at the negatively charged surface of the semiconductor allows a better separation of electron-hole pairs. These two phenomena can explain the selective deposition of rhodium on the platinum particles which are enriched in electrons by transfer from TiO₂ during irradiation. This study indicates that the second metal prefers to locate on a metal nanodot that already exists on semiconductors and finally forms core/shell bimetallic heteronanostructures, which could be of great interest in catalysis and photoelectronic devices.

Zheng *et al.*¹⁶ reported that Au, Ag, and Au-Ag BNPs were site-selectively photo-deposited on the reduction sites of TiO₂. Au-Ag loading on TiO₂ provides not only good activity performance for oxidizing 2-propanol but also high stability under visible light. They however focus on the catalytic aspect of their work and do not pay attention to the structure of what they call the Au-Ag BNPs. Tanaka and co-authors¹⁰ successfully synthesized core-shell Au-Pd particles supported on TiO₂ (Au@Pd-TiO₂) by using a two-step photodeposition method, and the Au was first reduced and deposited on TiO₂ via photoirradiation at $\lambda > 300$ nm by a 400 W high-pressure mercury arc, then Au-Pd core-shell structure was prepared by photoirradiation of the mixture of palladium chloride and Au/TiO₂ solution with the same mercury arc. They found that Au/TiO₂ and Au-free Pd/TiO₂ were inactive, whereas the core-shell Au@Pd/TiO₂ samples were active in the photocatalytic conversion of chlorobenzene and 2-propanol to benzene and acetone under visible light irradiation. Moreover, they indicated that the thickness control of Pd is important for both a satisfactory cocatalyst effect and absorption due to the Surface Plasmon Resonance (SPR) of Au nanoparticles. In a recent report, Sun *et al.*¹⁷ also applied a two-step deposition method to prepare bimetallic Au@Pd/TiO₂ catalysts with varied Pd deposition amounts by Hg lamp irradiation, and their results indicated that the Pd atoms were preferentially deposited on exposed Au surface in the form of a monolayer (**Figure 5.1**). They also mentioned the catalytic oxidation of

benzyl alcohol with prepared bimetallic Au@Pd/TiO₂ catalysts and showed that the benzyl alcohol conversion increased with Pd deposition amount at Pd loading below 0.049 wt.%, whereas the catalytic activities of the catalysts with higher Pd deposition amount remained nearly identical.

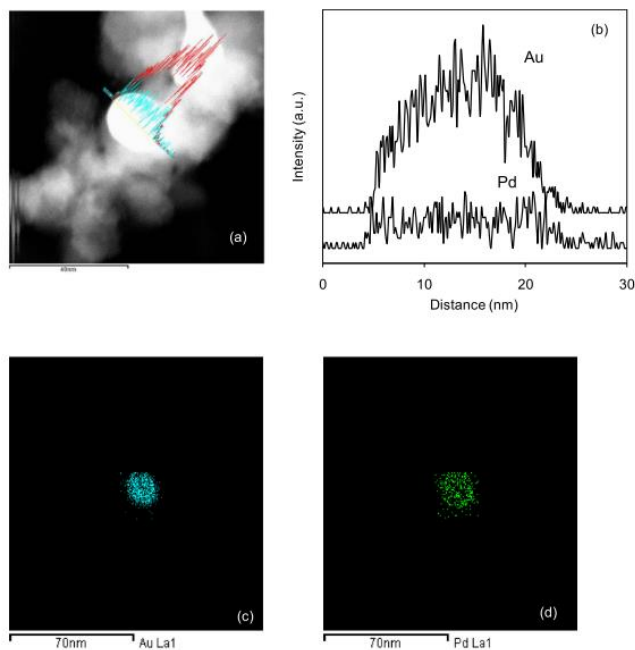


Figure 5.1 (a) TEM image, (b) EDS line-scanning profile, and elemental maps of (c) Au and (d) Pd for Au@Pd/TiO₂.¹⁷

In this chapter, a two-step deposition method is employed to synthesize bimetallic core-shell structures Au@Au-TiO₂, Au@Ag-TiO₂, and Au@Pd-TiO₂ by using the UV laser (364nm) as a light source. The effects of irradiation power, exposure time, hole scavenger, and chlorides ions on the formation of core-shell BNPs were studied.

5.2 Experimental methods

TiO₂ polyhedrons were used as the substrate and Au NDs were firstly deposited on TiO₂ followed by Ag or Pd due to the higher reduction potential of Au. The reaction solution was prepared by mixing TiO₂ aqueous solution (19 mM, 0.289 mL) and a fresh KAuCl₄ aqueous solution (10 mM, 50 μ L), and 0.5 mL of methanol. The pH of the

mixture was adjusted at 3.3 using a nitric acid solution. To remove the oxygen existing in the solution, the solutions were purged with Ar gas for 10 min and then mixed just before illumination. During the irradiation process, the cuvette was well sealed and the solution was stirred at a speed of 300 rpm. After the first step deposition, a given amount of the second metal precursor (KAuCl₄, AgNO₃, Na₂PdCl₄, and H₂PdCl₄) solution was added into the as-prepared Au-TiO₂ solution for the second round photodeposition. When mentioned, the synthesized Au-TiO₂ particles were also separated via centrifugation (18000g, 20 min) and washed with deionized water to remove the existing chloride ions and methanol in the solution and prevent flocculation or aggregation due to this anion. After purification by centrifugation, these Au-TiO₂ particles were redispersed into a pH 3.3 nitric acid solution and a new hole scavenger (methanol or sodium formate) and metal precursor were added to perform the second step deposition.

The procedure for preparation of the TEM grid is the following. The solution was treated by ultrasonication for 5 min to disperse the nanoparticles, and then one drop (3-4 μ l) of this solution was cast on a TEM grid. A paper tissue was used to absorb the liquid from the top side to the backside of the grid, which only allowed the liquid to pass through and leave the nanoparticles on the top side. Three or more nitric acid drops (at pH 3.3) were also cast to clean the sample particles.

5.3 Photodeposition of Au on Au-TiO₂

As shown in Chapter 3, we have already successfully synthesized Au-TiO₂ heterodimers. Here, in the first part, the second-step deposition was used to regrow Au on Au-TiO₂ to acquire Au-TiO₂ heterodimers with enlarged Au nanoparticles. To distinguish the initial Au-TiO₂ heterodimers which were used for further deposition, the catalysts made by the second deposition were named Au@Au-TiO₂.

5.3.1 Size-controlled deposition of Au on TiO₂ nanoparticles

As Au nanodots on TiO₂ will be acted as seeds and electrons sink for the deposition, the size of Au particles probably has great effects on the second-round photodeposition. Thus, Au–TiO₂ heterodimers with different sizes of Au were used as substrates for the second step deposition. Au–TiO₂ heterodimers with different sizes of Au particles were synthesized by adjusting the concentration of KAuCl₄ (0.125, 0.250, and 0.500 mM). Then, 0.125, 0.250, and 0.500 μmol of KAuCl₄ were added to the respective solution for the second-step deposition. In the irradiation process, a 56.1 mW applied power was adopted and the exposure time for each step deposition is 4 min, and [TiO₂] is 5.5 mM. The TEM images and histograms of the metal particle size distributions are presented in **Figure 5.2**. The size of the Au NDs and Au-TiO₂ nanoheterodimers (NHDs) yields were calculated based on TEM characterizations (**Table 5.1**). The NHDs yield was nearly unchanged comparing the first and second step deposition, which confirms that secondary nucleation is energetically less favorable than growing an already existing Au ND. Nonetheless, it was clearly shown that after the second-step deposition, the Au mean size increased from 7.6, 8.6, and 10.8 nm to 9.5, 11.5, and 15.1 nm, respectively. This phenomenon indicated that all the Au³⁺ ions added in the second step prefer to locate on the previously existing Au ND which is coherent with literature reports.^{4, 15}

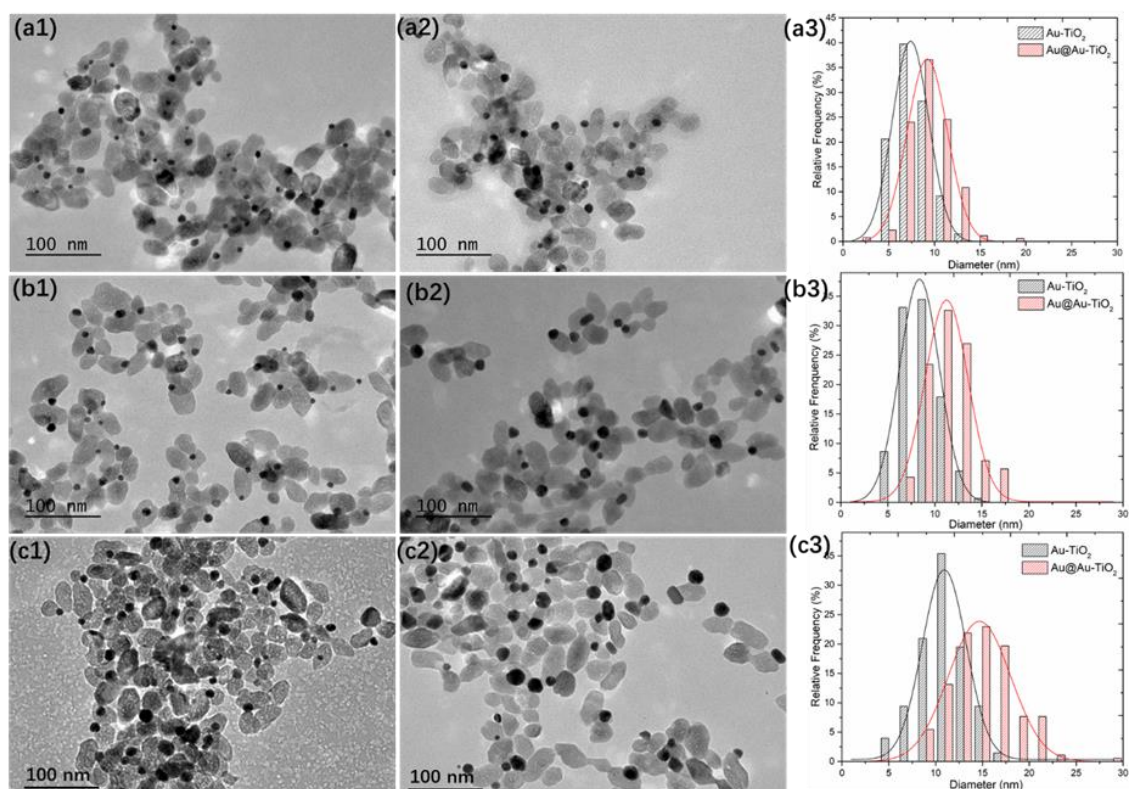


Figure 5.2 TEM images of Au-TiO₂ NHDs obtained by first step deposition (a1, b1, and c1) when [KAuCl₄] is 0.125, 0.250 and 0.500 mM, respectively. Then 0.125, 0.250, and 0.500 μmol KAuCl₄ were added to the corresponding solution to perform the second deposition (a2, b2, and c2), and their corresponding size distributions (a3, b3, and c3). Experimental conditions are: [TiO₂] = 5.5 mM, 50 vol.% methanol as a hole scavenger, the applied power and exposure time remaining the same for each step deposition, P_{applied} = 56.1 mW and t = 4 min.

As shown in **Table 5.1**, the sizes of Au particles measured from TEM images are very close to the estimated value which is calculated based on the NHDs yield obtained in experiments and assuming all the gold precursor including the first and second step was 100% consumed (see Appendix 1.3 and 1.4). Obviously, it can be confirmed that the gold precursors added in the reaction solution were completely consumed for synthesizing Au core and shell.

Table 5.1 Data of Au size and NHDs yield of Au-TiO₂ NHDs after first and second step depositions. Experimental conditions are: [TiO₂] = 5.5 mM, 50 vol.% methanol as a hole scavenger, applied power is 56.1mW and exposure time is 4 min for each step.

	KAuCl ₄ added (μmol)	Metal particle size(nm)	Predicted metal size	Heterodimer yield (%)	Au shell (nm)
First step	0.125	7.6 ± 1.9	8.0	46	0.95
Second step	0.125	9.5 ± 2.2	9.5	48	
First step	0.250	8.6 ± 2.0	8.9	57	1.20
Second step	0.250	11.5 ± 2.3	11.5	54	
First step	0.500	10.8 ± 2.5	11.4	55	2.15
Second step	0.500	15.1 ± 3.3	14.6	53	

Overall, we successfully obtained the Au@Au-TiO₂ with 0.95, 1.20, and 2.15 nm Au shells, and the experimental data were very close to our expectations. Moreover, it seems that the size of previously Au has no influence on the Au shell formation by second-step deposition.

The experimental and predicted sizes after the first step and the second step shown in **Table 5.1** are very close, meaning the gold ions added in either step are almost completely consumed.

5.3.2 Varying the KAuCl₄ amount added in the second step

In this section, we fixed the size of Au particles obtained in the first-step deposition, and different amounts of gold precursors were added for the second-step deposition to study whether the Au size could be controlled and gradually enlarged. The color of the sample solution changed when increasing the amount of KAuCl₄ (**Figure 5.3(a)**); the initial pink solution acquired during the first step deposition gradually deepened and turned dark purple with increasing the amount of KAuCl₄. The color change

indicates that the Au NDs are getting bigger. This is confirmed by the UV-vis spectra displayed in **Figure 5.3 (b)** which shows the continuous red-shift of the SPR band of Au from 535 to 561nm due to the increase of Au size.

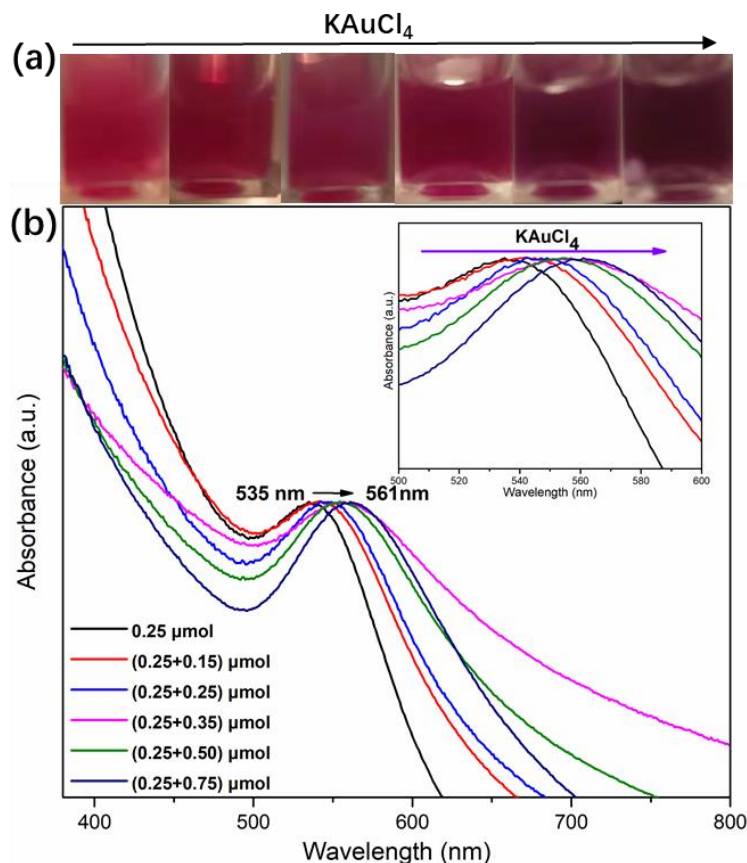


Figure 5.3 (a) Images of the product solution and after a two-step deposition and various concentrations of KAuCl₄ (0.15, 0.25, 0.35, 0.5, and 0.75 μmol), (b) UV-vis spectra of Au-TiO₂ NHDs solution. First step deposition: [TiO₂] = 5.5 mM, [KAuCl₄] = 0.25 mM (0.25 μmol of KAuCl₄), 50 vol.% methanol used as a hole scavenger, applied power of 56.1mW and exposure of 4min. Second step deposition: different amounts of KAuCl₄ (0.15, 0.25, 0.35, 0.5, and 0.75 μmol) were added to the prepared Au-TiO₂ solution, this solution was then irradiated for another 4 min with the same applied power.

The TEM characterization was also performed to study the variation of the gold size on the Au-TiO₂ NHDs (**Figure 5.4, Table 5.2**, see also **Figure 5.5**). Au NDs with an 8.7 nm mean diameter were synthesized by one-step deposition when the concentration of KAuCl₄ was 0.25 mM (0.25 μmol of KAuCl₄). It increased to 10.3 nm by adding an extra 0.15 μmol amount of KAuCl₄ for the second-step deposition. As shown by the histograms of Au NDs size distributions in **Figure 5.4**, the more KAuCl₄ was added and the bigger Au particles were observed. The detailed results are listed in **Table 5.2**.

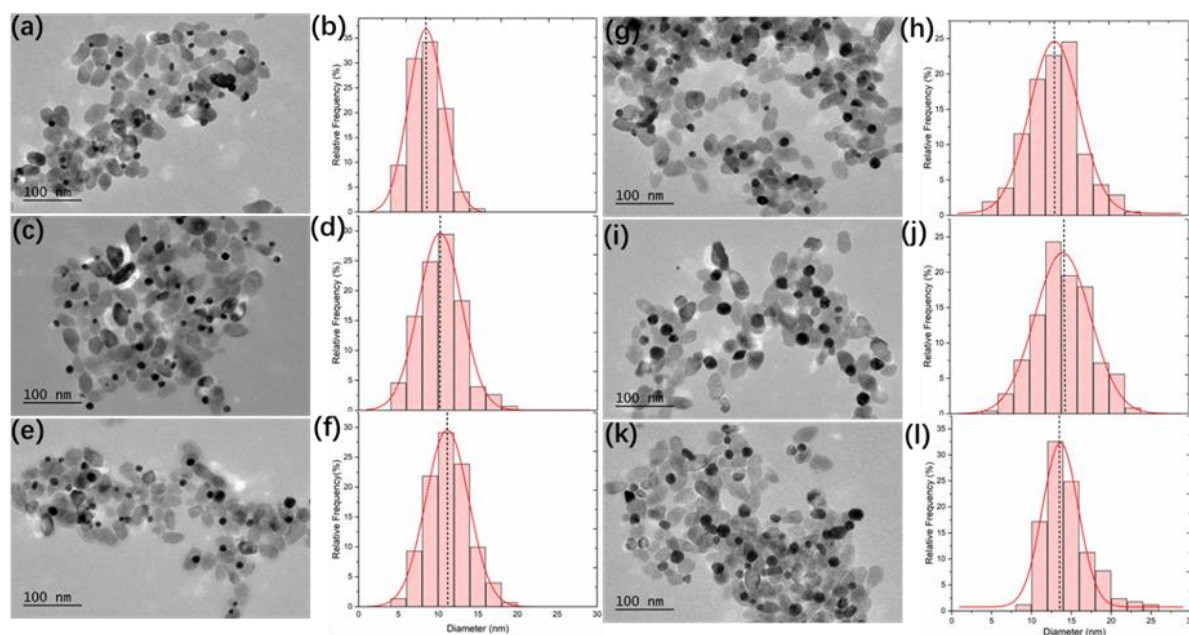


Figure 5.4 TEM images of Au-TiO₂ NHDs synthesized by one step (a), and two-step deposition with different KAuCl₄ contents (c, e, g, i, and k) and their corresponding size distributions (b, d, f, h, j, and l). First step deposition: [TiO₂] = 5.5 mM, [KAuCl₄] = 0.25 mM (0.25 μmol of KAuCl₄), 50 vol.% methanol as a hole scavenger, applied power of 56.1mW, and exposure time of 4 min. Second step deposition: 0.15 μmol (c), 0.25 μmol (e), 0.35 μmol (g), 0.5 μmol (i), and 0.75 μmol (k) of KAuCl₄ were added to the prepared Au-TiO₂ solution, then this solution was irradiated for another 4min by the same laser applied power as in the first step.

The NHDs yields (**Table 5.2**) of Au-TiO₂ are almost the same since they are in the narrow range of 44 to 53%. The Au NDs can be enlarged to 14.5 nm from the initial 8.7 nm, indicating an Au shell with a thickness of 2.9 nm was produced for the highest used KAuCl₄ ratio (0.25 μmol +0.75 μmol). Furthermore, the sizes of Au NDs are all very close to the estimated values (see Appendix 1.3) suggesting that the quantity of gold precursor was completely consumed to grow the shell on the preformed Au NDs.

Table 5.2 Data on Au NDS size and NHDs yield of Au-TiO₂ NPs made by one-step and two-step depositions with different KAuCl₄ contents. First step deposition: [TiO₂] = 5.5 mM, [KAuCl₄] = 0.25 mM (0.25 μmol of KAuCl₄), 50 vol.% methanol as a hole scavenger, applied power is 56.1 mW and exposure time is 4min. Second step deposition: different amounts of KAuCl₄ were added into the prepared Au-

TiO₂ solution, then irradiated this solution for another 4 min with the same power as in the first step. The value is calculated based on the heterodimer yield of Au-TiO₂ obtained by experiments and the assumption of the KAuCl₄ is 100% consumed (see Appendixes 1.3 and 1.4).

	KAuCl ₄ added (μmol)	Metal particle size (nm)	Predicted metal size (nm) ^a	Heterodimer yield (%)	Au shell (nm)
First step	0.25	8.7 ± 2.0	9.8	44	/
Second step	0.15	10.3 ± 2.7	10.7	53	0.80
	0.25	11.4 ± 2.6	12.2	45	1.35
	0.35	13.2 ± 2.3	13.1	44	2.25
	0.50	14.3 ± 3.4	13.4	51	2.8
	0.75	14.5 ± 2.9	14.8	51	2.9

The comparison of the Au NDs size with the estimated value is clearly shown in **Figure 5.5a**. The sizes of Au NDs measured from TEM images are pretty close to the estimated values ($D(t \rightarrow \infty) = \left(\frac{[Au^{3+}]_0}{Y[NP]} \cdot \frac{8v_{Au}}{\pi\kappa(\theta)} \right)^{1/3}$). Moreover, the very obvious increase tendency of Au size is displayed. In addition, we also analyzed this data using the modeling built-in in chapter 3 and the data variations perfectly fit the modeling (detail in chapter 3.4.5.4).

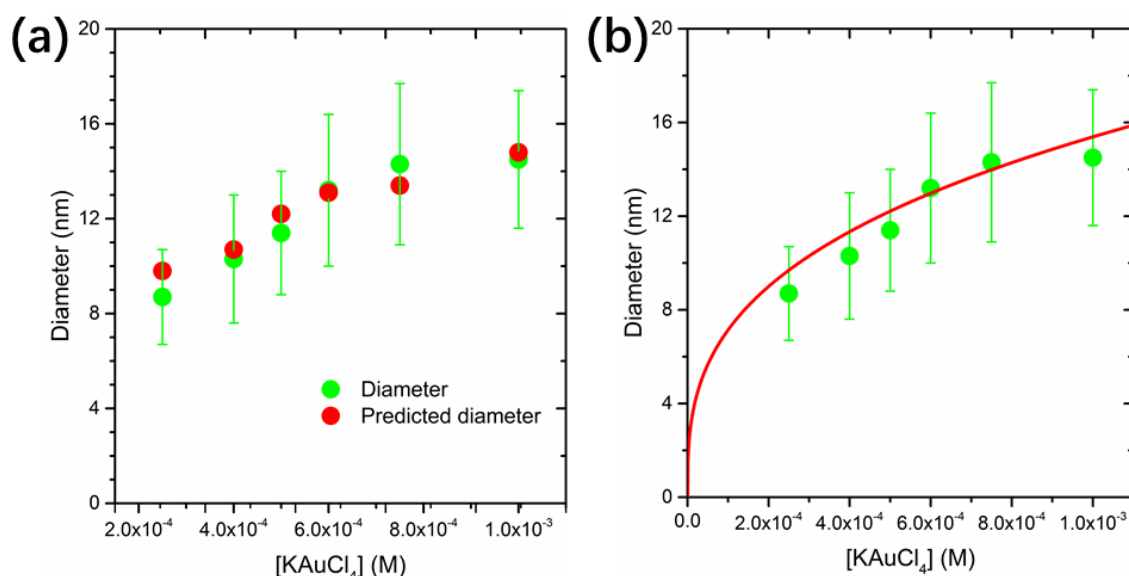


Figure 5.5 (a) experimental and predicted Au ND size of Au-TiO₂ HNDs made by two-step deposition with different KAuCl₄ contents. (b) The red curve is a fit according to the modeling in chapter 3 (part 3.4.5.4). First step deposition: [TiO₂] = 5.5 mM, [KAuCl₄] = 0.25 mM (0.25 μmol of KAuCl₄), 50 vol.% methanol as a hole scavenger, the applied power of 56.1mW, and the exposure time of 4 min.

5.3.3 Conclusion

In this section, we performed experiments on the photodeposition of Au on Au-TiO₂ NHDs by a two-step deposition. The results demonstrated that 1) the Au³⁺ ions added in the second step were preferentially reduced on the pre-existing Au NDs, 2) all of them were successfully covered with an Au shell, forming core-shell Au@Au-TiO₂ BNPs, 3); there was nearly no formation of a second smaller population of gold NPs so that all the gold was used to increase the size of the pre-existing ones. Furthermore, the Au shell can be controlled by varying the concentration of the gold precursor and the experimental data are very close to our expectations. This demonstrates that the two-step deposition is a very facile and precise approach to controlling and enlarging the Au NDs to target a specific size.

5.4 Photodeposition of Ag on Au-TiO₂

In this part, we aimed at synthesizing authentic bimetallic Au-Ag core-shell metal nanodots on TiO₂ by sequential deposition of Au and Ag on TiO₂ as a substrate. These heteronanoobjects were synthesized using the same procedures described above except we used AgNO₃ as the Ag precursor instead of KAuCl₄ in the second-round photodeposition. TEM images of the heterostructures and corresponding size distribution histograms of Au-Ag nanodots are presented in **Figure 5.6**. Au-TiO₂ heterodimers with Au NDs 9.1 nm in mean diameter were made in the first step of photodeposition. AgNO₃ solution (0.5 μmol of AgNO₃) was then added to the as-prepared Au-TiO₂ solution and the mixture was photoirradiated for the preparation of Au@Ag-TiO₂ heterostructures. The average diameter (9.1 nm) of Au NDs is highly consistent with the estimated value (9.7 nm, see the calculation Appendix 1.2).

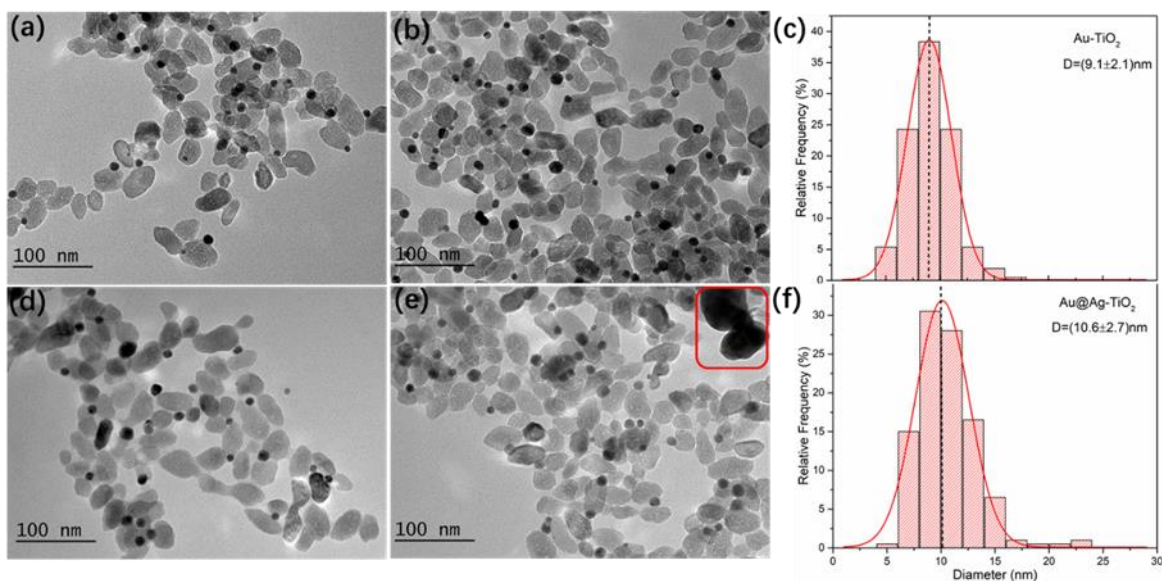


Figure 5.6 TEM images of Au-TiO₂ (a, b) and Au@Ag-TiO₂ (d, e) NHDs and their corresponding size distributions (c, f). Experimental conditions: First step deposition, [TiO₂] = 5.5 mM, [KAuCl₄] = 0.25 mM (0.25 μmol of KAuCl₄), 50 vol.% methanol as a hole scavenger, applied power is 56.1 mW and exposure time is 4 min. Second step deposition: 0.5 μmol of AgNO₃ was added to the prepared Au-TiO₂ solution, then this solution was irradiated for another 4 min by the same laser power as in the first step.

The yields of BNPs remained in the 45 to 51% range after the second-step deposition and the average size of the metallic side is 10.6 nm. Similar Heterodimer yields and increased metallic particle size indicated that the Ag grew on Au NDs without self-nucleation on TiO₂. However, the average size of the metal particles increased only to 10.6 nm which is much smaller than the predicted value (13.7 nm, see the calculation in Appendix 1.4). The Ag shell obtained is 0.75 nm, three times smaller than the estimated value (2.25 nm), implying that only a fraction of AgNO₃ was reduced for the construction of the Ag shell. The rest of the Ag⁺ ions did react with Cl⁻ anions that came from the dissociation of KAuCl₄ and finally formed AgCl as a by-product poorly soluble in water/methanol solution. This argument could be supported by the presence of extremely large nanoparticles around a hundred nanometers (**Figure 5.6e**).

Therefore, we performed some experiments with and without Cl⁻ ions to investigate the effect of Cl⁻ on photodeposition. Furthermore, the effects of different hole scavengers (methanol and sodium formate), exposure times, and laser powers on the

formation of the Ag shell were also studied.

5.4.1 Photodeposition of Ag on Au-TiO₂ without chloride ions

To avoid the presence of chloride ions, we extensively washed the Au-TiO₂ NHDs obtained in the first-step photodeposition. The purified Au-TiO₂ HNDs were redispersed in a pH 3.3 water solution thanks to HNO₃. We then studied the role of two different hole scavengers, *i.e.*, methanol and sodium formate (HCOONa).¹⁸ Moreover, different amounts of AgNO₃, different exposure times, and different illumination powers were applied.

5.4.1.1 HCOONa as a hole scavenger

The hole scavenger plays a critical role in photodeposition. The previous studies¹⁸ in our group have shown that HCOONa as a hole scavenger was more effective than methanol in depositing a single Ag particle onto the TiO₂ surface. Indeed, many tiny Ag nanodots were deposited on each TiO₂ nanoparticle instead of a single one when methanol was used as a hole scavenger. Therefore, HCOONa was also used as a hole scavenger in this deposition of Ag on Au-TiO₂ heterodimers.

5.4.1.1.1 Varying amounts of AgNO₃

We first synthesized Au-TiO₂ heterodimers with an average Au nanodot diameter of 10.5 nm. After removing chloride ions from the Au-TiO₂ solution by centrifugation/redispersion processes, different amounts of AgNO₃ (0.5, 1, and 2 μmol) and the same respective equivalents of HCOONa (0.5, 1, and 2 μmol) were added, and this solution was irradiated for 16 more min by the laser with an applied power of 56.1 mW. **Figure 5.7** shows the TEM images of the resulting Au@Ag-TiO₂ BNPs performed for different AgNO₃ concentrations.

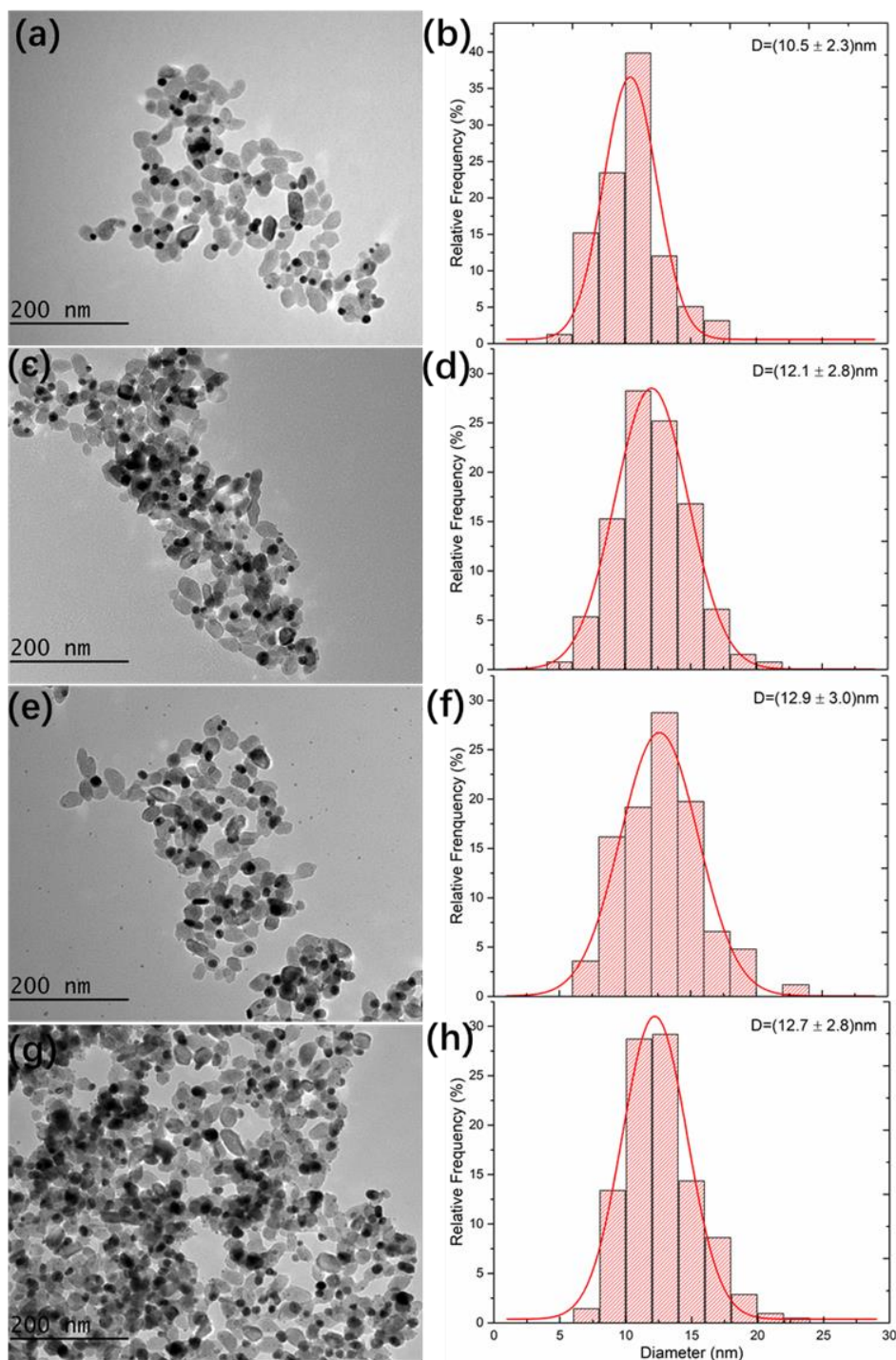


Figure 5.7 TEM images of Au-TiO₂ (a) and Au@Ag-TiO₂ (c, e, and g) NPs and their corresponding size distributions (b, d, f, and h). Experimental conditions: First step deposition, [TiO₂] = 5.5 mM, [KAuCl₄] = 0.5 mM (0.5 μmol of KAuCl₄), 50 vol.% methanol as a hole scavenger, applied power of 56.1 mW, and exposure time of 4 min. The Au-TiO₂ particles were separated *via* centrifugation (18000g, 20 min), washed one-time using deionized water, and redispersed into a pH 3.3 solution using nitric acid. Second step deposition: 0.5 (c), 1 (e), and 2 μmol (f) of AgNO₃ solution (50, 100, and 200 μl of 10 mM AgNO₃ solution) and one equivalent of HCOONa per AgNO₃ solution were added; this mixture solution was then irradiated for another 16 min with the same laser power.

The size of the metal particle increased from 10.5 to 12.1 nm, indicating that a thin Ag shell layer (0.8 nm) was deposited on the Au NDs. However, we also observe on the TiO₂ particles the formation of tiny metal NDs with a diameter smaller than 3 nm which are considered as Ag NDs because their diameter is much smaller than that of the Au NDs produced in the first deposition step (**Figure 5.7b**); their number also increases significantly with increasing the amount of AgNO₃. These tiny Ag NDs were not considered in the statistical measurement of the metal particle size.

Table 5.3 Data concerning the metallic particle size and heterodimer yields of the two-step syntheses of Au@Ag-TiO₂. First step deposition: [TiO₂] = 5.5 mM, [KAuCl₄] = 0.5 mM (0.5 μmol of KAuCl₄), 50 vol.% methanol as a hole scavenger, applied power is 56.1mW, and exposure time of 4 min. Second step deposition: different amounts of AgNO₃ and an equivalent of HCOONa per AgNO₃ were added; then this solution was irradiated for 16 more min by the laser with an applied power of 56.1 mW. The calculation of the predicted Ag shell can be seen in Appendix 1.4.

Sample	AgNO ₃ (mM)	NHDs yield (%)	Diameter of Metallic particle (nm)	Ag thickness (nm)	Predicted Ag shell thickness (nm)
Au-TiO ₂	0	52	10.5 ± 2.3	0	0
Au@Ag-TiO ₂	0.5	47	12.1 ± 2.8	0.8	1.7
Au@Ag-TiO ₂	1.0	51	12.9 ± 3.0	1.2	2.9
Au@Ag-TiO ₂	2.0	55	12.7 ± 2.8	1.1	4.5

By comparing the obtained and expected values listed in Table 5.3, the thickness of the Ag shell coated on Au particles was found much smaller than predicted. In addition, the Ag thickness increased slightly (0.8 nm to 1.2 nm) while increasing the AgNO₃ amount from 0.5 to 1.0 μmol to reach a plateau, even when up to 2.0 μmol of precursor were added. When the thickness of the Ag shell reaches a value close to ~ 1 nm, the Ag shell stops growing and an increasing amount of tiny individual Ag nanodots appears on the surface of TiO₂.

UV-vis spectroscopy was also performed on these samples (**Figure 5.8a**). There is a characteristic peak of Au nanodots at 542 nm for the Au-TiO₂ heterodimers. After the Ag deposition over Au-TiO₂, the SPR of the Au core shifts to a lower wavelength as a

result of the change of refractive index surrounding Au and the appearance of a new band at 408 nm due to Ag. This also implies that an Ag shell was successfully coated on Au nanoparticles.¹⁹⁻²¹ When adding and then increasing the amount of AgNO₃ from 0.5 to 1.0 μmol, we observe a blue shift of the position of the LSPR band to 530 nm indicating (i) the presence of a layer of Ag and (ii) the formation of a thicker layer of Ag, also coherent with the TEM results.

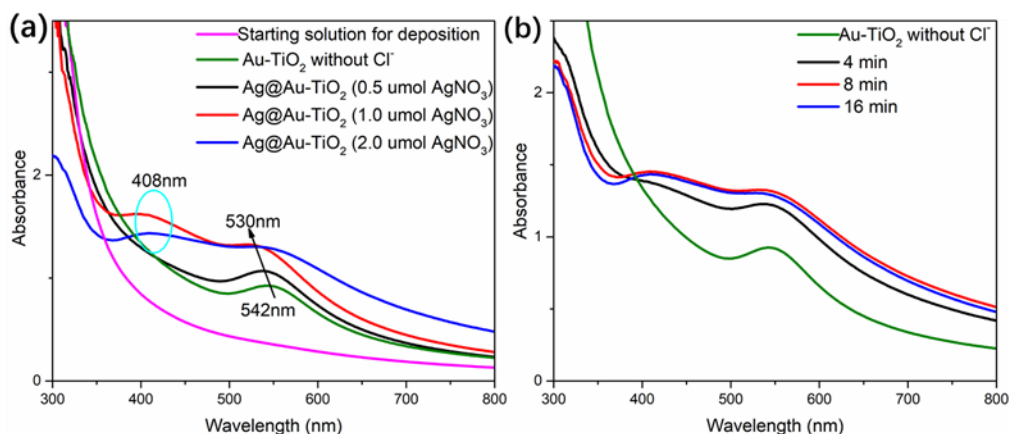


Figure 5.8 UV-vis spectra of reactant solutions. (a) different amounts of AgNO₃, (b) different exposure times when 2.0 μmol of AgNO₃ were added for the second-step deposition.

In the same way that the removal of electrons from a metal nanoparticle results in a slight red shift in the surface plasmon peak to higher wavelengths,²²⁻²³ it has also been observed experimentally, as here, that the surface plasmon peak of the gold core in the Au@Ag particle is blue-shifted with increasing Ag shell thickness.²⁴

In addition, different exposure times were performed for the second-step photodeposition to ensure there was enough time for Ag to deposit. **Figure 5.8b** displays the UV-vis spectra of the Au@Ag-TiO₂ samples synthesized after 4, 8, and 16 min second-step photodeposition times and 2.0 μmol of AgNO₃. The peak positions and SPR intensities are almost identical after 8 and 16 min exposure times. Moreover, the intensity of the absorption band at 408 nm at 4 min is weaker than that at 8 and 16 min, indicating the 4-min exposure time is not enough and that 8-min exposure is compulsory to ensure the deposition completion.

5.4.1.1.2 Influence of the laser power

From the above section, we found that the expected Ag shell was not acquired even with HCOONa as a hole scavenger and without Cl⁻ in solution. Instead, secondary nucleation occurred leading to some tiny Ag NDs on TiO₂. To inhibit this Ag secondary nucleation, we decided to reduce the laser power. This should decrease the reaction kinetics since it plays a significant role in crystal nucleation and growth. An applied power of 20 mW was adopted instead of 56.1 mW. The TEM results are shown in **Figure 5.9** and **Table 5.4**.

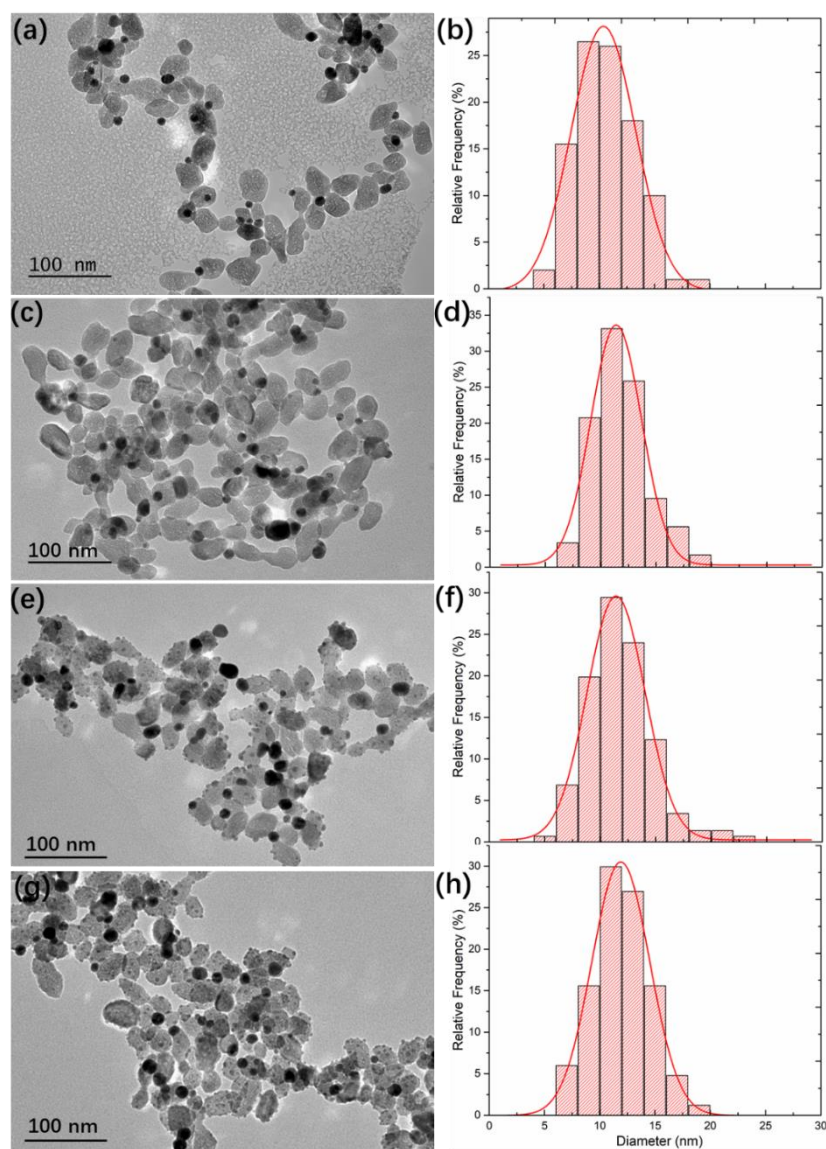


Figure 5.9 TEM images of Au-TiO₂ (a) and Au@Ag-TiO₂ (c, e, and g) NPs and their corresponding size distributions (b, d, f, and h). Experimental conditions: First step deposition, [TiO₂] = 5.5 mM, [KAuCl₄] =

0.5 mM (0.5 μmol of KAuCl₄), 50 vol.% methanol as a hole scavenger, an applied power of 56.1mW, and an exposure time of 4min. The Au-TiO₂ particles were separated by centrifugation (18000g, 20 min) and washed once using deionized water, and were redispersed into a pH 3.3 solution using a nitric acid solution for the second-step deposition. Second step deposition: 0.5 (c), 1 (e), and 2 μmol (f) of AgNO₃ and an equivalent of HCOONa per AgNO₃ solution were added; this solution was then irradiated for another 8 min by the laser with an applied power of 20 mW.

Table 5.4 Data concerning the metallic particle size and heterodimer yield. First step deposition: [TiO₂] = 5.5 mM, [KAuCl₄] = 0.5 mM (0.5 μmol of KAuCl₄), 50 vol.% methanol as a hole scavenger, an applied power of 56.1mW, and an exposure time of 4min. Second step deposition: different amounts of AgNO₃ and an equivalent of HCOONa per AgNO₃ were added; this solution was then irradiated for another 8 min by the laser with an applied power of 20 mW. The calculation of the predicted Ag shell can be seen in Appendix 1.4.

Sample	AgNO ₃ (mM)	NHDs yield (%)	Diameter of Metallic particle (nm)	Ag thickness (nm)	Predicted Ag shell thickness (nm)
Au-TiO ₂	0	52	10.6 ± 2.6	0	0
Au@Ag-TiO ₂	0.5	48	11.8 ± 2.5	0.6	1.7
Au@Ag-TiO ₂	1.0	49	11.8 ± 2.9	0.6	2.9
Au@Ag-TiO ₂	2.0	51	12.0 ± 2.5	0.7	4.5

Figure 5.9 shows there were no tiny Ag ND for 0.5 μmol of AgNO₃. However, many tiny Ag NDs were produced as soon as we increased this precursor concentration even with this low laser power applied. The Ag shell synthesized at low power was slightly thinner than that obtained at high power (**Tables 5.3** and **5.4**). This, therefore, indicates that low laser power is not better for the formation of an Ag layer on Au particles. It even seems to be the opposite; indeed, by comparing figures 5.7e and 5.9e, we can see that the number of tiny silver NDs is higher at low power.

5.4.1.2 Methanol as hole scavenger

As mentioned before, HCOONa, used as a hole scavenger, is efficient to deposit Ag on the TiO₂ surface. However, from the results we obtained previously, HCOONa may not be a good option because it easily induces many tiny Ag NDs directly on TiO₂ after having generated a given layer thickness on the Au particle. Here, we use again methanol as a hole scavenger to deposit Ag on Au-TiO₂ NHDs, still in the absence of

Cl⁻ ions. Different laser powers were applied. The TEM results are shown in **Figure 5.10** and **Table 5.5**.

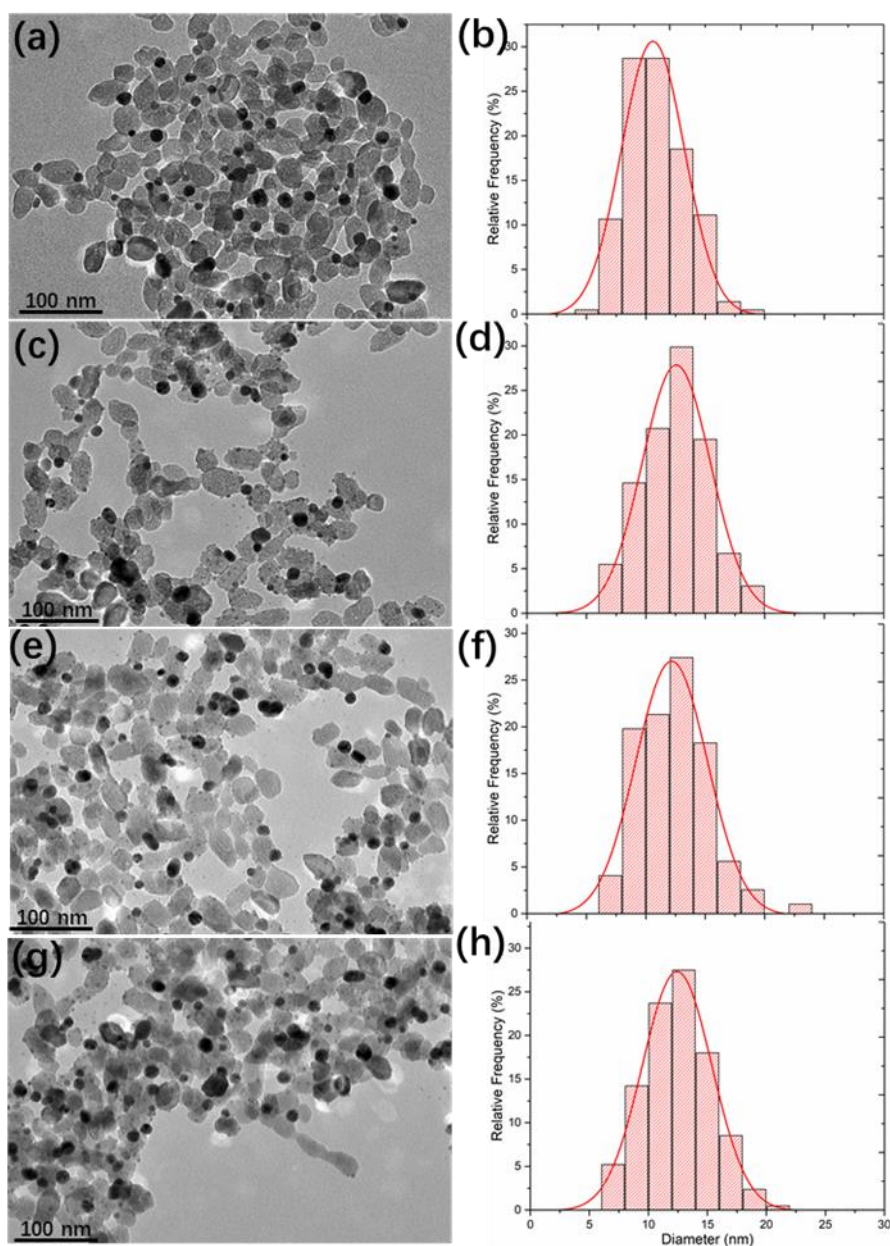


Figure 5.10. TEM images of Au-TiO₂ (a) and Au@Ag-TiO₂ (c, e, and g) NPs and their corresponding size distributions (b, d, f, and h). Experimental conditions: First step deposition, [TiO₂] = 5.5 mM, [KAuCl₄] = 0.5 mM (0.5 μmol of KAuCl₄), 50 vol.% methanol as a hole scavenger, applied power of 56.1mW, and exposure time of 4 min. Redisperison of the Au-TiO₂ particles with Cl⁻-free aqueous nitric acid (pH 3.3). Second step deposition: 0.5 μmol of AgNO₃, 50 vol.% methanol; this solution was then irradiated for another 16 min by the laser with applied powers of 10 (c), 20 (e), and 56.1 mW (f).

Here again, plenty of small Ag particles tend to form, and the thickness of the Ag

shell remains almost the same (0.8 nm) whatever the laser powers (**Table 5.5**). Comparing with the data above, we can conclude that 1) the Ag shell thickness does not seem to depend on the chemical nature of the hole scavenger used, methanol or HCOONa; 2) the appearance of many tiny Ag NDs is not either related to the kind of hole scavenger.

Table 5.5 Data concerning metallic particle size and heterodimer yields Au@Ag-TiO₂. First step deposition: [TiO₂] = 5.5 mM, [KAuCl₄] = 0.5 mM (0.5 μmol of KAuCl₄), 50 vol.% methanol as a hole scavenger, an applied power of 56.1 mW, and an exposure time of 4 min. Redispersion of the Au-TiO₂ particles with Cl⁻-free aqueous nitric acid (pH 3.3). Second step deposition: 0.5 μmol of AgNO₃ was added, 50 vol.% methanol as a hole scavenger; this solution was then irradiated for another 16 min using different applied laser powers. The calculation of the predicted Ag shells can be seen in Appendix 1.4.

Sample	Applied Power (mW, second step)	NHDs yield (%)	Diameter of NDsS (nm)	Ag thickness (nm)	Predicted Ag shell thickness (nm)
Au-TiO ₂	/	51	10.9 ± 2.5	0	0
Au@Ag-TiO ₂	10	50	12.5 ± 2.7	0.8	1.7
Au@Ag-TiO ₂	20	49	12.4 ± 2.9	0.75	1.7
Au@Ag-TiO ₂	56.1	51	12.5 ± 2.8	0.8	1.7

In a short conclusion, the second step for Ag deposition was carried out in this part by using Au-TiO₂ solution without Cl⁻ ions, and HCOONa or methanol as hole scavengers in the second-step deposition. By varying the exposure times, powers, and amounts of AgNO₃, we tried to increase the thickness of the Ag shell. It however remained quite constant and much thinner than the predicted value, with a maximum obtained thickness of about 1 nm. Moreover, once this value was reached and whatever the conditions, we systematically observed the formation of many tiny Ag NDs on the TiO₂ surface, which is far from our initial goal of synthesizing Au@Ag core-shell on the surface of TiO₂ particles.

5.4.2 Photodeposition of Ag on Au-TiO₂ with chloride ions

Since our attempts to work with chloride-free solutions based on the tendency of chlorides to precipitate Ag⁺ and form AgCl crystals failed in the case of Ag deposition on the Au-TiO₂ NHDs (the thickness of the Ag shell was much less than predicted, and there were many tiny Ag NDs located on TiO₂ which is a big issue to synthesize Au@Ag-TiO₂ heterodimers), we decided to go back to the primary protocol, adding the Ag precursor directly to the prepared Au-TiO₂ solution obtained in the first-step deposition. Exposure time, laser power, and precursor concentration were varied to achieve our goal.

5.4.2.1 Varying exposure times and laser powers

In this section, the Au-TiO₂ NHDs were prepared under the same condition as mentioned above. The diameter of the Au NDs is 10.7 (2.3) nm and the Heterodimer yield is around 48 %. Then 0.5 μmol of AgNO₃ was used to perform the second-step deposition with different applied powers and exposure times. The samples obtained under this condition did not show the presence of tiny Ag NDs on TiO₂ NPs which is completely different from what is observed when the system is chloride-free. Representative TEM images are shown in **Figure 5.11**.

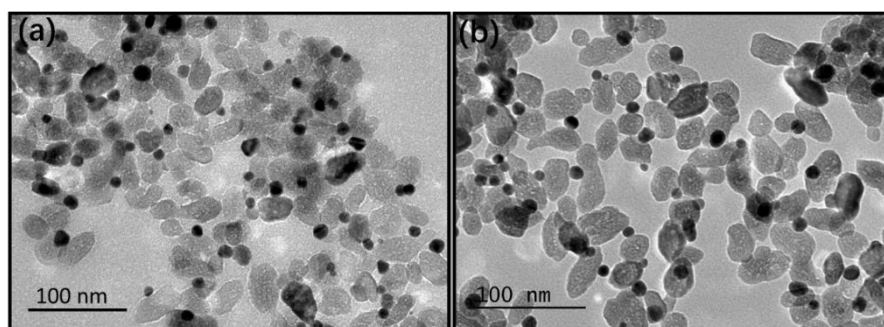


Figure 5.11 TEM images of Au-TiO₂ (a) and Au@Ag-TiO₂ (b). Au-TiO₂ synthesized condition: [KAuCl₄] = 0.5 mM, 50 vol.% methanol as a hole scavenger, the applied power is 56.1 mW, and the exposure time is 4 min. Au@Ag-TiO₂ was prepared with 0.5 μmol of AgNO₃, 4 min exposure time, and 56.1 mW applied power.

The size of the metallic nanoparticles, the predicted values, and heterodimer yields are presented in **Table 5.6**. The thickness of the Ag shell obtained with the different laser powers and exposure times is in the range of 0.5 and 0.9 nm which is once again much less than the predicted value (1.7 nm). It looks like the Ag shell gradually thickens with the increasing exposure time at a power of 56.1 mW, but there is no direct relationship between the Ag shell and the laser power. Since there is no obvious difference in these thickness values, it is difficult to see which condition is better for thick Ag shell formation.

Table 5.6 Data concerning the NDs size and heterodimer yields of Au@Ag-TiO₂. First step deposition: [TiO₂] = 5.5 mM, [KAuCl₄] = 0.5 mM, 50 vol.% methanol as a hole scavenger, applied power of 56.1 mW, and 4 min exposure time. Second step deposition: 0.5 μmol of AgNO₃ was added, and the second-step deposition was then performed by applying different powers and exposure times. The calculation of the predicted Ag shell can be seen in Appendix 1.4.

Applied power (mW)	Exposure time (min)	NHDs yield (%)	Diameter of NDs (nm)	Ag thickness (nm)	Predicted Ag shell thickness (nm)
10	16	53	12.4 ± 2.6	0.9	1.7
20	16	48	11.8 ± 2.8	0.6	1.7
56.1	16	52	12.3 ± 2.5	0.8	1.7
56.1	8	48	11.8 ± 2.4	0.6	1.7
56.1	4	47	11.7 ± 3.2	0.5	1.7

In addition to the TEM characterization, STEM combined with elemental mapping was employed to have a better insight into the morphology of the metal particles in the bimetallic structure. The elemental mapping of Au and Ag on the metal particle confirmed the presence of a core@shell structure of the Au@Ag particle with Au as the core and Ag as the shell and the results are shown in **Figure 5.12**. Since the Ag shell is very thin, the signal intensity is not as bright as we would expect but more explicit than the results from the literature.⁷ Moreover, We show here that the Ag prefers to grow on the big Au particles (**Figure 5.12b**) and only where gold is present. There is no additional growth of silver nanoparticles on previously bare TiO₂.

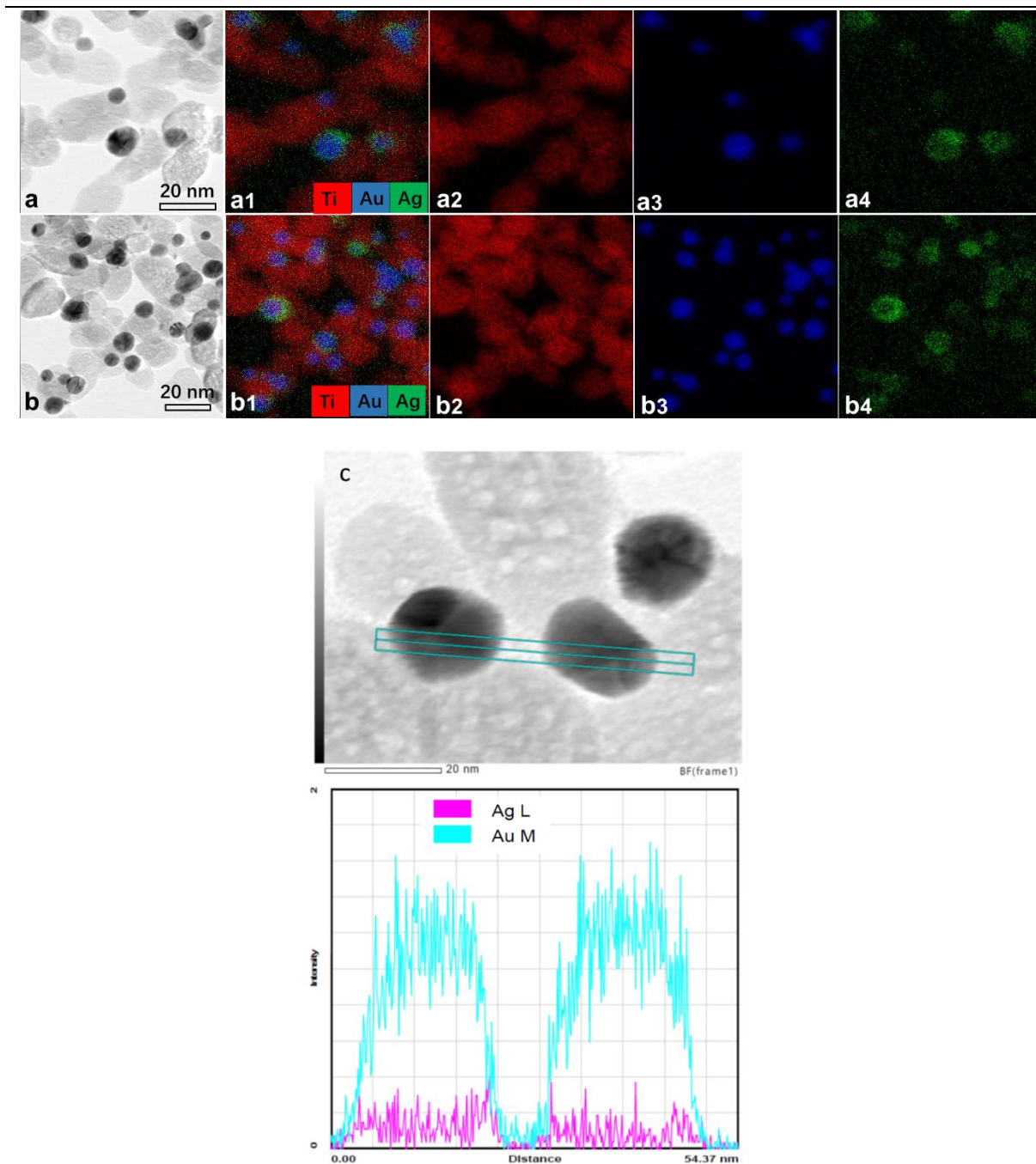


Figure 5.12 (a, b) SEM images of Au@Ag-TiO₂ and their corresponding elemental mapping of Ti, Au, and Ag. This sample is synthesized under the 10-mW applied power and 16 min exposure time (detailed sample information is shown in Table 5.6). c) STEM image and EDS line-scanning profile of two core-shell Au@Ag on their respective TiO₂ NP.

5.4.2.2 Varying the amounts of AgNO₃

Since there are Cl⁻ ions present in the Au-TiO₂ solution which is used for Ag

deposition it means that a fraction of the AgNO₃ in the solution reacts with these chlorides and cannot be used for the deposition. Here, we used different amounts of AgNO₃ to see if the thickness of the Ag shell could be increased with more precursors. The TEM images and data are shown in **Figure 5.13** and **Table 5.7**.

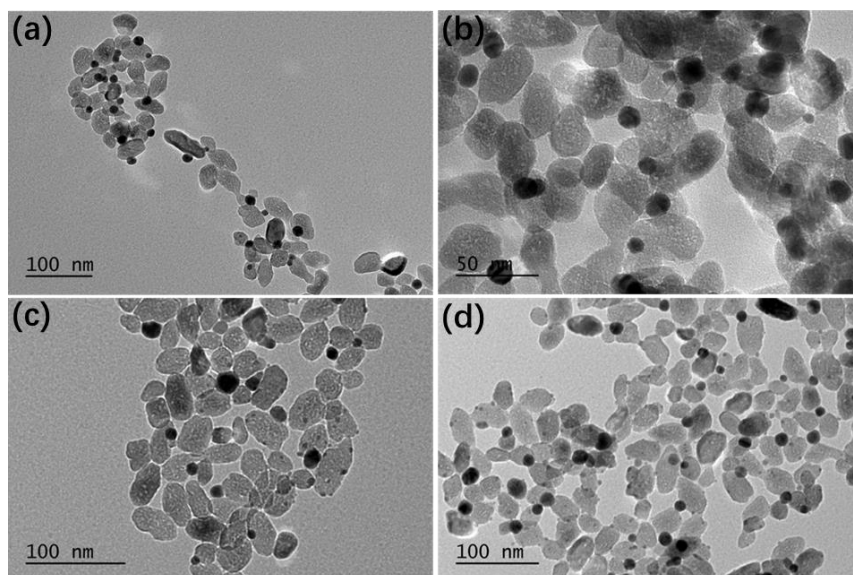


Figure 5.13 TEM images of Au@Ag-TiO₂ synthesized using different amounts of AgNO₃, 0.25 (a), 0.50 (b), 2.00 (c,) and 4.00 (d) μmol of AgNO₃ was used. The condition for preparing Au-TiO₂: [TiO₂] = 5.5 mM, [KAuCl₄] = 0.5 mM (0.5 μmol of KAuCl₄), 50 vol.% methanol as a hole scavenger, applied power of 56.1mW, and 4 min exposure time. Second step deposition: different amounts of AgNO₃ were added; this solution was then irradiated for another 16 min by the laser with a 56.1 mW applied power.

Table 5.7 Data of metallic particle size and heterodimer yield of Au@Ag-TiO₂. The condition for preparing Au-TiO₂: [TiO₂] = 5.5 mM, [KAuCl₄] = 0.5 mM (0.5 μmol of KAuCl₄), 50 vol.% methanol as a hole scavenger, applied power of 56.1mW, and 4 min exposure time. Second step deposition: different amounts of AgNO₃ were added; this solution was then irradiated for another 16 min by the laser with a 56.1 mW applied power. The calculation of the predicted Ag shell can be seen in Appendix 1.4.

Amount of AgNO ₃ (μmol)	NHDs yield (%)	Ag thickness (nm)	Predicted Ag shell thickness (nm)
0.25	50	0.4	1.1
0.5	51	0.8	1.7
2	48	0.7	4.8
4	50	0.8	7.1

Figure 5.13 shows no tiny Ag NDs for either 0.25 or 0.5 μmol of AgNO₃. The Ag shell gets thicker when AgNO₃ increases from 0.25 μmol to 0.5 μmol, (0.4 to 0.8 nm)

and then remains stable with some tiny Ag particles forming on the TiO₂ surface. Based on these results, we can conclude that excess AgNO₃ can easily induce the secondary nucleation of Ag NDs even if a partial consumption of AgNO₃ is taking place by the Cl⁻ ions. Moreover, we found that the thickest Ag shell available is around 1 nm.

To explain these results, we can refer to papers by Holmberg,²⁵ Lodsdail,²⁶ and Pekka.²⁴ These authors studied the bimetallic nanoparticles from a theoretical point of view and considered the case of core@shell systems. To understand where the electrons were localized in such M1@M2 NPs, they analyzed the atomic charge in the NPs. Concerning the charge equilibration, the most important question is whether the charge accumulates in the shell or the core of the NPs: increased degrees of freedom at a surface will attract electrons away from the core, although this could be counterbalanced by a strongly electronegative core element. For example, charge transfer from Ag to Au is common in Au/Ag NPs as the Au (2.4) is more electronegative than Ag (1.9),²⁷⁻²⁸ whereas the electronegativity of Pd and Pt, which is 2.2 in both cases, differs less compared to the Au Group elements,²⁹ and thus the charge transfer may be considered a less energetic driving force. Lodsdail *et al.*²⁶ also confirmed analyzing the charge segregation across bimetallic NPs that electrons accumulate on the NP surfaces irrespective of the core@shell composition, except in the case of Ag. Then for Au@Ag, the core tends to gain electron density, which is explained because of the low electronegativity of Ag (1.9) with respect to the other element (Au: 2.4); the same trend was observed with Pd: 2.2 and Pt: 2.2 as cores.

5.4.2.3 Depositing Ag on Au-TiO₂ which contains big Au particle

From the previous EDS result (**Figure 5.12**), we found that the Ag prefers to grow on the big Au particles, thus, Au-TiO₂ NHDs with big Au particles were used to perform the Ag deposition.

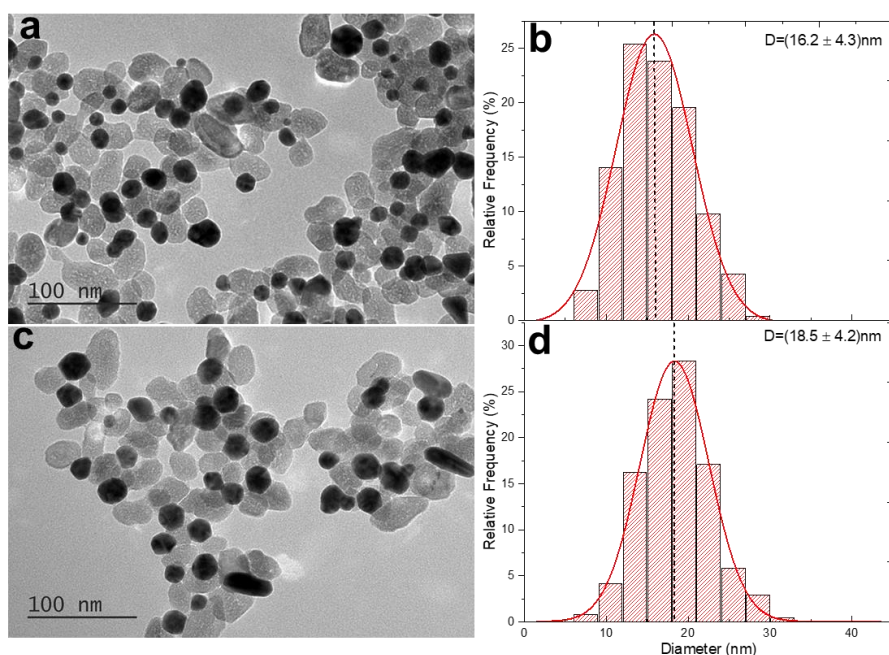


Figure 5.14 TEM images of Au-TiO₂ (a), and Au@Ag-TiO₂ (c) NPs and their corresponding size distributions (b and d). Experimental conditions: First step deposition, [TiO₂] = 1.1 mM, [KAuCl₄] = 0.5 mM, 50 vol.% methanol as a hole scavenger, applied power of 56.1mW, and exposure time of 4 min. Second step deposition: 0.5 μmol of AgNO₃ was added; this solution was then irradiated for 4 other min by the laser with an applied power of 56.1 mW.

As shown in **Figure 5.14**, the Au-TiO₂ particles were synthesized for a 1.1 mM concentration of TiO₂ and a mean diameter of Au particle of 16.2 (4.3) nm with a 70 % Heterodimer yield. After the second-step deposition, the diameter of the metallic particles increased to 18.5 (4.2) nm for a constant Heterodimer yield. The average Ag shell thickness was calculated to be 1.2 nm still smaller than the prediction (2.5 nm, Appendix 1.4).

5.4.3 Conclusion

In this section, photodeposition of Ag on Au-TiO₂ NHDs was performed by a two-step deposition method. To start, well-defined Au-TiO₂ nanoheterodimers were prepared by photodeposition. We have then systematically studied the influence of hole scavengers, laser power, and exposure time on the photodeposition of Ag on Au-

TiO₂. The Ag shell obtained is limited to around 1 nm which is less than the predicted value. This phenomenon can be explained by the theoretical analysis in reference.²⁶ Normally, the accumulation of electrons on the NP surfaces is independent of the core@shell composition, except in the case of Ag: for M@Ag, the core tends to gain electron density, which results from the low electronegativity of Ag (1.9) compared to other metallic elements (Au: 2.4; Pd: 2.2; Pt: 2.2).

5.5 Photodeposition of Pd on Au-TiO₂

Besides Ag, we also performed some experiments to introduce Pd on Au-TiO₂ heterodimers aiming at synthesizing bimetallic Au-Pd core-shell on TiO₂. In this part, we used the same procedure as before.

5.5.1 Effect of the hole scavenger

First of all, we synthesized Au-TiO₂ heterodimers with an average diameter of Au NDs of 10.4 ± 2.7 nm, with a heterodimer yield of around 51 %. Then the Na₂PdCl₄ (0.5 μ mol) solution was directly added to the as-prepared Au-TiO₂ solution. Finally, the second photodeposition was performed during an 8 min irradiation by a 56.1 mW laser. From the TEM characterization (**Figure 5.15**), the size of the BMPs particles increased to 11.7 (2.8) nm and the NHDs yield was about 53% (this size and this NHDs yield were measured and calculated without taking into account the tiny particles with a diameter smaller than 2 nm). However, compared to Au-TiO₂, there were some tiny Pd particles (diameter smaller than 2 nm) on TiO₂ after the second-step deposition which was probably due to the presence of methanol. According to some studies^{18, 30} and my work on the deposition of Pd on TiO₂ (Chapter 4), it seems that H₂O is itself an efficient hole scavenger for the Pd(II)–chloride complexes reduction, and the addition of an external hole scavenger induces the secondary nucleation of Pd resulting in some pure Pd on TiO₂.

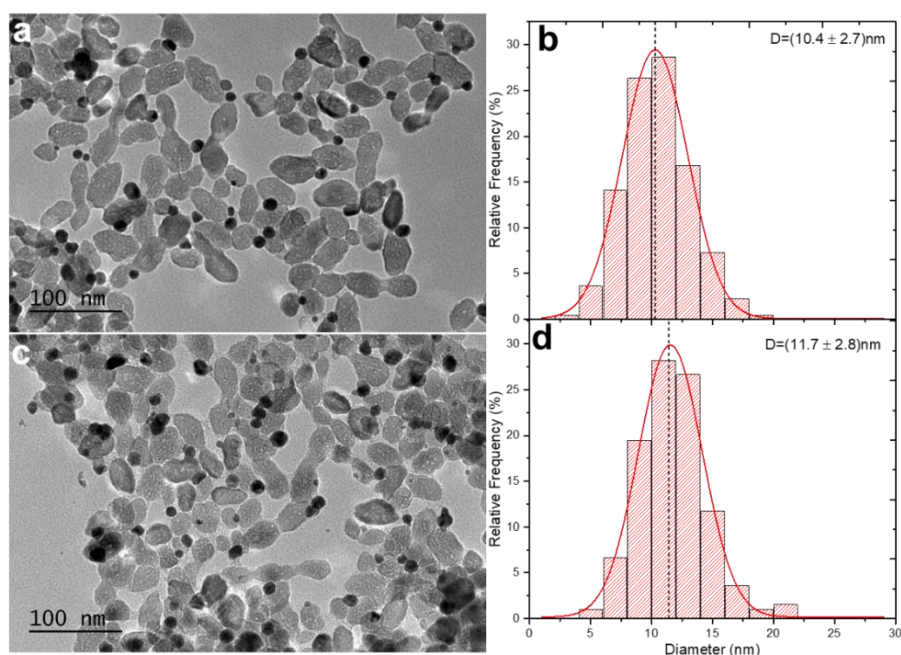


Figure 5.15 TEM images of Au-TiO₂ (a) and Au@Pd-TiO₂ (c) NPs and their corresponding size distributions (b and d). Experimental conditions: First step deposition, [TiO₂] = 5.5 mM, [KAuCl₄] = 0.5 mM, 50 vol.% methanol as a hole scavenger, applied power of 56.1 mW, and exposure time of 4 min. Second step deposition: 0.5 μmol of Na₂PdCl₄ was added; this solution was then irradiated for 8 more min by the laser with an applied power of 56.1 mW.

In addition to the TEM characterization, UV-Vis spectra of Au-TiO₂ and Au@Pd-TiO₂ solution were also performed to have a better understanding of the optical properties of these samples. As shown in **Figure 5.16**, there is a characteristic peak of Au nanodots at around 550 nm for Au-TiO₂ heterodimers. After the Pd deposition, the peak of this surface plasmon band exhibits a slight red shift and gets broader owing to an increase in the refractive index of the medium surrounding the Au particles.^{17, 31-32} Because the Pd shell has a strong damping effect on the dipole plasma oscillation of the Au core, the thin shell thickness can almost suppress the SPR peak of the Au core for the Au@Pd core-shell nanostructures.³³ Meanwhile, the absorption peak at 240 nm is the absorption of the Pd shell.³² These features prove the presence of Au@Pd core-shell.

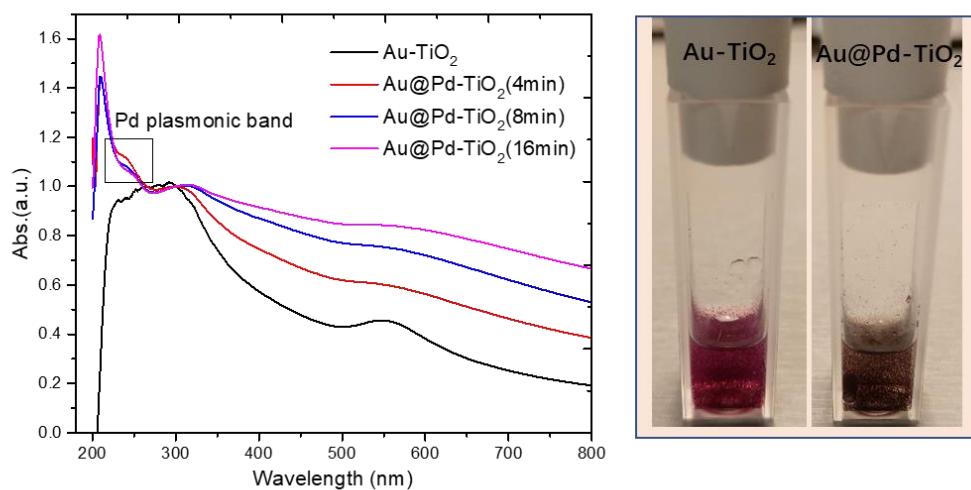


Figure 5.16 UV-vis spectra and picture of Au-TiO₂ and Au@Pd-TiO₂ NPs solutions. The color of the colloid solution changed from a red to a brown color after depositing Pd.

Since we know H₂O is itself an efficient hole scavenger to deposit Pd, attempts with no external hole scavenger were also performed to deposit Pd on Au-TiO₂ heterodimers. The pre-existing methanol in the Au-TiO₂ solution was removed by centrifugation before depositing Pd. In addition, different laser powers (56.1, 112 mW) were applied to check their effect on the Pd deposition. The TEM images of Au-TiO₂ and Au@Pd-TiO₂ particles and their size distributions are shown in **Figure 5.17**.

The size of the metallic particles increased from 10.4 to 11.6 nm after the second-step deposition indicating the formation of a Pd shell with 0.6 nm thickness. Based on the thickness and the heterodimer yield, we can calculate that around 30 % of the Pd precursor was reduced and used to form the Pd shell. When the applied laser power was higher (112 mW), a very close result was obtained.

The comparison of this result to that when the external hole scavenger (methanol) is present (**Figure 5.15**), shows that there is no change in the Pd thickness. However, some clusters of a few hundred nanometers could be observed by TEM. These clusters were revealed to be composed of the hard-to-solubilize starting palladium chloride material as evidenced by checking the TEM of the mother solution (**Figure 5.17**). Moreover, these clusters become smaller after the deposition process which

suggests their continuous dissolution to keep the equilibrium of palladium (II) in the reaction solution until it is completely consumed.

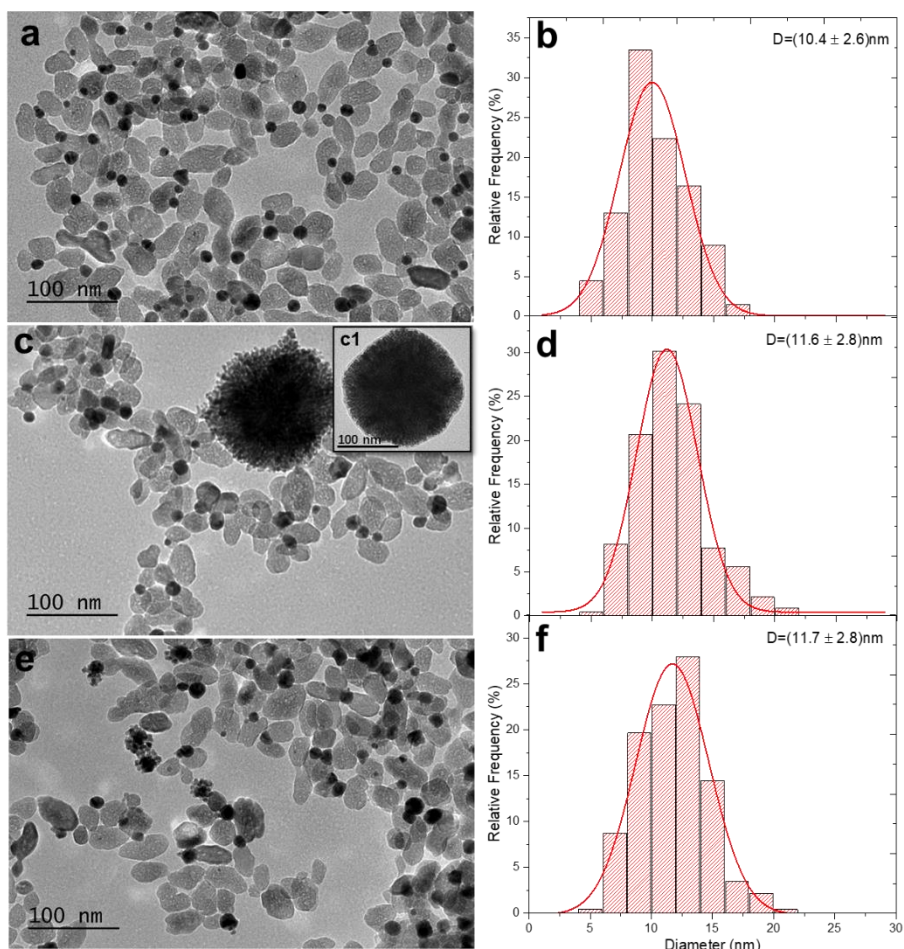


Figure 5.17 TEM images of Au-TiO₂ (a), Au@Pd-TiO₂ (c, e) NPs, and Na₂PdCl₄ solution (c1) and their corresponding size distributions (b, d, and f). Experimental conditions: First step deposition, [TiO₂] = 5.5 mM, [KAuCl₄] = 0.5 mM, 50 vol.% methanol as a hole scavenger, applied power of 56.1 mW, and exposure time of 4 min. The Au-TiO₂ particles were separated via centrifugation (18000g, 20 min) and washed once with deionized water and they were redispersed into pH 3.3 using a nitric acid solution for the second-step deposition. Second step deposition: 0.5 μmol of Na₂PdCl₄ was added; this solution was then laser irradiated for 8 more min with applied powers of 56.1 (c), and 112 (e) mW.

As we know, palladium (II) can form stable complexes with chloride. The complexation equilibria of Na₂PdCl₄ in water are strongly dependent on pH and pCl,³⁴³⁵ resulting in the formation of the different forms of the palladium chloride aqua complexes, [PdCl_n(H₂O)_{4-n}]²⁻ⁿ (n = 0-4). In addition, Kriek *et al.*³⁰ showed that the

photocatalytic reduction rate trend has the following decreasing order: PdCl₂(H₂O)₂ > [PdCl(H₂O)₃]⁺ > [Pd(H₂O)₄]²⁺ > [PdCl₃(H₂O)]⁻ > [PdCl₄]²⁻ with the neutral species PdCl₂(H₂O)₂ exhibiting the highest reduction rate (**Figure 5.18b**). Here the concentration of Na₂PdCl₄ in the reaction solution is 0.5 mM resulting in a pCl of 2.7 and the most active complex, [PdCl₂(H₂O)₂] is the main palladium (II) complex.

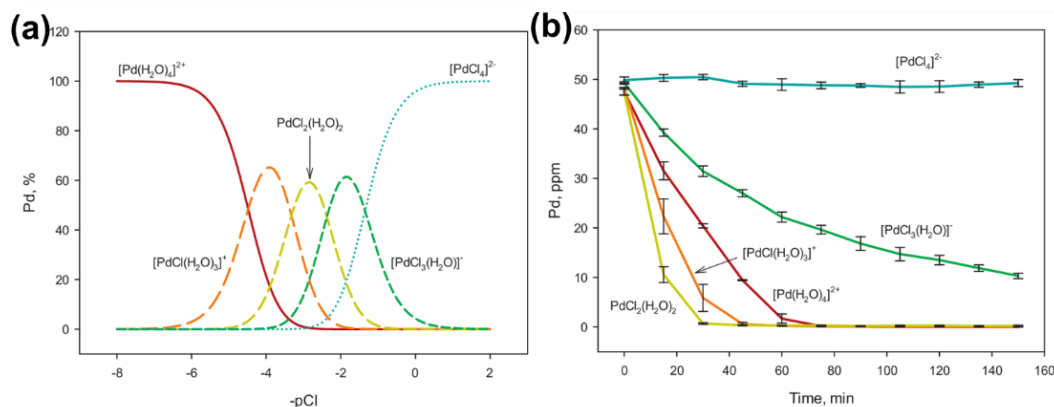


Figure 5.18 (a) Distribution of [PdCl_n(H₂O)_{4-n}]²⁻ⁿ-species as a function of - pCl (log[Cl⁻]) and (b) photocatalytic reduction trends of the [PdCl_n(H₂O)_{4-n}]²⁻ⁿ system (n = 0-4) in the absence of an added sacrificial reducing agent. The associated legends indicate those Pd(II)-complexes present in greater abundance at a specific chloride concentration at 25°C.³⁰

5.5.2 Different Pd precursors

Palladium(II) chloride itself is insoluble in water. For this reason, PdCl₂ was dissolved in 0.01 M hydrochloric acid solution and Pd²⁺ is mainly present as (H⁺)₂[PdCl₄]²⁻ complex or its aqua complexes depending on the pH and the pCl.³⁰ We dissolved the PdCl₂ into a pH 2 HCl solution (10 mM of PdCl₂ solution) then assuming a solution with a pCl of 1.70 containing mainly H⁺[PdCl₃(H₂O)]⁻. Then 50 μl of the PdCl₂ solution was added to the as-prepared Au-TiO₂ solution leading to a final pCl 3 where [PdCl₂(H₂O)₂] is prominent. Finally, an 8-min second-step deposition was performed under a 56.1mW applied power (**Figure 5.19**).

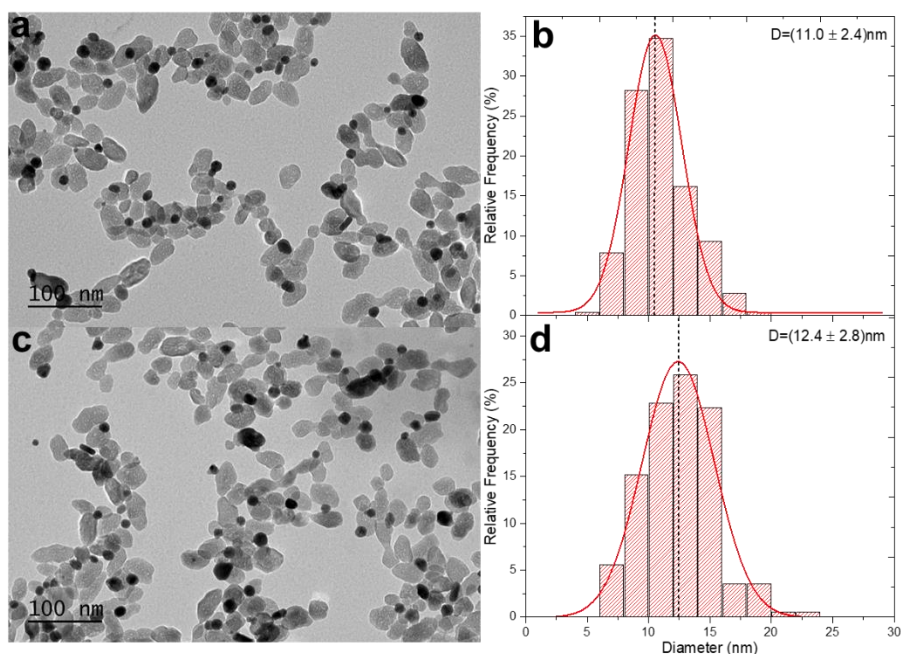
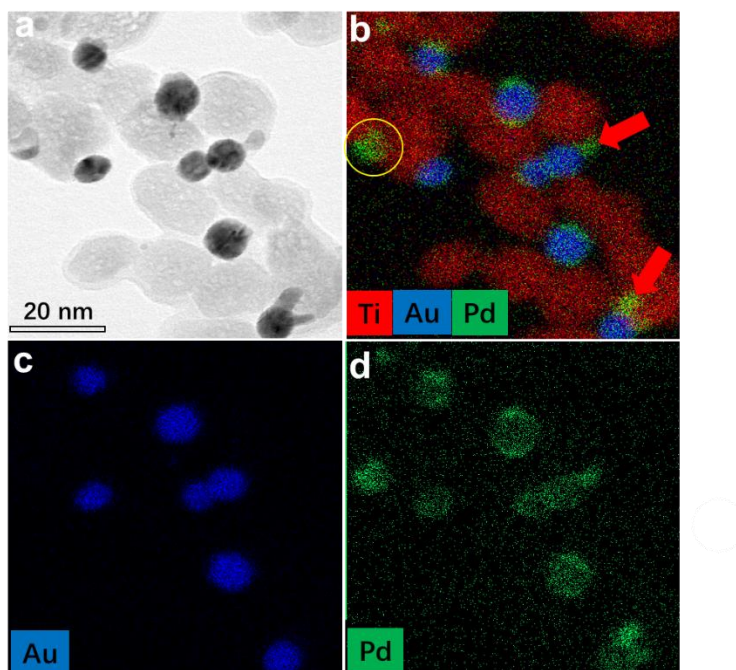


Figure 5.19 TEM images of Au-TiO₂ (a) and Au@Pd-TiO₂ (c) NPs and their corresponding size distributions (b and d). Experimental conditions: First step deposition, [TiO₂] = 5.5 mM, [KAuCl₄] = 0.5 mM, 50 vol.% methanol as a hole scavenger, applied power is 56.1 mW and exposure time is 4 min. Second step deposition: 0.5 μmol of PdCl₂ (dissolved in pH 2 HCl aqueous solution) was added; this solution was then irradiated for another 8 min by the laser with an applied power of 56.1 mW.

Figure 5.19 shows the TEM images of Au-TiO₂ and Au@Pd-TiO₂. As we can see, a layer of around 0.7 nm thickness of Pd-shell was coated onto the Au particles after the second deposition. Compared with Na₂PdCl₄ as a precursor, the Pd thickness was very close except that there are not any more clusters as with Na₂PdCl₄ probably because of the difference of nature of the counter cation and the fact that here we did not have to break the crystals' internal bonds *via* dissolution processes.

We also performed the EDS elemental mapping analysis on the Au@Pd-TiO₂ NPs (**Figure 5.20**). The clear spatial correlation between Au and Pd signals revealed that Pd atoms are in close contact with Au particles. Additionally, the elemental map of Au had a higher atomic density in the central region, while a slightly larger distribution area with a sparse center and dense edge was shown on the elemental map of Pd, confirming the formation of an Au@Pd core-shell particle on TiO₂. It is worth noting

that, first, there are also pure Pd particles (yellow circled in **Figure 5.20b**), and second, in some particles, the Pd shell on the Au core presents a uniform distribution, while some protrusions also appear (red arrows) in others. The biggest obstacle in creating a bimetallic core@shell structure is the lattice mismatch and when this lattice mismatch is larger than 5 %, the second material shows anisotropic growth on the seed particle.³⁶ Since the lattice mismatch between Au and Pd is 4.7% approaching 5%, the Pd growth on the Au core could be anisotropic, resulting in a nonuniform Pd shell as illustrated on the profiles shown in **Figures 5.20e** and **f**. **Figure 5.20e** is particularly illustrative since the profile shows from left to right a core-shell system, a pure Pd ND on TiO₂ and the Pd protrusions on gold (also shown on **Figure 5.20f**).



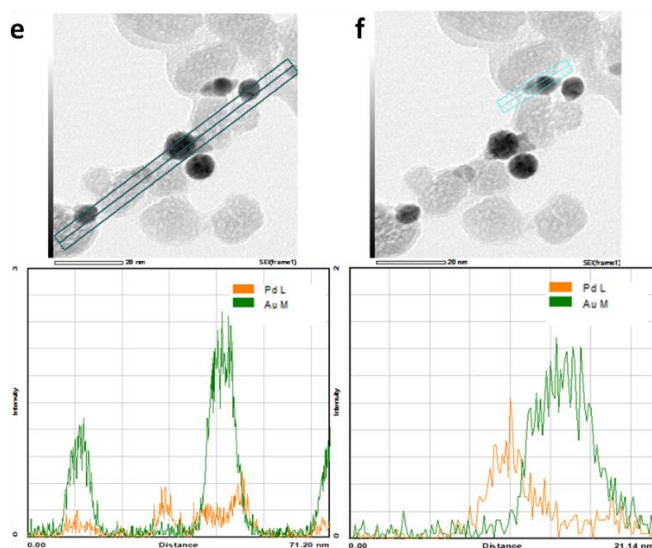


Figure 5.20 (a) SEM images of Au@Pd-TiO₂, (b, c, d,) the merged and corresponding elemental mappings of Ti, Au, and Pd. (e, f) two profiles showing the growth of Pd directly on TiO₂ and the Pd protrusions on gold and the lack of uniformity.

We then increased the amount of PdCl₂ to 1.0 μmol to study the influence of the amount of precursor. The result in **Figure 5.21** shows the thickness of the Pd shell (~0.7 nm) does not increase as expected. However, a higher palladium precursor concentration resulted in the formation of a few free big clusters and small clusters/dendrites around the Au core. This result could certainly be beneficial for the photocatalytic generation of H₂ thanks to the high active surface area developed.

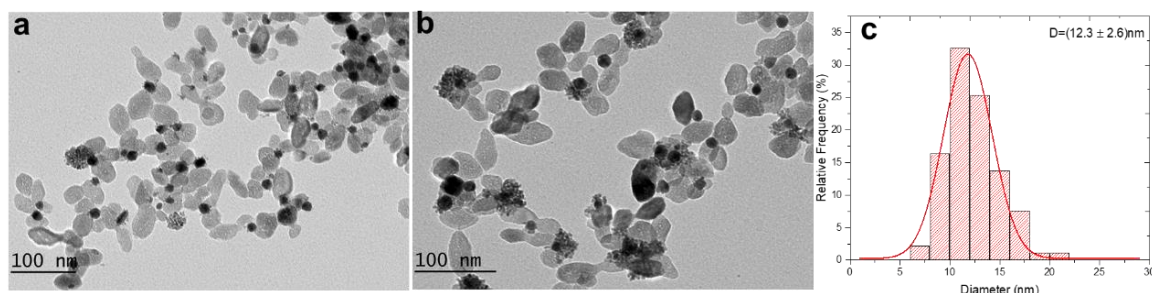


Figure 5.21 TEM images of Au@Pd-TiO₂ (a, b) NPs and size distributions (c). Experimental conditions: First step deposition, [TiO₂] = 5.5 mM, [KAuCl₄] = 0.5 mM, 50 vol.% methanol as a hole scavenger, applied power is 56.1 mW and exposure time is 4 min. Second step deposition: 1.0 μmol of PdCl₂ (dissolved in pH2 HCl aqueous solution) was added; then this solution was irradiated for another 4 min by the laser with an applied power of 56.1 mW.

As when depositing Ag on Au-TiO₂, we also used the big size Au particles for Pd deposition. The Au-TiO₂ particles starting from a 1.1 mM TiO₂ concentration, had a mean diameter of Au particle of 16.2 (4.1) nm with a 75 % yield of heterodimers (**Figure 5.22**). After the second-step deposition, the diameter of the metallic particles increased to 18.8 (4.2) nm and the heterodimer yield remained the same. The average Pd shell thickness (1.3 nm) is still lower than the predicted value (3.7 nm, Appendix 1.4), but is at least better than the previous result (0.6-0.7 nm). It looks like whenever the TiO₂ concentration is decreased, we favor both the NHDs yield (first step) and the shell thickness (second step). However, dilution means a longer mean free path and probably a longer reaction time to get a thicker shell on the one hand.

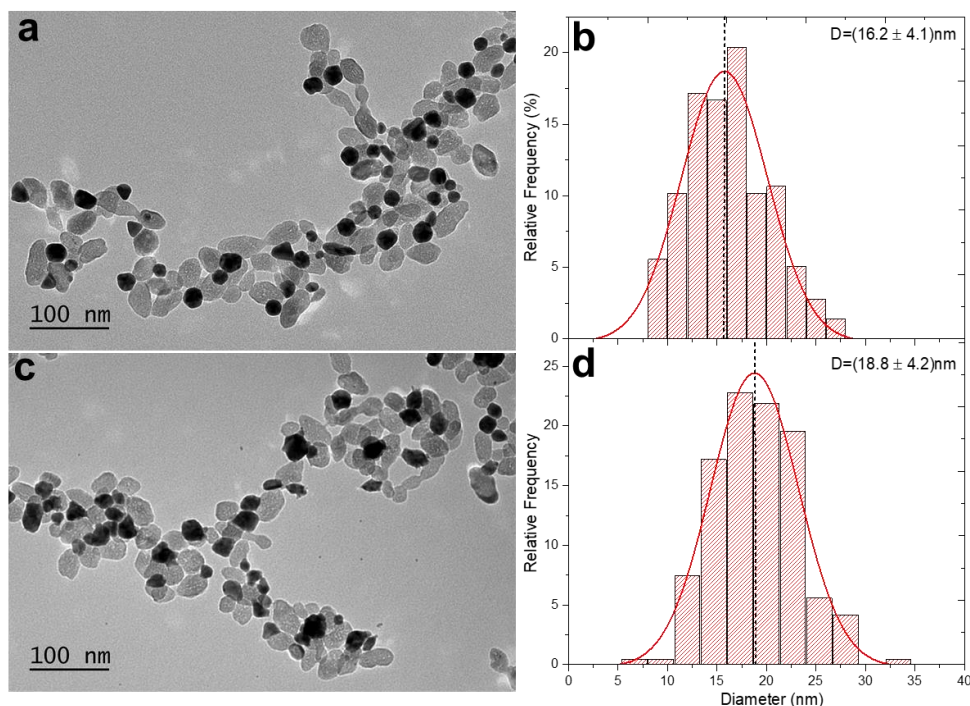


Figure 5.22 TEM images of Au-TiO₂ (a) and Au@Pd-TiO₂ (c) NPs and corresponding size distributions (b and d). Experimental conditions: First step deposition, [TiO₂] = 1.1 mM, [KAuCl₄] = 0.5 mM, 50 vol.% methanol as a hole scavenger, an applied power of 56.1 mW, and an exposure time of 4 min. Second step deposition: 0.5 μmol of PdCl₂ (dissolved in pH2 HCl aqueous solution) was added; this solution was then irradiated for another 8 min by the laser with an applied power of 56.1 mW.

On the other hand, the control of this Pd shell thickness proved to be very important to get both a satisfactory cocatalyst effect and absorption due to the SPR of Au

nanoparticles. It was reported¹⁰ that optical and physical properties of the Au NDs were completely shielded for a Pd thickness of 2.5 nm; then a Pd shell with a 0.5 -1.6 nm thickness as that obtained here might be much more interesting for the functionalization of Au/TiO₂ when considering both SPR aspect and Pd catalysis. The synthesis of this thin Pd shell on gold has been very difficult to achieve up to now by ordinary methods of core-shell preparation as mentioned by Tanaka.¹⁰

5.5.3 Conclusion

In this section, the photodeposition of Pd on Au-TiO₂ heterodimers was performed by a two-step deposition. The Pd shell was successfully deposited on the Au resulting in Au@Pd bimetallic core-shell structure onto TiO₂ particles. Compared to the deposition of Au and Ag on Au-TiO₂ heterodimers, the issue stems from the complexity of the palladium precursors. The solubility of Na₂PdCl₄ in H₂O is not so good and complexation equilibria of Na₂PdCl₄ in water are strongly dependent on pH and pCl, resulting in the formation of potential different forms of the palladium chloride aqua complexes, [PdCl_n(H₂O)_{4-n}]²⁻ⁿ (n = 0 - 4). These uncontrolled factors made the obtained Pd shell thicknesses at variance with expectations. Nevertheless, the thin palladium shell we synthesized (0.6-1.3 nm thick) is a favorable condition to improve the photocatalytic activity as reported in the references and we do not need to increase the Pd shell thickness blindly.

5.6 Conclusion

In this chapter, bimetallic core-shell structured Au@M-TiO₂ (M=Au, Ag, Pd) have been synthesized by a two-step photodeposition method using a UV laser as a light source. The Au particles were first photodeposited on the surface of TiO₂, followed by the deposition of another metal on the as-prepared Au-TiO₂ heterodimers in the second

step. The characterizations including TEM, UV-vis spectroscopy, and EDS mapping were performed and the results confirmed the existence of a core-shell structure. For the Au@Au core@shell, the Au shell can be precisely controlled by varying the gold precursor concentration; the maximum thickness we obtained is 2.9 nm and the size and thickness of the Au core and shell fit our expectations. For the Au@Ag system, it was very easy to produce some tiny Ag particles on the surface of TiO₂ particles and the Ag shell obtained was limited to around 1 nm thickness, less than expected, which results from the low electronegativity of Ag (1.9) compared to other Au (2.4). For the Au@Pd system, Pd showed a non-isotropic growth on the Au core resulting in a nonuniform Pd shell which was due to the big lattice mismatch between Au and Pd. The results of this study provide useful information for the design of functionalization of plasmonic photocatalysts by the formation of a core@shell structure.

5.7 References

1. Gupta, B.; Melvin, A. A.; Matthews, T.; Dash, S.; Tyagi, A. K., TiO₂ Modification by Gold (Au) for Photocatalytic Hydrogen (H₂) Production. *Renewable and Sustainable Energy Reviews* **2016**, *58*, 1366-1375.
2. Gomathi Devi, L.; Kavitha, R., A Review on Plasmonic Metal-TiO₂ Composite for Generation, Trapping, Storing and Dynamic Vectorial Transfer of Photogenerated Electrons Across the Schottky Junction in a photocatalytic System. *Applied Surface Science* **2016**, *360*, 601-622.
3. Forcherio, G. T.; Baker, D. R.; Boltersdorf, J.; Leff, A. C.; McClure, J. P.; Grew, K. N.; Lundgren, C. A., Targeted Deposition of Platinum onto Gold Nanorods by Plasmonic Hot Electrons. *The Journal of Physical Chemistry C* **2018**, *122* (50), 28901-28909.
4. Fernando, J. F. S.; Shortell, M. P.; Firestein, K. L.; Zhang, C.; Larionov, K. V.; Popov, Z. I.; Sorokin, P. B.; Bourgeois, L.; Waclawik, E. R.; Golberg, D. V., Photocatalysis with Pt–Au–ZnO and Au–ZnO Hybrids: Effect of Charge Accumulation and Discharge Properties of Metal Nanoparticles. *Langmuir* **2018**, *34* (25), 7334-7345.
5. Hung, S.-F.; Yu, Y.-C.; Suen, N.-T.; Tzeng, G.-Q.; Tung, C.-W.; Hsu, Y.-Y.; Hsu, C.-S.; Chang, C.-K.; Chan, T.-S.; Sheu, H.-S., The Synergistic Effect of a Well-Defined Au@Pt Core–Shell Nanostructure Toward Photocatalytic Hydrogen Generation: Interface Engineering to Improve the Schottky Barrier And Hydrogen-Evolved Kinetics. *Chemical Communications* **2016**, *52* (8), 1567-1570.
6. Kalisman, P.; Houben, L.; Aronovitch, E.; Kauffmann, Y.; Bar-Sadan, M.; Amirav, L., The Golden Gate to Photocatalytic Hydrogen Production. *Journal of Materials Chemistry A* **2015**, *3* (39), 19679-19682.
7. Zheng, Z.; Murakami, N.; Liu, J.; Teng, Z.; Zhang, Q.; Cao, Y.; Cheng, H.; Ohno, T., Development of Plasmonic Photocatalyst by Site-selective Loading of Bimetallic Nanoparticles of Au and Ag on Titanium(IV) Oxide. *ChemCatChem* **2020**, *12* (14), 3783-3792.
8. Liu, J.; Wu, Z.; He, Q.; Tian, Q.; Wu, W.; Xiao, X.; Jiang, C., Catalytic Application and Mechanism Studies of Argentite Chloride Coupled Ag/Au Hollow Heterostructures: Considering the Interface Between Ag/Au Bimetals. *Nanoscale Res Lett* **2019**, *14* (1), 35.
9. Jiang, H. L.; Akita, T.; Ishida, T.; Haruta, M.; Xu, Q., Synergistic Catalysis of Au@Ag Core-Shell Nanoparticles Stabilized on Metal-Organic Framework. *Journal of the American Chemical Society* **2011**, *133* (5), 1304-1306.
10. Tanaka, A.; Fuku, K.; Nishi, T.; Hashimoto, K.; Kominami, H., Functionalization of Au/TiO₂ Plasmonic Photocatalysts with Pd by Formation of a Core–Shell Structure for Effective Dechlorination of Chlorobenzene Under Irradiation of Visible Light. *The Journal of Physical Chemistry C* **2013**, *117* (33), 16983-16989.
11. Bhardwaj, S.; Pal, B., Photodeposition of Ag and Cu Binary Co-Catalyst onto TiO₂ for Improved Optical and Photocatalytic Degradation Properties. *Advanced Powder Technology* **2018**, *29* (9), 2119-2128.
12. Gao, D.; Liu, W.; Xu, Y.; Wang, P.; Fan, J.; Yu, H., Core-Shell Ag@Ni Cocatalyst on the TiO₂ Photocatalyst: One-Step Photoinduced Deposition and Its Improved H₂-Evolution Activity. *Applied Catalysis B: Environmental* **2020**, *260*, 118190.
13. Li, Y.-H.; Li, J.-Y.; Xu, Y.-J., Bimetallic Nanoparticles as Cocatalysts for Versatile Photoredox

Catalysis. *EnergyChem* **2021**, 3 (1), 100047.

14. Chen, Q.; Chen, X.; Fang, M.; Chen, J.; Li, Y.; Xie, Z.; Kuang, Q.; Zheng, L., Photo-Induced Au–Pd Alloying at TiO₂ {101} Facets Enables Robust CO₂ Photocatalytic Reduction Into Hydrocarbon Fuels. *Journal of Materials Chemistry A* **2019**, 7 (3), 1334-1340.

15. Fernandez, A.; Munuera, G.; Gonzalez-Elipe, A.; Espinos, J.; Herrmann, J.-M.; Pichat, P.; Leclercq, C., Photoassisted Deposition of Rhodium on Platinum/Titania Samples as a Method of Preparing Bimetallic Catalysts. *Applied catalysis* **1990**, 57 (1), 191-202.

16. Zheng, Z.; Murakami, N.; Liu, J.; Teng, Z.; Zhang, Q.; Cao, Y.; Cheng, H.; Ohno, T., Development of Plasmonic Photocatalyst by Site-selective Loading of Bimetallic Nanoparticles of Au and Ag on Titanium (IV) Oxide. *ChemCatChem* **2020**, 12 (14), 3783-3792.

17. Sun, J.; Han, Y.; Fu, H.; Qu, X.; Xu, Z.; Zheng, S., Au@Pd/TiO₂ with Atomically Dispersed Pd as Highly Active Catalyst for Solvent-Free Aerobic Oxidation of Benzyl Alcohol. *Chemical Engineering Journal* **2017**, 313, 1-9.

18. Bai, Q. Synthesis of Nano Heterodimers by Laser Photodeposition of Metal Nanodots on TiO₂ Nanoparticles. Université de Bordeaux, 2019.

19. Patra, K. K.; Gopinath, C. S., Bimetallic and Plasmonic Ag–Au on TiO₂ for Solar Water Splitting: An Active Nanocomposite for Entire Visible-Light-Region Absorption. *ChemCatChem* **2016**, 8 (20), 3294-3311.

20. Mao, K.; Zhou, Z.; Han, S.; Zhou, X.; Hu, J.; Li, X.; Yang, Z., A Novel Biosensor Based on Au@Ag Core-Shell Nanoparticles for Sensitive Detection of Methylamphetamine with Surface Enhanced Raman Scattering. *Talanta* **2018**, 190, 263-268.

21. Prabhawathi, V.; Sivakumar, P. M.; Boobalan, T.; Manohar, C. M.; Doble, M., Design of Antimicrobial Polycaprolactam Nanocomposite by Immobilizing Subtilisin Conjugated Au/Ag Core-Shell Nanoparticles for Biomedical Applications. *Mater Sci Eng C Mater Biol Appl* **2019**, 94, 656-665.

22. Templeton, A. C.; Pietron, J. J.; Murray, R. W.; Mulvaney, P., Solvent Refractive Index and Core Charge Influences on the Surface Plasmon Absorbance of Alkanethiolate Monolayer-Protected Gold Clusters. *The Journal of Physical Chemistry B* **2000**, 104 (3), 564-570.

23. Mulvaney, P.; Pérez-Juste, J.; Giersig, M.; Liz-Marzán, L. M.; Pecharrromán, C., Drastic Surface Plasmon Mode Shifts in Gold Nanorods Due to Electron Charging. *Plasmonics* **2006**, 1 (1), 61-66.

24. Peljo, P.; Manzanares, J. A.; Girault, H. H., Contact Potentials, Fermi Level Equilibration, and Surface Charging. *Langmuir* **2016**, 32 (23), 5765-5775.

25. Holmberg, N.; Laasonen, K.; Peljo, P., Charge Distribution and Fermi Level in Bimetallic Nanoparticles. *Physical chemistry chemical physics : PCCP* **2016**, 18 4, 2924-31.

26. Logsdail, A. J.; Paz-Bórbon, L. O.; Downing, C. A., DFT-Computed Trends in the Properties of Bimetallic Precious Metal Nanoparticles with Core@Shell Segregation. *The Journal of Physical Chemistry C* **2018**, 122 (10), 5721-5730.

27. Gould, A. L.; Heard, C. J.; Logsdail, A. J.; Catlow, C. R. A., Segregation Effects on the Properties of (AuAg)₁₄₇. *Physical Chemistry Chemical Physics* **2014**, 16 (39), 21049-21061.

28. Cerbelaud, M.; Ferrando, R.; Barcaro, G.; Fortunelli, A., Optimization of Chemical Ordering in AgAu Nanoalloys. *Physical Chemistry Chemical Physics* **2011**, 13 (21), 10232-10240.

29. Kittel, C., *Introduction to Solid State Physics*. 8th ed.; Wiley: New York, 2004; p 704.

30. Kriek, R. J.; Mahlamvana, F., Dependency on Chloride Concentration and 'in-Sphere'oxidation of H₂O for the Effective TiO₂-Photocatalysed Electron Transfer from H₂O to [PdCl_n (H₂O)_{4-n}]²⁻ⁿ (n= 0–4)

- in the Absence of an Added Sacrificial Reducing Agent. *Applied Catalysis A: General* **2012**, *423*, 28-33.
31. Wang, H.; Sun, Z.; Lu, Q.; Zeng, F.; Su, D., One-Pot Synthesis of (Au Nanorod)-(Metal Sulfide) Core-Shell Nanostructures with Enhanced Gas-Sensing Property. *Small* **2012**, *8* (8), 1167-1172.
32. Wang, H.; Sun, Z.; Yang, Y.; Su, D., The Growth and Enhanced Catalytic Performance of Au@Pd Core-Shell Nanodendrites. *Nanoscale* **2013**, *5* (1), 139-142.
33. Lee, Y. W.; Kim, M.; Kim, Z. H.; Han, S. W., One-step synthesis of Au@Pd core-shell nanooctahedron. *Journal of the American Chemical Society* **2009**, *131* (47), 17036-17037.
34. Cruywagen, J.; Kriek, R., Complexation of palladium (II) with chloride and hydroxide. *Journal of Coordination Chemistry* **2007**, *60* (4), 439-447.
35. Kettemann, F.; Wuithschick, M.; Caputo, G.; Kraehnert, R.; Pinna, N.; Rademann, K.; Polte, J., Reliable Palladium Nanoparticle Syntheses in Aqueous Solution: the Importance of Understanding Precursor Chemistry and Growth Mechanism. *CrystEngComm* **2015**, *17* (8), 1865-1870.
36. Liu, J.; Zhang, J., Nanointerface Chemistry: Lattice-Mismatch-Directed Synthesis and Application of Hybrid Nanocrystals. *Chemical reviews* **2020**, *120* (4), 2123-2170.

Chapter 6

Selective Photodeposition of Au Nanodots on Janus-Type $\text{Cu}_{2-x}\text{S}/\text{CuInS}_2$ Heteronanorods

Table of contents

Chapter 6.....	227
Selective Photodeposition of Au Nanodots on Janus-Type $\text{Cu}_{2-x}\text{S}/\text{CuInS}_2$ Heteronanorods	227
6.1 Introduction	231
6.2 Experiment.....	233
6.2.1 Chemicals.....	233
6.2.2 Synthesis of $\text{Cu}_{2-x}\text{S}/\text{CuInS}_2$ HNCs.....	233
6.2.3 Phase Transfer of KAuCl_4 from Water to Toluene.....	234
6.2.4 Laser-induced deposition of Au Nanodots onto $\text{Cu}_{2-x}\text{S}/\text{CuInS}_2$ HNCs.....	234
6.2.5 Characterization	235
6.3 Photodeposition of Au NDs on long $\text{Cu}_{2-x}\text{S}/\text{CuInS}_2$ HNCs	236
6.3.1 Characterization of $\text{Cu}_{2-x}\text{S}/\text{CuInS}_2$ HNCs.....	236
6.3.2 Laser-induced photodeposition of gold on $\text{Cu}_{2-x}\text{S}/\text{CuInS}_2$ HNCs.....	237
6.3.2.1 Effect of the hole scavenger on Au photodeposition	238
6.3.2.2 Effect of the laser beam intensity on the Au photodeposition	239
6.3.2.3 Effect of Au precursor on Au photodeposition	242
6.3.2.4 Effect of the exposure time on the Au photodeposition	245
6.3.2.5 Structural characterization of Au- $\text{Cu}_{2-x}\text{S}/\text{CuInS}_2$ hybrid HNCs	248
6.3.2.6 Formation mechanism of Au photodeposition on $\text{Cu}_{2-x}\text{S}/\text{CuInS}_2$ HNCs ...	253
6.3.3 Conclusion.....	254
6.4 References.....	256

6.1 Introduction

Colloidal metal-semiconductor hybrid nanocrystals (NCs) used as photocatalysts for solar-to-fuel conversion have been of particular interest in recent years since they usually exhibit more appealing photocatalytic performance than either side on their own due to the synergistic effects of each component, wherein the semiconductors provide tunable optical bandgaps and the metals offer superior reducing and catalytic properties.¹⁻³ Moreover, the coupling of metal nanodots and semiconductors allows the formation of a Schottky junction that promotes charge separation and transfer, thereby improving photocatalytic efficiencies.¹⁻³ To date, most metal-semiconductor systems are based on either metal oxides or Cd-based chalcogenides. Though metal oxides (e.g., TiO_2 , WO_3 , ZnO) exhibit excellent stability and photocatalytic activities, they have large bandgaps and are therefore active only at short wavelengths, thus being less efficient under sunlight irradiation.^{1, 3-4} Instead, Cd-based chalcogenides have suitable bandgaps and good photocatalytic efficiencies. However, they are highly restricted in practical applications due to their intrinsic toxicity and poor photostability because of the accumulation of holes during photochemical reactions.⁵⁻⁶

Cu-chalcogenide NCs are alternative semiconductors for coupling metal nanodots for the construction of highly efficient photocatalysts due to their lower toxicity, excellent photocatalytic activities, size, and composition-tunable bandgaps that match well in the solar range. The most commonly reported metal-Cu chalcogenide hybrid NCs are those metal nanodots decorated on binary Cu-chalcogenides, such as Au- Cu_2S heteronanodimers,⁷ Pt- Cu_{2-x}S hybrid nanoplatelets,⁸⁻⁹ Pt- Cu_{2-x}Se and Au- Cu_{2-x}Se heteronanodimers,¹⁰ dual plasmonic Au@ Cu_{2-x}E (E= S, Se) core@shell superparticles,¹¹⁻¹² and Au- Cu_{2-x}Te disk-on-dot heterostructures.¹³ With the advanced development of synthesis methods combined with a wealth of Cu-chalcogenide libraries, metal nanodots have also been successfully expanded to some more complicated structures, e.g., Au deposited on ternary CuInS_2 ,¹⁴⁻¹⁶ CuGaS_2 ,¹⁷ CuFeSe_2 ¹⁸ nanoparticles and quaternary $\text{Cu}_2\text{ZnSnS}_4$ nanostructures.¹⁹⁻²² Though the presence of metal nanodots on Cu-chalcogenide NCs improves their photocatalytic

performance several times, the efficiency is still lagging far behind compared to prototypical metal-decorated Cd-based semiconductors. For example, Amirav's group recently reported that the Pt-tipped $\text{CdSe}@\text{CdS}$ nanorods show a record 100% photon-to-hydrogen production efficiency under visible light illumination.²³

The key factor that influences charge separation is the control of the flow of photogenerated electrons and holes. Compared to single component Cu-chalcogenide semiconductors, the design of axially segmented heteronanocrystals (HNCs) with a type-II band alignment would be more attractive since this configuration allows an efficient spatial separation of electron-hole pairs under light irradiation. With a highly selective deposition of metal nanodots on the segmented nanostructure, it is expected to further control the flow of charge carriers. However, most up-to-date metal nanodot depositions are only limited to single component Cu-chalcogenide NCs and those on multi-component segmented Cu-chalcogenide HNCs have never been reported so far. This is mainly because Cu-chalcogenide HNCs are hard to be synthesized due to the fast diffusion rate of Cu^+ in the crystal lattices²⁴ as well as the difficulties in balancing the reactivities of multiple cations to anionic precursors.²⁵

In this work, we present a laser-based photodeposition approach to study the nucleation and growth of Au nanodots onto binary-ternary Janus-type $\text{Cu}_{2-x}\text{S}/\text{CuInS}_2$ HNCs in toluene. Compared to single component Cu-chalcogenides, the $\text{Cu}_{2-x}\text{S}/\text{CuInS}_2$ heteronanostructures have a sharp heterointerface and can form a typical type-II heterojunction, which is an ideal model to study the selective deposition of metal nanodots. To start, colloidal $\text{Cu}_{2-x}\text{S}/\text{CuInS}_2$ HNCs were prepared by a two-stage seeded-injection method reported in previous literature.²⁶ Subsequently, the Au nanodot was introduced onto the $\text{Cu}_{2-x}\text{S}/\text{CuInS}_2$ heteronanorods by photodeposition. The geometric distribution (*e.g.*, number and location) of Au nanodots as well as their sizes can be well controlled by tuning laser power, exposure time, hole scavengers, and precursors concentration. *Ex-situ* transmission electron microscopy (TEM) tracking demonstrates that the deposition of Au nanodots on the HNCs exhibits pronounced selectivity and experiences a gradual transition from Cu_{2-x}S tips to CuInS_2 parts. Experiments show that photodeposition is an efficient route to synthesize Au-

$\text{Cu}_{2-x}\text{S}/\text{CuInS}_2$ heterotrimers with versatility and predictability. The Au introduction and selective decoration will lead to an understanding of the primary physical mechanisms of charge carrier dynamics and design principles for achieving efficient photocatalytic activity which is important for developing more efficient and stable photocatalysts.

6.2 Experimental part

6.2.1 Chemicals

Indium nitrate hydrate ($\text{In}(\text{NO}_3)_3 \cdot x \text{H}_2\text{O}$, 99.9%), copper acetylacetonate ($\text{Cu}(\text{acac})_2$, 97%), copper(I) acetate (CuOAc , 97%), 1-dodecanethiol (1-DDT, $\geq 98\%$), oleic acid (OA, 90%), oleylamine (OLAM, 70%), Potassium gold chloride (KAuCl_4 , 99.995%), dodecylamine (DDA, 98%), anhydrous toluene, methanol, butanol, chloroform and ethanol were purchased from Sigma-Aldrich and used as received.

6.2.2 Synthesis of $\text{Cu}_{2-x}\text{S}/\text{CuInS}_2$ HNCs

The $\text{Cu}_{2-x}\text{S}/\text{CuInS}_2$ HNCs were synthesized by a two-stage seeded-injection method according to the previously reported procedures.²⁶ Cu_{2-x}S seed NCs were prepared by heating a mixture of $\text{Cu}(\text{acac})_2$ (0.79 g, 3 mmol), 15 mL of OLAM, and 15 mL of 1-DDT at 200 °C under N_2 protection for 2 h, followed by naturally cooling down to room temperature. The products were purified by the addition of an excess of isometric methanol and butanol solution and centrifuged at 2750 rpm for 10 min. The purification procedure was repeated 3 times. The Cu_{2-x}S NCs were then redispersed in 12 mL of anhydrous toluene and stored in a glovebox for further use.

For a typical seeded-injection reaction, 1 mL of the as-preformed Cu_{2-x}S NCs seeds stock solution was precipitated again according to the washing step mentioned above. The black precipitate was redispersed in 5 mL of 1-DDT. In the meantime, a mixture of $\text{In}(\text{NO}_3)_3 \cdot x \text{H}_2\text{O}$ (0.06 g, 0.2 mmol) and 4 mL of OA was degassed for 30 min at 120 °C before heating to 240 °C under N_2 protection. At this temperature, the as-prepared Cu_{2-x}S NCs seeds solution was rapidly injected into the hot $\text{In}(\text{NO}_3)_3$ -OA

solution and the mixed solution was allowed to react for 40 min. The reaction mixture was then naturally cooled down and washed with an excess of ethanol, followed by centrifugation at 2750 rpm for 10 min. The washing steps were repeated 3 times. The HNCs were finally redispersed in 5 mL of toluene and stored in a glovebox for further use.

6.2.3 Phase Transfer of KAuCl_4 from Water to Toluene

The phase transfer of KAuCl_4 from water to toluene was performed according to a previously reported approach.²⁷⁻²⁸ To start, an 8 mM KAuCl_4 aqueous solution was prepared by dissolving KAuCl_4 (30.2 mg, 0.08 mmol) in 10 mL of deionized water. Then, 2 mL of this as-prepared KAuCl_4 solution, were mixed with 2 mL of ethanol containing DDA (28 mg/mL). The mixture was vigorously shaken until a homogeneous solution was obtained and the solution was then let stand for 1 h. Subsequently, 2 mL of anhydrous toluene, were added into the mixture to allow the phase transfer from water to toluene. After 30 min, the upper layer, *viz.*, toluene, turned from transparent to light yellow, indicating the successful phase transfer. The Au precursors in toluene were carefully extracted using a pipette and were bubbled by argon for 10 min. Given the 100 % efficiency of the phase transfer, the obtained 8 mM KAuCl_4 toluene solution was diluted to 4 mM for further experiments.

6.2.4 Laser-induced deposition of Au Nanodots onto $\text{Cu}_{2-x}\text{S}/\text{CuInS}_2$ HNCs

The $\text{Cu}_{2-x}\text{S}/\text{CuInS}_2$ HNCs solution was diluted by a factor of ten in toluene under argon protection. Typically, 100 μL of the diluted HNCs solution were mixed with 749 μL of anhydrous toluene, 51 μL of the 4mM KAuCl_4 -toluene solution, and 100 μL of methanol in the dark. The mixture was transferred to a 1 cm path length sealed quartz cuvette and stirred at 300 rpm until the end of the experiments. The size of the laser in front of the cuvette was adjusted to be circular and 1 cm in diameter to be sure that

the whole solution was completely exposed to the laser light. The excitation power and exposure time were finely tuned according to the experimental needs. Once the experiment was done, the reaction was quenched by turning off the laser and adding 1 mL of acetone. The product was collected by centrifugation at 4000 rpm for 10 min and washed once by addition of 1 mL of isometric methanol and butanol solution, followed by centrifugation at 4,000 rpm for 10 min. The yield precipitate was redispersed in 0.5 mL of chloroform. All experiments were performed at room temperature. The beam power range at the exit of the laser head varies from $P_L = 0$ to 362 mW when changing the driving current, with a maximum current of 5.0 A. With a transmission of the setup of $P_i/P_L = 79\%$, the power range incident to the cuvette is $P_i = 0$ to 286 mW. Considering the transmission of the cuvette $P_t/P_i = 48\%$ when filled with Cu_{2-x}S/CuInS₂ HNCs solution, the beam intensity estimated in the middle of the cuvette is $I = \frac{2(P_i P_t)^{\frac{1}{2}}}{\pi \omega^2} = \frac{2P_L \times 55\%}{\pi \omega^2} = 0$ to 507 mW/cm² for a beam diameter $2\omega = 1$ cm.

6.2.5 Characterization

Samples for transmission electron microscopy (TEM) analysis were prepared by drop-casting a solution of NCs onto carbon-coated 200 mesh copper/nickel TEM grids. A few drops of chloroform were cast on the same side of the grid to wash away some remaining metal salts. TEM analysis was performed with three machines, a JEOL JEM1400 Plus microscope operating at 120 kV, an FEI-Technai 12 microscope operating at 100 kV, and an FEI Technai 20 microscope operating at 200 kV. High-resolution TEM (HRTEM), high-angle annular dark-field scanning TEM (HAADF-STEM), and elemental mapping were performed on a Talos F200X (Thermo Fisher Scientific) or JEOL 2100 operated at 200 kV. The elemental maps were collected in an area of 1024 × 1024 pixels with an acquisition time of 5-10 min using Esprit software from Bruker. The elemental quantification is done by adding up all the counts in the entire spectrum for each channel and all pixels within the area of interest. Samples for X-ray diffraction (XRD) analysis were prepared by uniformly spreading dried NCs

powder (~ 0.1 g) over a silicon wafer. XRD analyses were performed with a Bruker D2 Phaser, equipped with a $\text{Co K}\alpha$ x-ray source with a wavelength of 1.79026 Å.

6.3 Photodeposition of Au NDs on long $\text{Cu}_{2-x}\text{S}/\text{CuInS}_2$ HNCs

The $\text{Cu}_{2-x}\text{S}/\text{CuInS}_2$ HNCs were synthesized by a two-stage seeded-injection method. Then the Au nanodots were introduced on $\text{Cu}_{2-x}\text{S}/\text{CuInS}_2$ HNCs by laser-beam induced photodeposition. The nucleation and growth of Au nanodots onto binary-ternary $\text{Cu}_{2-x}\text{S}/\text{CuInS}_2$ heteronanocrystals (HNCs) in toluene were carefully studied. The effects of the hole scavengers and Au precursors, illumination power, and exposure time on geometric distribution (e.g., number and location) of Au nanodots as well as their sizes were investigated and are detailed.

6.3.1 Characterization of $\text{Cu}_{2-x}\text{S}/\text{CuInS}_2$ HNCs

Colloidal Janus-like $\text{Cu}_{2-x}\text{S}/\text{CuInS}_2$ HNCs were synthesized by the fast injection of a solution of as-preformed Cu_{2-x}S seed nanodisks dispersed in dodecanethiol into a hot indium oleate solution at 240 °C, while keeping the reaction at this temperature for 40 min (See Experimental part for details). High-angle annular dark-field scanning TEM (HAADF-STEM) image of $\text{Cu}_{2-x}\text{S}/\text{CuInS}_2$ HNCs shows pronounced contrast differences within single HNCs (**Figure 1a**). Corresponding two-dimensional elemental mapping (**Figure 1b**) reveals that the contrast differences come from two distinct components, *viz.*, binary Cu_{2-x}S (brighter part) and ternary CuInS_2 (darker part). The Cu_{2-x}S part has a monoclinic low chalcocite crystal structure with a Cu/S ratio of 1.6 ± 0.1 , while the CuInS_2 part has a hexagonal wurtzite crystal structure with a nearly stoichiometric composition. The X-ray diffraction pattern of the HNCs (**Figure 1c**) is dominated by the diffraction peaks of the hexagonal wurtzite CuInS_2 without obvious contributions from the Cu_{2-x}S tips, which is likely due to the small volume of the Cu_{2-x}S tip compared to that of the elongated CuInS_2 part, as well as the similar hexagonal closed packed S^{2-} sublattice in low-chalcocite Cu_{2-x}S and wurtzite CuInS_2 , as verified

previously.²⁶ The $\text{Cu}_{2-x}\text{S}/\text{CuInS}_2$ HNCs show a featureless absorption across a broad spectral range that covers the whole visible region, demonstrating that these nanomaterials can be used as efficient sunlight absorbers. (Figure 1d).

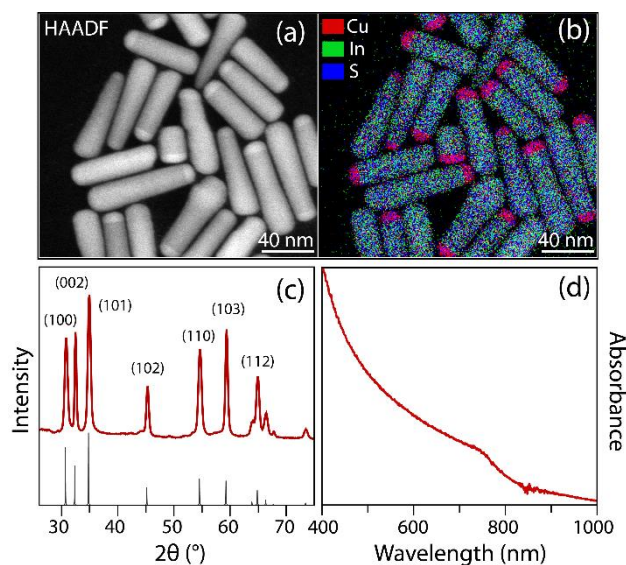


Figure 1. (a-b) HAADF-STEM image (a) and corresponding elemental mapping (b) of $\text{Cu}_{2-x}\text{S}/\text{CuInS}_2$ HNCs. (c-d) XRD patterns (a) and absorption spectrum (b) of $\text{Cu}_{2-x}\text{S}/\text{CuInS}_2$ HNCs (red line). The grey line in Figure 1c represents the hexagonal wurtzite CuInS_2 diffraction pattern (JCPDS Card 01-077-9459). Figure 1b is adapted from the ref.²⁶

6.3.2 Laser-induced photodeposition of gold on $\text{Cu}_{2-x}\text{S}/\text{CuInS}_2$

HNCs

The photodeposition experiments were conducted inside a 1 cm path length sealed quartz cuvette containing oleic acid/dodecanethiol capped $\text{Cu}_{2-x}\text{S}/\text{CuInS}_2$ HNCs, dodecylamine (DDA)-modified KAuCl_4 precursors in toluene, and methanol (MeOH) as hole scavengers. A laser with a continuous wavelength of 473 nm was used as an irradiation source to allow an efficient excitation of $\text{Cu}_{2-x}\text{S}/\text{CuInS}_2$ HNCs due to their broad absorption spectral range extended to ~ 800 nm (Figure 1d). After exiting from the laser head, the beam size is amplified to about 1 cm in diameter by passing through a cylindrical lens and another lens with a focal length of 70 mm. The enlarged beam is then sent to a $1 \times 1 \times 4$ cm³ sealed quartz cuvette with a solution volume of 1 mL. The solution is stirred continuously with a speed of 300 rpm under illumination at room

temperature to ensure a homogeneous dispersion throughout the whole reaction process.

6.3.2.1 Effect of the hole scavenger on Au photodeposition

Instead of conventional lamps, the use of a focused laser beam promotes the generation of a tremendous rate of electron-hole pairs. Apart from the electrons which may recombine with holes, many of them participate in the chemical reduction of Au^{3+} to Au^0 nanodots on the surface of $\text{Cu}_{2-x}\text{S}/\text{CuInS}_2$ HNCs. The excessive consumption of electrons leads to an imbalanced charge equilibrium due to the unreacted holes within the HNCs. In this case, a hole scavenger has to be added to the solution to avoid the accumulation of holes that are not conducive to the photostability of HNCs. In addition, the hole scavengers when consuming holes and thus reducing the recombination of electrons and holes improve the deposition efficiency. In the reaction system, MeOH was selected as a hole scavenger because of its high hole-trapping efficiency and good miscibility in nonpolar toluene, demonstrated in the photodeposition on Cd chalcogenide nanocrystals and TiO_2 particles.²⁹⁻³¹ **Figure 2** shows the photodeposition of Au nanodots on $\text{Cu}_{2-x}\text{S}/\text{CuInS}_2$ HNCs in the presence of different amounts of hole scavenger (0, 5, 10, 15% volume percentages). In the absence of MeOH, less than half of the HNCs show an Au deposition with a size of 6.1 ± 1.2 nm (**Figure 2a**). The ratio of HNCs with a single Au nanodot significantly increases in the presence of MeOH and reaches a maximum of 73% for 10% MeOH. Interestingly, the Au size increases to 7.5 ± 1.3 nm with the addition of MeOH, confirming the important role of the specific hole scavenger in photodeposition. Moreover, when deposited on the CuInS_2 elongated part, most Au nanodots locate on the side, in sharp contrast with the Au photodeposition on Cd chalcogenide nanorods which typically takes place at the tips.³¹⁻³⁴

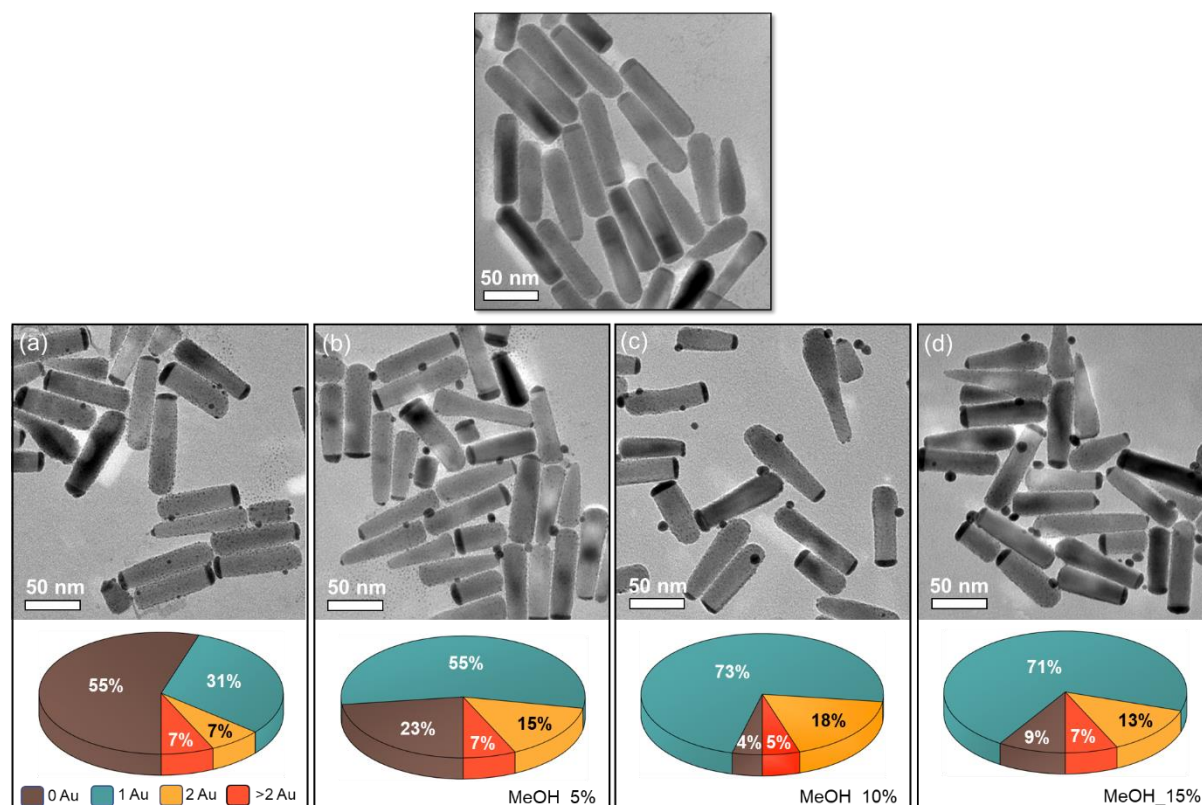


Figure 2. TEM images of starting material and (a-d) Au- $\text{Cu}_{2-x}\text{S}/\text{CuInS}_2$ HNCs obtained in the presence of different amounts of hole scavengers (MeOH, various volume percentages from 0 to 15%) in the reaction solution. Three-dimensional color pie chart (upper panel of each TEM image) of the number of Au nanodots on $\text{Cu}_{2-x}\text{S}/\text{CuInS}_2$ HNCs. The percentages of Au nanodot distributions are estimated by counting more than 200 nanoparticles. The laser power (P_L , exit laser head), the concentration of KAuCl_4 , and deposition time are 100 mW, 0.204 mM, and 32 min, respectively.

In the following, we perform experiments varying light intensity, gold precursor concentration, or exposure time with a fixed 10% vol. of methanol in the reaction medium.

6.3.2.2 Effect of the laser beam intensity on the Au photodeposition

Light intensity is an essential parameter for the electron-hole pair production rate which directly affects the photodeposition rate of Au nanodots on $\text{Cu}_{2-x}\text{S}/\text{CuInS}_2$ HNCs. We studied the influence of laser beam intensities on the photodeposition and varied the beam intensity I inside the cuvette from 28 to 420 mW/cm^2 ($P_L = 20, 50, 100, 200$,

and 300 mW) while the concentrations of hole scavenger (MeOH, 10%), Au precursor (0.204 mM) and HNC substrate, as well as the irradiation time (16 min), were fixed unless otherwise noticed. As expected, the size of Au nanodots on HNCs indeed gradually increased from 5.5 to 7.5 nm with the increase of illumination power (**Figures 3 and 4a**).

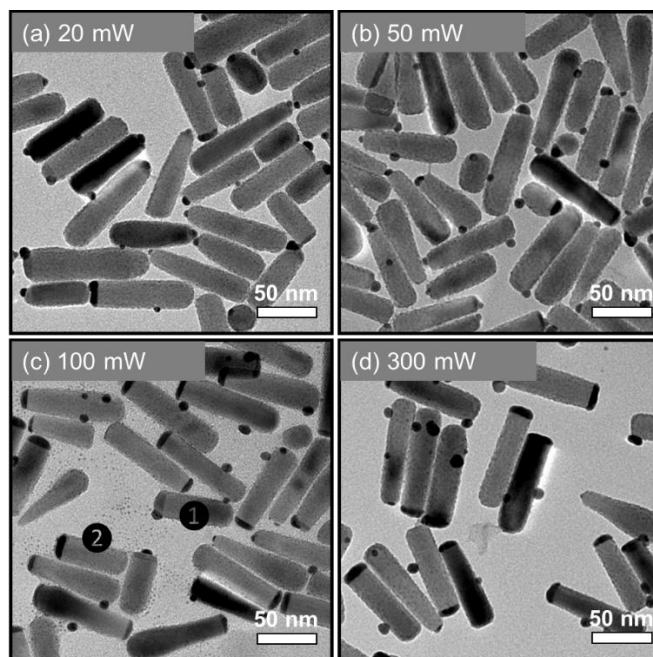


Figure 3. (a-d) TEM images of $\text{Au-Cu}_{2-x}\text{S}/\text{CuInS}_2$ HNCs obtained under different illumination intensities. The laser power (P_L) varies from 20 to 300 mW.

Figure 3 shows that in a single image, we can see the different stages of reaction achievements with the different nuances of grey of the HNCs (①, ②); we will come back on this issue in section 6.3.2.4.

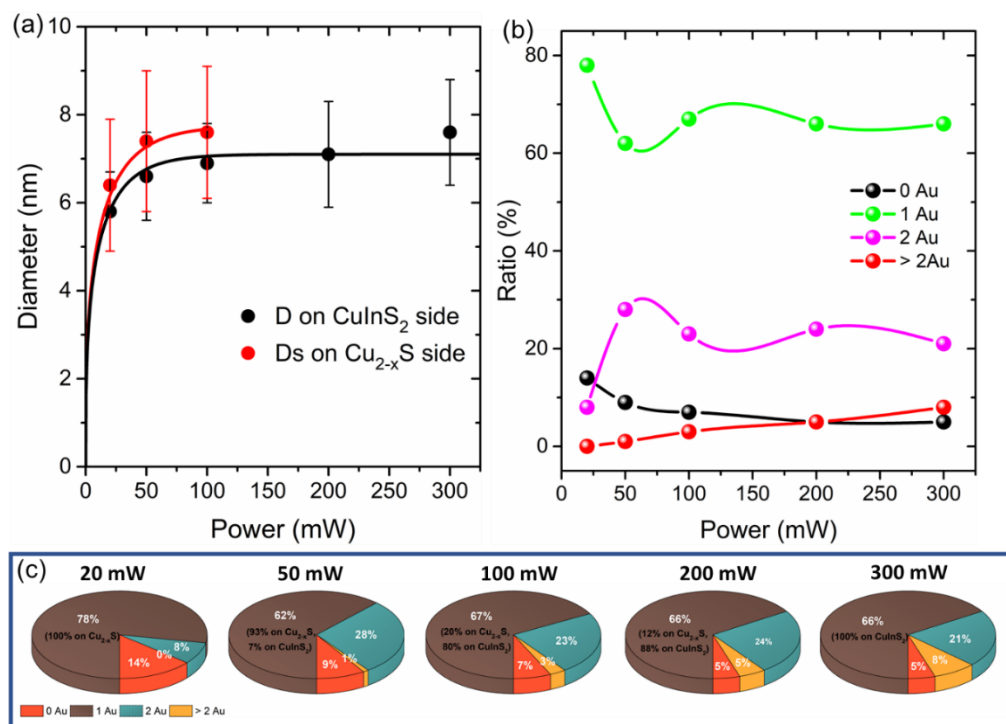


Figure 4. (a-b) Size (a) and distribution (b) of Au NDs on HNCs under different laser powers. (c) Three-dimensional color pie charts of the distribution of Au NDs on $\text{Cu}_{2-x}\text{S}/\text{CuInS}_2$ HNCs. The percentages of Au NDs distributions are estimated by counting more than 200 nanoparticles. The volume percentage of MeOH, concentration of KAuCl_4 , and deposition time are 10%, 0.204 mM, and 16 min, respectively.

The interface diameter (Ds) of Au on Cu_{2-x}S and the diameter of Au nanodots on CuInS_2 (D) were measured respectively because the Au nanodots decorated on Cu_{2-x}S side resemble caps while the Au nanodots on the CuInS_2 side are approximately spherical, illustrating a difference in wettability on the two surfaces. Moreover, as the power increases the ratio of single metal nanodots decreases from 78% to 66% while that of the multiple metal nanodots however experiences a slight increase from 0 to 10% (**Figure 4b,c**), which is completely opposite to the case of Au-tipped CdSe-CdS nanoheterodimers,³¹ suggesting that the photodeposition on $\text{Cu}_{2-x}\text{S}/\text{CuInS}_2$ HNCs is fundamentally different from that on Cd-based HNCs. Additionally, a note should be taken that the locations of Au nanodots on the HNCs differ at low and high illumination powers. At low power, the majority of Au nanodots are generally located at the tips of the Cu_{2-x}S part of HNCs while these metal dots seem to move to the side of the CuInS_2

part of HNCs at high illumination power (**Figure 3**). The variation of the overall length of the HNCs with the power (**Figure 5a**) is null while surprisingly, at first sight, the size (diameter and length) of Cu_{2-x}S gradually increases with the laser power (**Figure 5b**). The underlying reasons for these phenomena are discussed separately in Section 6.3.2.6.

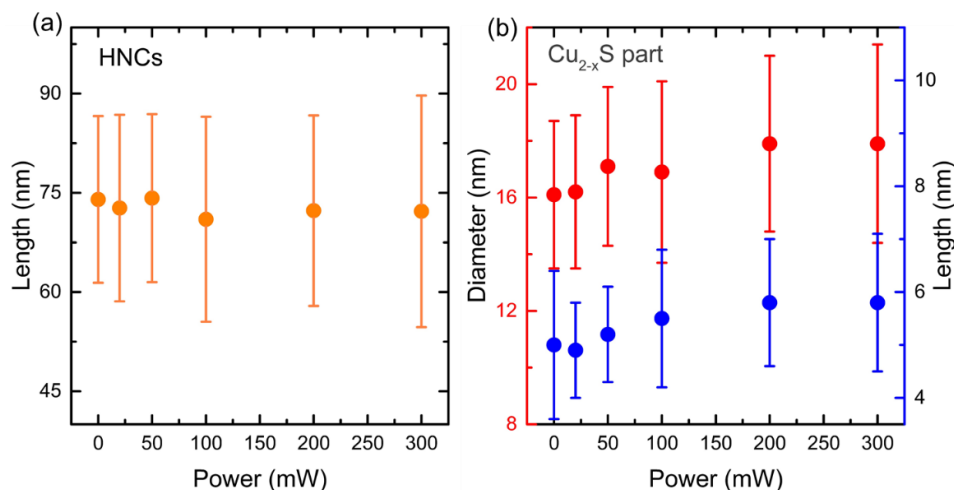


Figure 5. (a) Average length of the HNCs after deposition at different illumination powers. (b) The average diameter (red spheres, left Y-axis) and length (blue squares, left Y-axis) of the Cu_{2-x}S after deposition at different illumination powers.

6.3.2.3 Effect of Au precursor on Au photodeposition

To further control the growth of Au nanodots, the concentration of the Au precursor ($[\text{Au}^{3+}]$) was finely tuned while the other parameters were kept the same (10% vol. MeOH, power of 100 mW at exit laser, and exposure time of 16 min). TEM images in **Figure 6** clearly show that the size of Au nanodots increases with the $[\text{Au}^{3+}]$. Similar to the influence of illumination power, at low $[\text{Au}^{3+}]$, most Au nanodots (6.3 ± 1.4 nm) locate on the tip of HNCs, specifically on the Cu_{2-x}S end (**Figure 7**).

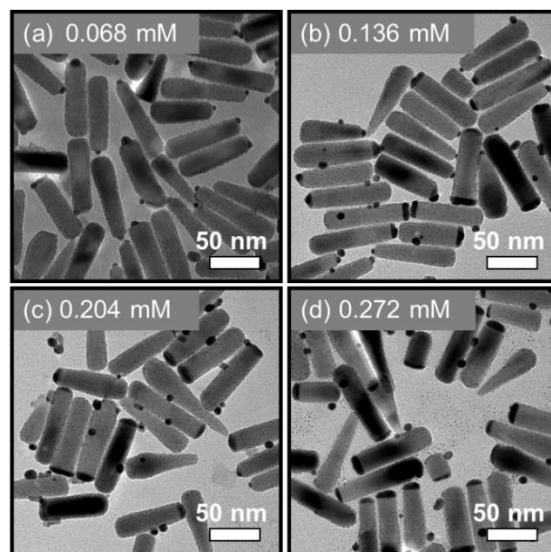


Figure 6. (a-d) TEM images of Au- $\text{Cu}_{2-x}\text{S}/\text{CuInS}_2$ HNCs obtained for different concentrations of Au precursors. The concentration varies from 0.068 to 0.272 mM. The volume percentage of MeOH, power at exit laser, and exposure time are 10%, 100 mW, and 16 min, respectively.

When the $[\text{Au}^{3+}]$ reaches 0.136 mM, the single Au ND deposition shares a nearly equal probability of growing on either side of the Janus structures (52% on Cu_{2-x}S parts and 48% on CuInS_2 parts). Moreover, the contact angle of Au nanodots on the Cu_{2-x}S side turns out to be $\leq 90^\circ$ while that on the CuInS_2 part is $\geq 90^\circ$. As the $[\text{Au}^{3+}]$ increases, nearly no individual Au nanodots are present on the Cu_{2-x}S parts, and almost all of them are on the side of CuInS_2 and exhibit an average size of ~ 7.5 nm (**Figure 7**). Additionally, the contrast of Cu_{2-x}S becomes darker compared to that of the elongated CuInS_2 (as in **Figure 3c**). As in the case of high intensity, we also observe with increasing gold precursor concentration that the resulting HNCs show this dark contrast of the Cu_{2-x}S parts concomitantly to the disappearance of the corresponding Au nanodots. This tends to indicate a change in the composition of this same Cu_{2-x}S zone possibly with the formation of an Au-containing alloy even if Au_2S via cation exchange has been observed.³⁵ Additionally, the size of these Cu_{2-x}S zones also slightly increased (**Figure 8b**), a phenomenon already observed when varying the laser powers.

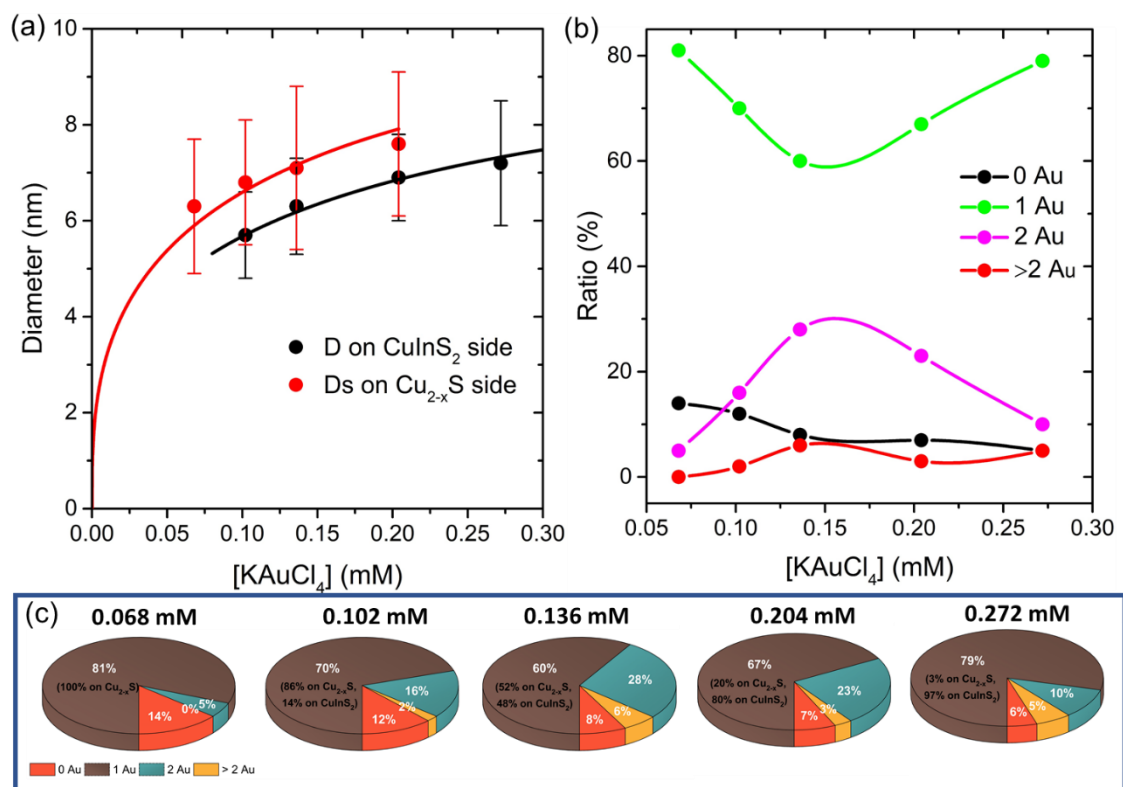


Figure 7. (a-b) Size (a) and distribution (b) of Au nanodots on HNCs with different gold precursor concentrations. (c) Three-dimensional color pie chart of the number of Au nanodots on $\text{Cu}_{2-x}\text{S}/\text{CuInS}_2$ HNCs. The percentages of Au nanodot distributions are estimated by counting more than 200 nanoparticles. The volume percentage of MeOH, P_L , and deposition time are 10%, 100 mW, and 16 min, respectively. The concentration varies from 0.068 to 0.272 mM.

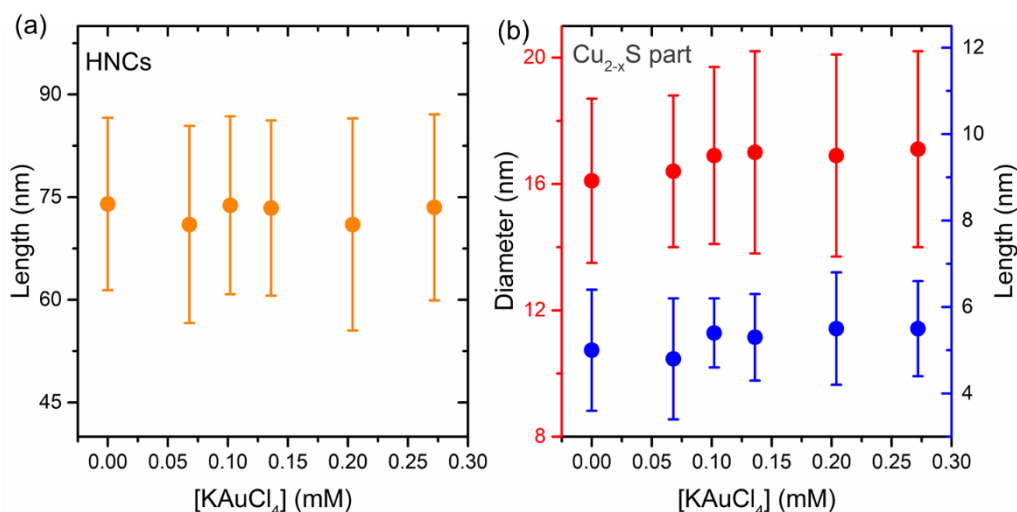


Figure 8. (a) Average length of the HNCs after deposition at different gold precursor concentrations. (b) The average diameter (red spheres, left Y-axis) and length (blue squares, left Y-axis) of the Cu_{2-x}S after deposition at different gold precursor concentrations.

6.3.2.4 Effect of the exposure time on the Au photodeposition

To understand the overall process of photodeposition, *ex-situ* TEM measurements were performed at different exposure times while all the other parameters were kept the same (10% vol. MeOH, P_L of 100 mW, and $[\text{Au}^{3+}]$ of 0.204 mM). For very short times (< 4 min), tiny single dots (5.3 nm) can be found on the Cu_{2-x}S tips (**Figure 9a, b**). With the increase of illumination time up to 8 min, the size of the Au NDs reaches ~7.5 nm and individual Au nanodots (~6.5 nm) start to grow on the side of elongated CuInS_2 (**Figure 9c**). Longer illumination time leads to the formation of multiple Au NDs. For example, at 16 min, the ratio of single, two, and multiple Au NDs reaches ~67%, 23%, and 3%, respectively (**Figure 10c**). For illumination time > 16 min, no Au NDs can be found anymore on the Cu_{2-x}S side of the HNCs, and the size of the Au NDs on the CuInS_2 side gradually increases up to ~8 nm at an irradiation of 64 min (**Figure 9d- f** and **Figure 10a**).

At 16 min of exposure, **Figure 9d** shows the presence of different types of nanoobjects: ① CuInS_2 grown on their own (they are not really cylindrical), ② $\text{Cu}_{2-x}\text{S}/\text{CuInS}_2$ HNCs with one Gold nanodot growing on the copper sulfide tip, ③ $\text{Cu}_{2-x}\text{S}/\text{CuInS}_2$ HNCs which seem to have the copper sulfide tip completely covered or alloyed with gold (see once again the difference of darkness of tips with sample ①), ④ $\text{Cu}_{2-x}\text{S}/\text{CuInS}_2$ HNCs with one gold ND growing on the copper sulfide tip and one on the CuInS_2 one, ⑤ $\text{Cu}_{2-x}\text{S}/\text{CuInS}_2$ HNCs which seem to have the copper sulfide tip completely covered or alloyed with gold so that it now looks like a nail head.

These interesting transitions indicate that the nucleation and growth of Au nanodots on $\text{Cu}_{2-x}\text{S}/\text{CuInS}_2$ HNCs may proceed in two ways

- (i) two sequential deposition steps, *i.e.*, selective deposition of Au on Cu_{2-x}S tips followed by the growth of Au on the side of CuInS_2 parts or
- (ii) assuming two growth laws with a rate much larger on Cu_{2-x}S than on CuInS_2 .

Moreover, with the increase of the exposure time, the volume as well as the contrast of Cu_{2-x}S part in HNCs gradually increase (**Figure 11b**). This phenomenon has also

been observed while intensifying the illumination power and increasing the gold ions concentration. It indicates that the Cu_{2-x}S part in HNCs should experience an obvious change of composition either by incorporating Au into Cu_{2-x}S or by converting Cu_{2-x}S into Au_2S *via* cation exchange under laser exposure at room temperature³⁶ or completing the deficient composition of this tip leading to a $\text{Cu}_{2-x}\text{Au}_x\text{S}/\text{CuInS}_2$ object on which gold NDs are then susceptible to photonucleate and grow leading to **5**.

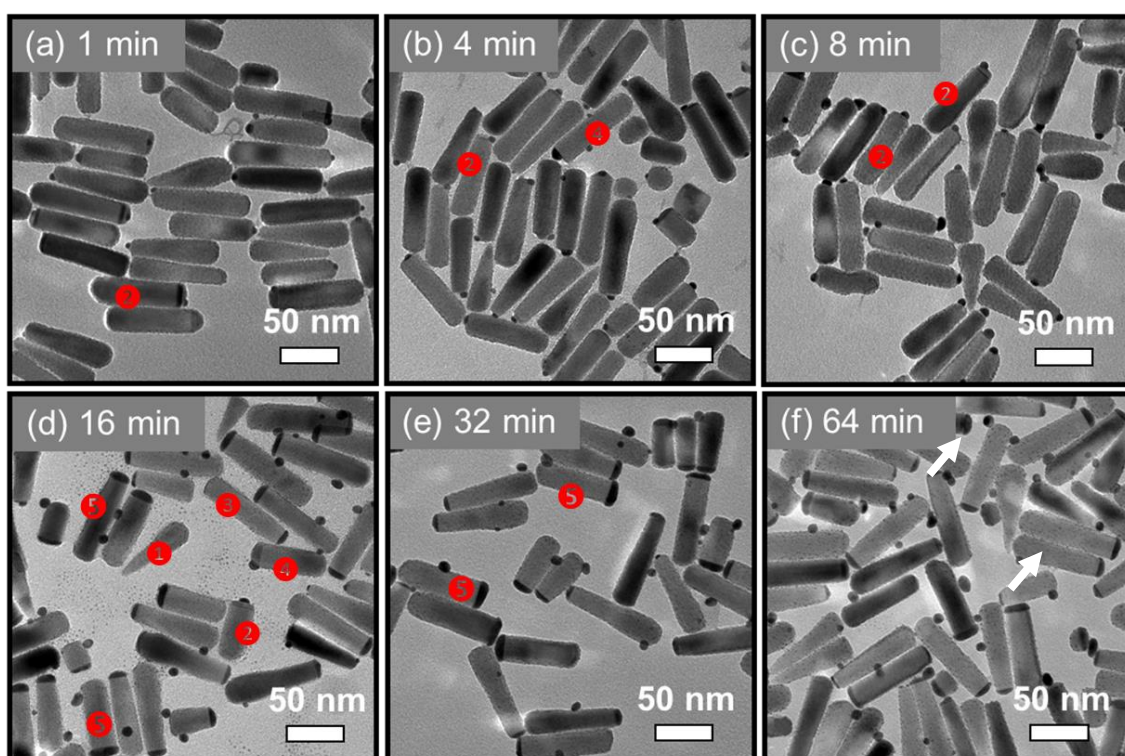


Figure 9. (a-f) TEM images of $\text{Au-Cu}_{2-x}\text{S}/\text{CuInS}_2$ HNCs obtained under different illumination times. The illumination time varies from 1 to 64 min.

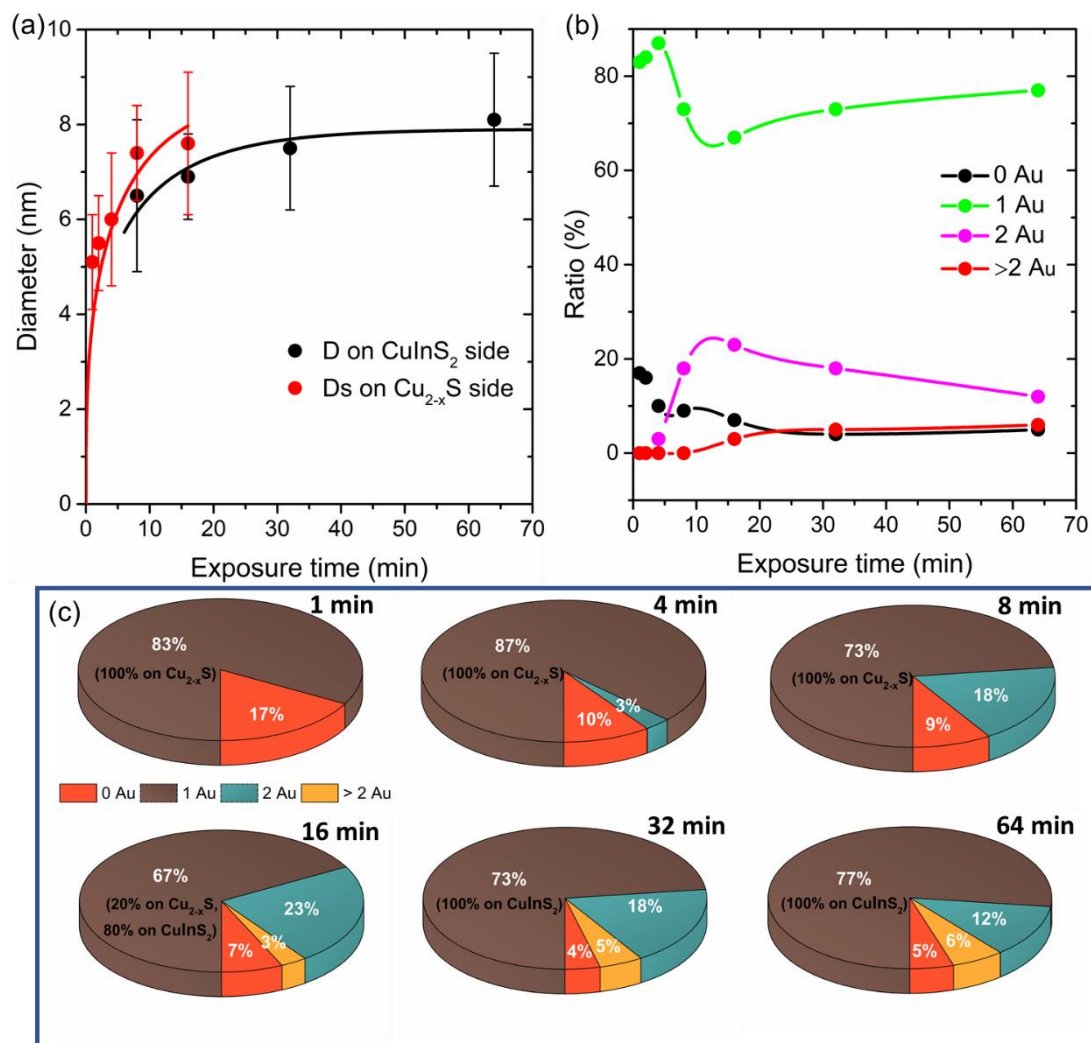


Figure 10. (a-b) Size (a) and distribution (b) of Au nanodots on HNCs with different exposure times. (c) Three-dimensional color pie chart of the number of Au nanodots on $\text{Cu}_{2-x}\text{S}/\text{CuInS}_2$ HNCs. The percentages of Au nanodot distributions are estimated by counting more than 200 nanoparticles. The volume percentage of MeOH, P_L , and $[\text{KAuCl}_4]$ are 10%, 100 mW, and 0.204 mM, respectively. The exposure times vary from 1 to 64 min.

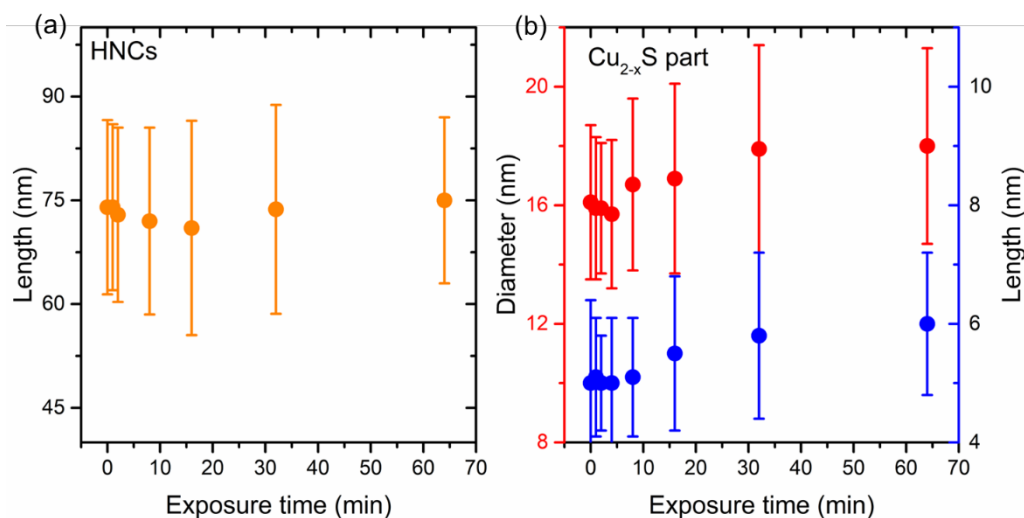


Figure 11. (a) Variation of the average length of the HNCs after deposition with the exposure time. (b) The average diameter (red spheres, left Y-axis) and length (blue squares, left Y-axis) of the Cu_{2-x}S after deposition at different exposure times.

6.3.2.5 Structural characterization of Au- $\text{Cu}_{2-x}\text{S}/\text{CuInS}_2$ hybrid HNCs

To reveal the underlying mechanisms of the selective photodeposition of Au nanodots on the $\text{Cu}_{2-x}\text{S}/\text{CuInS}_2$ HNCs, high-resolution TEM images of the Au- $\text{Cu}_{2-x}\text{S}/\text{CuInS}_2$ hybrid HNCs with different photodeposition times were performed. As demonstrated by **Figure 12a**, before photodeposition, the Cu_{2-x}S tip of the HNCs have the monoclinic low chalcocite crystal structure while the elongated CuInS_2 rods have the hexagonal wurtzite crystal structure, which is consistent with previous reports.^{11, 26} In the initial photodeposition step (~ 8 min), small single nanodots with a size of ~ 7 nm are successfully deposited on the side of Cu_{2-x}S tips. These individual nanodots are highly crystalline with a crystal lattice d-spacing of ~ 0.2 nm which can be indexed to the (200) plane of cubic Au metals (Figure 12b). Interestingly, when keeping photodeposition for another few minutes, the Au nanodots on the Cu_{2-x}S tips disappear accompanied by an obvious increase of the contrast and a crystal lattice d-spacing change from 0.34 to 0.38 nm (**Figure 12c**), indicating a non-negligible change of composition in Cu_{2-x}S tips either by the diffusion of the mobile Au atoms into Cu_{2-x}S or by the conversion of Cu_{2-x}S into Au_2S via cation exchange assuming anyway an oxidation process at this point. Indeed, a closer look at the part Cu_{2-x}S tips discloses

a new lattice fringe with a d-spacing of 0.29 nm, which can be referred to as the (111) plane of Au_2S (**Figure 12c,d**). With an increase in photodeposition time (~ 32 min), extra single Au nanodots are observed on the side of elongated CuInS_2 nanorods, as evidenced by the high-resolution TEM image in **Figure 12d**.

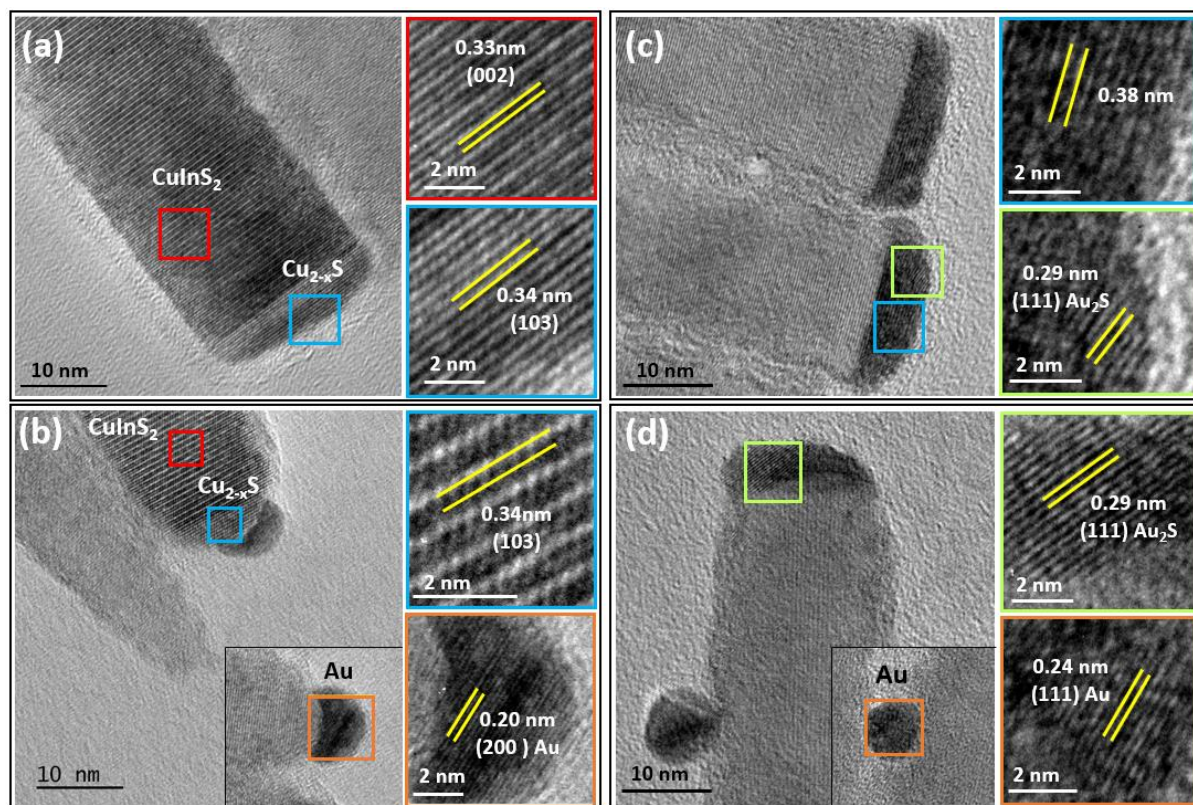


Figure 12. (a) High-resolution TEM image of $\text{Cu}_{2-x}\text{S}/\text{CuInS}_2$ HNCs. The Cu_{2-x}S tip (blue square) and elongated CuInS_2 rod (red square) can be indexed to monoclinic low chalcocite and hexagonal wurtzite crystal structures, respectively. (b) High-resolution TEM image of $\text{Au}-\text{Cu}_{2-x}\text{S}/\text{CuInS}_2$ hybrid HNCs with a photodeposition time of 8 min. Single nanodots (orange square) are deposited on the side of Cu_{2-x}S tips. The crystal lattice d-spacing of the nanodots matches well with the (200) plane of cubic Au nanoparticles. (c) High-resolution TEM of $\text{Au}-\text{Cu}_{2-x}\text{S}/\text{CuInS}_2$ hybrid HNCs with a photodeposition time of 16 min. The Au nanodots on the side of Cu_{2-x}S disappear while the contrast and d-spacing (blue square) of the Cu_{2-x}S tips increase. The crystal lattice d-spacing of some part (green square) of Cu_{2-x}S tips matches well with the (111) plane of cubic Au_2S . (d) High-resolution TEM of $\text{Au}-\text{Cu}_{2-x}\text{S}/\text{CuInS}_2$ hybrid HNCs with a photodeposition time of 16 min. An extra Au nanodot (orange square) deposits on the side of the elongated CuInS_2 part.

To further determine whether Au forms a shell around Cu_{2-x}S or penetrates in the Cu_{2-x}S layer, a two-dimensional elemental mapping was carried out to measure the composition of Cu_{2-x}S tips shown in **Figure 12c**. Before electron beam illumination,

the Au-containing Cu_{2-x}S tips show a strong contrast compared to the elongated CuInS_2 in the HNCs (**Figure 13a**). However, after 8 min the initial flat surface of the Cu_{2-x}S part turns to be irregular, which can be attributed to the structural rearrangement in a form of phase separation of metallic Au leaking out from the $\text{Au}_{2-x}\text{S}-\text{Cu}_{2-x}\text{S}$ or the alloyed $\text{Cu}_x\text{Au}_y\text{S}_2$ tips. This can be easily understood since Au_2S has a metastable crystal structure and can be readily reduced to metallic Au under a strong electron beam illumination (**Figure 13b**, **Figure 14**), which has also been observed in a previous report.³⁶ This poor stability of Au-containing Cu_{2-x}S tips under electron beam illumination makes the identification of their structure and composition extremely challenging. Nevertheless, we noticed that after the leakage of metallic Au from the Cu_{2-x}S tips, a weak contrast remains in the HNCs though their volume decreases as evidenced by the line scan of single Au- $\text{Cu}_{2-x}\text{S}/\text{CuInS}_2$ hybrid HNCs shown in **Figure 15**. It suggests that the Cu_{2-x}S are partially exchanged by Au_2S , being highly consistent with the high-resolution TEM images shown in **Figure 12c,d**. Further delicate in-depth elemental mapping is needed to unmask the detailed composition of Au-containing Cu_{2-x}S .

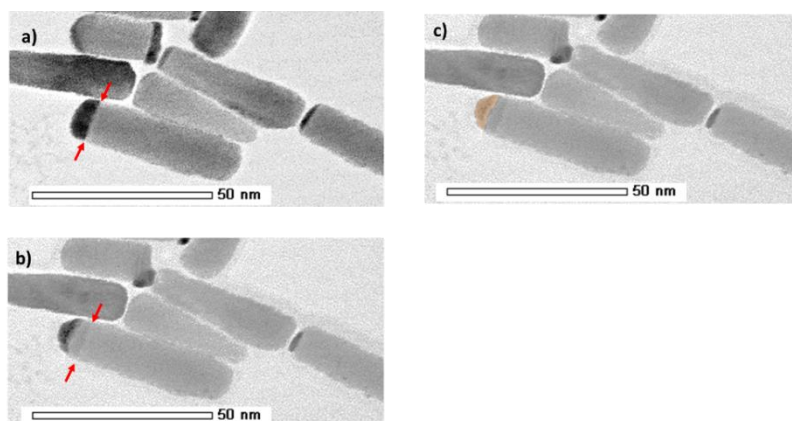


Figure 13. STEM images of Au-covered $\text{CuS}_2\text{-CuInS}_2$ a) just before the accumulation for EDS mapping; b) after the last accumulation. Red arrows in a) indicate the separation between the CuInS_2 component and the gold-containing Cu_{2-x}S one. Red arrows in b) indicate the separation between the CuInS_2 component and the Cu_{2-x}S one. The orange cap schematizes the gold deposit formed after the electron beam interaction.

Figure 14 additionally shows the different elemental mappings of the same region as in **Figure 13**. We retrieve the presence of S and Cu (**Figure 14e,f**) all along the rod length with respectively higher content on the corresponding parts. Indium is also selectively located on one part of the rods and the gold dot/cap does grow on the opposite side of Indium (Figure 14i).

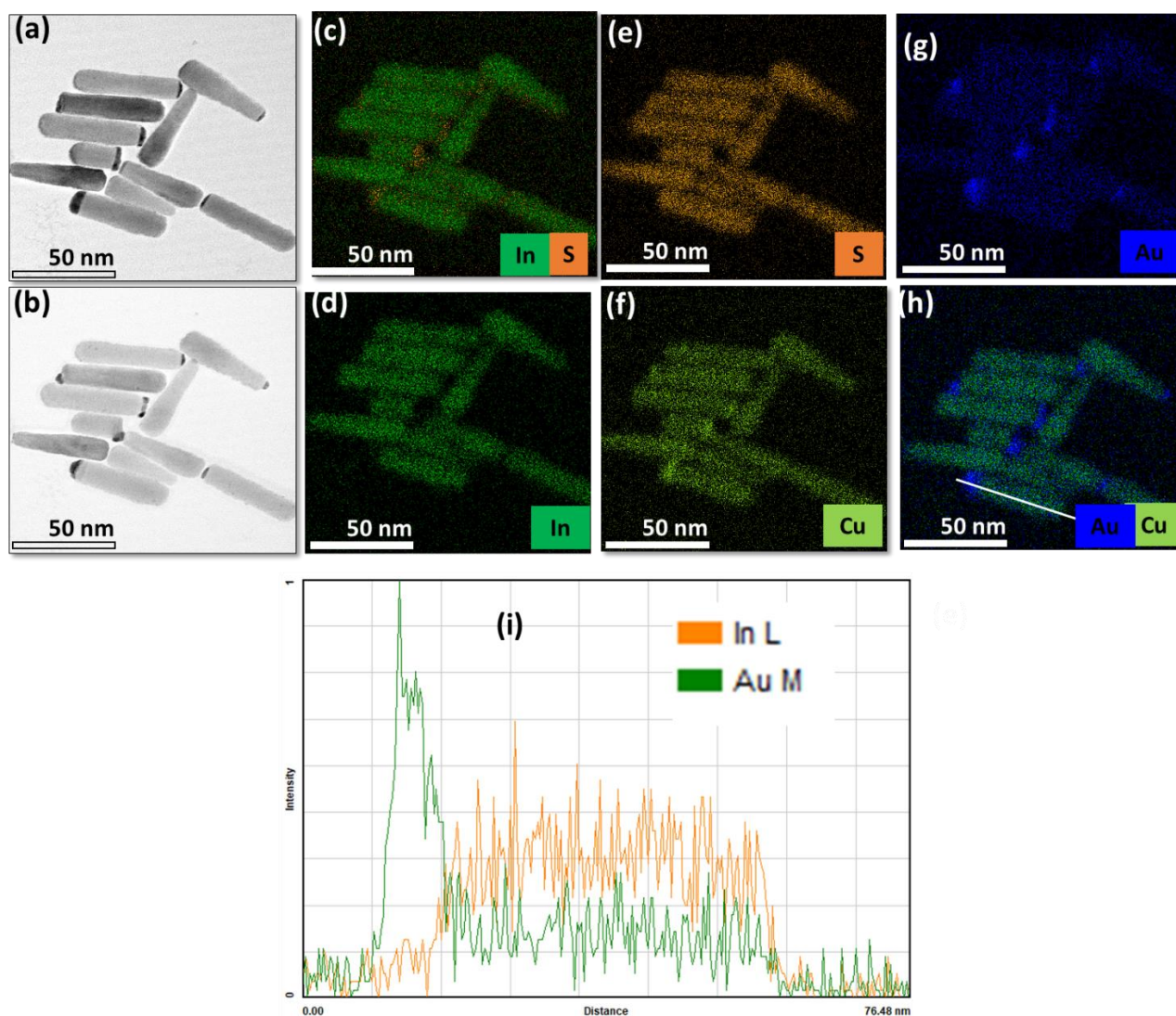


Figure 14. STEM image (a, b), and corresponding elemental mapping (c-g) of Au- $\text{Cu}_{2-x}\text{S}/\text{CuInS}_2$ HNCs. (a) is captured at the beginning of the scan and (b) is after an 8 min scan. (i) is the line-scan distribution profile.

If we add the copper profile to **Figure 14i** we obtain **Figure 15** which effectively shows a crossing between the ratios of copper and gold (zoom in **Figure 15b**) but the accumulation process of the technique cannot help in the discrimination. **Figure 15c**

also confirms that gold is only present where there is an excess of copper and no indium.

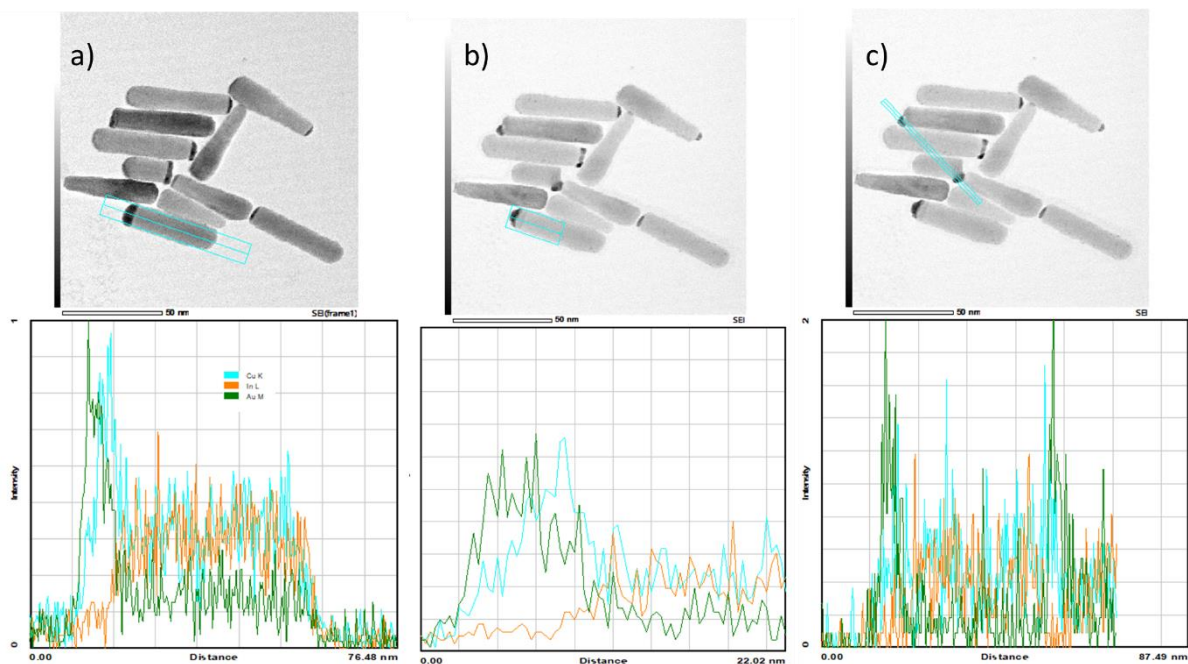


Figure 15. Elemental concentration profiles along one Au capped $\text{Cu}_{2-x}\text{S}/\text{CuInS}_2$ HNCs. (a) all rod b) only the copper-gold side; c) profile showing two gold dots on two different rods.

We also performed EDS profiles on HNCs bearing an identified gold nanodot on the pure copper side (**Figures 16 a,d, and b,e**). They confirm as HR-TEM not only the presence of the gold ND on the Cu_{2-x}S side but also (Figure 16c) the size increase of this dot under the electron beam.

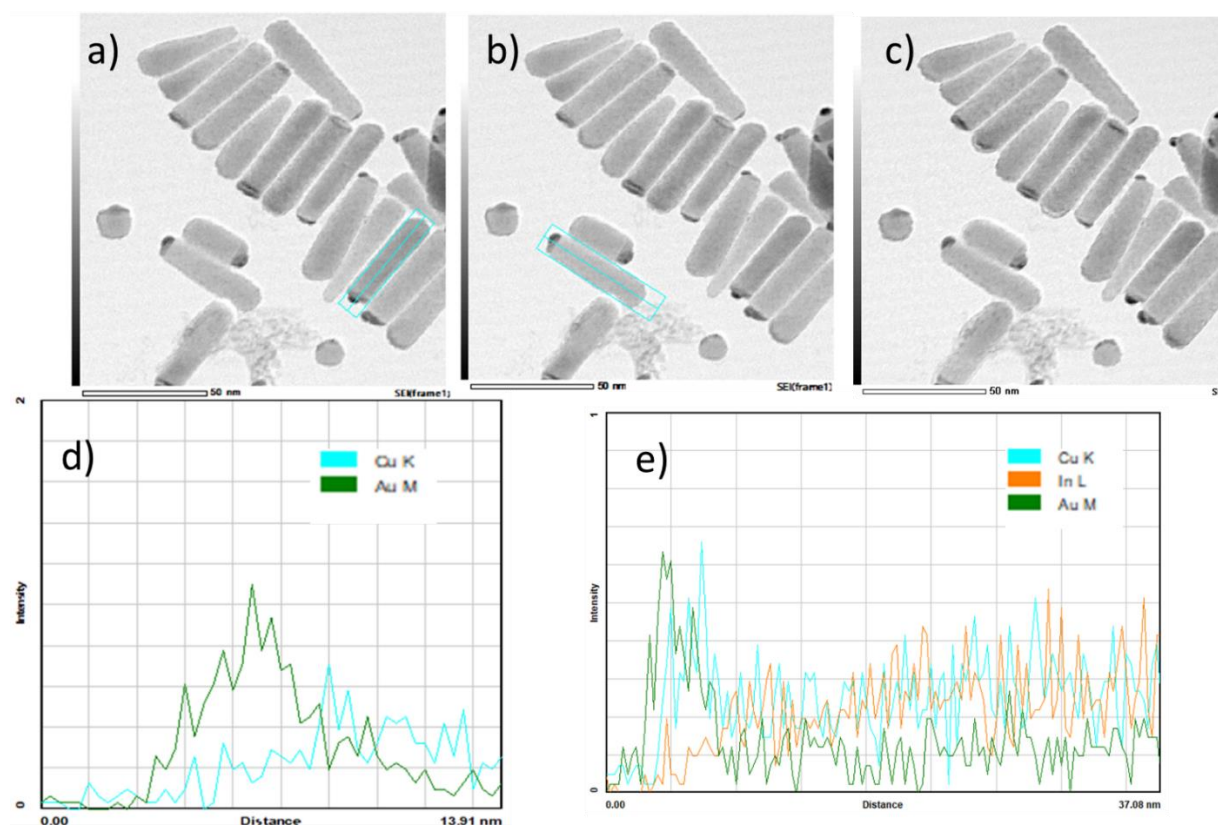


Figure 16. STEM image before electron beam interaction and Elemental concentration profiles along Au capped $\text{Cu}_{2-x}\text{S}/\text{CuInS}_2$ HNCs bearing an identified gold nanodot (a,d) and (b,e). (c) Same STEM image after 8 min accumulation showing the size increase of the gold nanodots.

6.3.2.6 Formation mechanism of Au photodeposition on $\text{Cu}_{2-x}\text{S}/\text{CuInS}_2$ HNCs

According to the results shown above, we propose that the formation mechanism of Au photodeposition on $\text{Cu}_{2-x}\text{S}/\text{CuInS}_2$ HNCs follows the three sequential stages listed below (**Figure 17**).

Stage 1: In the initial step, $[\text{Au}^{3+}]$ is preferentially reduced to Au^0 and deposited on Cu_{2-x}S tips. On the one hand, it may be due to the high number of defects on the Cu_{2-x}S sides as a result of the high mobility of Cu^+ in the crystal lattice.²⁴ On the other hand, it could be possible due to the low lattice mismatch between Cu_2S and Au which allows the epitaxy growth of Au nanodots on the surface of Cu_2S , as evidenced by the fact that the (102) planes of the hexagonal Cu_2S and the (111) planes of cubic Au have the

same distance $d = 2.4 \text{ \AA}$.³⁷ The growth of the Au nanodots is proportional to the illumination time and highly consistent with the calculations.

Stage 2: Under continuous irradiation, Au nanodots are unstable on such a surface and tend to either form a shell around the Cu_2S and block deposition on this side *or* merge with Cu_{2-x}S to reduce the surface energy and internal defects. The incorporation of Au into Cu_{2-x}S leads to an increase of bandgap and band re-alignment with CuInS_2 ,³⁸ which leads to the formation of type-II heterostructures.

Stage 3: Along with the incorporation of Au into Cu_{2-x}S , the surface energy and internal defects decrease and the alloyed $\text{Cu}_x\text{Au}_y\text{S}_2$ tips are no longer competitive to allow the deposition of Au nanodots. In contrast, the newly-formed staggered band alignment between the alloyed $\text{Cu}_x\text{Au}_y\text{S}_2$ and CuInS_2 promotes the photogenerated electrons flow from $\text{Cu}_x\text{Au}_y\text{S}_2$ to CuInS_2 and the photodeposition of the Au nanodots along the side of the elongated CuInS_2 parts.

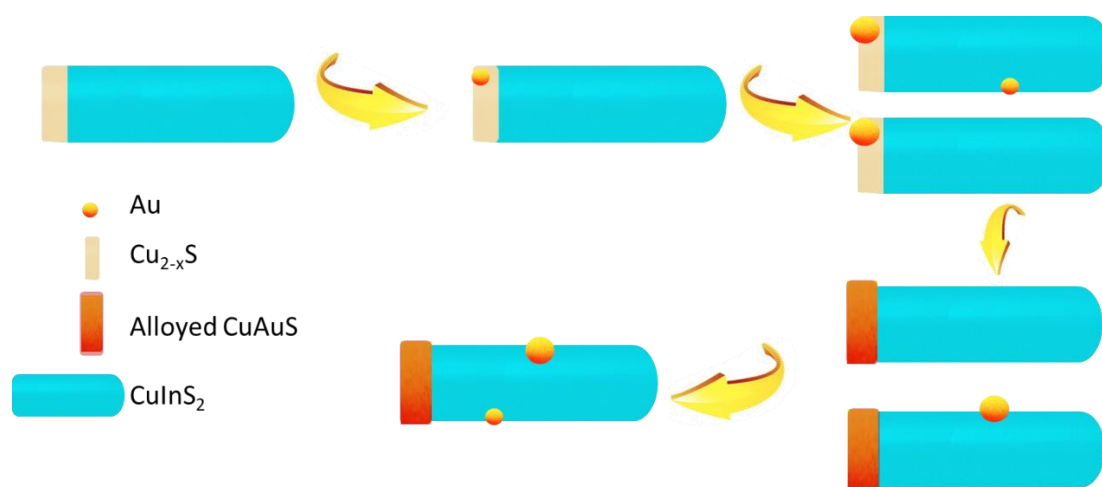


Figure 17. Illustration diagram of the Au photodeposition on $\text{Cu}_{2-x}\text{S}/\text{CuInS}_2$ HNCs.

6.3.3 Conclusion

In summary, we have developed a laser-based photodeposition approach to study the nucleation and growth of Au nanodots onto binary-ternary $\text{Cu}_{2-x}\text{S}/\text{CuInS}_2$ heteronanocrystals in toluene. The geometric distribution (e.g., number and location)

of Au nanodots, as well as their sizes, can be well controlled by tuning the concentration of the hole scavengers and Au precursors, illumination power, and exposure time. *Ex-situ* TEM tracking demonstrates that the deposition of Au nanodots on the HNCs exhibits pronounced selectivity and experiences a sequential transition from Cu_{2-x}S tips to CuInS_2 . Individual Au nanoparticles prefer to first nucleate and grow on the tips of Cu_{2-x}S parts. Under continuous irradiation, Au nanodots are forced to be dissociated and merged with Cu_{2-x}S to reduce the energy of the surface and internal defects. The incorporation of Au into Cu_{2-x}S leads to an increase in bandgap and band re-alignment with CuInS_2 , which gives rise to a true type-II heterostructure. This staggered band alignment promotes the photogenerated electrons to flow from Cu_{2-x}S to CuInS_2 and accelerates the photodeposition of Au nanodots on the side of elongated CuInS_2 parts. The Au introduction and selective decoration will lead to an understanding of the primary physical mechanisms of charge carrier dynamics and design principles to achieve efficient photocatalytic activity which is important for developing more efficient and stable photocatalysts.

6.4 References

1. Zada, A.; Muhammad, P.; Ahmad, W.; Hussain, Z.; Ali, S.; Khan, M.; Khan, Q.; Maqbool, M., Surface Plasmonic-Assisted Photocatalysis and Optoelectronic Devices with Noble Metal Nanocrystals: Design, Synthesis, and Applications. *Adv. Funct. Mater.* **2020**, *30* (7), 1906744.
2. Volokh, M.; Mokari, T., Metal/Semiconductor Interfaces in Nanoscale Objects: Synthesis, Emerging Properties and Applications of Hybrid Nanostructures. *Nanoscale Adv.* **2020**, *2* (3), 930-961.
3. Kumar, A.; Choudhary, P.; Kumar, A.; Camargo, P. H. C.; Krishnan, V., Recent Advances in Plasmonic Photocatalysis Based on TiO₂ and Noble Metal Nanoparticles for Energy Conversion, Environmental Remediation, and Organic Synthesis. *Small* **2021**, 2101638.
4. Wenderich, K.; Mul, G., Methods, Mechanism, and Applications of Photodeposition in Photocatalysis: A Review. *Chem. Rev.* **2016**, *116* (23), 14587–14619.
5. Yuan, Y.-J.; Chen, D.; Yu, Z.-T.; Zou, Z.-G., Cadmium Sulfide-Based Nanomaterials for Photocatalytic Hydrogen Production. *J. Mater. Chem. A* **2018**, *6* (25), 11606-11630.
6. Yang, K.; Yang, Z.; Zhang, C.; Gu, Y.; Wei, J.; Li, Z.; Ma, C.; Yang, X.; Song, K.; Li, Y.; Fang, Q.; Zhou, J., Recent Advances in CdS-based Photocatalysts for CO₂ Photocatalytic Conversion. *Chem. Eng. J.* **2021**, *418*, 129344.
7. Motl, N. E.; Bondi, J. F.; Schaak, R. E., Synthesis of Colloidal Au–Cu₂S Heterodimers via Chemically Triggered Phase Segregation of AuCu Nanoparticles. *Chemistry of Materials* **2012**, *24* (9), 1552-1554.
8. Wolf, A.; Hinrichs, D.; Sann, J.; Miethe, J. F.; Bigall, N. C.; Dorfs, D., Growth of Cu_{2-x}Se–CuPt and Cu_{1.1}S–Pt Hybrid Nanoparticles. *J. Phys. Chem. C* **2016**, *120* (38), 21925–21931.
9. Fenton, J. L.; Hodges, J. M.; Schaak, R. E., Synthetic Deconvolution of Interfaces and Materials Components in Hybrid Nanoparticles. *Chemistry of Materials* **2017**, *29* (14), 6168–6177.
10. Gan, X. Y.; Sen, R.; Millstone, J. E., Connecting Cation Exchange and Metal Deposition Outcomes via Hume–Rothery-Like Design Rules Using Copper Selenide Nanoparticles. *Journal of the American Chemical Society* **2021**, *143* (21), 8137–8144.
11. Zhu, H.; Wang, Y.; Chen, C.; Ma, M.; Zeng, J.; Li, S.; Xia, Y.; Gao, M., Monodisperse Dual Plasmonic Au@Cu_{2-x}E (E= S, Se) Core@Shell Supraparticles: Aqueous Fabrication, Multimodal Imaging, and Tumor Therapy at in Vivo Level. *ACS Nano* **2017**, *11* (8), 8273–8281.
12. Zou, Y.; Sun, C.; Gong, W.; Yang, X.; Huang, X.; Yang, T.; Lu, W.; Jiang, J., Morphology-Controlled Synthesis of Hybrid Nanocrystals via a Selenium-Mediated Strategy with Ligand Shielding Effect: The Case of Dual Plasmonic Au–Cu_{2-x}Se. *ACS Nano* **2017**, *11* (4), 3776–3785.
13. Sen, S.; Shyamal, S.; Mehetor, S. K.; Sahu, P.; Pradhan, N., Au-Cu_{2-x}Te Plasmonic Heteronanostructure Photoelectrocatalysts. *J. Phys. Chem. Lett.* **2021**, *12* (47), 11585–11590.
14. Patra, B. K.; Khilari, S.; Pradhan, D.; Pradhan, N., Hybrid Dot–Disk Au-CuInS₂ Nanostructures as Active Photocathode for Efficient Evolution of Hydrogen from Water. *Chemistry of Materials* **2016**, *28* (12), 4358-4366.

15. Ghosh, A. B.; Saha, N.; Sarkar, A.; Dutta, A. K.; Maji, S. K.; Adhikary, B., Observation of Enhanced Photocurrent Response in M-CuInS₂ (M = Au, Ag) Heteronanostructures: Phase Selective Synthesis and Application. *New Journal of Chemistry* **2017**, *41* (2), 692–701.
16. Tang, S.-Y.; Medina, H.; Yen, Y.-T.; Chen, C.-W.; Yang, T.-Y.; Wei, K.-H.; Chueh, Y.-L., Enhanced Photocarrier Generation with Selectable Wavelengths by M-Decorated-CuInS₂ Nanocrystals (M = Au and Pt) Synthesized in a Single Surfactant Process on MoS₂ Bilayers. *Small* **2019**, *15* (8), 1803529.
17. Ghosh, A. B.; Saha, N.; Sarkar, A.; Dutta, A. K.; Satra, J.; Adhikary, B., Single Source Precursor Driven Phase Selective Synthesis of Au–CuGaS₂ Heteronanostructures: An Observation of Plasmon Enhanced Photocurrent Efficiency. *Dalton Transactions* **2018**, *47* (4), 1071–1081.
18. Wen, H.; Li, H.; He, S.; Chen, F.; Ding, E.; Liu, S.; Wang, B.; Peng, Y., Constructing Two-Dimensional CuFeSe₂@Au Heterostructured Nanosheets with An Amorphous Core and A Crystalline Shell for Enhanced Near-Infrared Light Water Oxidation. *Nanoscale* **2018**, *10* (5), 2380–2387.
19. Dilsaver, P. S.; Reichert, M. D.; Hallmark, B. L.; Thompson, M. J.; Vela, J., Cu₂ZnSnS₄–Au Heterostructures: Toward Greener Chalcogenide-Based Photocatalysts. *J. Phys. Chem. C* **2014**, *118* (36), 21226–21234.
20. Regulacio, M. D.; Han, M.-Y., Multinary I-III-VI₂ and I₂-II-IV-VI₄ Semiconductor Nanostructures for Photocatalytic Applications. *Accounts of chemical research* **2016**, *49* (3), 511–519.
21. Yu, X.; Du, R.; Li, B.; Liu, L.; Zhang, Y., Cu₂ZnSnS₄–AuAg Heterodimers and Their Enhanced Catalysis for Oxygen Reduction Reaction. *J. Phys. Chem. C* **2017**, *121* (12), 6712–6720.
22. Ganai, A.; Maiti, P. S.; Houben, L.; Bar-Ziv, R.; Bar Sadan, M., Inside-Out: The Role of Buried Interfaces in Hybrid Cu₂ZnSnS₄–Noble Metal Photocatalysts. *J. Phys. Chem. C* **2017**, *121* (12), 7062–7068.
23. Kalisman, P.; Nakibli, Y.; Amirav, L., Perfect Photon-to-Hydrogen Conversion Efficiency. *Nano letters* **2016**, *16* (3), 1776–1781.
24. Wang, L.-W., High Chalcocite Cu₂S: A Solid-Liquid Hybrid Phase. *Physical Review Letters* **2012**, *108* (8), 085703.
25. Coughlan, C.; Ibáñez, M.; Dobrozhan, O.; Singh, A.; Cabot, A.; Ryan, K. M., Compound Copper Chalcogenide Nanocrystals. *Chem. Rev.* **2017**, *117* (9), 5865–6109.
26. Xia, C.; van Oversteeg, C. H. M.; Bogaards, V. C. L.; Spanjersberg, T. H. M.; Visser, N. L.; Berends, A. C.; Meeldijk, J. D.; de Jongh, P. E.; de Mello Donega, C., Synthesis and Formation Mechanism of Colloidal Janus-Type $\text{Cu}_{2-x}\text{S}/\text{CuInS}_2$ Heteronanorods via Seeded Injection. *ACS Nano* **2021**, (15), 9987–9999.
27. Chakraborty, S.; Xing, G.; Xu, Y.; Ngiam, S. W.; Mishra, N.; Sum, T. C.; Chan, Y., Engineering Fluorescence in Au-Tipped, CdSe-Seeded CdS Nanoheterostructures. *Small* **2011**, *7* (20), 2847–2852.
28. Yang, J.; Levina, L.; Sargent, E. H.; Kelley, S. O., Heterogeneous Deposition of Noble Metals on Semiconductor Nanoparticles in Organic or Aqueous Solvents. *J. Mater. Chem.* **2006**, *16* (41), 4025–4028.
29. Essafri, I.; Ghoufi, A., Microstructure of Nonideal Methanol Binary Liquid Mixtures. *Physical Review E* **2019**, *99* (6), 062607.

30. Bai, Q.; Shupyk, I.; Vauriot, L.; Majimel, J.; Labrugere, C.; Delville, M.-H.; Delville, J.-P., Design of Metal@Titanium Oxide Nano-Heterodimers by Laser-Driven Photodeposition: Growth Mechanism and Modeling. *ACS Nano* **2021**, *15* (2), 2947-2961.
31. Hao, J.; Liu, H.; Wang, K.; Sun, X. W.; Delville, J.-P.; Delville, M.-H., Hole Scavenging and Electron-Hole Pair Photoproduction Rate: Two Mandatory Key Factors to Control Single-Tip Au-CdSe/CdS Nanoheterodimers. *ACS Nano* **2021**, *15* (9), 15328-15341.
32. Mokari, T.; Sztrum, C. G.; Salant, A.; Rabani, E.; Banin, U., Formation of Asymmetric One-Sided Metal-Tipped Semiconductor Nanocrystal Dots and Rods. *Nature materials* **2005**, *4* (11), 855.
33. Habas, S. E.; Yang, P.; Mokari, T., Selective Growth of Metal and Binary Metal Tips on CdS Nanorods. *J. Am. Chem. Soc.* **2008**, *130* (11), 3294-3295.
34. Menagen, G.; Macdonald, J. E.; Shemesh, Y.; Popov, I.; Banin, U., Au Growth on Semiconductor Nanorods: Photoinduced versus Thermal Growth Mechanisms. *J. Am. Chem. Soc.* **2009**, *131* (47), 17406-17411.
35. Wang, X.; Liu, X.; Zhu, D.; Swihart, M. T., Controllable Conversion of Plasmonic Cu_{2-x}S Nanoparticles to Au₂S by Cation Exchange and Electron Beam Induced Transformation of Cu_{2-x}S-Au₂S Core/Shell Nanostructures. *Nanoscale* **2014**, *6* (15), 8852-8857.
36. Hernández-Pagán, E. A.; O'Hara, A.; Arrowood, S. L.; McBride, J. R.; Rhodes, J. M.; Pantelides, S. T.; Macdonald, J. E., Transformation of the Anion Sublattice in the Cation-Exchange Synthesis of Au₂S from Cu_{2-x}S Nanocrystals. *Chemistry of Materials* **2018**, *30* (24), 8843-8851.
37. Kim, Y.; Park, K. Y.; Jang, D. M.; Song, Y. M.; Kim, H. S.; Cho, Y. J.; Myung, Y.; Park, J., Synthesis of Au-Cu₂S Core-Shell Nanocrystals and Their Photocatalytic and Electrocatalytic Activity. *The Journal of Physical Chemistry C* **2010**, *114* (50), 22141-22146.
38. Adeleye, D.; Lomuscio, A.; Sood, M.; Siebentritt, S., Lifetime, Quasi-Fermi Level Splitting and Doping Concentration of Cu-Rich CuInS₂ Absorbers. *Materials Research Express* **2021**, *8* (2), 025905.

Conclusions and Perspectives

In this thesis, we worked on the following objectives:

- (1) to introduce monometallic (Au, Ag, and Pd) and bimetallic core-shell (Au@Au, Au@Ag, and Au@Pd) nanodots (NDs) on the surface of TiO₂ nanoparticles (NPs) by photodeposition method in a simple cuvette setup using UV laser as a source;
- (2) to photodeposit Au NPs on the Janus-type Cu_{2-x}S-CuInS₂ heteronanorods in organic media with a blue laser as a light source;
- (3) to investigate the growth law of the metal NPs during the photodeposition process and built a growth model.

To fulfill these goals, in **chapter 1**, a bibliography study on principles and recent advances in the photodeposition of metals on colloidal semiconductor nanocrystals was done. Then, two different cuvette setups were built with UV (364 nm) and blue (473 nm) lasers as sources for photodeposition (**chapter 2**). The setup configuration and laser control for the photodeposition were introduced. In **chapter 3**, Au-TiO₂ nanoheterodimers (NHDs) were synthesized successfully and a close to 100% yield of Au-TiO₂ NHDs was achieved by managing the concentration of KAuCl₄ and TiO₂. Especially, the adsorption mechanism of methanol and gold precursor on TiO₂ during photodeposition was investigated. It was illustrated that the photodeposition of metals onto TiO₂ was driven by physisorption by fitting the experimental data. The final size of Au NDs can be accurately predicted in particular the growth completion. In **chapter 4**, Other metal Ag and Pd NDs were deposited on the surface of TiO₂, and Ag-TiO₂ and Pd-TiO₂ are also synthesized. The effects of the hole scavenger, laser power, and exposure time on the size and distribution of metal particles are discussed. The growth of Ag and Pd NDs is also in agreement with the model developed for gold. In **Chapter 5**, the project was extended from monometallic photodeposition to bimetallic core-shell NPs photodeposition. Au-TiO₂ NHDs were used as templates, Au, Ag, and Pd cations could be reduced on the Au site by a second step photodeposition process, forming a core-shell structure attached to the surface of TiO₂. For the Au@Au core@shell, the Au shell can be precisely controlled by varying the gold precursor concentration and

the size and thickness of the Au core and shell fit our expectations. For the Au@Ag system, the Ag shell obtained was limited to around 1 nm thickness which was less than expected, which results from the low electronegativity of Ag (1.9) compared to other Au (2.4). For the Au@Pd system, Pd showed a non-isotropic growth on the Au core resulting in a nonuniform Pd shell which was due to the lattice mismatch between Au and Pd. **In chapter 6**, Au NDs were introduced onto Cu_{2-x}S/CuInS₂ heteronanorods by photodeposition in toluene. We studied the nucleation and growth of Au NDs and the geometric distribution (e.g., number and location) of Au NDs as well as their sizes can be well controlled by tuning laser power, exposure time, hole scavengers, and precursors concentration.

From the perspective of the project, some more work needs to be done to solve the multi-particle problem since the results of Ag NDs deposited on TiO₂ and Au-TiO₂ are not very ideal, PVP could be present during the deposition process to solve this multinucleation problem of silver. Beyond the photoreduction of metal ions on semiconductors, research about introducing metal oxides (e.g., NiO, CoOx, MnOx, and RuO₂) on TiO₂ by photo-oxidation needs to be studied. M1-TiO₂-M2 (M1: metal oxide; M2: noble metal) photocatalysts modified with binary cocatalysts could also be considered.

For the deposition of Au NDs onto Cu_{2-x}S/CuInS₂ heteronanorods in toluene, different long nanorods should be applied and used for investigating the effects on deposition and clearing the mechanism of the evolution in the deposition process.

Last but not least, some catalytic performances of as-prepared catalysts should be tested shortly.

Appendix 1

Prediction of metal size deposited on TiO₂ nanoparticles

A1.1 Concentration of TiO₂ particles

The TiO₂ particle is a polyhedron with (11±2), (11±2), and (18±4) nm in half-axis lengths. Assuming ellipsoidal TiO₂ NPs, the volume of one particle is

$$V_{TiO_2} = \frac{4}{3} \times \pi \times 11 \times 11 \times 18 = 9.12 \times 10^{-24} m^3.$$

Using $\rho_{TiO_2} = 3.9 g/cm^3$ for the density of anatase, so the mass of a single TiO₂ particle is

$$m_{(1)TiO_2} = \rho_{TiO_2} \times V_{TiO_2} = 3.9 \times 9.12 \times 10^{-18} g = 3.56 \times 10^{-17} g.$$

When the TiO₂ concentration is 5.5 mM (atomic concentration), the total mass of TiO₂ in a 1mL solution is

$$m_{TiO_2} = c_{TiO_2} \times V_{sol} \times M_{TiO_2} = 5.5 \times 1 \times 79.87 \times 10^{-6} g = 4.39 \times 10^{-4} g.$$

So in 1mL and 5.5 mM TiO₂ solution, the number of TiO₂ NPs is

$$N_{TiO_2} = \frac{m_{TiO_2}}{m_{(1)TiO_2}} = \frac{4.39 \times 10^{-4}}{3.56 \times 10^{-17}} = 1.23 \times 10^{13}.$$

Thus, the number density of TiO₂ nanoparticles is

$$D_{TiO_2}^* = 1.23 \times 10^{13} / mL.$$

A1.2 Estimation of the size of Au NDs deposited on TiO₂ particles

The contact angle of a gold nanodot onto TiO₂ is around 140° as illustrated below.

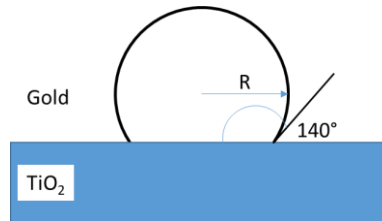


Figure A1.1 Picture of Au deposited on TiO₂

In this case, the volume of the spherical cap is given by $V = \pi D^3 \Gamma(\theta) / 8$ where $\Gamma(\theta) = \left(\frac{2}{3} - \cos \theta + \frac{1}{3} \cos^3 \theta \right)$. With a 140° contact angle, one finds $\Gamma(\theta) = 1.2829$. This calculation refers to Henry's report¹.

For a solution with a volume $V_{sol} = 1 mL$ and given concentrations of TiO₂ and Au³⁺ are

c_{TiO_2} (mM) and $c_{Au^{3+}}$ (mM), respectively, if we assume the Au³⁺ consumption is 100%, so the total mass of reduced Au is

$$m_{Au} = 100\% \times V_{sol} \times c_{Au^{3+}} \times M_{Au} = 1 \times c_{Au^{3+}} \times 1.97 \times 10^{-4} g = 1.97 \times c_{Au^{3+}} \times 10^{-4} g.$$

Assuming the Nanoheterodimers (NHDs) yield is ε , so the number of Au particles is

$$N_{Au} = \varepsilon \times V_{sol} \times \frac{c_{TiO_2} \times 1.23 \times 10^{16}}{5.5} = \varepsilon \times C_{TiO_2} \times 2.24 \times 10^{12}.$$

Then the mass of a single Au particle is

$$m_{1Au} = \frac{m_{Au}}{N_{Au}} = \frac{1.97 \times c_{Au^{3+}} \times 10^{-4} g}{\varepsilon \times C_{TiO_2} \times 2.24 \times 10^{12}} = \frac{c_{Au^{3+}}}{\varepsilon \times C_{TiO_2}} \times 8.79 \times 10^{-17} g.$$

Then we can deduce the diameter of the Au particle,

$$m_{1Au} = V_{1Au} \times 19.3 g/cm^3$$

$$\frac{c_{Au^{3+}}}{\varepsilon \times C_{TiO_2}} \times 8.79 \times 10^{-17} g = 1.2829 \times \pi D^3 / 8 \times 19.3$$

$$D = 20.8 \times \sqrt[3]{\frac{c_{Au^{3+}}}{\varepsilon \times C_{TiO_2}}} nm.$$

For example, assuming the NHDs yields ε are 50% and 100%, when the concentration of TiO₂ is 5.5mM and Au³⁺ is 0.5mM, the estimated size of the Au particles should be

$$D_{\varepsilon=50\%} = 20.8 \times \sqrt[3]{\frac{0.5}{0.5 \times 5.5}} = 11.78 nm$$

$$D_{\varepsilon=100\%} = 20.8 \times \sqrt[3]{\frac{0.5}{1 \times 5.5}} = 9.35 nm.$$

A1.3 General method to estimate the size of the metal (Au, Ag, Pd) NDs on TiO₂ particles

For a solution with a volume $V_{sol} = 1$ ml and given concentrations of TiO₂ and metallic precursor c_{TiO_2} (mM) and c_M (mM), respectively, if we assume the precursor consumption is 100%, so the total mass of reduced metal is

$$m_M = 100\% \times V_{sol} \times c_{Au^{3+}} \times M_M = c_{Au^{3+}} M_M.$$

Assuming the Janus yield is ε , so the number of metal particles is

$$N_M = \varepsilon \times V_{sol} \times \frac{c_{TiO_2} \times D_{TiO_2}^*}{5.5} = \frac{V_{sol} \times c_{TiO_2} \times \varepsilon \times D_{TiO_2}^*}{5.5}.$$

Then the mass of a single metal particle is

$$m_{1M} = \frac{m_M}{N_M} = \frac{5.5 \times m_M}{V_{sol} \times \varepsilon \times c_{TiO_2} \times D_{TiO_2}^*}.$$

Here, for the volume of a single metal particle, we also use the same method as Au, $V_{1M} = \pi D^3 \Gamma(\theta)/8$. one finds $\Gamma(\theta)=1.2829$ when the contact angle is 140°.

Then we can deduce the diameter of the metal particle,

$$m_{1M} = V_{1M} \times \rho_M \quad \text{with,}$$

$$\frac{5.5 \times c_{Au^{3+}} \times M_M}{V_{sol} \times \varepsilon \times C_{TiO_2} \times D_{TiO_2}^*} = 1.2829 \times \pi D^3 / 8 \times \rho_M$$

$$D_M = 2.22 \times \sqrt[3]{\frac{c_{Au^{3+}} M_M}{\rho_M \times V_{sol} \times \varepsilon \times C_{TiO_2} \times D_{TiO_2}^*}} = \left[9.6 \times \left(\frac{c_{Au^{3+}} M_M}{\rho_M \times \varepsilon \times C_{TiO_2}} \right)^{\frac{1}{3}} \right] nm$$

a) When the metal is Au, $M_{Au} = 196.97 \text{ g/mol}$, $\rho_{Au} = 19.30 \text{ g/cm}^3$,

$$D_{Au} = \left[20.8 \times \left(\frac{c_{Au^{3+}}}{\varepsilon \times C_{TiO_2}} \right)^{\frac{1}{3}} \right] nm$$

b) When the metal is Ag, $M_{Ag} = 108.87 \text{ g/mol}$, $\rho_{Ag} = 10.49 \text{ g/cm}^3$,

$$D_{Ag} = \left[20.9 \times \left(\frac{c_{Ag^+}}{\varepsilon \times C_{TiO_2}} \right)^{\frac{1}{3}} \right] nm$$

c) When the metal is Pd, $M_{Pd} = 106.42 \text{ g/mol}$, $\rho_{Pd} = 12.02 \text{ g/cm}^3$,

$$D_{Pd} = \left[19.9 \times \left(\frac{c_{Pd^{2+}}}{\varepsilon \times C_{TiO_2}} \right)^{\frac{1}{3}} \right] nm$$

A1.4 Estimation of the metal size of the second-step deposition

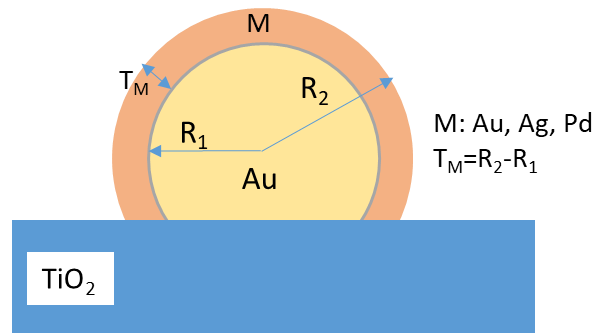


Figure A1.2 Scheme of metal deposited on Au-TiO₂

First, we assume that the Au-TiO₂ was synthesized in a 1 mL solution when the concentration of TiO₂ is c_{TiO_2} (mM) and the diameter of Au particles on TiO₂ is 2R₁ (nm), the NHDs yield of Au-TiO₂ is ε . Then α μ mol of the metal M precursor was added for the shell

formation and assuming the M precursor consumption is 100%, then we started the deduction.

The volume of the bimetallic core-shell structure is composed of the volume of the Au core and the M shell, so the volume of a single M shell is,

$$V_{1M\ shell} = V_{1(core-shell)} - V_{1Au\ core} = \frac{\pi D_2^3 \Gamma(\theta)}{8} - \frac{\pi D_1^3 \Gamma(\theta)}{8} = 4.03 \times (R_2^3 - R_1^3).$$

As the NHDs yield of Au-TiO₂ is ε , so the number of core-shell structured metal particles is

$$N_{M\ shell} = \varepsilon \times V_{sol} \times \frac{c_{TiO_2} \times D_{TiO_2}^*}{5.5} = \frac{c_{TiO_2} \times \varepsilon \times D_{TiO_2}^*}{5.5}.$$

The mass of the metal M shell should be this,

$$m_{M\ shell} = N_{M\ shell} \times V_{1M\ shell} \times \rho_M = 0.73 \times c_{TiO_2} \times \varepsilon \times D_{TiO_2}^* \times \rho_M \times (R_2^3 - R_1^3)$$

$$m_{M\ shell} = \alpha \times M_M \times 10^{-6}$$

Thus, we can deduce R_2 is,

$$R_2 = \left(\frac{111 \times \alpha \times M_M}{c_{TiO_2} \times \varepsilon \times \rho_M} + R_1^3 \right)^{1/3} \text{ nm}$$

$$D_{Core-shell} = 2R_2 = \left(\frac{888 \times \alpha \times M_M}{c_{TiO_2} \times \varepsilon \times \rho_M} + 8R_1^3 \right)^{1/3} \text{ nm}$$

The thickness of the M shell is,

$$T_{Core-shell} = R_2 - R_1 = \left[\left(\frac{111 \times \alpha \times M_M}{c_{TiO_2} \times \varepsilon \times \rho_M} + R_1^3 \right)^{1/3} - R_1 \right] \text{ nm}$$

a) When the metal is Au, $M_{Au} = 196.97 \text{ g/mol}$, $\rho_{Au} = 19.30 \text{ g/cm}^3$,

$$D_{Core-shell} = \left(\frac{888 \times \alpha \times M_{Au}}{c_{TiO_2} \times \varepsilon \times \rho_{Au}} + 8R_1^3 \right)^{1/3} = \left(\frac{9.06 \times 10^3 \times \alpha}{c_{TiO_2} \times \varepsilon} + 8R_1^3 \right)^{1/3} \text{ nm}$$

b) When the M metal is Ag, $M_{Ag} = 108.87 \text{ g/mol}$, $\rho_{Ag} = 10.49 \text{ g/cm}^3$,

$$D_{Core-shell} = \left(\frac{888 \times \alpha \times M_{Ag}}{c_{TiO_2} \times \varepsilon \times \rho_{Ag}} + 8R_1^3 \right)^{1/3} = \left(\frac{9.22 \times 10^3 \times \alpha}{c_{TiO_2} \times \varepsilon} + 8R_1^3 \right)^{1/3} \text{ nm}$$

c) When the M metal is Pd, $M_{Pd} = 106.42 \text{ g/mol}$, $\rho_{Pd} = 12.02 \text{ g/cm}^3$,

$$D_{Core-shell} = \left(\frac{888 \times \alpha \times M_{Pd}}{c_{TiO_2} \times \varepsilon \times \rho_{Pd}} + 8R_1^3 \right)^{1/3} = \left(\frac{7.86 \times 10^3 \times \alpha}{c_{TiO_2} \times \varepsilon} + 8R_1^3 \right)^{1/3} \text{ nm}$$

Appendix 2

Characterization techniques

The TEM analyses were performed on three machines, a JEOL JEM1400 Plus microscope operating at 120 kV, an FEI-Technai 12 microscope operating at 100 kV, and an FEI Technai 20 microscope operating at 200 kV. High-resolution TEM (HRTEM), high-angle annular dark-field scanning TEM (HAADF-STEM), and elemental mapping were performed on a Talos F200X (Thermo Fisher Scientific) and a JEOL 2100 operating at 200 kV.

The UV-vis absorption spectra were recorded with a SHIMADZU UV-3600 UV-Vis-Nir spectrophotometer using 10 mm cuvettes.

X-ray diffraction (XRD) measurements were carried out at room temperature with a PANalytical X'pert Pro MPD diffractometer using a Cu K α 1 radiation, $\lambda = 1.540\ 598\ \text{\AA}$. and Bragg-Brentano geometry. $2\ \theta$ was in the range between 8° and 80° with a step size of 0.02° .

References

1. Henry, C. R., Growth, Structure and Morphology of Supported Metal Clusters Studied by Surface Science Techniques. *Crystal Research and Technology: Journal of Experimental and Industrial Crystallography* **1998**, 33 (7-8), 1119-1140.

Titre : Synthèse d'hétérostructures métal-semiconducteur par photodéposition laser

Résumé :

Un montage utilisant des cuvettes et des lasers UV et bleu comme sources de lumière a été construit pour effectuer la photodéposition de nanodots métalliques (NDs) sur des nanoparticules (NPs) de TiO₂ et des nano-hétérostructures de type Janus de Cu_{2-x}S-CuInS₂ en solution aqueuse et organique respectivement. Trois types de NDs métalliques différents, à savoir Au, Ag, Pd, sont introduits en surface des NPs de TiO₂, et des NDs d'Ag sont déposés sur Cu_{2-x}S-CuInS₂. Plusieurs techniques, dont le TEM/HRTEM, la cartographie EDS et la spectroscopie UV-vis, sont utilisées pour caractériser la taille, la morphologie et la distribution des NDs métalliques. Les nanohétérodimères (NHDs) Au-TiO₂ sont synthétisés avec succès ; un rendement de NHDs Au-TiO₂ proche de 100% est obtenu en gérant la concentration des NPs TiO₂ et du précurseur d'or. En particulier, le mécanisme d'adsorption du méthanol et du précurseur d'or sur le TiO₂ pendant la photodéposition est étudié. En comparant les données expérimentales obtenues dans des microcanaux et des cuvettes, le modèle établi décrit le processus dynamique global de la croissance des NDs d'Ag sur le TiO₂, de la loi de croissance en $t^{1/3}$ à l'achèvement. La taille finale des NDs d'Ag peut être prédite avec précision par le modèle, en particulier la fin de la croissance. De plus, des NPs d'Ag et de Pd d'autres métaux ont été déposées sur la surface de TiO₂, et des NHDs d'Ag-TiO₂ et de Pd-TiO₂ ont également été synthétisés. Les effets du piègeur de trous, de la puissance du laser et du temps d'exposition sur la taille et la distribution des NDs métalliques sont étudiés. De plus, la croissance des NDs d'Ag et de Pd suit le modèle proposé pour la croissance de l'Ag. Le projet est étendu à la photodéposition de NDs bimétalliques cœur-coquille où Au, Ag et Pd sont introduits sur des NHDs Au-TiO₂ par une seconde étape de photodéposition, formant une structure cœur-coquille à la surface des NPs TiO₂. Pour le système Au@Au core@shell, la coquille d'Ag peut être contrôlée avec précision en faisant varier la concentration du précurseur d'or ; la taille et l'épaisseur du cœur et de la coquille d'Ag correspondent à nos attentes. Pour le système Au@Ag, la coquille d'Ag obtenue est limitée à environ 1 nm d'épaisseur, ce qui résulte de la faible électronégativité de l'Ag (1,9) par rapport à l'Ag (2,4). Pour le système Au@Pd, le Pd présente une croissance non isotrope sur le cœur d'Ag, ce qui entraîne une coquille de Pd non uniforme en raison de l'important décalage de réseau entre Au et Pd. Enfin, des NDs d'Ag sont introduits sur des hétéro-nanorods de Cu_{2-x}S-CuInS₂ par photodéposition dans le toluène avec un laser bleu. La nucléation et la croissance des Ag NDs sont étudiées et la distribution géométrique (i.e., le nombre et la distribution) des Ag NDs, ainsi que leurs tailles, peuvent être bien contrôlées en réglant la puissance du laser, le temps d'exposition, les piègeurs de trous et la concentration des précurseurs.

Mots clés : Métal noble, laser, photodéposition, hétérostructures, oxyde métallique et semi-conducteurs sans cadmium

Title : Synthesis of Metal-semiconductor Heterostructures by Laser Photodeposition

Abstract :

Cuvette setup with UV and blue laser as light sources are built to perform photodeposition of metals nanodots (NDs) onto TiO₂ nanoparticles (NPs) and Janus-typed Cu_{2-x}S-CuInS₂ nano-heterostructures in aqueous and organic solution respectively. Three different metal NDs, i.e., Au, Ag, Pd, are introduced on the surface of TiO₂ NPs, and Au NDs are deposited on Cu_{2-x}S/CuInS₂. Several techniques, including TEM/HRTEM, EDS mapping, and UV-vis spectroscopy, are performed to characterize the size, morphology, and distribution of the metal NDs. Au-TiO₂ nanoheterodimers (NHDs) are successfully synthesized and a close to 100% yield of Au-TiO₂ NHDs is achieved by managing the concentration of TiO₂ NPs and gold precursor. Especially, the adsorption mechanism of methanol and gold precursor on TiO₂ during photodeposition is investigated. By comparing the experimental data obtained in microchannels and cuvette setups, the established model describes the overall dynamic process of Au ND growth on TiO₂ from 1/3 growth state to completion. The final size of Au NDs can be accurately predicted by the model in particular the growth completion. In addition, other metal Ag and Pd NPs were deposited on the surface of TiO₂, and Ag-TiO₂ and Pd-TiO₂ NHDs are also synthesized. The effects of the hole scavenger, laser power, and exposure time on the size, and distribution of metal NDs are investigated. Moreover, the growths of Ag and Pd NDs both follow the proposed model for Au growth. The project is extended to bimetallic core-shell NDs photodeposition and Au, Ag and Pd are introduced on Au-TiO₂ NHDs by a second step photodeposition, forming a core-shell structure on the surface of TiO₂ NPs. For the Au@Au core@shell, the Au shell can be precisely controlled by varying the gold precursor concentration and the size and thickness of the Au core and shell pretty much fit our expectations. For the Au@Ag system, the Ag shell obtained is limited to around 1 nm thickness which results from the low electronegativity of Ag (1.9) compared to other Au (2.4). For the Au@Pd system, Pd shows a non-isotropic growth on the Au core resulting in a nonuniform Pd shell due to the big lattice mismatch between Au and Pd. Finally, Au NDs are introduced onto Cu_{2-x}S/CuInS₂ heteronanorods by photodeposition in toluene with a blue laser. The nucleation and growth of Au NDs are studied and the geometric distribution (e.g., number and location) of Au NDs, as well as their sizes, can be well controlled by tuning laser power, exposure time, hole scavengers, and precursors concentration.

Keywords : Noble metal, Laser, photodeposition, heterostructures, metal oxide, and cadmium-free semiconductors

Unité de recherche 5026

Institut de Chimie de la Matière Condensée de Bordeaux (ICMCB), UMR5026